Rapid Curing and Boron Modification of Polysilazane-Derived Functional Coatings

TECHNISCHE
UNIVERSITÄT
DARMSTADT

Disperse
Feststoffe

MERCK

Rapid Curing and Boron Modification of Polysilazane-Derived Functional Coatings

Schnelle Aushärtung und Bormodifizierung Polysilazan-abgeleiteter funktionaler Schichten

Genehmigte kumulative Dissertation von M.Sc. Ying Zhan aus Jiangxi, China

Fachbereich Material- und Geowissenschaften

Darmstadt, Technische Universität Darmstadt

Jahr der Veröffentlichung der Dissertation auf TUprints: 2022

URN: urn:nbn:de:tuda-tuprints-230048

Tag der Einreichung: 16.09.2022

Tag der mündlichen Prüfung: 27.10.2022

Erklärungen laut Promotionsordnung

§8 Abs. 1 lit. c PromO

Ich versichere hiermit, dass die elektronische Version meiner Dissertation mit der schriftlichen Version übereinstimmt.

§8 Abs. 1 lit. d PromO

Ich versichere hiermit, dass zu einem vorherigen Zeitpunkt noch keine Promotion versucht wurde. In diesem Fall sind nähere Angaben über Zeitpunkt, Hochschule, Dissertationsthema und Ergebnis dieses Versuchs mitzuteilen.

§9 Abs. 1 PromO

Ich versichere hiermit, dass die vorliegende Dissertation selbstständig und nur unter Verwendung der angegebenen Quellen verfasst wurde.

§9 Abs. 2 PromO

Die Arbeit hat bisher noch nicht zu Prüfungszwecken gedient.

Darmstadt, den 16.09.2022

_____

(Ying Zhan)

The present cumulative dissertation summarizes the essential scientific findings reported to the scientific community in the following peer-reviewed articles. Article reprints [1]–[3] are enclosed in the Chapter *Publications* at the end of this work.

[1] **Y. Zhan**, R. Grottenmüller, W. Li, F. Javaid, R. Riedel, Evaluation of mechanical properties and hydrophobicity of room-temperature, moisture-curable polysilazane coatings, *Journal of Applied Polymer Science*, 138 (2021) 50469.

[2] **Y. Zhan**, W. Li, R. Grottenmüller, C. Minnert, T. Krasemann, Q. Wen, R. Riedel, Rapid curing of polysilazane coatings at room temperature via chloride-catalyzed hydrolysis/condensation reactions, *Progress in Organic Coatings*, 167 (2022) 106872.

[3] **Y. Zhan**, W. Li, T. Jiang, C. Fasel, E. Ricohermoso, J. Bernauer, Z. Yu, Z. Wu, F. Müller-Plathe, L. Molina-Luna, R. Grottenmüller, R. Riedel, Boron-modified perhydropolysilazane towards facile synthesis of amorphous SiBN ceramic with excellent thermal stability, *Journal of Advanced Ceramics*, 11 (2022) 1104–1116.

Acknowledgments

Abstract

The growing demand for high-performance and long-lasting materials in our society has promoted the robust development of coating systems. Polysilazane is among the most widely investigated types of coating materials due to its strong adhesion to almost all kinds of substrate materials and its great potential to be modified to obtain tailored properties for a variety of applications. This dissertation presents the simple and cost-effective preparation of polysilazane-based coatings intended to be applied as protective, easy-to-clean, and anti-corrosion coatings in the field of automotive and transportation, architecture and construction, and industrial facilities.

A typical spin coating process followed by moisture curing under ambient conditions is employed to obtain polysilazane coatings with industrial favorable thicknesses (5–7 μm). A systematic study of six polysilazane coatings provides insight into the relationship between moisture curing behavior, film formation, and final coating properties. The molecular structure of polysilazanes is found to play a key role in the crosslinking rate and degree, thereby affecting the coating performance. An intuitive guide to selecting suitable polysilazanes for specific applications is provided.

Though moisture curing is of advantage to real-life applications, it often takes a longer time than other curing methods to crosslink organopolysilazane (OPSZ) films at room temperature. Two approaches have been developed to facilitate the moisture curing of OPSZ coatings. In the first approach, the curing time of OPSZ coating is shortened from 19 h to 1 h with the assistance of a nucleophilic catalyst, tetrabutylammonium chloride (TBAC). It is found that 1.6 times more of the Si–H and Si–NH groups are hydrolyzed, and 2 times more of the Si–O–Si groups are formed in the TBAC-catalyzed OPSZ coating. The significantly increased crosslinking rate and degree result in a dense and smooth film with double value of hardness and quadruple value of elastic modulus compared to the uncatalyzed coating. In the second approach OPSZ is reacted with borane dimethyl sulfide complex to obtain highly crosslinked boron-modified OPSZ (BOPSZ) prior to the coating process. The resultant BOPSZ coating exhibits not only improved moisture curing rate and degree, but also higher hydrophobicity (contact angle = 101.1°) as opposed to the boron-free OPSZ coating with a contact angle of 88.7°. Enhanced corrosion resistance of the BOPSZ coating against HCl is thus achieved. So far, polysilazane coatings with outstanding surface hardness, high hydrophobicity, and remarkable chemical stability are successfully prepared at room temperature with greatly reduced processing time. Moreover, the thermal behavior and polymer-to-ceramic conversion of boron-modified perhydropolysilazanes are experimentally and theoretically studied. Boron incorporation induces the formation of rigid

B–N bonds, which restricts the atomic motion of nitrogen in the ternary Si–B–N network. Therefore, the crystallization of the amorphous silicon nitride is suppressed, and the thermal stability is improved. A preliminary groundbreaking work for the development of SiBN ceramic coatings as e.g. thermal barrier coating is laid.

Zusammenfassung

Die in unserer Gesellschaft wachsende Nachfrage nach leistungsstarken und langlebigen Materialien hat zu einer zunehmenden Entwicklung von Beschichtungssystemen geführt. Hierbei zählen Polysilazane zu den am meisten untersuchten Beschichtungsmaterialien, da sie eine starke Haftung auf zahlreichen unterschiedlichen Substratmaterialien aufweisen, sowie die Möglichkeit bieten, maßgeschneiderte Eigenschaften für eine Vielzahl von Anwendungen zu erzielen. In dieser Dissertation wird eine einfache, kostengünstige Herstellungsmethode Polysilazan-basierter Beschichtungen vorgestellt, welche als schützende, leicht zu reinigende und korrosionsbeständige Schicht, in den Bereichen Automobil und Transport, Architektur und Bauwesen, sowie in industriellen Anlagen Anwendung finden.

Ein typisches Spin-Coating-Verfahren mit anschließendem Feuchtigkeitshärten unter Umgebungsbedingungen wird verwendet, um Polysilazan-Beschichtungen mit einer industriell präferierten Schichtdicke (5–7 μm) zu erhalten. Sechs verschiedene Polysilazan-Schichten werden systematisch untersucht, um Aufschluss über die Zusammenhänge zwischen Aushärtungsverhalten, Schichtbildung und den daraus resultierenden Beschichtungseigenschaften zu erhalten. Die Molekularstruktur der Polysilazane ist ausschlaggebend für deren Vernetzungseigenschaften und Vernetzungskinetik und beeinflusst daher die Leistung der Beschichtung. Ein intuitiver Leitfaden für die Auswahl anwendungsbezogener Polysilazane wird bereitgestellt.

Obwohl die Feuchtigkeitshärtung bei realen Anwendungen von Vorteil ist, dauert die Vernetzung von Filmen aus Organopolysilazan (OPSZ) bei Raumtemperatur oft länger als bei anderen Härtungsmethoden. Zwei Ansätze wurden entwickelt, um die Feuchtigkeitshärtung zu erleichtern. Beim ersten Ansatz lässt sich die Aushärtezeit der OPSZ mit Hilfe des nukleophilen Katalysators Tetrabutylammoniumchlorid (TBAC) von 19 auf 1 Stunde verkürzen. Durch die Verwendung des Katalysators werden 1,6-mal mehr Si–H und Si–NH Gruppen hydrolysiert und die Anzahl an Si–O–Si Gruppen in der OPSZ-Beschichtung wird verdoppelt. Die deutlich erhöhte Vernetzungsrate und der erhöhte Vernetzungsgrad führen zur Bildung eines dichten und glatten Films mit doppelter Härte und vierfachem Elastizitätsmodul verglichen mit der nicht katalysierten Beschichtung. Beim zweiten Ansatz wird vor dem Beschichtungsverfahren hochvernetztes Bor-modifiziertes OPSZ (BOPSZ) durch Reaktion von OPSZ mit Borandimethylsulfid-Komplex hergestellt. Die daraus resultierende BOPSZ Beschichtung weist neben einer verbesserten Feuchtaushärtungsgeschwindigkeit und einem stärkerem Vernetzungsgrad auch eine höhere Hydrophobie mit einem Kontaktwinkel von 101,1° im Vergleich zur OPSZ Beschichtung mit 88,7° als Kontaktwinkel auf. Dadurch wird eine

verbesserte Korrosionsbeständigkeit gegen HCl erzielt. Polysilazan-Beschichtungen mit herausragender Oberflächenhärte, hoher Hydrophobie und bemerkenswerter chemischer Stabilität wurden bei Raumtemperatur mit deutlich verringerter Prozessdauer erfolgreich hergestellt. Des Weiteren wird die thermische Stabilität sowie die Polymer-Keramik-Transformation eines mit Bor-modifizierten Perhydropolysilazans experimentell und theoretisch untersucht. Die Zugabe von Bor führt zur Bildung starrer B–N Bindungen, welche die atomare Bewegung von Stickstoff im ternären Si–B–N einschränken. Auf diese Weise wird die Kristallisation von amorphem Siliziumnitrid unterdrückt und die thermische Stabilität erhöht. Hierdurch ist ein erster Grundstein zur Entwicklung keramischer SiBN-Beschichtungen z. B. als Wärmedämmschicht gelegt.

Table of Contents

List of Abbreviations

3D	Three-dimensional
APTES	3-Aminopropyltriethoxysilane
ATR	Attenuated total reflection
BMS	Borane dimethyl sulfide
BOPSZ	Boron-modified organopolysilazane
BPHPS	Boron-modified perhydropolysilazane
BPSZ	Boron-modified polysilazane
CA	Contact angle
CSM	Continuous stiffness measurement
D1033	Durazane 1033
D1500-rc	Durazane 1500 rapid cure
D1500-sc	Durazane 1500 slow cure
D1800	Durazane 1800
D2250	Durazane 2250
D2850	Durazane 2850
DTA	Differential thermal analysis
EDX	Energy dispersive X-ray spectroscopy
FTIR	Fourier-transform infrared spectroscopy
GPC	Gel permeation chromatography
HRTEM	High-resolution transmission electron microscopy
MD	Molecular dynamics
MS	Mass spectrometry
MSD	Mean-square displacement
NMR	Nuclear magnetic resonance

OPSZ	Organopolysilazane
PC	Polycarbonate
PDC	Polymer-derived ceramics
PDF	Pair distribution function
PHPS	Perhydropolysilazane
PSZ	Polysilazane
RH	Relative humidity
RT	Room temperature
SAED	Selected area electron diffraction
SEM	Scanning electron microscopy
TBAC	Tetrabutylammonium chloride
TBAF	Tetrabutylammonium fluoride
TEM	Transmission electron microscopy
TG	Thermogravimetry
TGA	Thermogravimetric analysis
THF	Tetrahydrofuran
XRD	X-ray diffraction

List of Symbols

h_c	Contact depth
h_f	Film thickness
h_{max}	Maximum displacement
h_r	Residual displacement
E_i	Elastic modulus (of the indenter)
E_r	Reduced modulus
P_{max}	Maximum load
v_i	Poisson's ratio (of the indenter)
h	Penetration displacement
θ	Contact angle
A	Contact area
E	Elastic modulus, Young's modulus (of the sample)
H	Hardness
P	Load
Ra	Roughness average
S	Initial unloading stiffness
k	Empirically determined constant
v	Poisson's ratio (of the sample)
α	Empirically determined constant
π	Mathematical constant
ω	Angular velocity
ϵ	Geometric constant

List of Figures

List of Tables

1. Introduction

The continuous development of society promotes the advancement of materials towards high performance, cost efficiency, and long-lasting durability. However, environmental factors (weathering, high humidity or temperature, exposure to salt water, etc.), normal wear and tear, and possible vandalism (e.g., graffiti) can cause corrosion, damage, or even failure of many types of materials. These material flaws can be highly concerning in the application fields such as marine sectors, automotive parts, building facades, and industrial facilities due to maintenance and safety requirements. In these cases, coatings are often applied as an efficient solution to provide protection, give specific functions, keep up appearances, and extend the lifetime of the substrate materials by modifying their surface properties.

Over the last two decades, silicon-containing polymers have attracted a considerable amount of attention as suitable coating materials owing to their superior thermal stability and chemical resistance compared to most organic coating materials [4,5]. Among them, polysilazane consisting of Si–N–Si backbone emerged as an outstanding coating material due to its i) liquid nature, which enables simple and cost-effective deposition methods [6]; ii) strong adhesion to a variety of materials (metals, plastics, glasses, and ceramics) by chemical bonding [7]; and iii) potential to be modified and functionalized for different applications. Moreover, polysilazanes are known as precursors for preparing multielement ceramics at relatively low temperatures via the polymer-derived ceramics route, which gives rise to a simple fabrication of ceramic coatings for components with complex shapes [8].

In view of the above-mentioned advantages, polysilazane coatings have been extensively studied for applications such as dielectric, anti-graffiti, anti-adherent, anti-corrosion, anti-scratch, environmental barrier, and thermal barrier coatings [9–13]. The global polysilazane market was valued at USD 14.64 million in 2021 and is expected to grow at a compound annual growth rate of 17.68% from 2021 to 2027 [14]. The market share of industrial coatings accounts for 80% of all applications (industrial coatings, ceramic precursors, composite materials, others). Though it is an expanding field with great potential, there are still challenges to overcome. Currently, research on polysilazane coatings is mostly focused on addressing the following objectives:

i. *Performance enhancement*. Improvement of coating properties such as hardness, chemical stability, uniformity, etc.

ii. *Tailoring of coating properties.* Chemical modification of polysilazanes before the coating process allows obtaining coatings with tailored thermal, hydrophobic, electric properties, etc.

iii. *Preparation of polysilazane-derived ceramic coatings.* Investigation of the polymer-to-ceramic transformation and property optimization of the obtained ceramic coatings.

In this dissertation, polysilazane coatings are prepared via spin coating followed by moisture curing under ambient environment and temperature. The crosslinking behavior, film formation, and resulting properties of different polysilazane coatings are systematically studied in the first section. The second and third sections describe two approaches for preparing polysilazane coatings with significantly enhanced film quality, mechanical properties, hydrophobicity, and chemical stability. Performance improvement of the films is achieved by adding a nucleophilic catalyst tetrabutylammonium chloride to increase the curing rate and degree of polysilazanes. Coatings with tailored hydrophobicity and chemical stability are attained by boron modification of polysilazanes. Both methods considerably shorten the processing time by accelerating the curing process. In addition, the thermal behavior and polymer-to-ceramic conversion of boron-modified polysilazanes are elaborated, which lays the foundation for the fabrication of ceramic coatings.

2. Fundamentals

This chapter introduces the fundamentals related to the research findings underlying in this dissertation, including the theoretical background and the state of the art.

2.1. Polysilazanes

Polysilazanes (PSZ) are polymers consisting of basic Si–N backbone with various reactive and/or inert side groups attached to the Si or N atoms. Depending on the type of the side groups, polysilazanes are classified into inorganic and organic polysilazanes. The typical inorganic polysilazane is perhydropolysilazane (PHPS) with exclusively hydrogen side groups, as shown in Figure 2.1a. In organopolysilazane (OPSZ, Figure 2.1c), at least one carbon-containing side group (CH_3, $HC=CH_2$, etc.) is bonded to the silicon atom. Both PHPS and OPSZ follow a complex macromolecular structure consisting of linear, cyclic, and three-dimensional chains with a wide range of molecular weight, as shown in Figure 2.1b and d, respectively [15,16].

(a)　　　　　　　　　　(b)

(c)　　　　　　　　　　(d)

R = H, CH_3, $HC=CH_2$, $(CH_2)_3Si(OEt)_3$
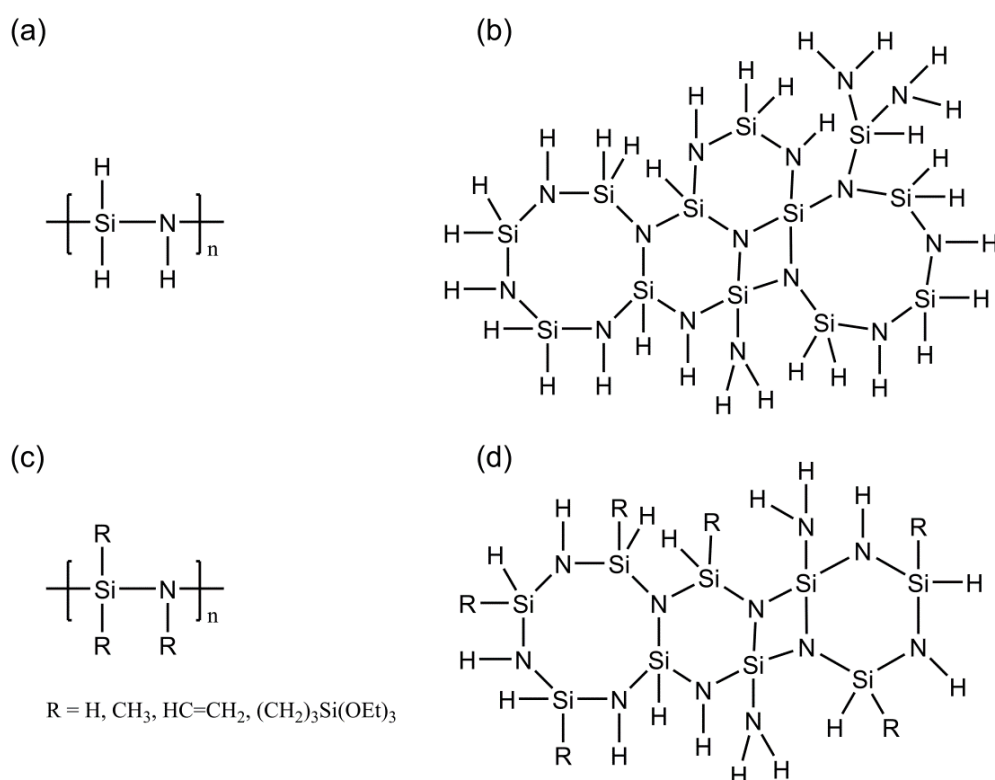
Figure 2.1 Simplified chemical formulas of (a) perhydropolysilazane (PHPS) and (c) organopolysilazane (OPSZ). (b) and (d) illustrate the possible molecular structures of PHPS and OPSZ, respectively.

Several methods to synthesize polysilazanes have been extensively investigated. Most of these methods can be classified into three categories: i) polycondensation of halide substituted silanes

and amines; ii) ring-opening polymerization of cyclosilazanes; iii) copolymerization of cyclosilazanes [17]. Due to its simplicity, the most commonly used synthesis route of polysilazane is polycondensation of aminosilanes obtained by ammonolysis or aminolysis of chlorosilane, as shown in Figure 2.2. In the two-step reactions, chlorine atoms of the starting material, dichlorosilane, are first substituted by ammonia or different amines to form aminosilanes, which subsequently condense to PHPS (when R = H) or OPSZ (when R = CH_3, $HC=CH_2$, etc.).
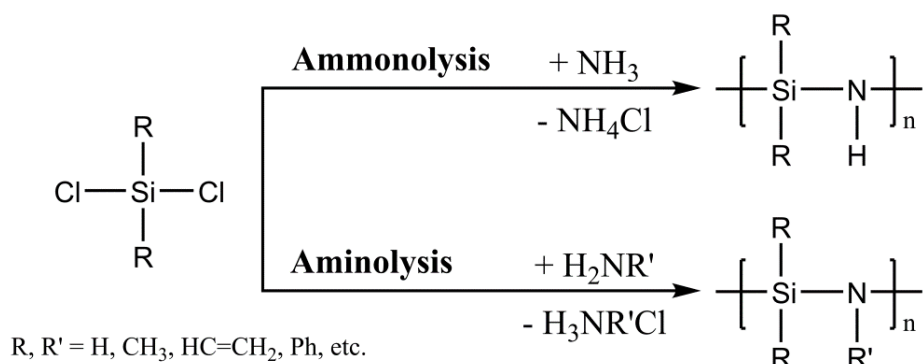
Figure 2.2 Synthesis routes of polysilazane by ammonolysis or aminolysis of dichlorosilane. Adapted from [18].

The ammonolysis and aminolysis of dihalogenosilanes were first reported by Stock and Somieski [19] for the synthesis of oligosilazanes in 1921. In 1964, Krüger and Rochow successfully prepared OPSZ by ammonolysis of organosilicon chlorides and discussed in detail the structure, spectra, properties, and reactions [20]. A large number of studies and patents followed up and have been summarized in several review articles [6,8,18,21,22].

One main disadvantage of these synthesis routes is the difficulty to remove the precipitated NH_4Cl or $H_3NR'Cl$ formed during the reactions from the polymeric product [23], which is both time-consuming and cost-intensive. Another problem is that these methods produce a high proportion of low molecular weight species that are easily volatile [16]. An improved synthesis method, which was developed by Abel et al. [24] in 1999 to tackle the above-mentioned problems, is currently used in the industry (Merck KGaA) for the manufacture of polysilazanes. In this method, chlorosilanes are added to an excess of liquid ammonia that applies as a reactant and as a solvent. The reaction byproduct NH_4Cl or $H_3NR'Cl$ dissolves in liquid ammonia, which facilitates the isolation of polysilazane products. In addition, the ionized and dissolved NH_4Cl catalyzed the substitution of Si–H bond with Si–Cl bond, which further ammonolyze to form aminosilanes that condense to polysilazanes with linear and cyclic structures.

At present, a wide product portfolio of polysilazanes is commercially available. Polysilazanes with various side groups are synthesized by ammonolysis of dichlorosilanes with different R

groups (Figure 2.2). Six of them have been investigated in this work, namely Durazane 1033 (D1033), Durazane 1500 rapid cure (D1500-rc), Durazane 1500 slow cure (D1500-sc), Durazane 1800 (D1800), Durazane 2250 (D2250), and Durazane 2850 (D2850), which are produced by Merck, KGaA, Darmstadt (Figure 2.3).

The most known application of polysilazanes is as polymeric precursors in the field of polymer-derived ceramics (PDCs). After thermal treatment in an inert atmosphere, polysilazanes can be transformed into Si_3N_4 and SiCN ceramics with tailored molecular structures [6,25]. Due to the versatile possibilities of processing and shaping complex ceramic systems via the PDC route compared to conventional processing of ceramic powders or pastes, polysilazanes are promising precursors for the production of ceramic fibers [26–31], ceramic-matrix composites [32–35], highly porous components [36–38], anode material for energy storage application [39–41], etc. Particularly, polysilazane is widely considered a promising material for coating applications, which will be discussed further in Chapter 2.4.
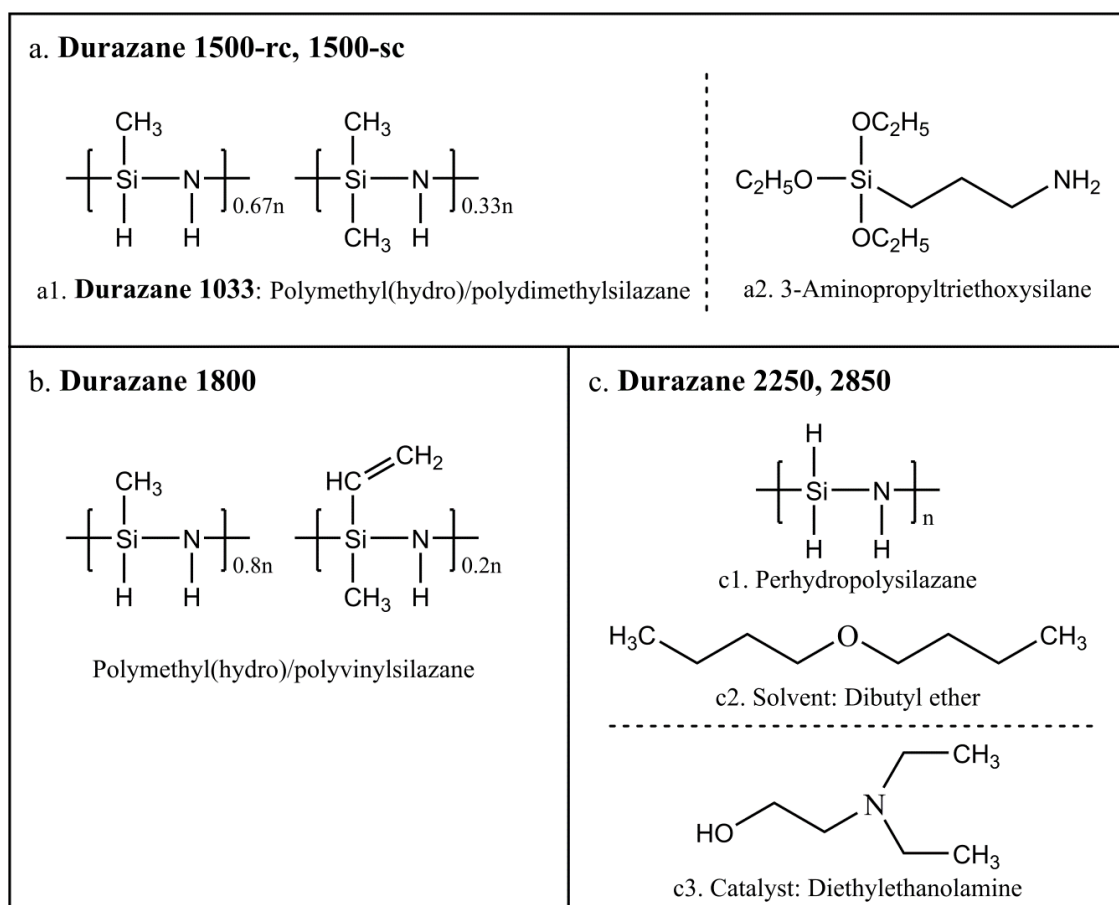
Figure 2.3 Molecular structures of Durazane polysilazanes. (a) Durazane 1500 is 3-aminopropyltriethoxysilane-modified Durazane 1033 (a1). Durazane 1500 rapid cure (rc) has a higher fraction of 3-aminopropyltriethoxysilane than Durazane 1500 slow cure (sc). (b) Durazane 1800. (c) Durazane 2250 (20 wt% solution of perhydropolysilazane (c1) in dibutyl ether (c2)). Durazane 2850 is produced by further adding 0.5 wt% of diethylethanolamine (c3) as a catalyst. Adapted from Ref. [1] with permission of John Wiley and Sons.

2.2. Curing behavior of polysilazanes

Polysilazanes can be converted to organic/inorganic materials with three-dimensional structures via the crosslinking process. Through proper curing processes, mixtures of oligomers and low molecular weight polysilazanes are transformed into infusible and insoluble thermosets, resulting in changes in composition and properties, and an increase in ceramic yield during the PDC transformation process [5,16,42]. The most common techniques to induce crosslinking reactions are thermal treatment [9,43–46], moisture curing [47–52], vacuum ultraviolet radiation in the presence of oxygen [53–55], and plasma polymerization [56,57]. In this work, crosslinking of polysilazanes was carried out mainly by moisture curing and thermal curing.

2.2.1. Thermal curing

Thermal curing of polysilazanes is of advantage in processing PDCs due to its simplicity and no introduction of additional elements into the polymer structure [22]. Depending on the substituted side groups, four major reactions can take place during the thermal curing of polysilazanes under inert atmosphere: i) hydrosilylation (100–120 °C), ii) transamination (200–400 °C), iii) dehydrocoupling (ca. 300 °C), and iv) vinyl polymerization (> 300 °C) [6,35,46,58–62].

As illustrated in Figure 2.4a, transamination reactions occur in the temperature range of ca. 200–400 °C with the release of ammonia, resulting in mass loss and reduced nitrogen content in the final product. Dehydrocoupling reactions (Figure 2.4b) involving Si–H and N–H groups start at ca. 300 °C with the generation of hydrogen and lead to the formation of Si–Si and Si–N bonds. Polysilazanes that have unsaturated vinyl groups can additionally be crosslinked by hydrosilylation reactions and vinyl polymerization. Hydrosilylation reactions (Figure 2.4c) occur in different positions of the vinyl groups at relatively low temperatures (100–120 °C) and form Si–C–Si and Si–C–C–Si bridges. Polymerization of the vinyl groups (Figure 2.4d) occurs at higher temperatures (> 300 °C) and no mass loss is involved. According to the investigation of Yive et al. [45], the crosslinking activity of these four reactions is sorted as: hydrosilylation > dehydrocoupling > transamination > vinyl polymerization.

a. Transamination

$$3 \ -Si-N(H)-Si- \ \longrightarrow \ 2 \ -Si-N(Si)-Si- \ + \ NH_3$$

b. Dehydrocoupling

$$-Si-N(H)-Si- \ + \ -Si-H \ \longrightarrow \ -Si-N(Si)-Si- \ + \ H_2$$

$$2 \ -Si-H \ \longrightarrow \ -Si-Si- \ + \ H_2$$

c. Hydrosilylation

$$-Si-H \ + \ -Si-CH=CH_2$$

α - addition $\longrightarrow \ -Si-CH(CH_3)-Si-$

β - addition $\longrightarrow \ -Si-CH_2-CH_2-Si-$

d. Vinyl polymerization

$$n \ (-Si-)HC=CH_2 \ \longrightarrow \ [(-Si-)CH-CH_2]_n$$
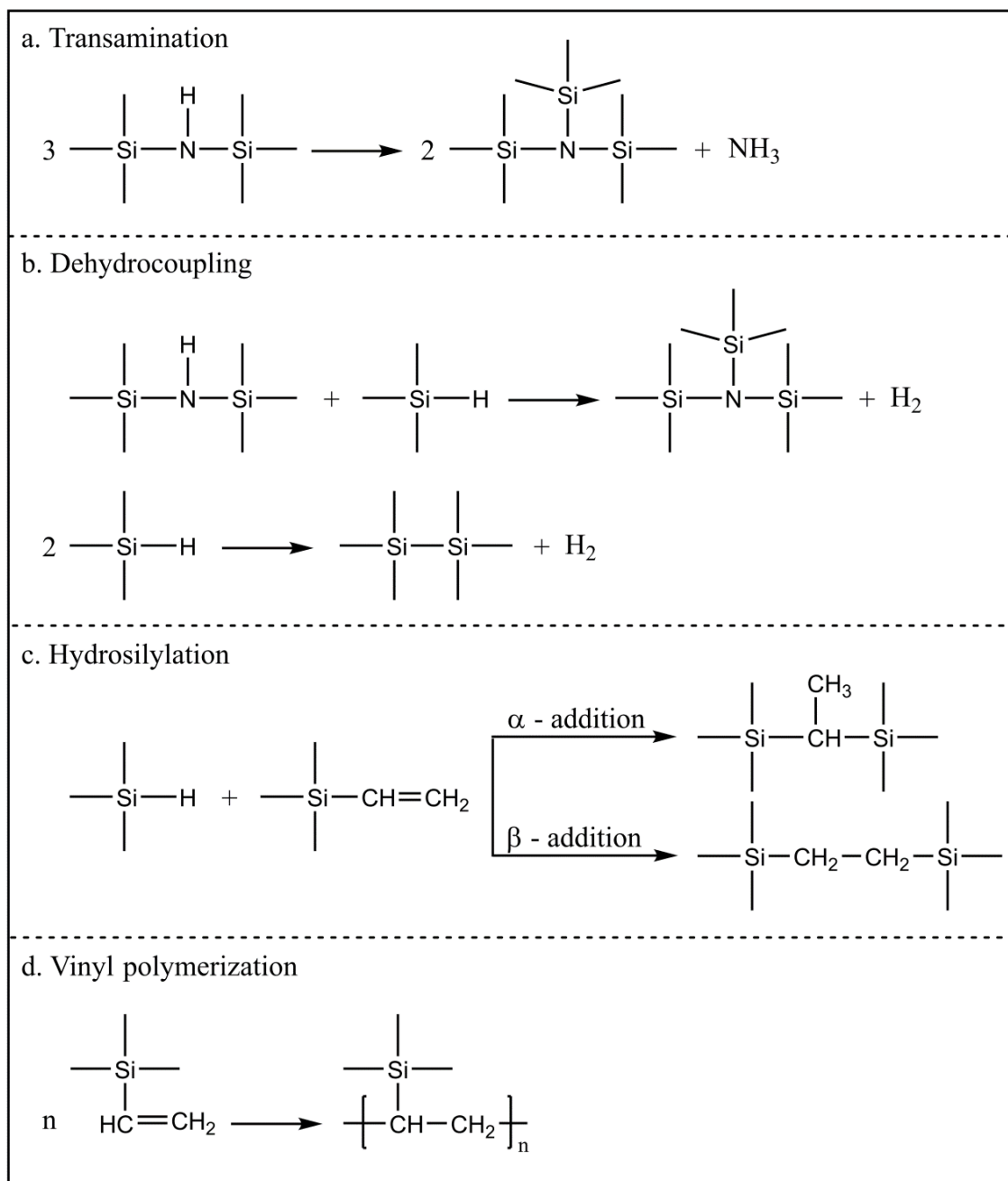
Figure 2.4 Thermal curing mechanisms of polysilazanes: (a) transamination; (b) dehydrocoupling; (c) hydrosilylation; and (d) vinyl polymerization reactions.

2.2.2. Moisture curing

Polysilazanes with hydrolyzable side groups, e.g. Si–H, Si–NH, and Si-OEt groups, can be crosslinked via hydrolysis and condensation reactions in ambient environment at low temperatures or even at room temperature [17,49,63]. This feature is of advantage for the cost-effective and easy-to-handle preparation of polysilazane-based coatings, especially where a substrate with a low melting point is used and thermal curing is not applicable [10,13,50,64,65]. As shown in Figure 2.5a, the presence of atmospheric water leads to hydrolysis of Si–H, Si–NH,

and Si–OEt groups, forming Si–OH groups with the release of hydrogen, ammonia, and ethanol, respectively. Subsequent condensation (Figure 2.5b) of the formed silanol group with another silanol group, or with Si–H and Si–NH$_2$ groups takes place, and Si–O–Si network is formed. Condensation of the silanol groups was found to proceed instantaneously after the hydrolysis reaction, indicating that hydrolysis is the rate-limiting step in the moisture curing of polysilazanes [47,50,66].
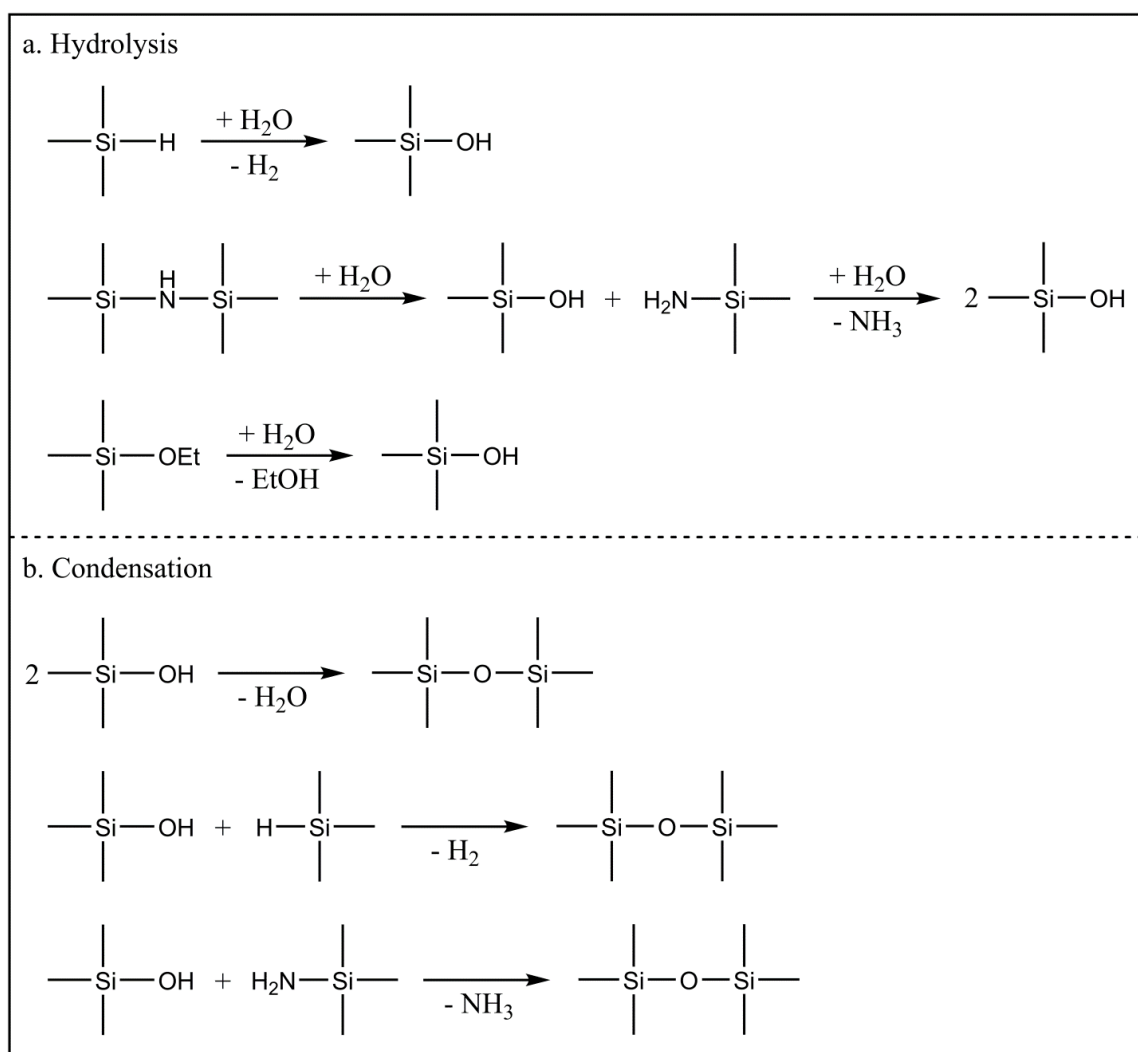
Figure 2.5 Moisture curing mechanisms of polysilazanes: (a) hydrolysis and (b) condensation reactions.

The crosslinking behavior of polysilazanes is directly influenced by the substituted side groups. It was reported by Marceaux et al. [65] that Si–OEt group has the highest hydrolysis rate among the three mentioned hydrolyzable groups. Dargère et al. [63] have systematically investigated the hydrolysis–condensation reactions of hydridosilazane and concluded that Si–NH group has higher reactivity towards hydrolysis than Si–H group, which has been confirmed by Müller et al. [47] Non-hydrolyzable side groups on the Si atoms, i.e. Si–CH$_3$ and Si–CH=CH$_2$ groups, were

reported to have a steric hindrance effect on the hydrolysis of polysilazanes [50,63]. Consequently, OPSZ that have abundant inert side groups are less reactive to hydrolysis compared with PHPS and hence crosslink slower in this way.

2.2.3. Acceleration of the curing processes

External assistance is often applied to accelerate the moisture curing of polysilazanes. Increasing temperature (up to 400 °C) is found to be a simple and effective way to increase the curing rate of polysilazanes under ambient environment [7,10,48,51,67–70]. The rise of temperature provides energy for both the hydrolysis and condensation reactions and a complete crosslinking of polysilazanes can be achieved [71]. However, the positive effect of temperature increase on the curing rate is compensated by a decrease in humidity. It was reported by Müller et al. [47] and Bauer et al. [50] that the hydrolysis rate can be enhanced by increasing the humidity [47,50]. Though the impact of humidity on the curing rate at room temperature is insignificant in ambient atmosphere (relative humidity > 20%), it becomes evident in very dry atmosphere, i.e., relative humidity lower than 7%. Therefore, a moistening furnace is recommended for accelerating the moisture curing process [50].

The use of catalysts is preferred in some studies to accelerate the curing process of polysilazanes near room temperature as no additional equipment is required. Ammonia and amines are extensively applied as efficient basic catalysts to accelerate the curing of polysilazanes [15,50,64,66,67,71–74]. By exposing to ammonia vapor or immersing in aqueous ammonia or amine solutions, hydrolysis of polysilazanes is highly promoted in terms of efficiency and crosslinking degree [67,71]. Hydrogen peroxide has also been proved to be an effective oxidizing catalyst for accelerating the moisture curing of polysilazane [67,71,75,76]. It was found by Morlier et al. [71] that after immersion into a hydrogen peroxide solution for a short time, hydrolysis of Si–H and Si–NH groups was almost completed and led to the formation of highly hydroxylated silica. In recent years, the well-known nucleophilic catalyst tetrabutylammonium fluoride (TBAF) is given special attention for controllable and selective crosslinking of OPSZ [13,29,77,78]. The Si–H bonds are nucleophilically activated by TBAF for simultaneous reactions with N–H groups and O–H groups, and the crosslinking rate and degree are hence increased [79–81]. Additionally, calcium borohydride bis(tetrahydrofuran) is used as an inhibitor to terminate the crosslinking of polysilazane, resulting in crosslinked polysilazanes with controlled meltability and viscoelasticity for the manufacture of fibers.

In this work, tetrabutylammonium chloride (TBAC) is applied as an effective catalyst for the curing of polysilazane in ambient atmosphere and temperature without the use of any inhibitors or additional equipment.

2.3. Boron modification of polysilazanes

Chemical modification of polysilazanes has been widely investigated to incorporate additional elements for the production of quaternary Si–M–C–N (M = B, Al, Ti, Zr, Fe, Hf, etc.) ceramics with desired properties via the PDC route [22,35,82–91]. It has been shown that the chemical modification strongly influenced i) the crosslinking behavior of the polymeric precursors, ii) the thermal stability, iii) the crystallization behavior, and iv) the microstructure of the resulting Si–M–C–N ceramics.

Boron modification of polysilazanes as precursors has received much attention in the last decades due to the highly improved thermal stability, creep and oxidation resistance, and high-temperature mechanical properties of Si–B–C–N ceramics obtained by the PDC route [92–97]. It was found by Riedel et al. [92] that the polyborosilazane-derived $Si_{3.0}B_{1.0}C_{4.3}N_{2.0}$ ceramic was thermally stable against decomposition up to temperatures of ca. 2000 °C, while SiCN materials started to decompose at temperatures above 1400 °C. Due to their superior properties, boron-modified polysilazanes (BPSZ) derived SiBCN ceramics have aroused great enthusiasm among researchers in the fabrication of fibers [28,98–100], coatings [101–104], matrix composites, and monoliths [33,105–111].

Boron modification of polysilazanes is achieved by chemical reactions between the functional groups of polysilazanes and boron compounds, i.e. boranes, borazines, BCl_3, borate derivatives, etc [93,101,102,112–118]. Synthesis of boron-modified polysilazanes and the transformation of BPSZ to Si–B–C–N ceramics have been comprehensively summarized in several review articles [22,59,88,119–121]. Among the great variety of possible boron modification methods for polysilazanes, hydroboration (Figure 2.6a) [122,123] or dehydrocoupling (Figure 2.6b) [124] reactions between the vinyl groups or N–H groups and the boranes are frequently used to prepare BPSZ, where boron is appropriately distributed in the materials [125–134]. Viard et al. [133] have investigated in detail the chemical mechanisms involved in the modification of a poly(vinylmethyl-co-methyl)silazane with different amounts of borane dimethyl sulfide (BMS). Combining FTIR and NMR results, they have found that hydroboration reaction was predominant when the boron content is low. As the boron content increased (5 < Si/B ≤ 15), hydroboration and dehydrocoupling were competing reactions, and at a certain Si/B ratio (≤ 5) dehydrocoupling solely occurred. The incorporation of boron has been proven to highly increase the crosslinking degree of the modified-polysilazanes. Therefore, the chemistry and crosslinking degree of BPSZ can be well-controlled by varying the boron content, and the processability of the precursor is improved.

This work has investigated the effect of boron incorporation on the crosslinking and pyrolytic behaviors of polysilazanes with different substituted groups. The synthesized boron-modified polysilazanes have been applied for the preparation of hydrophobic coating and SiBN ceramic.
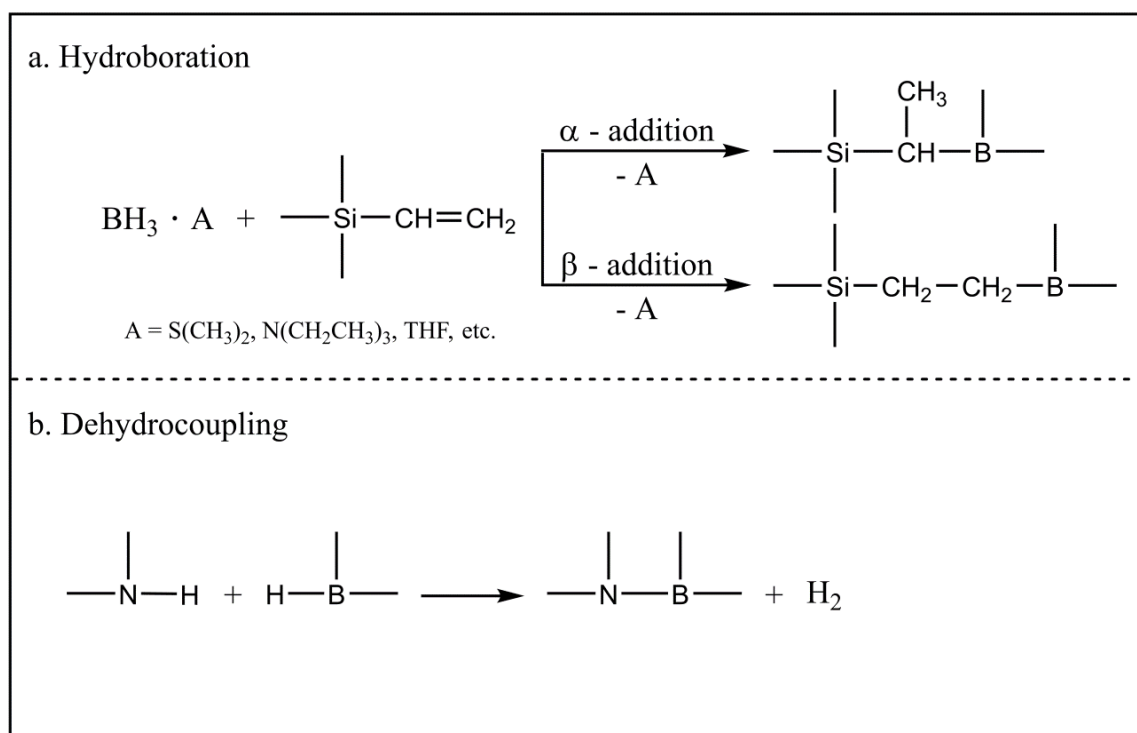
Figure 2.6 Boron modification of polysilazanes using borane complexes: (a) hydroboration and (b) dehydrocoupling reactions.

2.4. Polysilazane-derived coatings

Polysilazanes have been broadly applied as coating materials because of their strong adhesion to nearly all kinds of substrate materials and potential to be modified and tailored to obtain specific properties for different applications [5,7,30]. Taking advantage of its liquid nature, most of the economic and simple deposition techniques are applicable to polysilazane systems, such as dip coating [50,74], spin coating [55,72], spray coating [13,135], roll coating [136], etc.

After deposition, polysilazane coatings are crosslinked to thermoset materials with enhanced thermal, mechanical, and chemical stability [11,67,73,137,138]. These polymeric coatings with tailored molecular structures and chemical compositions have been studied to modify surface properties of common structural materials for various applications, such as anti-graffiti [10,68,139], anti-fouling [65,140,141], anti-adherent [13], anti-corrosive [48,77,140,142], and gas barrier coatings [53,71,136,143,144].

Polysilazane coatings can be further converted into SiO_2, SiCO, SiCN, or Si_3N_4 ceramic coatings via the PDC route [52,135,145–151]. In some cases, suitable fillers were introduced into the systems to minimize or compensate the shrinkage of precursors during pyrolysis [12,52,70,152–154]. Thus, thicker ceramic coatings (> 1 μm) can be obtained without cracking and spalling. Due to their superior thermal and mechanical properties, polysilazane-derived ceramic coatings are promising candidates for inter-layer dielectrics [9,155], corrosion-resistant coatings [52,145,153], oxidation-resistant coatings [146,152,156,157], thermal and environmental barrier coatings [12,54,158–160], wear protection coatings [161], and high-end membranes with controlled porosity [38,104].

2.4.1. Spin coating technique

Spin coating technique was chosen in this work for the highly reproducible fabrication of polysilazane coatings with controllable film thickness. Due to its comprehensive advantages of low cost, simple operation, high reproducibility, and low amount of coating material required, spin coating has been extensively studied theoretically and experimentally [162–168].

Spin coating (Figure 2.7) can be divided into three consecutive processes: i) deposition, ii) liquid ejection, and iii) solvent evaporation [169–171]. A certain amount of coating material is first deposited at the center of a substrate, which is either static or spinning at a low angular velocity. The material is then centrifugally driven and ejected from the edge of the substrate at a higher spin speed. Evaporation of solvents occurs during and after the spinning process, resulting in the formation of a film with desired thickness.
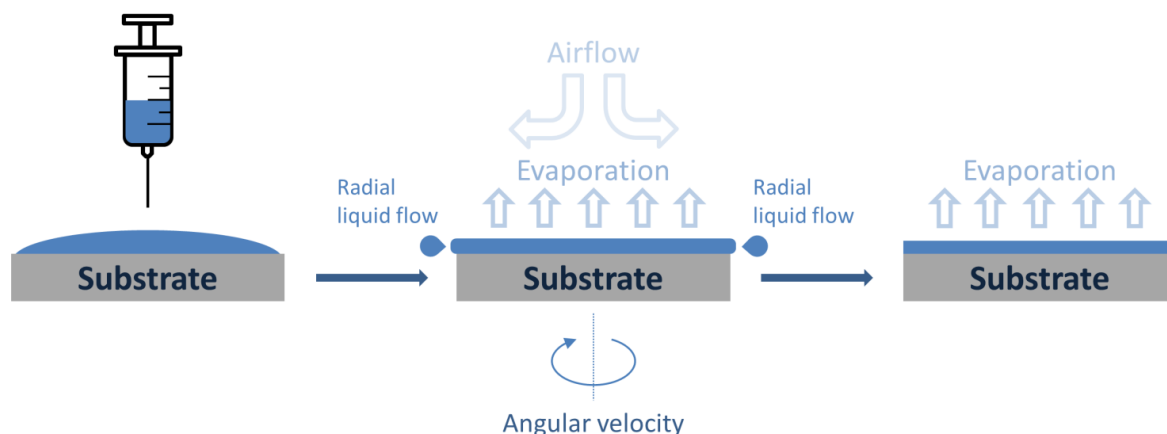
Figure 2.7 Schematics of the spin coating processes using a static dispense method: i) deposition (left), ii) liquid ejection (middle), and iii) solvent evaporation (right).

Several processing parameters are involved in the spin coating processes, e.g., dispense volume, spin speed, acceleration, spin time, etc. The correlation between processing parameters and film thickness has been studied in a great deal of experimental work and concludes in a generalized form [169,172]:

$$h_f = k\omega^{-\alpha} \tag{2-1}$$

where h_f is the film thickness, ω is the angular velocity, while k and α are empirically determined constants. As the angular velocity increases, the degree of centrifugal force increases. Thus, more material is ejected from the substrate and a thinner film is obtained. Constants k and α are mainly affected by the physical properties of the coating solutions, i.e., viscosity, concentration of the solutes, volatility of the solvent, and wettability of the polymer to the substrates [167,173–175]. The dispense volume, rate of deposition, and spin time have been found to have limited or no effects on the film thickness [173,176]. In addition to the intrinsic properties of the coating solution, the morphology of the spin-coated films is influenced by the polymer/substrate and polymer/air interfacial interactions [169,177]. In summary, the selection of suitable processing parameters for the production of uniform films with desired thickness should be adjusted accordingly for different materials.

2.4.2. Properties

Adhesion

Polysilazanes are well-known to have good adhesion to a variety of substrate materials, such as metals, glasses, ceramics, plastics, etc. The strong adhesion of polysilazanes to the substrates is

obtained through physical and chemical interactions [7,178]. Owing to the low surface tension of the liquid coating solutions, good wetting of polysilazanes onto the substrates is acquired, which allows a physical adhesion of polysilazane to a rough surface by mechanical interlocking [117,178,179]. However, for substrates with small surface roughness, the contribution of physical adhesion to total adhesion is low. The strong adhesion is mainly attributed to the chemical interactions between the polysilazane coatings and the substrates [7,13,69,178]. As shown in Figure 2.8, polysilazanes with Si–H and Si–NH groups react with –OH groups at the surface of substrates, forming oxygen bridges between the coating and substrate with the release of H_2 and NH_3. In addition, hydrolysis of Si–H and Si–NH groups occurs in the presence of humidity to form silanol groups, which condense subsequently with –OH groups at the surface of substrates, leading to the formation of oxygen bridges and release of water (see Figure 2.5).
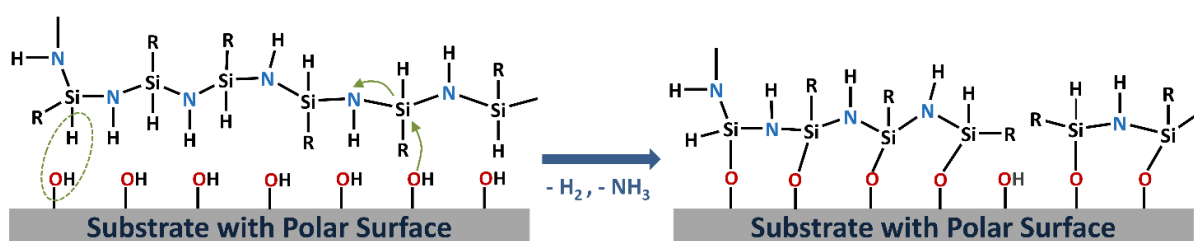
Figure 2.8 Chemical reactions between Si–H, Si–NH groups of polysilazane and –OH groups at the surface of the substrate lead to the formation of oxygen bridges, and thus strong adhesion of the polysilazane coating to the substrate.

To achieve good adhesion of polysilazane coating to the substrate, pre-treatments of the substrate are essential. A cleaning procedure of the substrate is normally carried out prior to the coating process to remove possible contaminations or weak boundary layers, which are detrimental to the formation of covalent bonds between coating and substrate [5,180]. Depending on the materials, substrates can be cleaned mechanically (e.g., by grinding and polishing) and chemically (e.g., by solvents, acids, or bases) [178,181]. Furthermore, suitable surface engineering, e.g., sandblasting, chemical etching, plasma treatment, etc., has been conducted in some studies to improve the adhesion of polymers to metals by either increasing the surface roughness or cleaning and activating the surface of substrates [10,12,47,65,69,139,149,181,182].

Adhesion can be quantitatively evaluated by direct adhesion measurements such as peel tests, lap shear tests, scratch tests, etc., along with visual characterizations of the fracture surface [178,183,184]. Depending on the type of test, different mechanical forces are applied to break, tear, or delaminate the coatings on the substrate. The failure resistance of the coating under

mechanical forces reflects the strength of adhesion. In this work, a standard cross-cut test (DIN EN ISO 2409) [185] has been applied to evaluate the adhesion of polysilazane coatings to different substrates.

Mechanical properties

Measuring and understanding the mechanical response is critical for material research and application development. Hardness (H) and elastic modulus (E) are among the most extensively studied mechanical properties of polysilazane coatings [5,179].

In general terms, hardness is an engineering property that implies the resistance of a material to plastic deformation under mechanical forces. It can be affected by various factors including i) nature of the material (e.g., atomic bond energy), ii) film properties (e.g., microstructure of the film, film thickness, type of substrate), iii) testing parameters (e.g., testing methods, shape of indenter, temperature), etc. [186,187]. On the contrary, elastic modulus is an intrinsic property of a material, which implies the resistance of the material to elastic deformation and is often referred to as Young's modulus. At a fundamental level, elastic modulus is a measure of interatomic bond energy and atomic packing density [6].

Measurements of the hardness and elastic modulus of polysilazane-based coatings cured or pyrolyzed under different conditions have been carried out in several studies. Günthner et al. [52] have investigated the change of H and E during the conversion of polysilazane films to amorphous ceramic films in nitrogen and in air. They have found that both H and E improved with the increase of pyrolysis temperature, which was attributed to the increased crosslinking degree and densification of the films during the heat treatment. This finding has been confirmed in other research articles [9,30,73,160]. In this regard, several approaches to promote a higher degree of crosslinking of polysilazane-based coatings have been explored such as exposure to ammonia, immersion in a liquid solution of hydrogen peroxide, and additional ultraviolet irradiation, etc., which all led to the increase in both H and E [66,67]. Furthermore, the pyrolysis atmosphere has been shown to have an explicit influence on the H and E [52]. In the temperature region up to 400 °C, polysilazane-based coatings showed higher H and E because the crosslinking in air was faster than that in nitrogen. At temperatures above 800 °C, polysilazane coatings pyrolyzed in air transformed to SiO_x films, which had lower H and E values than that of the Si(C)N films obtained by pyrolyzing polysilazane coatings in nitrogen. This can be explained by the more rigid bonding architecture of Si(C)N than that of SiO_x systems [6].

Nanoindentation is an advanced method for determining the hardness and elastic modulus of thin films. One of the most important improvements in nanoindentation testing is the

continuous stiffness measurement (CSM) technique, which allows dynamic measurements of mechanical properties at any point along the loading process [188–191]. During CSM, a load to the indenter tip is applied to force the tip into the surface while simultaneously superimposing a harmonic force to enable a minimal harmonic displacement (2–4 nm). A typical load-displacement curve attained by performing a nanoindentation CSM on an elastoplastic material with a Berkovich indenter is shown in Figure 2.9 (left), where P and h designate the load and penetration displacement, respectively. The deformation patterns formed during the indentation processes are illustrated on the right side of Figure 2.9.
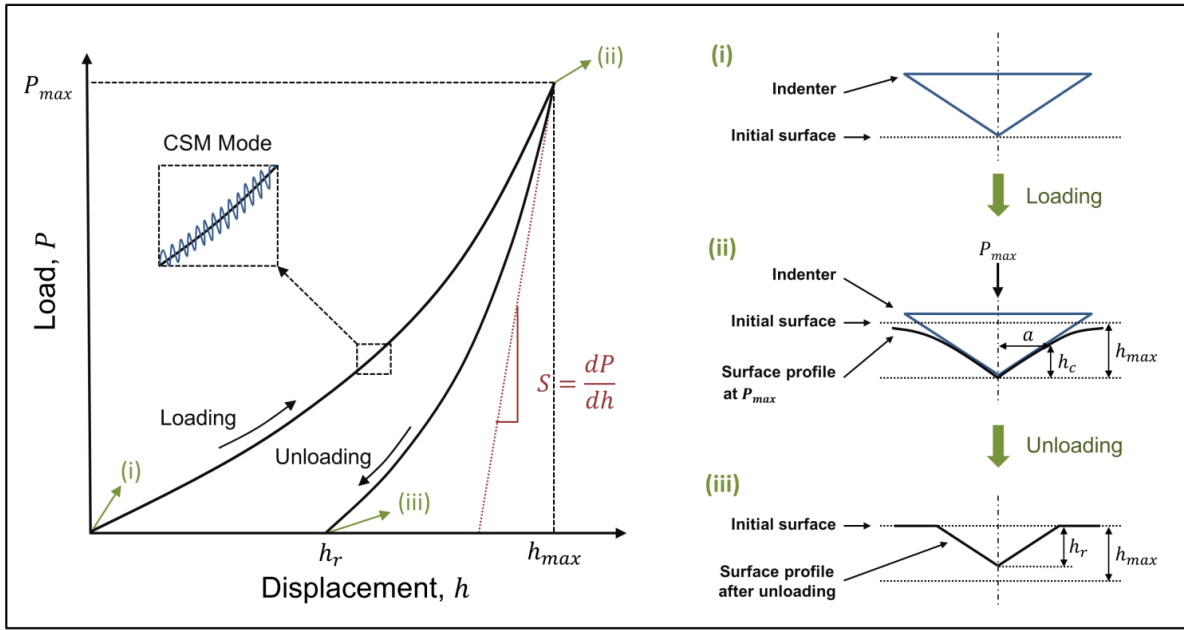
Figure 2.9 Left: A typical load-displacement curve obtained from a nanoindentation continuous stiffness measurement (CSM) on an elastoplastic material. Right: Deformation patterns formed during nanoindentation processes with a Berkovich indenter (i) before loading, (ii) at the maximum load, and (iii) after unloading. Based on Oliver and Pharr. [189]

Several important quantities can be extracted from the load-displacement curve: the maximum load P_{max}, the maximum displacement h_{max}, the initial unloading stiffness S, and the residual displacement h_r. According to the Oliver and Pharr model [188,189], hardness and elastic modulus can be calculated using the following equations. Hardness is defined as:

$$H = \frac{P_{max}}{A} \tag{2-2}$$

where P_{max} is the maximum load and A is the contact area, which is a function of the contact depth h_c:

$$A = F(h_c) \, . \tag{2-3}$$

The area function is established after the tip geometry calibration. The contact depth h_c is defined as the depth where the indenter is in contact with the specimen. It can be calculated using Eq. (2-4):

$$h_c = h_{max} - \epsilon \frac{P_{max}}{S} \tag{2-4}$$

where h_{max} is the displacement at the maximum load, ϵ is a constant that depends on the geometry of the indenter, and S is the initial unloading stiffness. S is given by:

$$S = \frac{dP}{dh} = \frac{2}{\sqrt{\pi}} E_r \sqrt{A} \tag{2-5}$$

where E_r is the reduced modulus, which is defined by

$$\frac{1}{E_r} = \frac{(1 - v^2)}{E} + \frac{(1 - v_i^2)}{E_i} \tag{2-6}$$

where E and E_i are elastic modulus of the sample and indenter, respectively. v and v_i are Poisson's ratio of the sample and indenter, respectively.

Hydrophobicity

Hydrophobicity is a physical property describing the water repellency of a material. A hydrophobic surface is only partially wetted or not wetted by water molecules. To quantify the wettability of a solid surface by a liquid, Thomas Young [192] defined an angle of contact between the solid-liquid interface and the liquid-vapor interface, which is denoted as contact angle θ. The trigonometric relations between the contact angle and the forces acting on a liquid droplet in equilibrium on a solid surface are illustrated in Figure 2.10 and described in the Young equation:

$$\gamma_{SV} = \gamma_{SL} + \gamma_{LV} \cos \theta \tag{2-7}$$

where θ is the contact angle, γ_{SV}, γ_{SL}, and γ_{LV} are the solid-vapor, solid-liquid, and liquid-vapor interfacial tensions, respectively.

Conventionally, a surface is considered hydrophobic when its static water contact angle θ is greater than 90° and hydrophilic when θ is smaller than 90° [193]. The contact angle of OPSZ-derived coatings is typically in the range of 90–100°, which enables applications such as anti-graffiti, anti-adherent, and self-cleaning coatings [10,11,13,194]. In order to further enhance the hydrophobicity, some researchers modified polysilazanes with fluorine compounds to decrease the surface energy [69,77,195]. The resulting fluorine-modified polysilazane coatings are

superamphiphobic with a water contact angle up to 175° ± 3° [69]. Barroso et al. [13] introduced poly(tetrafluoroethylene) particles into the polysilazane coatings and hence increased the water contact angle up to 144.6° ± 5.3° due to the reduction of the surface free energy. Wang et al. [70] have systematically investigated the change of surface energy as a function of temperature during the conversion of PHPS to amorphous SiON films in air. They have found that the contact angle of the PHPS films decreased abruptly at the temperature of ca. 300 °C, which was attributed to the compositional and microstructural evolutions during the heat treatment and thus resulted in an increase in surface energy. Similar findings that the contact angle decreases with increasing temperature (in certain temperature windows) have been reported in other research articles [9,13,138].

Hydrophobicity characterization of polysilazane-based coatings is often done by measuring the static contact angle using the sessile drop method with a goniometer [139,142,158]. The equilibrium shape of the water drop is captured by a camera and the contact angle is determined by fitting the contour of the drop and the baseline at the solid-liquid interface (see Figure 2.10).
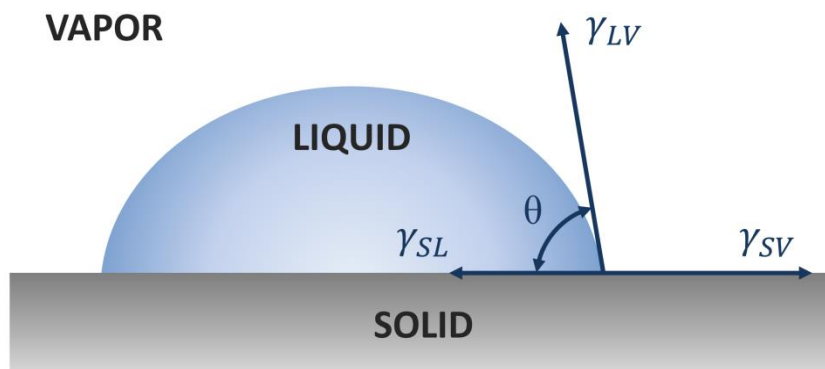
Figure 2.10 Schematic of a liquid drop on an ideal solid surface, where θ is the contact angle, γ_{SV} is the surface tension of the solid, γ_{LV} is the surface tension of the liquid, and γ_{SL} is the solid-liquid interfacial tension.

3. Results and Discussion

This chapter mainly summarizes and discusses the major scientific findings published in the research articles [1–3]. In Section 3.1, a comparative evaluation of the curing behavior and physical properties of six commercially available polysilazane coatings is presented. The molecular structure of polysilazanes is found to play a key role in the coating-substrate adhesion and the physical properties of the resulting films. Based on the molecular structure, an intuitive guide to the coating material selection is provided. In order to increase the curing rate and degree of polysilazane coating under ambient atmosphere and temperature, tetrabutylammonium chloride (TBAC) is introduced to the polysilazane system as an effective catalyst. A dense and smooth film free from large irregularities with improved hardness and elastic modulus is thus obtained. The catalytic effect of TBAC on the moisture curing of polysilazane coating is detailed in Section 3.2. The final section (Section 3.3) exhibits the successful synthesis of several boron-modified polysilazanes (BPSZ) for the preparation of hydrophobic coating and amorphous SiBN ceramic. The chemical and thermal stability of the polysilazane-derived coatings and ceramics are highly improved in the presence of boron.

3.1. Curing behavior and physical properties of polysilazane coatings: A comparative evaluation

The content of this chapter is partially published in:

[1] **Y. Zhan**, R. Grottenmüller, W. Li, F. Javaid, R. Riedel, Evaluation of mechanical properties and hydrophobicity of room-temperature, moisture-curable polysilazane coatings, Journal of Applied Polymer Science, 138 (2021) 50469.

In the present chapter, the moisture-curing behavior of bulk polysilazane is investigated by elemental analysis and Fourier-transform infrared spectroscopy (FTIR). Based on our former work [196], six commercially available polysilazanes have been spin-coated on polycarbonate (PC) substrates and cured under ambient atmosphere and temperature. Comprehensive characterizations of the curing behavior, film thickness, coating-substrate adhesion, surface morphology, mechanical properties, and hydrophobicity of the PSZ coatings have been conducted. Finally, a benchmark evaluation of the curing rate and physical properties of different polysilazane-derived coatings is presented.

Durazane 1500 rapid cure (Figure 2.3a) consisting of polymethyl(hydro)/polydimethylsilazane (D1033) and 3-aminopropyltriethoxysilane (APTES) substituted groups was applied as an example for the investigation of moisture-curing behavior of polysilazanes. 50 mL of Durazane

1500-rc liquid was cured at room temperature (RT, ~23 °C) for 168 h either in synthetic dry air (water content < 2 ppmv) or ambient air (with 40%–55% relative humidity). Variation of elemental oxygen and nitrogen contents in the D1500-rc samples during the curing process was analyzed and is shown in Figure 3.1a. In the absence of water, oxygen and nitrogen contents in D1500-rc remain unchanged, indicating that polysilazane is stable against oxidation in air at RT. When exposed to the ambient environment with relative humidity (RH) of 40% to 55%, the nitrogen content of cured D1500-rc decreases from 15.0 ± 0.1 wt% to 4.7 ± 0.1 wt%, and the oxygen content increases from 7.4 wt% to 28.2 ± 0.3 wt% after 168 h of curing. Figure 3.2 presents the suggested crosslinking mechanisms of D1500-rc cured in ambient air. During the crosslinking process, Si–H, Si–NH, and Si–OC$_2$H$_5$ groups are converted to Si–O groups via hydrolysis and condensation reactions (see Subsection 2.2.2). Theoretically, the pristine D1500-rc contains 16.8 wt% of nitrogen and 7.2 wt% of oxygen (from APTES), while the completely converted D1500-rc contains 2.3 wt% of nitrogen and 29.1 wt% of oxygen. The calculated elemental contents are in good agreement with the experimental results. Based on the theoretical oxygen content, the crosslinking degree of D1500-rc is calculated. As can be seen in Figure 3.1b, most of the crosslinking reactions (90.2% ± 0.7%) take place in the first 72 h. Afterward, the curing process slows down and 95.0% ± 1.4% of the reactions are complete after 168 h of curing. A plateau state of curing is reached. The FTIR spectra shown in Figure 3.1c correspond well with the elemental analysis results. As the curing time increases, Si–H (at ca. 2125 cm^{-1}) and Si–NH (at 1168 cm^{-1}) groups are continuously consumed via hydrolysis reactions, accompanied by the generation of H$_2$ and NH$_3$, respectively. The formed Si–OH groups subsequently condense to Si–O–Si (at ca. 1022 cm^{-1}) groups and hence increase the oxygen content. Moreover, Si–O–R groups (at 1077 and 1105 cm^{-1}) from APTES are transformed into Si–O–Si with the release of C$_2$H$_5$OH [50,52]. Finally, almost all hydrolyzable groups in D1500-rc are consumed and converted to Si–O–Si groups after 168 h of curing.
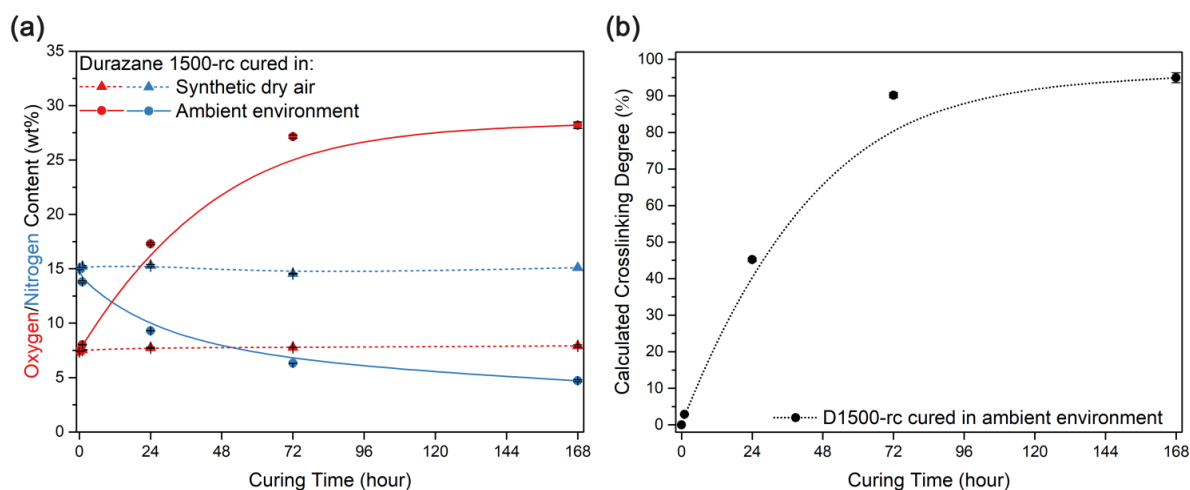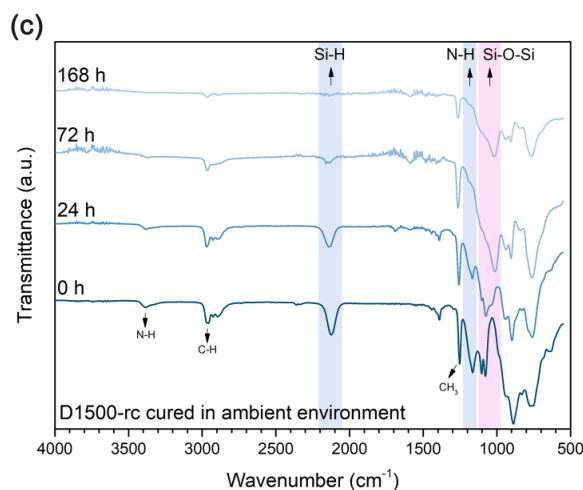
Figure 3.1 (a) Elemental contents of oxygen and nitrogen in the Durazane 1500-rc cured in synthetic dry air and ambient environment at room temperature as a function of curing time. (b) Calculated Crosslinking degree of D1500-rc after curing in ambient environment for 1, 24, 72, and 168 h (based on the calculation of theoretical oxygen content). (c) ATR-FTIR spectra of D1500-rc after 0, 24, 72, and 168 h of curing in ambient environment. Adapted from Ref. [1] with permission of John Wiley and Sons.
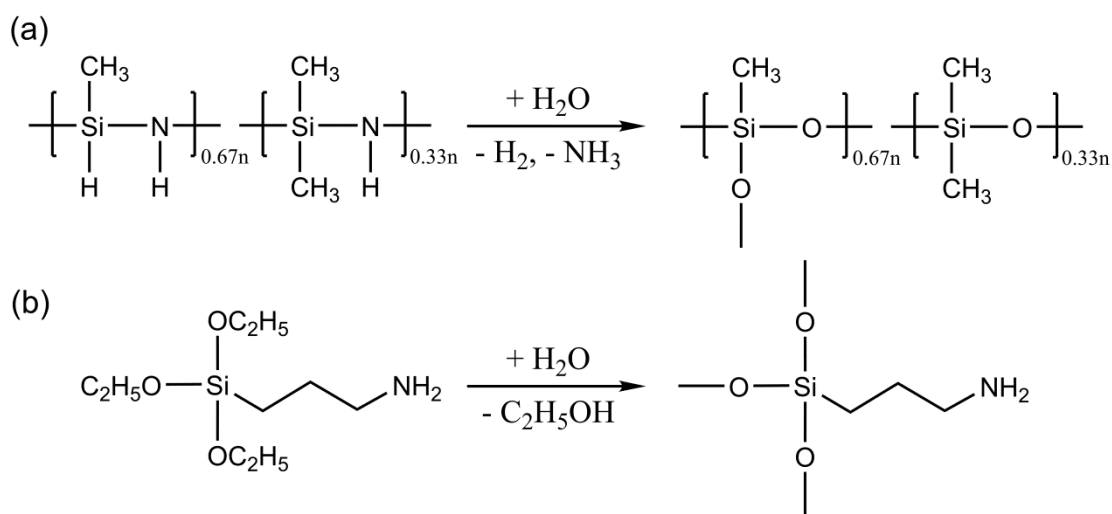
Figure 3.2 Theoretical crosslinking routes of Durazane 1500-rc cured in water containing environment, assuming i) the (a) polymethyl(hydro)/polydimethylsilazane and (b) 3-aminopropyltriethoxysilane (APTES) are physically mixed in the D1500-rc solution, and ii) all of the Si–H, Si–NH, and Si–OC$_2$H$_5$ groups are transformed to Si–O groups via hydrolysis and condensation reactions. Adapted from Ref. [1] with permission of John Wiley and Sons.

Six polysilazanes with different composition (see Figure 2.3), denoted as D1033, D1500-rc, D1500-sc, D1800, D2250, and D2850, were spin-coated on polycarbonate substrates. During the coating process, different spin speeds were selected for each organopolysilazane (because of their different viscosity) to obtain films with an industrially favorable thickness of 5 to 7 μm. Coatings derived from perhydropolysilazanes, which contain 80% of solvent, are much thinner

with a thickness of ca. 1.5 μm. The applied spin speed and the profilometer-measured film thickness of polysilazane coatings are listed in Table 3.1.

The spin-coated polysilazane films were crosslinked to solid films in ambient environment and temperature. The dry to touch time (see Table 3.1), which is commonly used in the coating industry to indicate the time when the coated films can be handled and processed without being damaged, is employed to estimate the curing rate of the polysilazane coatings. Perhydropolysilazane coatings with large numbers of hydrolyzable side groups (Si–H, Si–NH) and thinner film thickness present the shortest dry to touch time (0.5 min for D2850, 6 min for D2250), indicating a fast curing process. Organopolysilazane coatings containing side groups (Si–CH$_3$, Si–CH=CH$_2$) that are inert at RT cure much slower. D1800 coating requires ca. 32 h to reach the dry to touch condition, while D1033 coating needs 19 h. With the addition of APTES, D1500-sc and D1500-rc coatings crosslink faster, which need respectively 80 min and 26 min to achieve the dry to touch state.

The obtained polysilazane films (except for D1033 coating) are dense, transparent, crack-free, and have a smooth and even surface morphology as shown in Figure 3.3b (where D1500-rc coating is taken as an example) and Figure 3.4. Durazane 1033 consisting of a large amount of Si–CH$_3$ groups exhibits a poor wetting on the PC substrate, resulting in the failure of film formation (Figure 3.3c). Two methods of improving the D1033 coating have been investigated and will be presented in Sections 3.2 and 3.3.
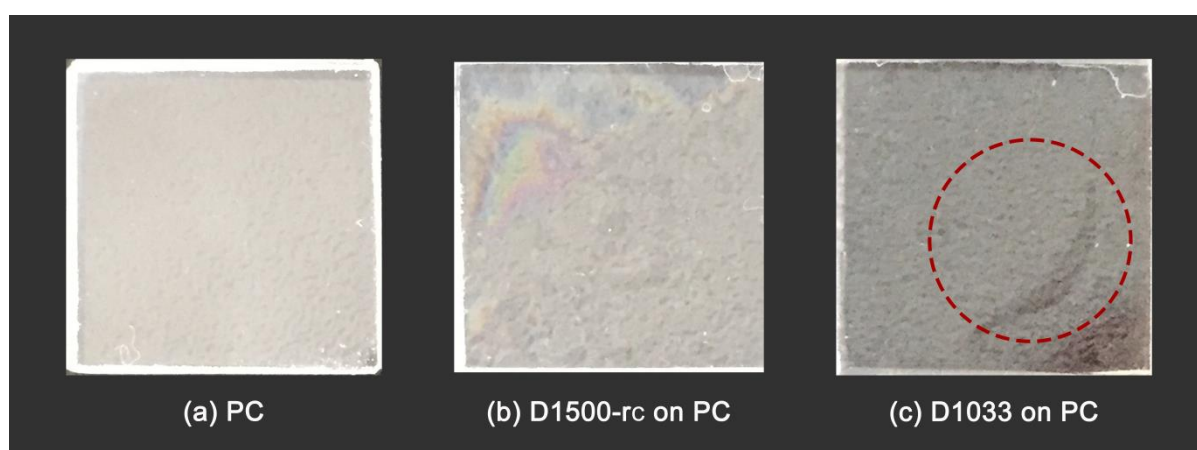
Figure 3.3 Optical images of (a) polycarbonate substrate, (b) Durazane 1500-rc coating, and (c) Durazane 1033 coating cured in ambient environment and temperature for 24 h. Due to insufficient wetting, D1033 failed to form a film on the substrate.
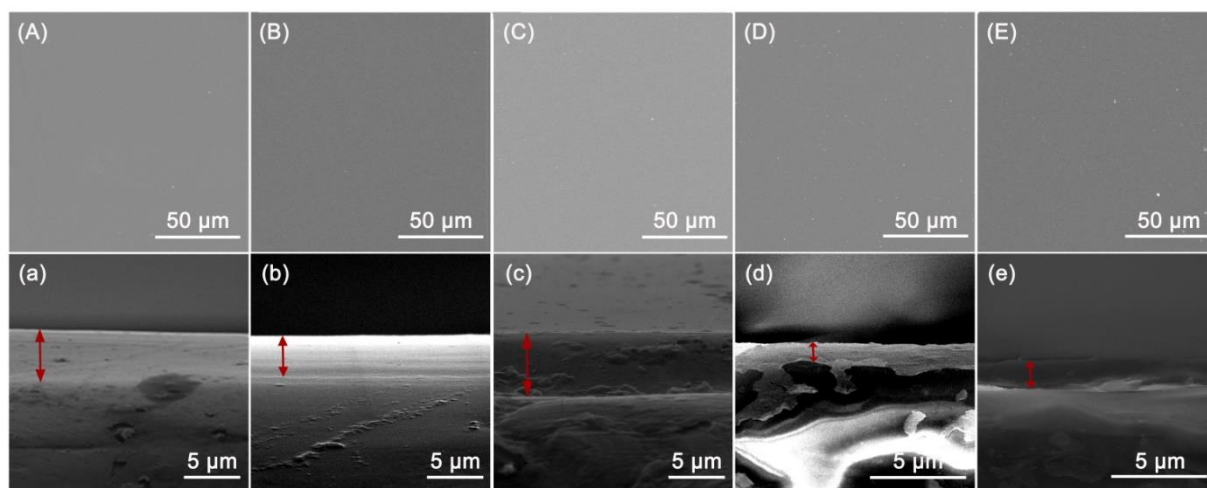
Figure 3.4 SEM images of the (A–E) surfaces and (a–e) cross-sections of D1500-rc, D1500-sc, D1800, D2250, and D2850 coatings, respectively, cured in ambient environment and temperature for 30 d. Adapted from Ref. [1] with permission of John Wiley and Sons.

Nanoindentation was used to determine the hardness and elastic modulus of polysilazane coatings. During the curing process, the H and E values of the PSZ coatings increase along with the curing time until reaching a plateau, which to a certain extent indicates the limits of the crosslinking degree for the specific PSZ coating. The time for different PSZ coatings to reach the plateaus is detailed in Ref. [1]. Table 3.1 lists the H and E values of different PSZ coatings after curing under ambient conditions for 30 d. A clear difference between OPSZ coatings (D1500-sc, D1500-rc, and D1800) and PHPS coatings (D2250, D2850) is shown. Among the three investigated OPSZ coatings, D1500-rc coating possesses the highest hardness and elastic modulus of 0.29 GPa and 2.9 GPa, respectively. D1500-sc coating that has fewer APTES-substituted groups exhibits lower hardness (0.11 GPa) and elastic modulus (1.4 GPa). D1800 coating shows the lowest hardness (0.05 GPa) and modulus (0.4 GPa) since it has the least amount of hydrolyzable groups, which leads to the lowest crosslinking degree among all the investigated polysilazanes. Compared to the OPSZ coatings, PHPS coatings have a larger amount of Si–H and Si–NH groups, which react with water to form a rigid Si–O–Si network. The higher crosslinking degree of PHPS coatings leads to higher H and E values. The hardness and elastic modulus of D2250-derived coating are measured as 0.64 GPa and 3.58 ± 0.01 GPa, respectively. D2850 coating (PHPS with 0.5 wt% diethylethanolamine) has the highest values of hardness (1.89 ± 0.01 GPa) and elastic modulus (8.5 ± 0.03 GPa) among all investigated films. Furthermore, the H and E of the used polycarbonate substrate are 0.19 GPa and 2.9 GPa, respectively. The relatively higher H and E values of D1500-rc, D2250, and D2850 films imply potential applications of the polysilazanes as protective coatings for PC-based materials.

The water contact angle is measured to assess the hydrophobicity of polysilazane coatings. In the crosslinking process, the water contact angle of PSZ coating first decreases because of the consumption of hydrophobic Si–H groups and the formation of hydrophilic Si–OH and Si–NH$_2$ groups [1]. Subsequent condensation reactions deplete the Si–OH and Si–NH$_2$ groups, forming a 3D Si–O–Si network. The diffusion and reorientation of polar Si–O bonds toward the polar water droplet is hindered by the highly crosslinked Si–O–Si network. A hydrophobic recovery [197,198] of the PSZ coatings is observed. Eventually, the water contact angle stabilizes when the curing plateau (as described above) is reached. The contact angle of PSZ coatings after curing in ambient environment and temperature for 30 d is compared in Table 3.1. Organopolysilazane coatings having abundant hydrophobic groups (e.g., Si–CH$_3$ and Si–CH=CH$_2$ groups) that are excluded from the crosslinking reactions at RT are hydrophobic. D1800 coating displays the largest contact angle of 103.3° ± 0.5°, while D1500-sc and D1500-rc coatings have contact angles of 98.4° ± 2.4° and 95.4° ± 0.7°, respectively. The defective D1033 film exhibits a contact angle of 90.9° ± 0.8°. On the contrary, the PHPS-based D2250 and D2850 coatings are considered hydrophilic with contact angles of 83.9° ± 0.8° and 85.9° ± 0.8°, respectively.

Adhesion of polysilazane coatings on polycarbonate substrates is optically evaluated after the standard cross-cut tape tests. Figure 3.5 compares the optical microscopy images of cross-cut polysilazane coatings after curing for 1, 3, and 7 d under ambient conditions. Based on the DIN EN ISO 2409 [185], coatings are graded from Gt 0 (best adhesion, no detachment of the coating after the test) to Gt 5 (worst adhesion, detachment of the coating > 65% of the tested area). D1500-sc (Figure 3.5b) and D1800 (Figure 3.5c) coatings demonstrate excellent adhesion to the polycarbonate substrate once they are dry to touch. The fast-cured D1500-rc coating with a higher amount of 3-aminopropyltriethoxysilane shows the worst adhesion to PC. The entire coating has been peeled off during the pull-off test (Figure 3.5a). The adhesion of PHPS coatings to PC develops with the curing time. On the 1st day of curing, D2250 (Figure 3.5d) and D2850 (Figure 3.5e) coatings display poor adhesion to PC, which can be explained by the lower amount of oxygen bridges formed between the diluted polysilazanes (contain residual dibutyl ether solvent) and substrate surface. As time goes on, further reactions occur at the interface of the coating and substrate, and the number of oxygen bridges increases. Consequently, the adhesion of D2250 and D2850 coatings to the PC substrates is improved from Gt 5 and Gt 4 to Gt 1, respectively.

In summary, the molecular structure of polysilazanes plays a key role in the moisture-curing behavior, film formation, coating-substrate adhesion, hydrophobicity, and mechanical properties of the resultant films. The investigated properties of the different polysilazane coatings cured under ambient conditions are comparatively assessed in Figure 3.6.
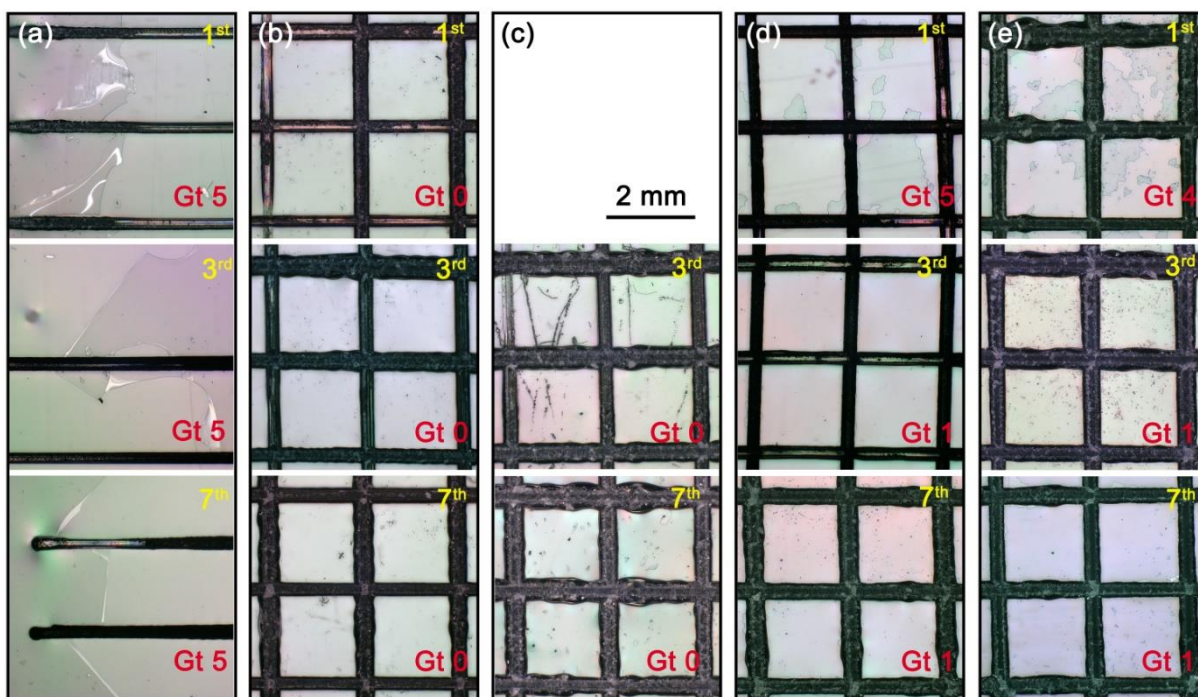
Figure 3.5 Optical microscopy images of polysilazanes coated on polycarbonate substrates after standard DIN EN ISO 2409 cross-cut tape test: (a) D1500-rc, (b) D1500-sc, (c) D1800, (d) D2250, (e) D2850 coatings after 1, 3, and 7 days of curing under ambient environment and temperature. Adapted from Ref. [1] with permission of John Wiley and Sons.
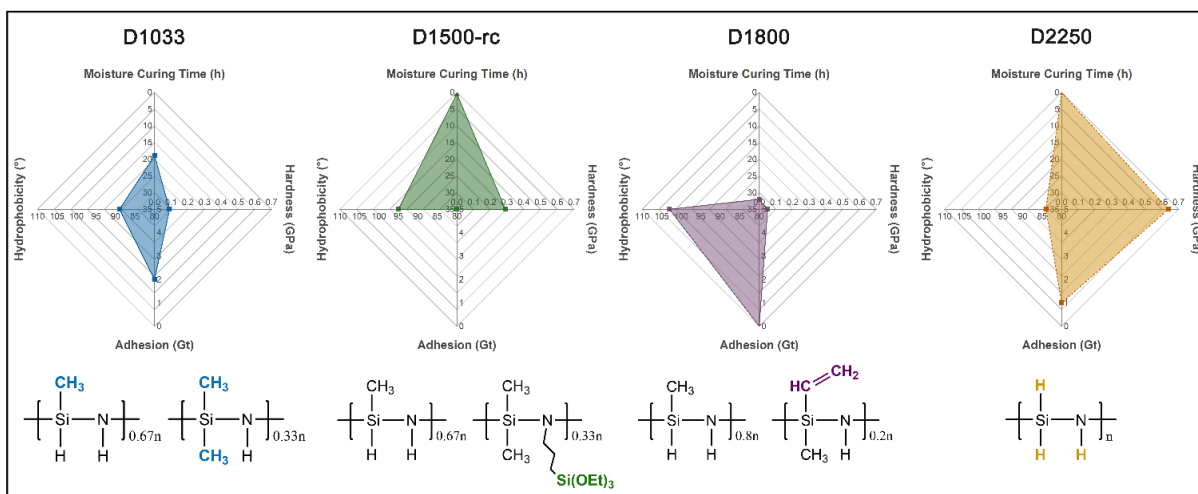
Figure 3.6 Assessment of moisture curing rate, hardness, coating-substrate adhesion, and hydrophobicity of different polysilazane coatings using radar charts.

Table 3.1 Applied spin speed and physical properties of polysilazanes and polysilazane-derived coatings cured under ambient atmosphere and temperature for 30 days. Adapted from Ref. [1] with permission of John Wiley and Sons.

Polysilazanes	Side Groups	Viscosity (mPa·s, 20°C)	Selective Spin Speed (rpm)	Thickness (μm)	Dry to Touch Time (min)	Hardness (GPa)	Elastic Modulus (GPa)	Contact Angle (°)
D1033	Si–H, Si–NH, Si–CH$_3$	16	700	n.a.	1140 (19 h)	n.a.	n.a.	90.9 ± 0.8
D1500-sc	Si–H, Si–NH, Si–CH$_3$, N–(CH$_2$)$_3$Si(OEt)$_3$	20–30	700	6.68 ± 0.15	80	0.11	1.40	98.4 ± 2.4
D1500-rc	Si–H, Si–NH, Si–CH$_3$, N–(CH$_2$)$_3$Si(OEt)$_3$	12–20	700	5.86 ± 0.19	26	0.29	2.90	95.4 ± 0.7
D1800	Si–H, Si–NH, Si–CH$_3$, Si–CH=CH$_2$	20–50	1500	6.22 ± 0.77	1920 (32 h)	0.05	0.40	103.3 ± 0.5
D2250	Si–H, Si–NH	< 5	500	1.56 ± 0.04	6	0.64	3.58 ± 0.01	83.9 ± 0.8
D2850	Si–H, Si–NH	<5	500	1.54 ± 0.09	0.5	1.89 ± 0.01	8.50 ± 0.03	85.9 ± 0.8

3.2. Curing acceleration of polysilazane coating via chloride-catalyzed hydrolysis and condensation reactions

The content of this chapter is published in:

[2] **Y. Zhan,** W. Li, R. Grottenmüller, C. Minnert, T. Krasemann, Q. Wen, R. Riedel, Rapid curing of polysilazane coatings at room temperature via chloride-catalyzed hydrolysis/condensation reactions, Progress in Organic Coatings, 167 (2022) 106872.

The previous chapter described the failure of forming Durazane 1033 film. In the present chapter, a method for improving the film formation and coating properties of D1033 is introduced. In this method, tetrabutylammonium chloride is added as an effective catalyst for the curing of D1033 in ambient atmosphere and temperature without applying any inhibitors. The catalytic effect of TBAC is investigated by FTIR and gel permeation chromatography (GPC). The suggested catalysis mechanism is elaborated. A TBAC-catalyzed D1033 coating with greatly improved film quality and mechanical properties is presented.

In order to improve the curing rate and degree of Durazane 1033, ten potential catalysts were tested by the employment of ATR-FTIR (see Ref. [2]). Tetrabutylammonium chloride is selected as a favorable catalyst for the moisture-curing of polysilazane because of its good catalytic ability, relatively low price, and colorless feature. Figure 3.7a compares the ATR-FTIR spectra of pure D1033 and with the addition of different amounts of TBAC after 24 h of curing in ambient environment (45–60% RH) and temperature ($\sim$23 °C). As detailed in Subsection 2.2.2 and illustrated in Figure 3.8 (blue box), Si–H (2120 cm^{-1}) and Si–NH (1160 cm^{-1}) groups from polysilazane are hydrolyzed by atmospheric water to form Si–OH groups, which are subsequently condensed to Si–O–Si (1051 cm^{-1}) groups. A clear improvement in the crosslinking of D1033 by adding TBAC is observed in Figure 3.7b. The relative absorbance of Si–H, Si–NH, and Si–O–Si bands is calculated by integrating the corresponding peak area using Si–CH$_3$ band (1252 cm^{-1}, which is considered to be inert) as the reference peak. The spectrum of pure D1033 is set as the start point (1 for Si–H and Si–NH bands, 0 for Si–O–Si band). Compared to the pure D1033, more Si–H and Si–NH groups are reacted and more Si–O–Si groups are produced in the TBAC-catalyzed polysilazane. The maximum catalytic effect is obtained when 2 wt% of TBAC is added. Around 49% and 70% of the Si–H groups (blue) and Si–NH groups (green) are consumed respectively, while the relative absorbance of Si–O–Si band (red) rises to 4.13. The catalytic activity is diminished when the TBAC content further increases to 3–4 wt%, which is attributed to the steric hindrance of the tetrabutylammonium cation ((C_4H_9)$_4$N$^+$) during the catalysis reactions [198].
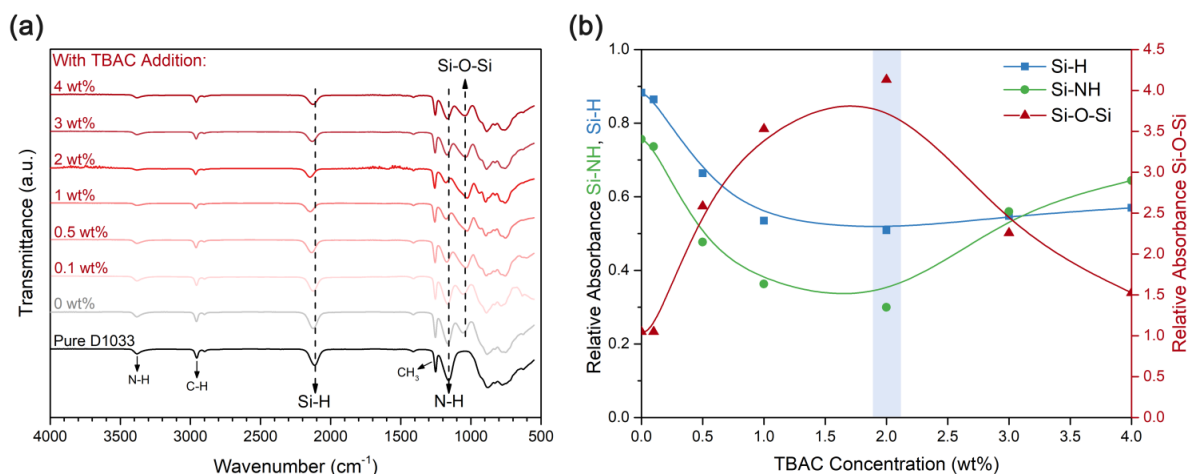
Figure 3.7 (a) ATR-FTIR spectra of pure Durazane 1033 and with the addition of different amounts of tetrabutylammonium chloride (TBAC) cured for 24 h in ambient environment and temperature. (b) Calculated relative absorbance (relative to Si–CH₃) of Si–H, Si–NH, and Si–O–Si groups as a function of TBAC concentration. Adapted from Ref. [2].
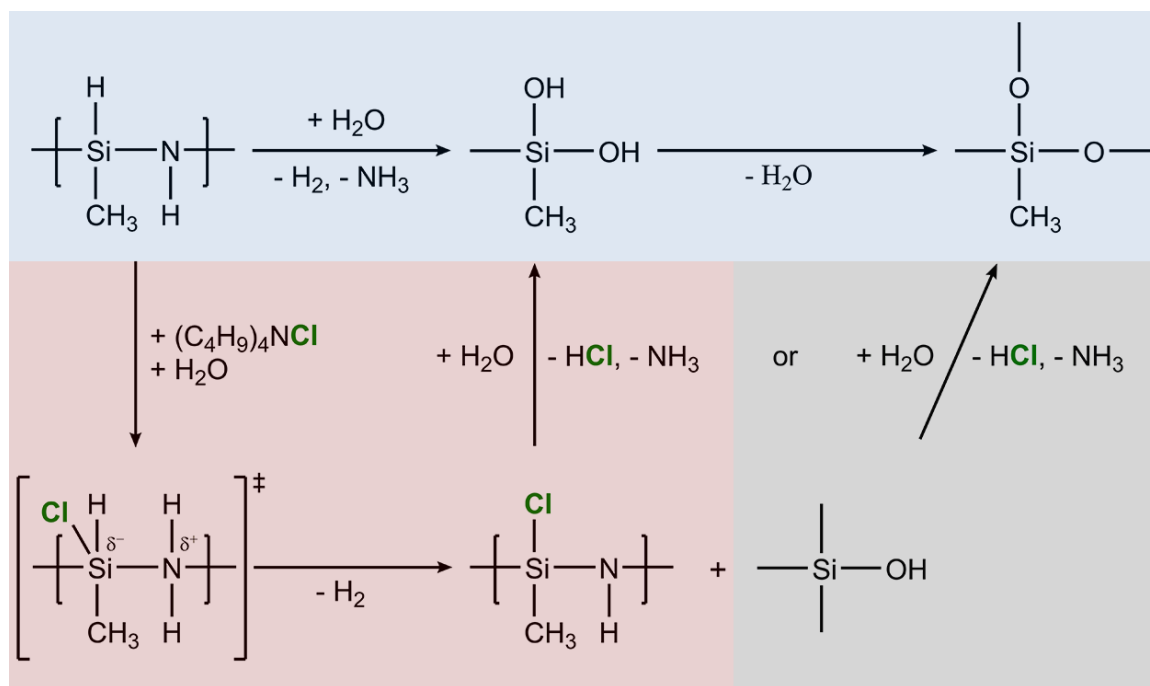
Figure 3.8 Suggested catalytic reaction mechanisms of tetrabutylammonium chloride (TBAC) on the moisture-curing of Durazane 1033. Blue box: crosslinking of polysilazane via hydrolysis and condensation reactions. Red box: nucleophilic substitution reaction routes. Grey box: possible reaction between Si–Cl and Si–OH groups. Reproduced from Ref. [2].

The suggested catalytic mechanism of TBAC on the hydrolysis and condensation reactions of polysilazane is outlined in Figure 3.8. When a small amount of nucleophilic catalyst TBAC ($(C_4H_9)_4NCl$) is added to the polysilazane, the electrophilic silicon from the polarized Si–N bond

is under attack while the nitrogen is protonated [24,199,200]. A transient Si–Cl bond is formed with the release of hydrogen. Following this, the Si–Cl bond is nucleophilically substituted by an –OH group from the water molecule (red box), which consequently accelerates the hydrolysis of PSZ. The byproduct HCl provides an acidic environment wherein the hydrolysis is further catalyzed [24]. Based on the work of Sneh et al. [201] and Lu et al. [112], a possible condensation reaction between Si–Cl and Si–OH groups to form Si–O–Si groups is hypothesized in Figure 3.8 (grey box). Consequently, more Si–H and Si–NH groups are consumed and more Si–O–Si groups are produced, which are in line with the FTIR results presented in Figure 3.7.

The GPC results shown in Figure 3.9 validate the catalytic effect of TBAC on the moisture-curing of PSZ. Before the GPC measurements, the crosslinked sample was first diluted in tetrahydrofuran (THF). The well-stirred solution was filtered with a syringe filter (0.2 μm) before injecting into the GPC device. As is well-known, polysilazane is a thermosetting polymer with a highly crosslinked 3D network after proper curing, which is insoluble in tetrahydrofuran. Therefore, particles and insoluble material larger than 0.2 μm have been removed in the filtration process and only the clear soluble portion of the sample solution was analyzed by GPC. Figure 3.9a shows a significant difference in the development of the average molecular weight (M_w) between D1033 and TBAC-catalyzed D1033 after curing for 3 h to 10 d in ambient environment at RT. The M_w is determined using the corresponding molar mass distribution curves attained by GPC (Figure 3.9b and c). Both samples exhibit the highest M_w after some time of curing. Before the peak, the M_w increases along with the curing time, indicating a steady increase in the crosslinking degree. After that, the highly crosslinked samples containing a large amount of the 3D networks are no longer soluble in THF. Particles with higher crosslinking degrees have been filtered out before the measurement. The obtained M_w is thus decreased. It is apparent from Figure 3.9a that the TBAC-catalyzed D1033 reaches the M_w peak after 6 h of curing, which is 24 times faster than that of the pure D1033 sample (that needs 144 h), confirming the catalytic effect of TBAC.
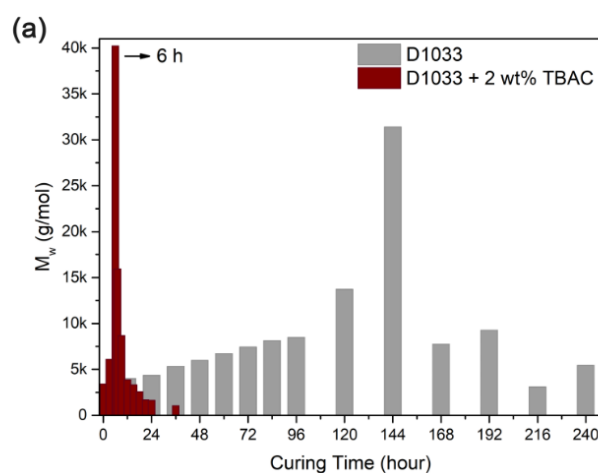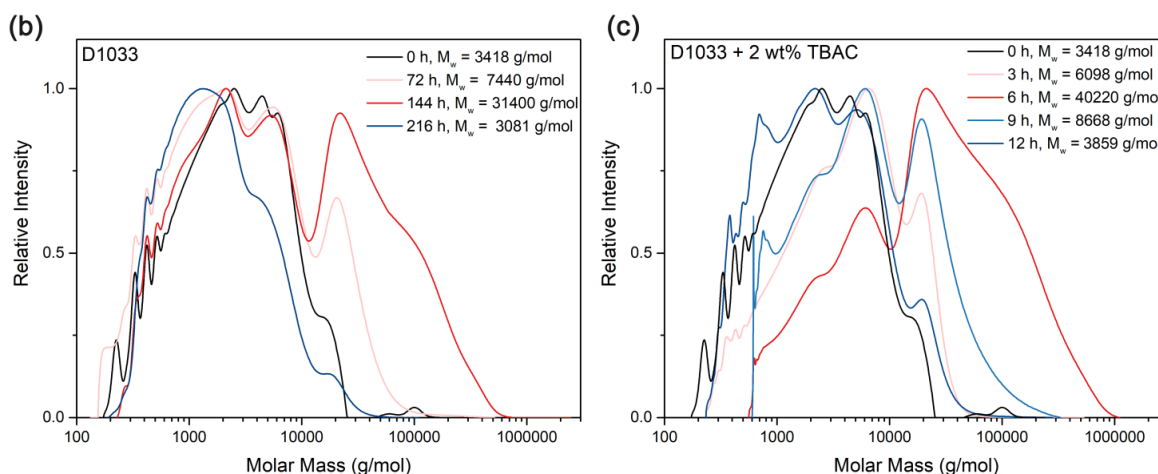
Figure 3.9 (a) Average molecular weight (Mw) of Durazane 1033 with and without the addition of 2 wt% of TBAC as a function of curing time. Molar mass distribution of soluble (b) D1033 after curing for 0, 72, 144, 216 h and (c) TBAC-catalyzed D1033 after curing for 0, 3, 6, 9, and 12 h in ambient environment and temperature. Note that insoluble material and particles with sizes larger than 0.2 μm were filtered out and would not be measured by gel permeation chromatography. Adapted from Ref. [2].

Durazane 1033 and that with 2 wt% of TBAC were spin-coated on Si(100) wafers at a spin speed of 700 rpm (predetermined in Section 3.1) and cured under ambient conditions at RT. As was mentioned in the previous chapter, D1033 failed to form a film on the PC substrate because of insufficient wetting. Similar failure is observed on the spin-coated D1033 on the Si wafer. As shown in Figure 3.10a and b, D1033 coating exhibits a moon-like surface morphology full of bowl-shaped cavities and uneven bumps and ridges. In contrast to that, the TBAC-catalyzed D1033 coating (Figure 3.10d and e) has an even and smooth surface without large irregularities. This significant improvement in the surface morphology of TBAC-catalyzed PSZ coating is attributed to its accelerated drying process. As recorded, D1033 coating was dry to touch in around 19 h. Under the same conditions, the TBAC-catalyzed D1033 coating requires only ca. 1 h to reach the dry-to-touch state, indicating a much faster curing rate. On this account, the catalyzed PSZ coating crosslinked quickly to a solid film (with low mobility) before the liquid phase began to significantly move and shrink to form the cavities.

The catalytic effect of TBAC on the moisture-curing of D1033 coating is verified by FTIR and EDX analysis. Figure 3.11a provides a straightforward comparison between the relative absorbance of Si–H, Si–NH, and Si–O–Si groups (calculated from the FTIR spectra) in D1033 coatings with and without 2 wt% of TBAC. After 6 h of curing, around 39% of the Si–H and 62% of the Si–NH groups in the TBAC-catalyzed D1033 coating reacted to form Si–O–Si groups, which is consistent with the development of M_w observed from the GPC results (Figure 2.1Figure 3.9). After curing for 24 h, the Si–H and Si–NH bands in the catalyzed coating

decrease respectively by 48% and 63%, compared to 31% and 35% for the uncatalyzed PSZ coating. Finally, the TBAC-catalyzed D1033 coating has 49% and 28%, while the uncatalyzed D1033 coating has 68% and 55% of the remaining Si–H and Si–NH groups after 72 h of curing, respectively. The half amount of the remaining Si–H groups in the TBAC-catalyzed PSZ coating can be justified by their lower sensitivity to hydrolysis in comparison with the Si–NH groups [63]. Additionally, residual Si–H groups are trapped in the highly crosslinked polymer network and further hydrolysis is hindered. Nevertheless, 1.6 times more of the Si–H and Si–NH groups are consumed when the TBAC is added. In the meantime, the relative absorbance of Si–O–Si vibration in the catalyzed D1033 coating reaches the highest point of 3.32, which is about 2 times more than that of the uncatalyzed PSZ coating (1.64).

Elemental compositions of the uncatalyzed and TBAC-catalyzed D1033 coatings after 24, 48, and 72 h of curing under ambient conditions were determined by EDX analysis (see the supplementary information of [2]). The calculated Si/C, Si/N, and Si/O molar ratios as a function of curing time are compared in Figure 3.11b. The Si/C molar ratio remains constant throughout the curing process, implying that the Si–CH$_3$ groups are excluded from the crosslinking reactions at RT. This finding supports our approach used for the calculation of relative absorbance from the FTIR spectra. The Si/N (Si/O) molar ratio of both coatings increases (decreases) over time, while the numerical values of TBAC-catalyzed PSZ coating are larger (smaller) than that of the uncatalyzed PSZ coating. Evidence from the EDX study indicates that the TBAC-catalyzed D1033 coating achieves a higher crosslinking degree, where a larger amount of O is incorporated in the network compared to the uncatalyzed D1033 coating.
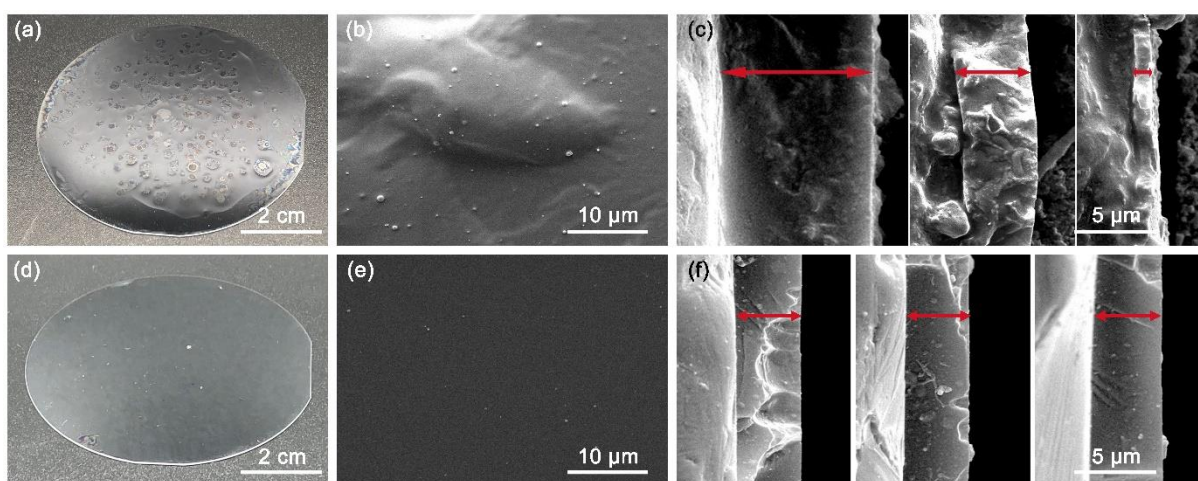
Figure 3.10 Optical and SEM images showing the surface morphologies (a, b, d, e) and cross-sections (e, f) of Durazane 1033 (top row) and the TBAC-catalyzed D1033 (bottom row) coatings on Si wafers after curing in ambient environment and temperature for 7 d. Adapted from Ref. [2].
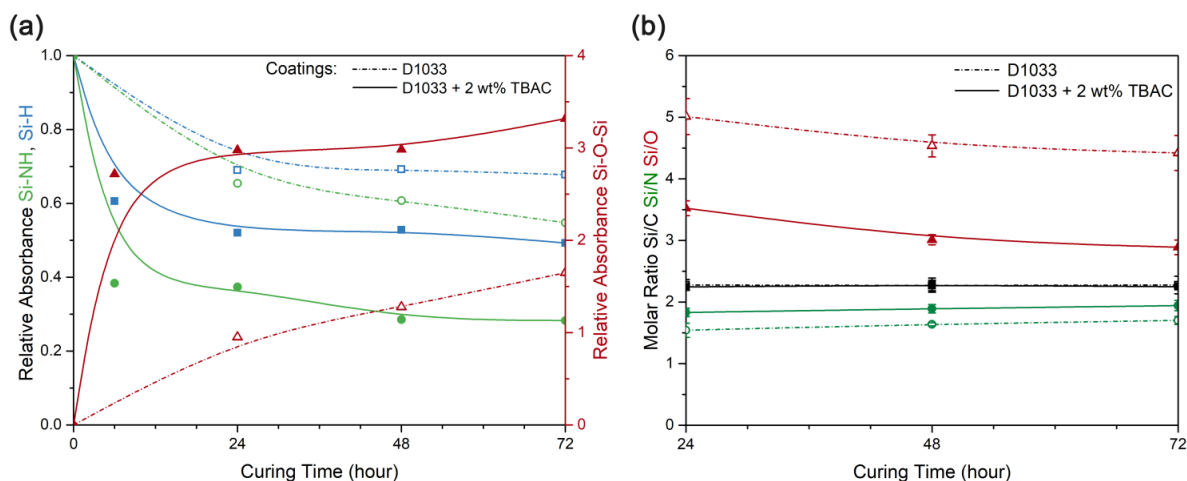
Figure 3.11 (a) Relative absorbance (relative to Si–CH₃) of Si–H, Si–NH, and Si–O–Si groups as a function of curing time calculated from the ATR-FTIR spectra of Durazane 1033 coating (dash-dot line) and with the addition of 2 wt% of TBAC (solid line). (b) Calculated Si/C, Si/N and Si/O molar ratios of Durazane 1033 coatings (dash-dot line) and with the addition of 2 wt% of TBAC (solid line) after 24, 48, and 72 h of curing under ambient conditions. Detailed elemental compositions are obtained by energy-dispersive X-ray spectroscopy. Adapted from Ref. [2].

The profilometry-determined thicknesses of D1033 and TBAC-catalyzed D1033 coatings after 7 d of curing under ambient conditions are 5.3 ± 2.7 μm and 4.9 ± 0.2 μm, respectively. The average surface roughnesses of the corresponding films are 2.6 ± 1.1 μm and 0.3 ± 0.1 μm, respectively. These results are in good agreement with the cross-sections shown in Figure 3.10c and f. The thickness of the uncatalyzed D1033 coating (Figure 3.10c) varies at different spots, ranging from 1 to10 μm. In contrast, the cross-section of TBAC-catalyzed D1033 coating (Figure 3.10f) displays a uniform thickness of ca. 5 μm throughout the entire film.

Nanoindentation was employed to measure the hardness and elastic modulus of the coatings. The results shown in Figure 3.12a were averaged over a penetration depth of 500 to 800 nm to exclude the substrate effect. After 30 d of curing under ambient conditions, D1033 coating exhibits a hardness of 0.09 ± 0.002 GPa and an elastic modulus of 0.4 ± 0.01 GPa. A significant improvement in the mechanical properties is noted when the TBAC is added. With the curing process being catalyzed, the crosslinking degree of the coating is largely increased. Eventually, the TBAC-catalyzed D1033 coating has a hardness of 0.16 ± 0.005 GPa and an elastic modulus of 1.63 ± 0.05 GPa, which is about 2-fold and 4-fold to that of the uncatalyzed coating, respectively.

Despite the addition of TBAC, the wettability of the catalyzed PSZ coating remains in the same range as the uncatalyzed coating after curing for 30 d in ambient environment and temperature. As shown in Figure 3.12b, D1033 coating oscillates between being hydrophilic or hydrophobic

at different measured spots and has an average water contact angle of 88.7° ± 3.4°. With the addition of TBAC, a more uniform wetting state is obtained throughout the film surface, resulting in an average water contact angle of 90.6° ± 1.3°, which is considered to be slightly hydrophobic.
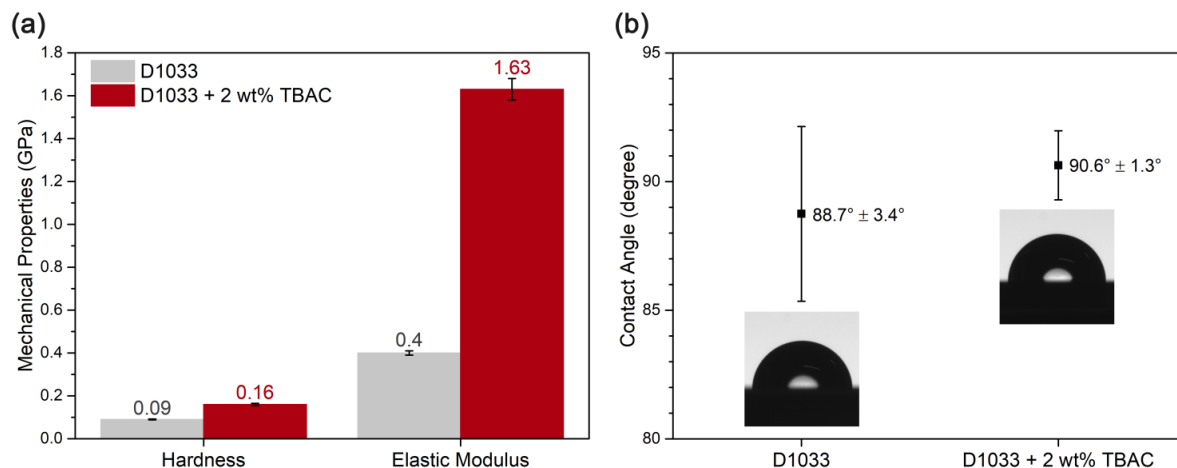
Figure 3.12 Physical properties of spin-coated Durazane 1033 and with the addition of 2 wt% of TBAC on Si wafers after curing in ambient environment and temperature for 30 d: (a) Hardness and elastic modulus, (b) water contact angle (insets are the optical images of sessile water droplets resting on the corresponding films). Adapted from Ref. [2].

Adhesion of the uncatalyzed and TBAC-catalyzed D1033 coatings to the Si wafer after 7 d of curing under ambient conditions is evaluated via the cross-cut tape test (experimental details and classification standard are outlined in Section 3.1). Figure 3.13 presents the optical images of the tested films. Large defects with colorful interference patterns appear on the uncatalyzed D1033 coating, confirming the coexistence of thick and thin film regions. With the addition of 2 wt% of TBAC, the film quality is greatly enhanced, showing a smooth and even surface morphology. The adhesion of both coatings is classified as Gt 2 according to the DIN EN ISO 2409 standard [185], i.e., 5–15% of the tested area is peeled off after the cross-cut tape test. However, the appearance of the detached areas on the coatings is different. Peeling of the uncatalyzed D1033 coating occurs only in areas with thicker film thickness. Oppositely, consistent detachments are shown along the cutting line of the TBAC-catalyzed PSZ coating.

To sum up, TBAC has been proved to be an efficient catalyst for the moisture-curing of D1033 at RT. The addition of TBAC not only accelerates the hydrolysis and condensation reactions of D1033 but also increases the crosslinking degree of the resultant films. Hence, a polysilazane film with significantly improved coating quality and enhanced mechanical properties is obtained.
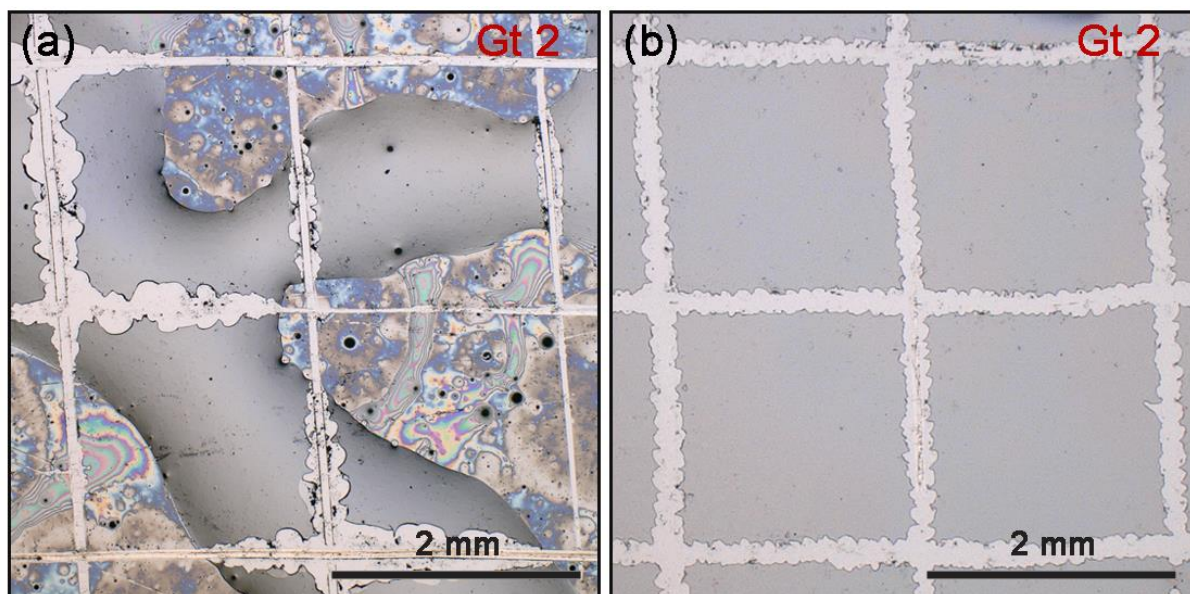
Figure 3.13 Optical microscopy images of polysilazane coatings on Si wafers after standard DIN EN ISO 2409 cross-cut tape test: (a) Durazane 1033 and the (b) TBAC-catalyzed D1033 coatings after curing in ambient environment and temperature for 7 d. Adapted from Ref. [2].

3.3. Boron modification of polysilazanes towards preparation of hydrophobic coating and amorphous SiBN ceramic

This chapter is divided into three sections. The first section describes the successful synthesis of boron-modified organopolysilazanes (BOPSZ) and perhydropolysilazanes (BPHPS) with varying chemical compositions. The second section presents the potential of applying BOPSZ-derived films as easy-to-clean and corrosion-resistant coatings. In the third section, the BPHPS is applied as a single-source precursor for the preparation of amorphous SiBN ceramic.

3.3.1. Synthesis of boron-modified polysilazanes

Different amounts of borane dimethyl sulfide complex (BMS) were used to modify OPSZ (Durazane 1033) and PHPS (Durazane 2250). The boron-modified OPSZ and PHPS are denoted as BOPSZx and BPHPSx, respectively, where x is the set Si/B molar ratio. To obtain soluble BOPSZs for the coating application, the Si/B molar ratio is chosen as 5, 10, and 15 for the modification of OPSZ. For the application of BPHPS-derived SiBN ceramic, the Si/B molar ratios for modifying PHPS are 1, 2, and 5. The detailed synthesis process is elaborated in reference [3].

Boron-modified organopolysilazanes

Figure 3.14a compares the ATR-FTIR spectra of Durazane 1033, synthesized BOPSZs, and BMS. As has been illustrated in Chapter 3.2, typical absorption bands of N–H (1160, 3383 cm^{-1}), C–H (2958 cm^{-1}), Si–H (2120 cm^{-1}), and Si–CH$_3$ (1252 cm^{-1}) are shown in the FTIR spectrum of OPSZ. With the addition of BMS, N–H and Si–H groups of OPSZ and B–H (1090, 2391 cm^{-1}) groups of BMS are consumed, while B–N groups (ca. 1315 cm^{-1}) are formed simultaneously, as shown in the spectra of BOPSZx samples. Boron modification of OPSZ by BMS is accomplished through the dehydrocoupling reactions between N–H (Si–H) and B–H groups, as proposed in Figure 3.15. It is worth noting that Si–B band appears possibly in the wavelength range of 548 and 955 cm^{-1} [202], which overlaps with the Si–N–Si (705–935 cm^{-1}) band and hence could not be distinguished. The relative absorbance of Si–H, Si–NH, B–N, and B–H bands

as a function of B/Si molar ratio is shown in Figure 3.14b. As the boron content increases, Si–H and Si–NH groups reduce in comparable amounts, while the amount of B–N groups increases significantly. The existence of B–H bands in BOPSZs after the synthesis reveals that the silazane-bonded B–H groups have not been completely reacted.

Liquid state ^{1}H, ^{11}B, ^{13}C, and ^{29}Si nuclear magnetic resonance (NMR) spectroscopy was performed on the OPSZ and BOPSZ5 samples dissolved in CDCl$_3$. The obtained spectra are referenced to tetramethylsilane and are shown in Figure 3.16. The ^{1}H NMR spectrum (Figure 3.16a) of the OPSZ sample exhibits three prominent signals related to the different hydrogen environments at 0.13–0.23 (SiC**H**$_3$), 0.5–1.1 (N**H**), and 4.4–4.9 ppm (Si**H**) [133]. After the boron modification, the NH signal reduces and a new signal appears at around 1.3 ppm in the ^{1}H NMR spectrum of BOPSZ5, which is assigned to the B–**H** units [203]. This result shows evidence of the dehydrocoupling reactions between B–H and N–H groups, as revealed by the FTIR spectra. The ^{11}B NMR spectrum (Figure 3.16b) of the BOPSZ5 exhibits relatively broad and overlapping signals centered at 30 and 34 ppm, characteristic of distorted trigonal **B**X$_3$ sites, which can be assigned respectively to **B**N$_3$ and **B**N$_2$Si (**B**N$_2$H) [97]. The ^{13}C NMR spectra (Figure 3.16c) of both samples present broad signals at –2.3–4.4 ppm (SiC**H**$_3$). The ^{29}Si signals (Figure 3.16d) of both samples appear at –32 (**Si**CN$_3$), –23 (**Si**HCN$_2$), and –14 – –4 ppm (**Si**C$_2$N$_2$) [99]. There is a significant broadening of these signals in the BOPSZ5 sample, which is explained by the increased crosslinking of the precursor microstructure.
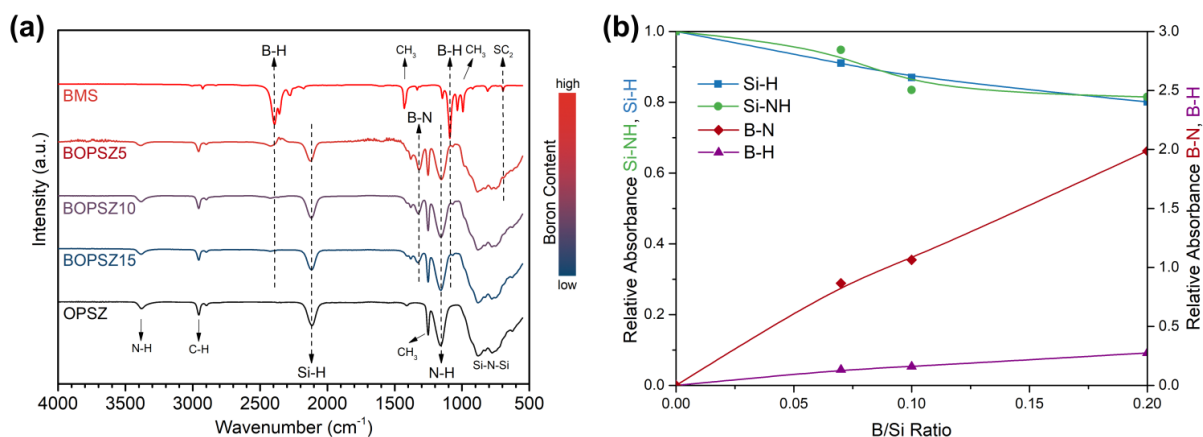
Figure 3.14 (a) ATR-FTIR spectra of organopolysilazane (OPSZ) Durazane 1033 and OPSZ modified with different amounts of borane dimethyl sulfide (BOPSZx, x is the set Si/B molar ratio). (b) Calculated relative absorbance (relative to Si–CH$_3$) of Si–H, Si–NH, B–H, and B–N groups as a function of B/Si molar ratio.
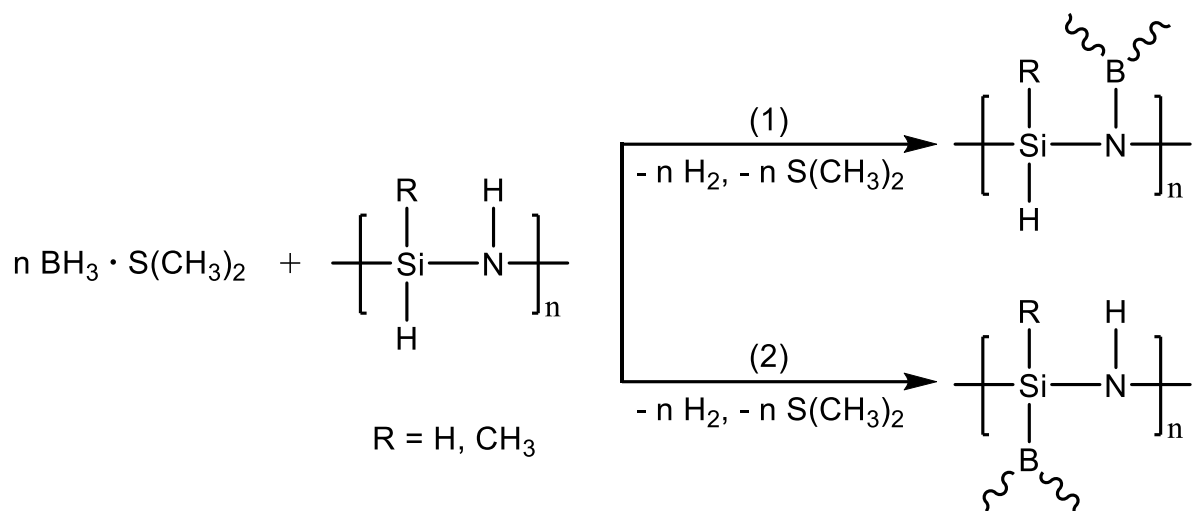
Figure 3.15 Suggested reaction mechanisms of polysilazane and borane dimethyl sulfide.
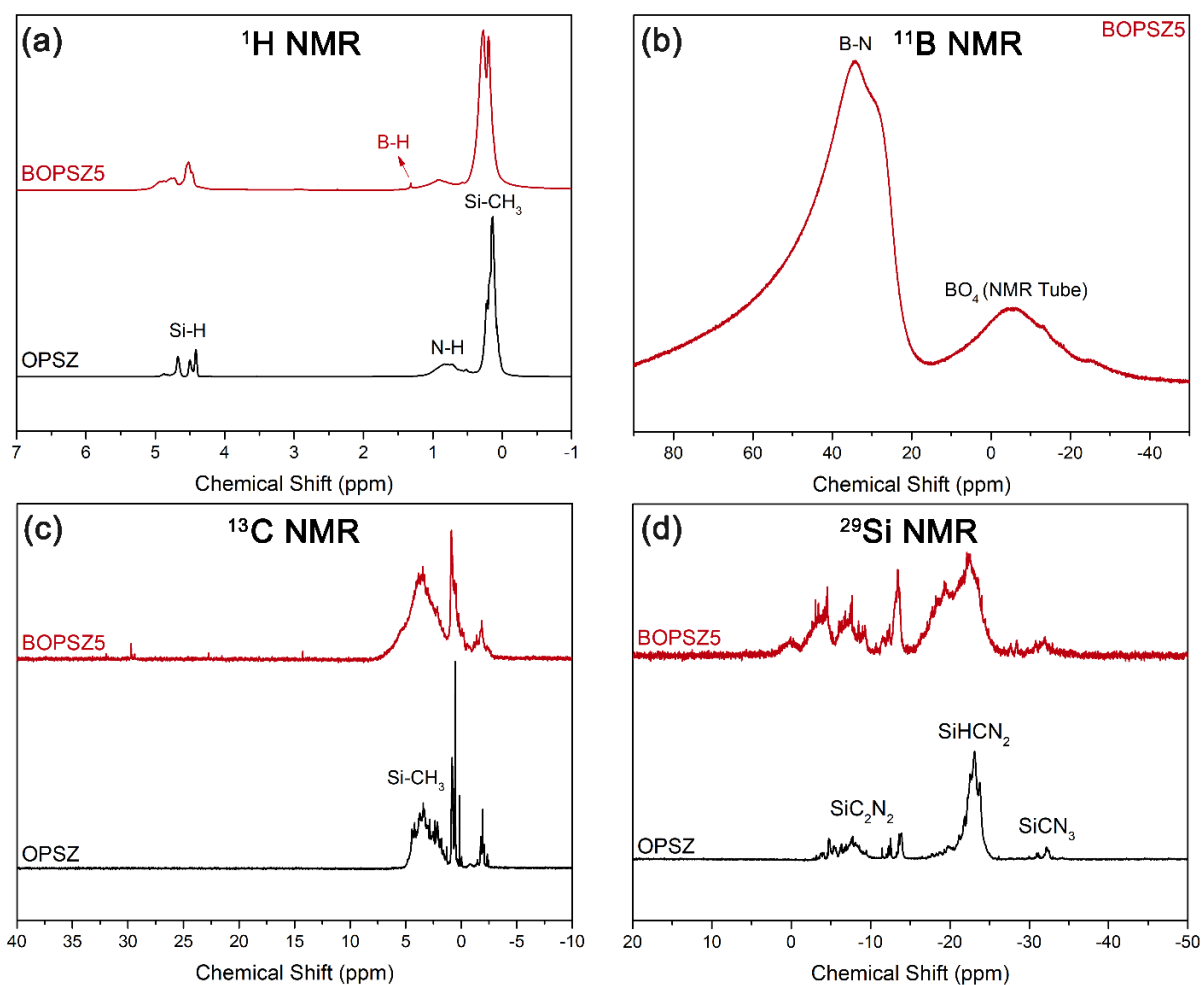
Figure 3.16 (a) ^{1}H, (b) ^{11}B, (c) ^{13}C, and (d) ^{29}Si liquid NMR spectra of organopolysilazane (OPSZ) Durazane 1033 and boron modified-OPSZ with a Si/B ratio of 5. The samples were dissolved in CDCl$_3$ solvent.

Boron-modified perhydropolysilazanes

Boron modification of PHPS by BMS was carried out using the identical synthetic method. Figure 3.17 compares the ATR-FTIR spectra of dried PHPS, synthesized BOPSZs and BMS. Without the reference Si–CH$_3$ band, the intensity of all spectra was normalized to [0, 1] to enable the comparison of the bands. Compared with the dried PHPS, intensities of Si–H (2159 cm^{-1}) and N–H (1120, 3302 cm^{-1}) bands in BPHPS samples decrease with increasing boron content. Most of the N–H groups are consumed when the set Si/B ratio is 1, whereas a considerable amount of Si–H groups remain in the sample. The results show that the chemical reactivity of Si–H towards boron modification is lower than that of the N–H groups. The appearance of B–N band at the wavelength of ca. 1315 cm^{-1} indicates that the boron modification mechanism of PHPS by BMS is similar to that of OPSZ (Figure 3.15). However, dehydrocoupling between N–H and B–H is favored. Moreover, the C–H (2786–2995 cm^{-1}) vibrations appeared in the spectra of the BPHPS samples stem from the residual solvent dibutyl ether and toluene.

Chemical composition of the BPHPS2 is obtained by elemental analysis and summarized in Table 3.2. It is confirmed that boron has been successfully incorporated into the PHPS network. The empirical Si/B molar ratio of the synthesized BPHPS2 is calculated as 5.49, which is larger than the set value of 2. The loss of boron during the synthesis is explained by i) the evaporation of BMS during the synthesis and drying process, and ii) that borane did not react with PHPS stoichiometrically due to steric hindrance imposed by the polymer structure. A similar observation has been reported by Viard et al. [133]. The existence of C and O is attributed to the residual solvents (dibutyl ether and toluene) and the water contamination during the elemental analysis.
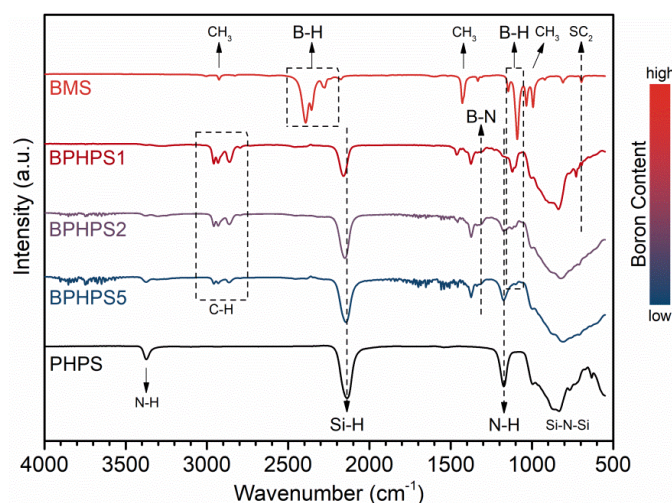
Figure 3.17 ATR-FTIR spectra of dried perhydropolysilazane (PHPS) Durazane 2250 and PHPS modified with different amounts of borane dimethyl sulfide (BPHPSx, x is the set Si/B molar ratio). Adapted from Ref. [3].

Table 3.2 Elemental composition of boron-modified perhydropolysilazane with a Si/B ratio of 2. Data is obtained by elemental analysis. Adapted from Ref. [3].

Elemental Composition (wt%)						Calculated Si/B ratio	Empirical Formula
Si	B	N	H	C	O		
55.80	3.99	24.00	5.07	3.90	6.49	5.49	$Si_{1.00}B_{0.18}N_{0.86}(C_{0.16}O_{0.21}H_{0.55})$

3.3.2. Boron-modified organopolysilazane-derived coating

Chapter 3.2 concluded that by increasing the curing rate and degree the film formation and coating quality of D1033 were significantly improved. In this context, a similar curing investigation was carried out on the boron-modified OPSZ samples. Figure 3.18a compares the ATR-FTIR spectra of OPSZ (D1033) and the synthesized BOPSZs after 24 h of curing in ambient environment (45–60% RH) and temperature (~23 °C). The moisture curing mechanism of OPSZ has been elaborated in Chapter 3.1 and 3.2. During the crosslinking processes, Si–H (2120 cm^{-1}) and Si–NH (3383 cm^{-1}) groups are hydrolyzed to form Si–OH groups, which condense readily to Si–O–Si (1022–1054 cm^{-1}) groups. In addition, the moisture-sensitive B–N groups in the BOPSZs samples (see Figure 3.14) are completely hydrolyzed to form boric acid as suggested in equations (3-1) and (3-2) [204,205]. The B–H groups are hydrolyzed to form B–OH groups (Eq. (3-3)), which react with Si–OH groups to form B–O–Si groups [206]. The reaction mechanisms are confirmed by the emergence of –OH (ca. 3210 cm^{-1}), B–O (1341–1410 cm^{-1}) and B–O–Si (ca. 940 cm^{-1}) bands, and the disappearance of B–N bands (ca. 1315 cm^{-1}) in the FTIR spectrum of BOPSZ5.

$$2B–N + 3H_2O \longrightarrow B_2O_3 + 2NH_3 \qquad (3\text{-}1)$$

$$B_2O_3 + 3H_2O \longrightarrow 2H_3BO_3 \qquad (3\text{-}2)$$

$$B–H + H_2O \longrightarrow B–OH + H_2 \qquad (3\text{-}3)$$

$$B–OH + Si–OH \longrightarrow B–O–Si + H_2O \qquad (3\text{-}4)$$
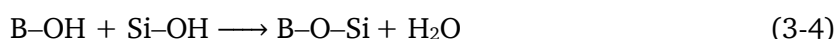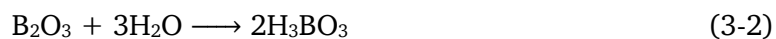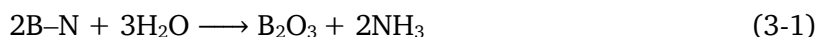
The relative absorbance of the hydrolyzable groups (Si–H and Si–NH groups) and the newly emerged groups (Si–O–Si and B–O groups) as a function of B/Si ratio is displayed in Figure 3.18b. With the addition of boron, more Si–H and Si–NH groups are consumed and more Si–O–Si groups are formed compared to the pure OPSZ, indicating that a higher crosslinking degree is achieved in the BOPSZs samples. As the B/Si ratio increases from 0.07 to 0.1, Si–H

and Si–NH groups keep reducing from 73% and 36% to 69% and 23%, respectively. The highest amount of Si–O–Si groups among the BOPSZs is obtained when the B/Si ratio is 0.1. With more boron incorporated in the network, BOPSZ5 (B/Si = 0.2) has relatively fewer Si–O–Si groups but more B–O groups after crosslinking in ambient conditions.

The solubility of BOPSZs in toluene decreases with the increase of boron incorporation into the polymer structure. BOPSZ5 was barely dissolved in the solvent and thus excluded from the coating application. BOPSZ10 which has a higher crosslinking degree was dissolved in toluene with a ratio of 30 wt%. The solution was spin-coated on a Si(100) wafer at a spin speed of 700 rpm and cured under ambient conditions. The coating was dry to touch within 1 h. The profilometry-determined thickness and roughness of the BOPSZ10-derived coating are 2.2 $\pm$ 0.9 μm and 0.06 $\pm$ 0.03 μm, respectively. As shown in Figure 3.19d and e, the BOPSZ10-derived coating exhibits an even surface morphology as anticipated compared to the OPSZ coating (Figure 3.19a and b). This again proves that the film formation and coating quality of the PSZ can be improved by increasing the curing rate. However, due to the insufficient solubility of BOPSZ10 in toluene, small particles are visible to be uniformly distributed on the coating.

The chemical stability of the coating is expected to be enhanced with the incorporation of boron. The resistance of the OPSZ and BOPSZ10-derived films against aggressive environments is investigated by exposing the coatings to 0.1 N HCl and 0.1 N NaOH water solutions for 24 h and visually inspected by an optical microscope. The basic NaOH solution is not an aggressive environment for both coatings as no obvious corroded areas are visible under the microscope. On the contrary, the OPSZ coating is highly corroded by HCl (Figure 3.19c), whereas only small defects appear on the BOPSZ10-derived coating (Figure 3.19f). Compared to OPSZ coating, the improved corrosion resistance of BOPSZ10-derived film against HCl is attributed to i) its higher crosslinking degree, thereby forming a denser physical barrier to retard the diffusion of HCl in the coating; ii) its increased hydrophobicity (Figure 3.20), which reduces the contact area between HCl and the coating; and iii) its smoother surface, which limits the corrosion through pre-existing defects. The above results demonstrate the potential of applying BOPSZ-derived films as corrosion-resistant and easy-to-clean coatings of various materials for use in high-rise buildings, marine coatings, and infrastructures.
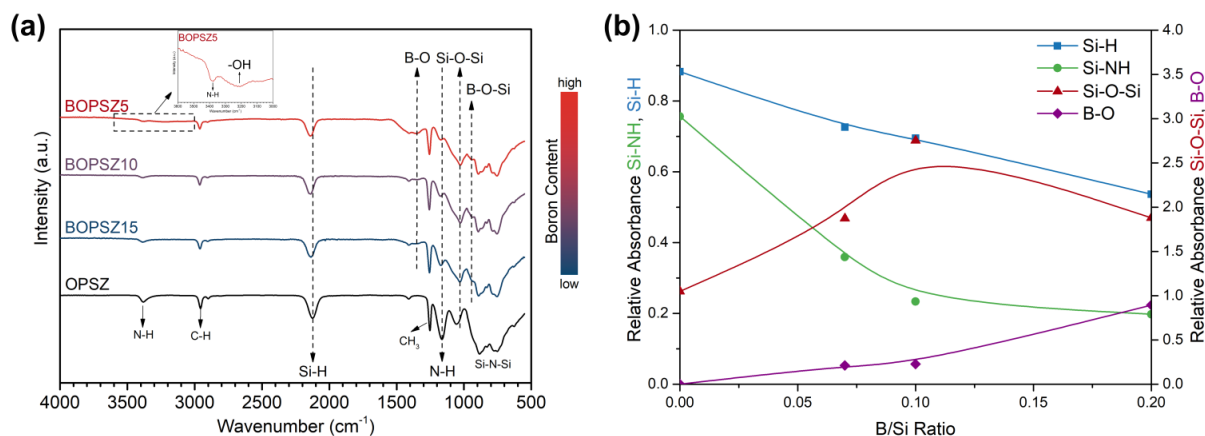
Figure 3.18 (a) ATR-FTIR spectra of organopolysilazane (OPSZ) Durazane 1033 and boron-modified organopolysilazanes (BOPSZx, x = Si/B molar ratio) after 24 h of curing in ambient environment and temperature. Inset shows the zoom-in region (3000–3600 cm^{-1}) of the BOPSZ5 spectrum. (b) Calculated relative absorbance (relative to Si–CH$_3$) of Si–H, Si–NH, Si–O–Si, and B–O groups as a function of B/Si molar ratio.
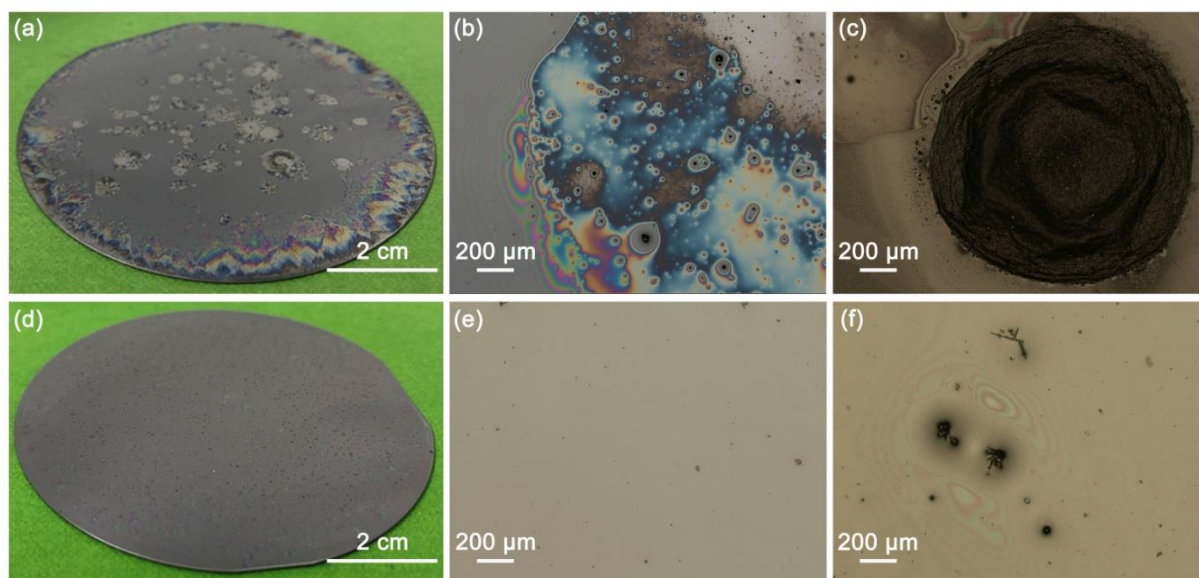
Figure 3.19 Optical images of (a, b) organopolysilazane Durazane 1033 and (d, e) 30 wt% of boron-modified organopolysilazane BOPSZ10 (in toluene) spin-coated on Si wafers and cured under ambient conditions for 7 d. (c) and (f) are the corresponding films after exposing to 0.1 N HCl water solution for 24 h.
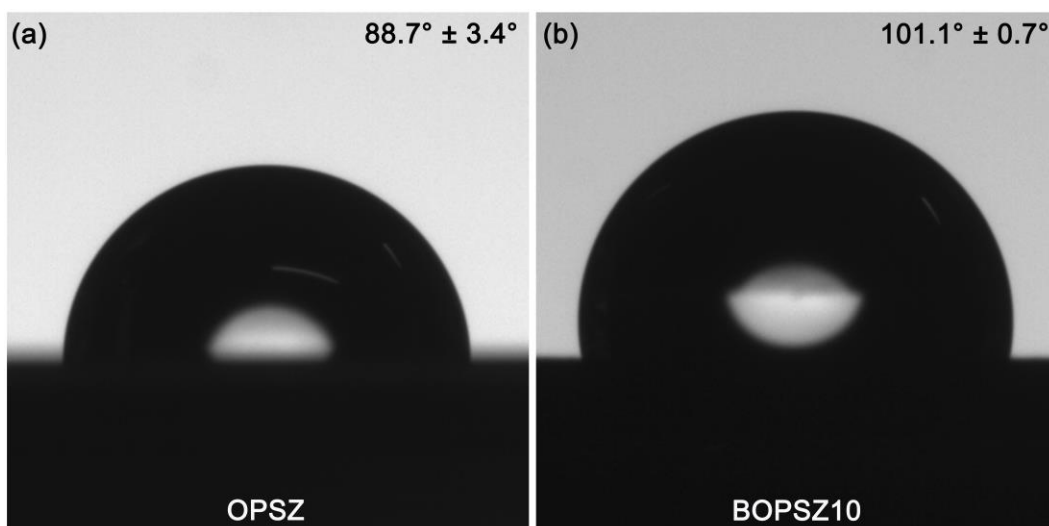
Figure 3.20 Optical images of sessile water droplets resting on (a) the organopolysilazane Durazane 1033 film and (b) the boron-modified organopolysilazane BOPSZ10 film cured under ambient conditions for 7 d.

3.3.3. Boron-modified perhydropolysilazane-derived SiBN ceramics

SiBN ceramics are considered to be the most promising microwave transparent materials applied under harsh environments owing to their outstanding thermal stability and low dielectric constant [207]. In this subsection, the preparation and characterization of the SiBN ceramics derived from the synthesized boron-modified PHPS precursors (BPHPSx, where x is the set Si/B molar ratio) are elaborated.

Experimental results

SiBN ceramics with varying chemical compositions were successfully prepared from the carbon- and chlorine-free BPHPSx precursors via the PDC route under N_2. The polymer to ceramic transformation of the precursors was characterized by thermogravimetric analysis/differential thermal analysis (TGA/DTA) coupled with evolved gas analysis and ex situ FTIR. As shown in Figure 3.21a, the TG curves of the precursors are divided into three stages along the temperature range.

From room temperature to approximately 170 °C, the dried PHPS exhibits a marginal weight loss of 1 wt%, while the BPHPS5, 2, and 1 precursors display evident mass loss of 4 wt%, 3 wt% and 8 wt%, respectively. It is confirmed by the ion current profiles of the volatiles (m/z = 27–72) (partly shown in Figure 3.21c and Figure S1b, c in Ref. [3]) recorded during the pyrolysis of BPHPSx that the mass loss is caused by the volatilization and decomposition of low-molecular-weight oligomers, especially silane and the residual solvent (dibutyl ether). Dehydrocoupling reactions between Si–H (N–H) and B–H groups proceed with the release of

H$_2$, which are verified by the exothermic peak detected in the DTA measurement of BPHPS2 (Figure 3.21b) and the ion current profile of H$_2$ (Figure 3.21c). As further supported by the FTIR spectra of BPHPS2 (Figure 3.21d), the Si–H, N–H and B–H bands reduce substantially, and the C–H groups from the solvent disappear at 200 °C.

In the second stage (170–800 °C), the dried PHPS undergoes a major weight loss of 22 wt%, which is contributed to the dehydrocoupling and transamination reactions, along with bond redistribution and thermal decomposition [6]. The ceramic yield of PHPS at ~800 °C is 77 wt%, which is consistent with the former reported data [208]. The weight loss of the precursors during the polymer to ceramic transformation is reduced considerably after boron modification. The higher crosslinking degree of the BPHPSx samples diminishes the depolymerization and thermolysis and thus results in a significantly increased ceramic yield of the boron-modified precursors. The BPHPS1, 2, and 5 samples have ceramic yields of 88 wt%, 92 wt%, and 91 wt% at 800 °C, respectively. It is worth noting that the ceramization of BPHPS2 has been finished between 500 °C and 800 °C according to the ex situ FTIR spectra (Figure 3.21d), where Si–H and N–H bands vanish at 800 °C.

The thermal behavior of the BPHPSx precursors with different Si/B molar ratios varies beyond 800 °C. The BPHPS2-derived ceramic is thermally stable until the end of the measurement (1300 °C). BPHPS5 sample that has less boron incorporation experiences a 3 wt% of mass loss between 800 °C and 930 °C due to thermal decomposition, which is corroborated by the endothermic peak shown in the DTA curve (Figure S1a in Ref. [3]). With more boron content, the BPHPS1 sample gains 3 wt% of mass between 600 °C and 1300 °C and has a final ceramic yield of ~91 wt%. The analyzed mass gain is ascribed to the reaction between surplus boron and N$_2$ [209,210].

After a parallel assessment, further evaluation focuses more on the BPHPS2-derived ceramic due to its good thermal stability. The chemical composition of the BPHPS2-derived ceramic pyrolyzed at 1100 °C is quantitively determined by elemental analysis. As can be seen in Table 3.3, the obtained Si/B molar ratio of 10.51 is larger than the set value (2), which is explained by the additional loss of boron due to the volatilization of borane species during the polymer-to-ceramic conversion. After annealing at 1300 °C, the residual carbon has been removed and the formation of SiBN ceramic is confirmed. In summary, compared with the former reported ceramic yield (~55 wt% [211], 72 wt% [212]) of SiBN ceramics obtained via other synthesis methods, a higher ceramic yield was achieved with the current method (88 wt%–92 wt%).

Table 3.3 Elemental composition of BPHPS2-derived ceramic (pyrolyzed at 1100 °C) obtained by elemental analysis. Adapted from Ref. [3].

Elemental Composition (wt%)						Calculated Si/B ratio	Empirical Formula
Si	B	N	H	C	O		
68.50	2.56	23.00	0.84	3.36	1.36	10.51	$Si_{1.00}B_{0.10}N_{0.67}(C_{0.11}O_{0.04}H_{0.34})$
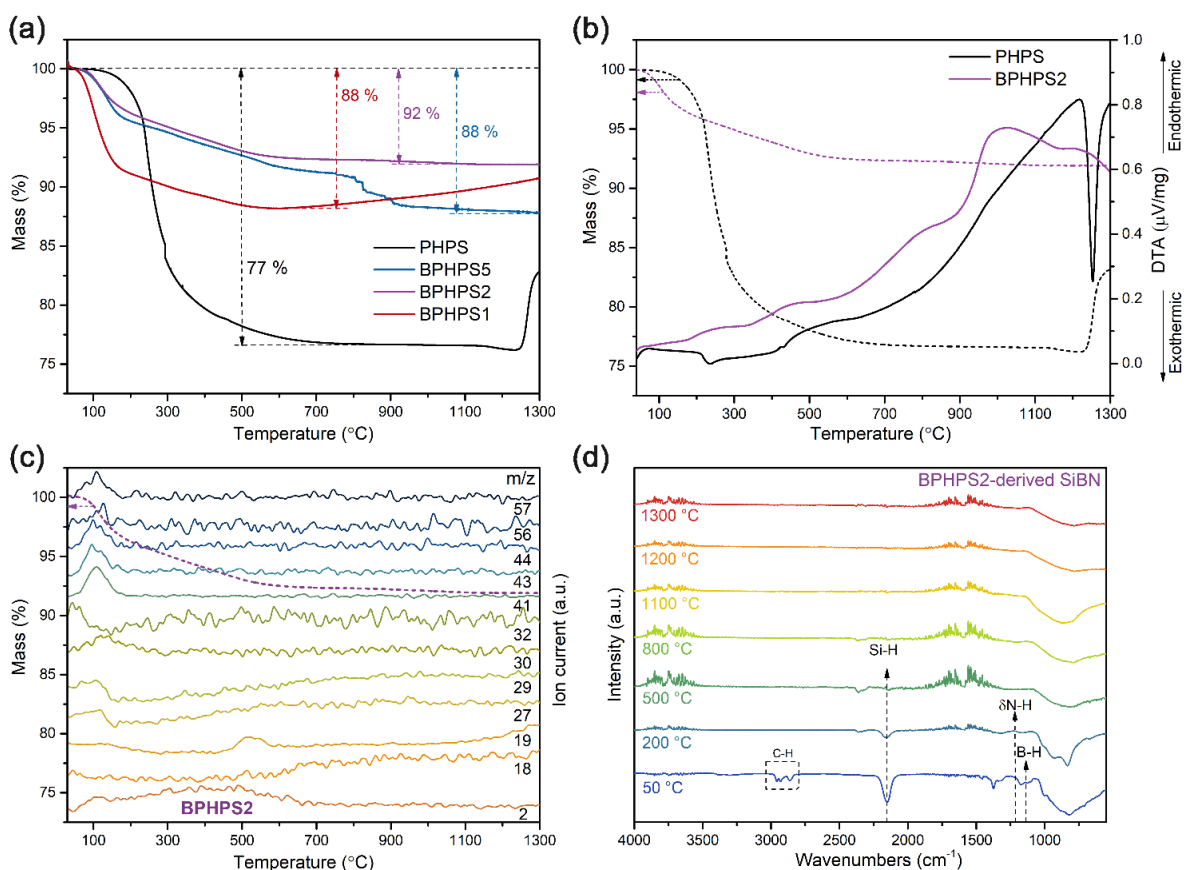
Figure 3.21 (a) TG curves recorded for dried PHPS and BPHPSx (x = Si/B molar ratio) under N_2. (b) TG (dashed lines) and DTA (bold lines) curves of dried PHPS and BPHPS2 under N_2. (c) Ion current profiles (bold lines) of typical mass fragments during pyrolysis of BPHPS2 up to 1300 °C under N_2: hydrogen (m/z = 2), water (m/z = 18, 19), C_2H_3 (m/z = 27), SiH_4 (m/z = 29, 30, 32), amines (m/z = 41, 43, derivatives of Me_2NH), CO_2 (m/z = 44), C_4H_9 (m/z = 56, 57). Dashed line represents the corresponding TG curve. (d) FTIR spectra of BPHPS2 recorded at different temperatures. Adapted from Ref. [3].

Table 3.4 Carbon content of BPHPS1-, BPHPS2-, and BPHPS5-derived ceramics (annealed at 1300 °C in N_2) obtained by elemental analysis. Adapted from Ref. [3].

Sample	BPHPS1-derived ceramic	BPHPS2-derived ceramic	BPHPS5-derived ceramic
Carbon Content (wt%)	0.35	0.49	0.24

The PHPS and BPHPSx samples pyrolyzed at 1100 °C have been further annealed at 1200 °C and 1300 °C. The structural evolution and crystallization behavior of the annealed samples are investigated by X-ray diffraction (XRD), transmission electron microscopy (TEM), and EDX spectroscopy. Figure 3.22 compares the XRD patterns of the PHPS- and BPHPSx-derived ceramics. All the as-prepared ceramics annealed at 1100 °C are X-ray amorphous. The boron-free PHPS-derived ceramic annealed at 1200 °C exhibits a low-intensity reflection of α-Si_3N_4, while the BPHPSx-derived ceramics remain X-ray amorphous. Crystallization of the PHPS-derived ceramic is induced between 1200 °C and 1300 °C, which is evidenced by the α-Si_3N_4 phase identified in the XRD pattern at 1300 °C, the mass gain of 6 wt% shown in the TG curve (Figure 3.21a) and the exothermal peak detected in the DTA curve (Figure 3.21b) [213]. On the contrary, increasing the temperature to 1300 °C results in a slight crystallization of α-Si_3N_4 microcrystals in the BPHPS5- and BPHPS2-derived ceramics, while the XRD pattern of the BPHPS1-derived ceramic stays X-ray amorphous. It is clearly demonstrated that the boron incorporation hinders the crystallization of both Si_3N_4 and BN, which is attributed to the higher crystallization temperature of the formed ternary Si–B–N system [214,215].
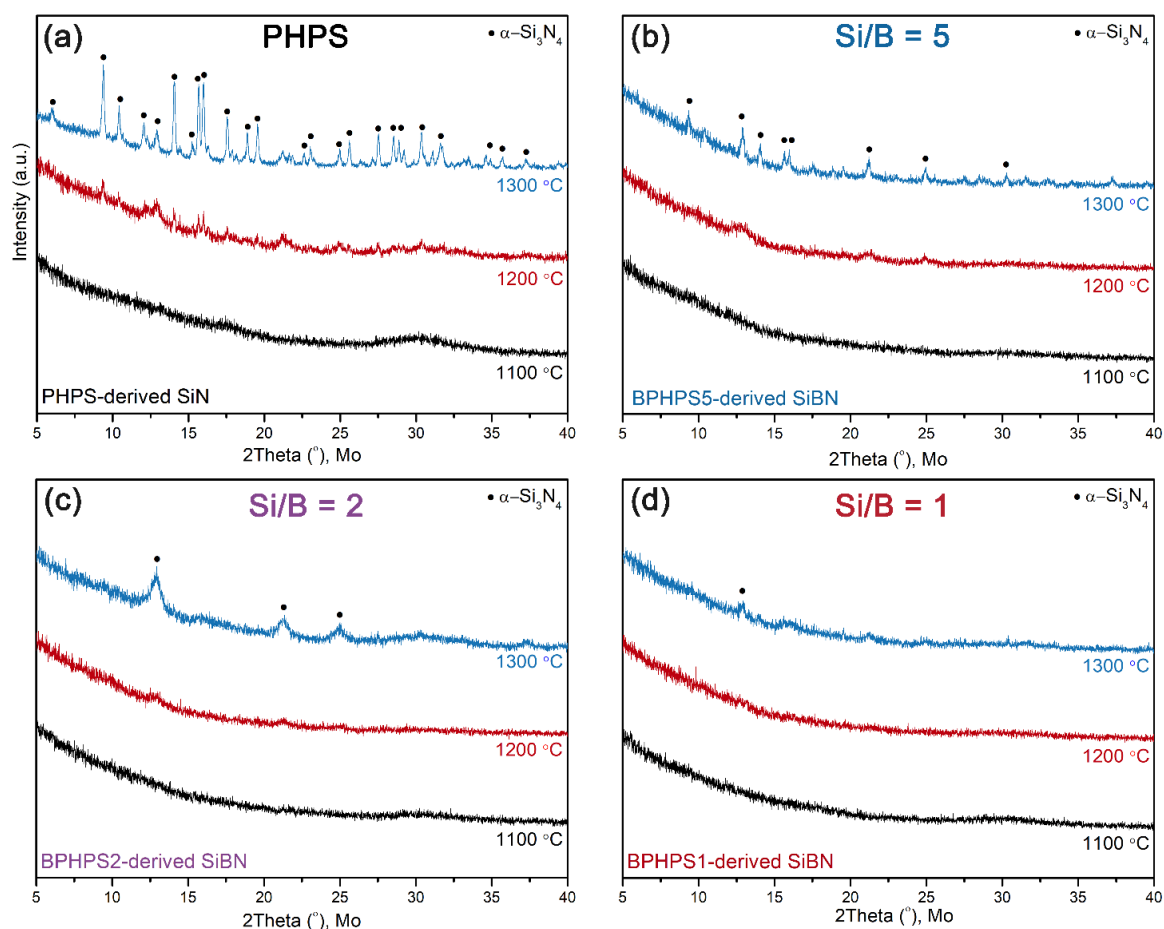
Figure 3.22 XRD patterns of as-pyrolyzed (a) PHPS and (b)–(d) BPHPSx (x = Si/B molar ratio) samples annealed for 2 h at different temperatures. Adapted from Ref. [3].

Figure 3.23 compares the high-resolution TEM (HRTEM) images and the selected area electron diffraction (SAED) patterns of the PHPS- and BPHPS2-derived ceramics annealed at 1300 °C. The HRTEM image of PHPS-derived ceramic (Figure 3.23a) indicates the crystalline structure with the lattice fringe of 0.21 nm attributed to the d-spacing of (202) α-Si_3N_4 lattice plane (JPCDS card no. 09–0250). The corresponding SAED pattern (inset in Figure 3.23a) shows the diffraction spots of the α-Si_3N_4 crystals. In contrast, the HRTEM image and the SAED pattern (Figure 3.23b) affirm that the BPHPS2-derived ceramic is amorphous after annealing at 1300 °C. This result further supports the conclusion that the boron incorporation suppresses the crystallization of Si_3N_4.
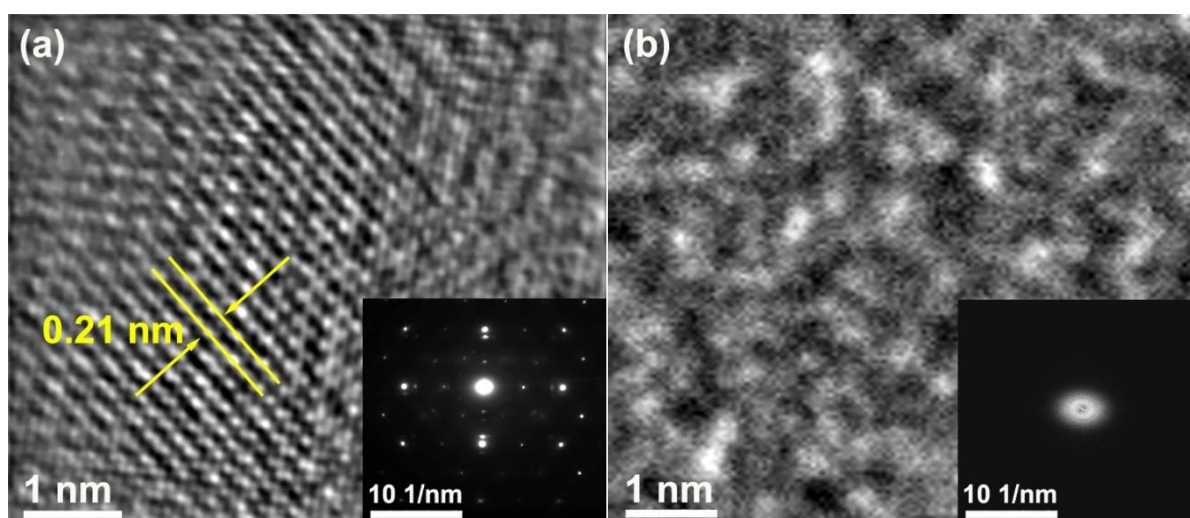
Figure 3.23 Filtered high-resolution TEM images of (a) PHPS- and (b) BPHPS2-derived ceramics annealed at 1300 °C. Insets are the corresponding SAED patterns. Adapted from Ref. [3].

Molecular dynamics simulation

Besides experimental techniques, molecular dynamics (MD) simulation has been conducted to investigate the molecular structure and the atomic-level diffusion behavior of amorphous silicon nitride and SiBN ceramics. The coordination number and pair distribution function (PDF) of four amorphous ceramic systems (Si_3N_4, $Si_3B_{0.6}N_{4.6}$, $Si_3B_{1.5}N_{5.5}$, and $Si_3B_3N_7$) have been simulated at a temperature of 1300 °C using the Tersoff many-body potentials [216]. Details of the simulated systems and simulation processes can be found in Ref. [3].

Figure 3.24a and b present the total and partial PDFs of silicon nitride and SiBN ceramics, where all PDFs converge to a constant value of 1 for radii larger than 0.5 nm, indicating a long-range amorphous disorder in the ceramics. The short-range atomic arrangements are revealed by comparing the peaks. Sharp peaks at a distance of ~0.17 nm appear in the total PDFs of all investigated ceramics, which corresponds well to the Si–N distance shown in the partial PDFs.

The simulated Si–N bond length (~0.17 nm) is analogous to the values estimated experimentally (0.173–0.175 nm) [217–219]. The B–N pair stands out at a distance of 0.149 nm in the partial PDF of $Si_3B_{1.5}N_{5.5}$ ceramic, which can be found in the total PDFs of all SiBN ceramics, indicating a strong bonding between boron and nitrogen elements. This characteristic distance is consistent with the B–N bond length obtained from experiments and density functional theory calculations (0.144–0.156 nm) [220,221]. As the boron content increases, the height of this peak increases, suggesting that more boron atoms surrounding any given nitrogen atom. Compared to the Si–N or B–N pairs, the Si–B pair (~0.28 nm) has a much lower height in the partial PDF of $Si_3B_{1.5}N_{5.5}$ ceramic, indicating that the formation of Si–B bond is disfavored.

The coordination numbers of Si and N elements calculated from the PDFs are displayed in Figure 3.24c as a function of the B/Si atomic ratio. The coordination number of Si surrounded by N ($Si_{(N)}$) decreases slightly whereas the $Si_{(B)}$ increases with the increasing B/Si atomic ratio, implying that the probability of Si–B bond formation rises when more boron atoms are added. At the bottom of the figure, the coordination number $N_{(B)}$ increases as the B/Si atomic ratio increases, while the coordination number of $N_{(Si)}$ decreases. It is well demonstrated that the boron incorporation has a larger impact on the N sites than that on the Si sites.
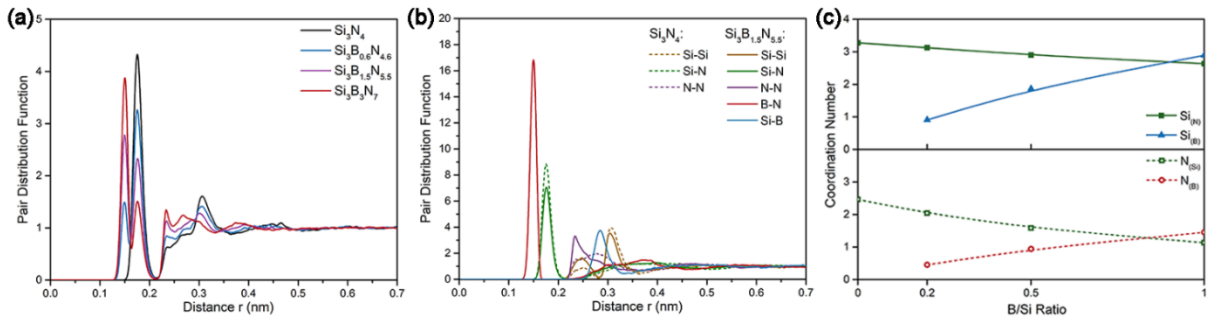
Figure 3.24 (a) Total pair distribution functions for amorphous ceramics Si_3N_4 (black), $Si_3B_{0.6}N_{4.6}$ (blue), $Si_3B_{1.5}N_{5.5}$ (purple), and $Si_3B_3N_7$ (red). (b) Partial pair distribution functions calculated from Si_3N_4 (dashed lines) and $Si_3B_{1.5}N_{5.5}$ (solid lines) for Si–Si, Si–N, N–N, B–N, and Si–B pairs. (c) Coordination numbers as a function of B/Si ratio for central atoms of Si (top) surrounded by N atoms and B atoms, and N (bottom) surrounded by Si atoms and B atoms. Adapted from Ref. [3].

The atomic diffusion behavior of Si, N, and B atoms in amorphous silicon nitride and SiBN ceramics is evaluated by the simulated mean-square displacement (MSD), as shown in Figure 3.25a–c. The MSDs of Si are comparable in all investigated ceramics, suggesting that the Si atomic mobility is virtually unaffected by the boron incorporation. On the contrary, the N atomic diffusivity in SiBN ceramics is lower than that in the Si_3N_4 ceramic and it decreases further with increasing boron content. The MSDs of B decrease at the same time. Combining

the findings observed in Figure 3.24, it can thus be suggested that the formed B–N bonds are not only copious but also strong in the Si–B–N systems, which restrict the atomic motion of N and B and hence improve the system stability. Further analyses on the atomic self-diffusion coefficients (Figure 3.25d) obtained from the limiting slopes of MSDs (in the range of 900–1100 ps) support this assumption. The self-diffusion coefficients of nitrogen and boron decrease significantly with increasing boron content due to the strong mutual attraction of B and N. The presence of rigid B–N bonds prevents N atoms from diffusing in the Si–B–N network and impedes the formation of crystallites at elevated temperatures. Similar behaviors are found as well for the relaxation properties in the SiBN ceramics, e.g., van-Hove correlation functions and intermediate scattering functions, which are detailed in the Supporting Information of Ref. [3].

In conclusion, the existence of boron allows the formation of rigid B–N bonds and consequently reduces the atomic diffusivity of the nitrogen in the Si–B–N network. Therefore, the thermal stability of amorphous Si–B–N is considerably enhanced relative to amorphous Si–N.
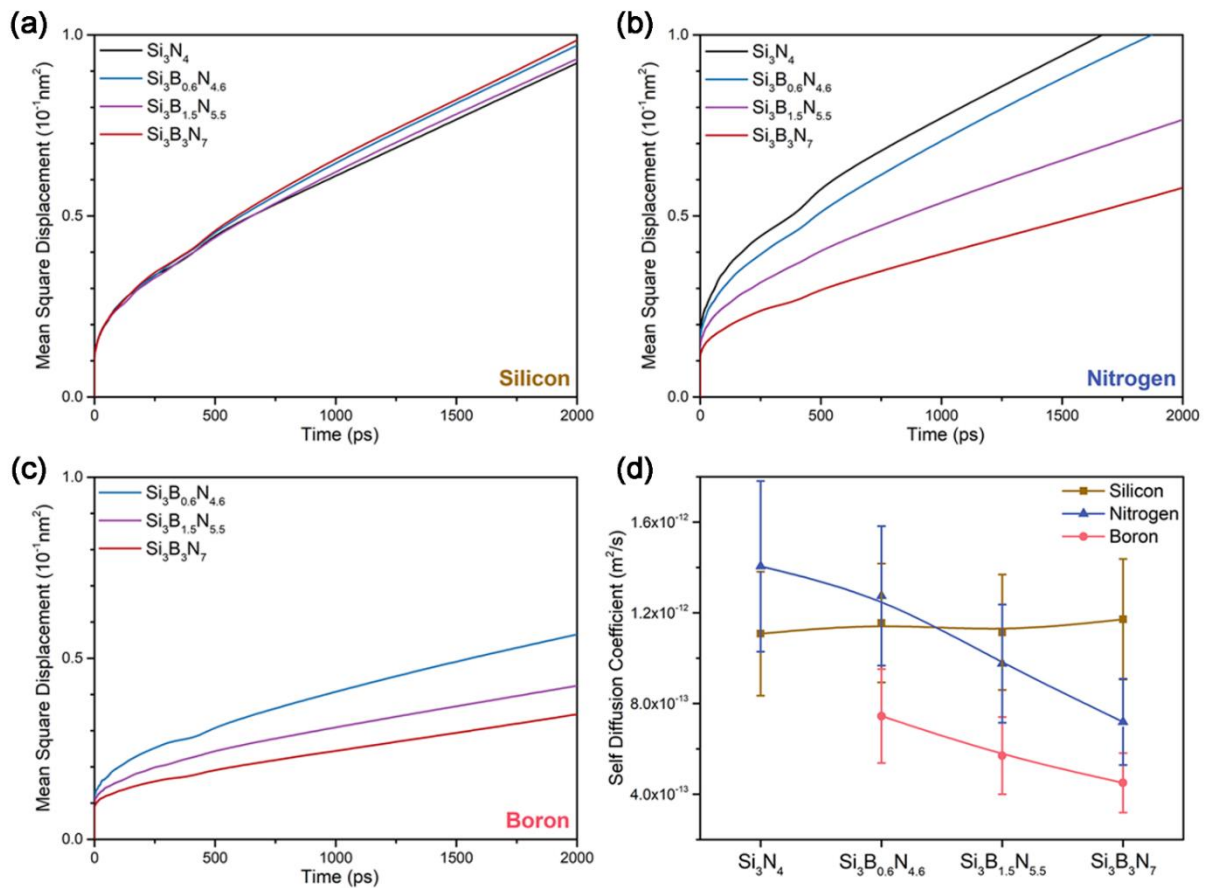
Figure 3.25 Mean-square displacement curves of (a) silicon, (b) nitrogen, and (c) boron atoms, and (d) the corresponding atomic self-diffusion coefficients in SiBN ceramics with different elemental compositions at 1300 °C. Adapted from Ref. [3].

4. Conclusions and Outlook

This research work aims to prepare polysilazane-based coatings at room temperature for the applications of protective, easy-to-clean, or anti-corrosion coatings. This goal has been achieved by i) understanding the moisture curing behavior and film formation of different polysilazane coatings, and by ii) improving the film properties via either catalyst or boron modifier. As a result, polysilazane coatings with significantly improved film quality, enhanced mechanical properties, hydrophobicity, and chemical stability have been successfully fabricated at room temperature, and with greatly reduced processing time.

Polysilazane coatings with industrial favorable thicknesses of 5–7 μm are easily prepared via spin coating followed by moisture curing at room temperature. A systematic evaluation of six different polysilazane coatings allows us to identify the role of molecular structure contributing to the crosslinking rate and degree, and thus to the film properties. The inorganic perhydropolysilazane (PHPS) coatings that have thinner thicknesses crosslink much faster under ambient conditions and exhibit higher hardness and elastic modulus, while the organopolysilazane (OPSZ) coatings display higher hydrophobicity. An intuitive guide to the coating material selection is thus provided (Figure 4.1).
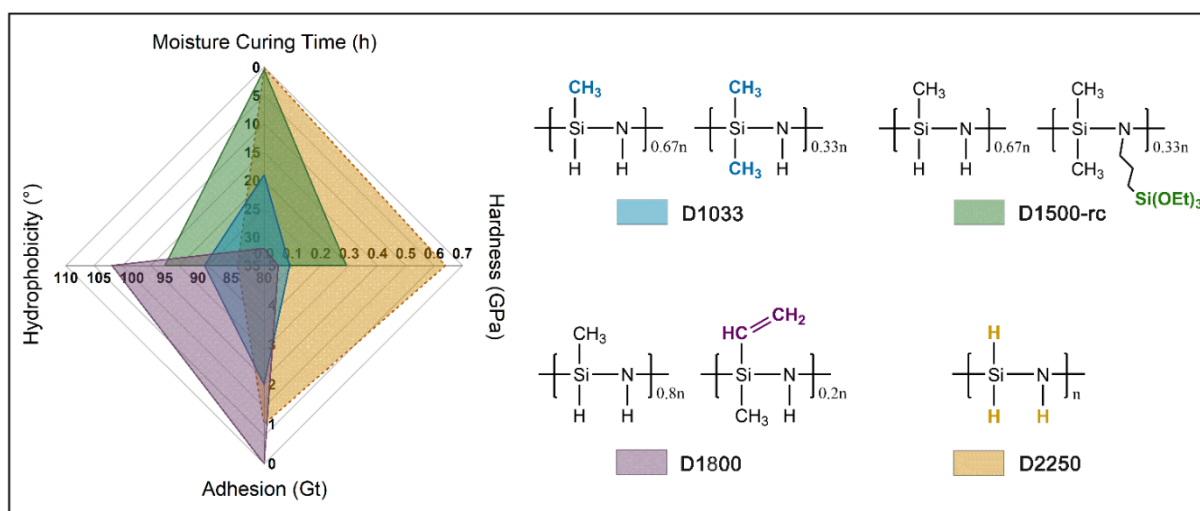
Figure 4.1 Comparative evaluation of the moisture curing rate, hardness, coating-substrate adhesion, and hydrophobicity of polysilazane coatings with different molecular structures.

In order to reduce the processing time and enhance the film properties of polysilazane (especially OPSZ) coatings for industrial applications, two methods have been used to facilitate the crosslinking processes. The first approach applied tetrabutylammonium chloride (TBAC) as an effective catalyst for the moisture curing of organopolysilazane (Durazane 1033) coating in ambient atmosphere and temperature. The Si–H groups of the OPSZ are nucleophilically

attacked by chloride ions to form transient Si–Cl groups, which are nucleophilically substituted by–OH groups via reaction with H_2O from the moisture environment. The byproduct HCl provides an acidic environment for further catalysis. Finally, the reactions between Si–Cl and Si–OH groups as well as the condensation of two Si-OH groups promote the formation of Si–O–Si groups. The Fourier-transform infrared spectroscopy (FTIR) results show that 1.6 times more of the Si–H and Si–NH groups are consumed in a shorter time (the dry-to-touch time for the uncatalyzed and the TBAC-catalyzed D1033 coatings are ca. 19 h and 1 h, respectively), while 2 times more of the Si–O–Si groups are formed. The gel permeation chromatography and energy dispersive X-ray spectroscopy support the findings that the TBAC not only accelerates the moisture curing of the OPSZ but also increases the crosslinking degree of the coating. Compared to the uncatalyzed D1033, which experiences a failure of film formation due to poor wetting to the substrates (polycarbonate and Si wafer), a dense and smooth film free from large irregularities is obtained with the TBAC-catalyzed D1033. Owing to the highly improved coating quality and the much higher crosslinking degree, the TBAC-catalyzed D1033 coating amounts double the value of hardness and quadruple the value of elastic modulus compared to that of the uncatalyzed coating.

In the second approach, polysilazanes were reacted with borane dimethyl sulfide complex to obtain boron-modified organopolysilazanes (BOPSZ) and perhydropolysilazanes (BPHPS) with varying chemical compositions. It has been verified by FTIR and nuclear magnetic resonance spectroscopy that the modification is accomplished through dehydrocoupling reactions between N–H (Si–H) and B–H groups. A high crosslinking degree is achieved in the synthesized boron-modified polysilazanes. The BOPSZ has been coated under ambient conditions. The incorporation of boron accelerates the moisture curing rate and degree. A dense film with an even surface morphology and higher hydrophobicity (101.1°) as compared to that of the pristine OPSZ (D1033) coating (88.7°) is obtained. The corrosion resistance of the polysilazane coating against highly corrosive HCl is greatly enhanced due to the improved film quality and the highly crosslinked network. The BPHPSs have been applied as carbon- and chlorine-free single-source precursors for the preparation of SiBN ceramics via the polymer-derived ceramic route under N_2. A facile and economic synthesis method with high ceramic yield (92 wt%) is thereby attained as opposed to the former reported ammonolysis synthesis process. The X-ray diffraction results reveal that the crystallization at T > 1000 °C is effectively suppressed in BPHPS-derived ceramics with increasing boron content. Molecular dynamics simulation provides a rational explanation that by adding boron rigid B–N bonds are formed with the consequence that the self-diffusion coefficient of nitrogen in the ternary Si–B–N network is decreased. Therefore, the thermal stability of the amorphous SiBN ceramic with respect to crystallization and

decomposition is considerably enhanced if compared with the thermal behavior of the boron-free silicon nitride derived from pure PHPS.

Taken together, this dissertation presents two approaches for preparing polysilazane-based coatings with outstanding surface hardness, high hydrophobicity, and remarkable chemical stability (Figure 4.2). The organopolysilazane-derived materials are promising candidates for protective, easy-to-clean, and anti-corrosion coatings applied in vehicles, commercial and residential buildings, and industrial plants. Further investigation on the coating formulation needs to be done to upscale the materials and their processing to realize the aforementioned technical applications. In addition, research on the boron-modified perhydropolysilazane-derived ceramics has laid the groundbreaking work for the development of thermally stable SiBN ceramic coatings with various functional properties such as microwave transparency, low dielectric constant, environmental or thermal barrier effect, etc.
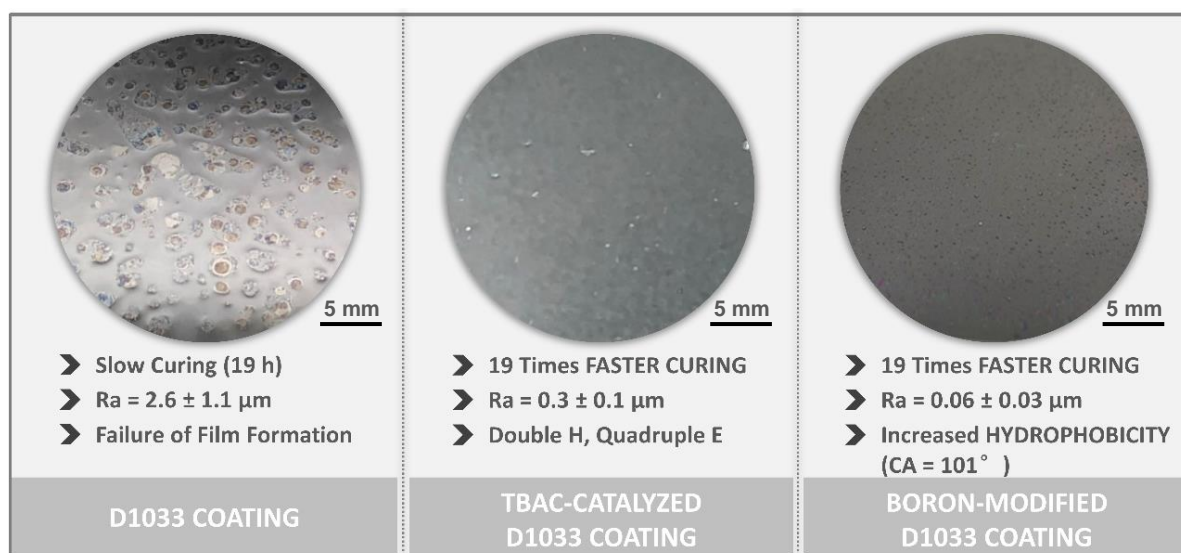
Figure 4.2 Parallel comparison of the pristine D1033, TBAC-catalyzed D1033, and boron-modified D1033 coatings demonstrates the significant improvement of polysilazane coatings in coating uniformity, moisture curing rate, mechanical properties, and hydrophobicity after TBAC catalysis or boron modification.

5. References

1. Zhan, Y., Grottenmüller, R., Li, W., Javaid, F. & Riedel, R. Evaluation of mechanical properties and hydrophobicity of room-temperature, moisture-curable polysilazane coatings. *J. Appl. Polym. Sci.* **138**, 50469 (2021).

2. Zhan, Y., Li, W., Grottenmüller, R., Minnert, C., Krasemann, T., Wen, Q. & Riedel, R. Rapid curing of polysilazane coatings at room temperature via chloride-catalyzed hydrolysis/condensation reactions. *Prog. Org. Coat.* **167**, 106872 (2022).

3. Zhan, Y., Li, W., Jiang, T., Fasel, C., Ricohermoso, E., Bernauer, J., Yu, Z., Wu, Z., Müller-Plathe, F., Molina-Luna, L., Grottenmüller, R. & Riedel, R. Boron-modified perhydropolysilazane towards facile synthesis of amorphous SiBN ceramic with excellent thermal stability. *J. Adv. Ceram.* **11**, 1104–1116 (2022).

4. Plueddemann, E. P. Silane adhesion promoters in coatings. *Prog. Org. Coat.* **11**, 297–308 (1983).

5. Barroso, G., Li, Q., Bordia, R. K. & Motz, G. Polymeric and ceramic silicon-based coatings–a review. *J. Mater. Chem. A* **7**, 1936–1963 (2019).

6. Colombo, P., Riedel, R., Sorarù, G. D. & Kleebe, H.-J. *Polymer derived ceramics: from nano-structure to applications*. (DEStech Publications, Inc, 2010).

7. Amouzou, D., Fourdrinier, L., Maseri, F. & Sporken, R. Formation of Me-O-Si covalent bonds at the interface between polysilazane and stainless steel. *Appl. Surf. Sci.* **320**, 519–523 (2014).

8. Colombo, P., Mera, G., Riedel, R. & Soraru, G. D. Polymer-derived ceramics: 40 years of research and innovation in advanced ceramics. *J. Am. Ceram. Soc.* **93**, 1805–1837 (2010).

9. Kim, S. D., Ko, P. S. & Park, K. S. Perhydropolysilazane spin-on dielectrics for inter-layer-dielectric applications of sub-30 nm silicon technology. *Semicond. Sci. Technol.* **28**, 35008 (2013).

10. Rossi, S., Deflorian, F. & Fedel, M. Polysilazane-based coatings: corrosion protection and anti-graffiti properties. *Surf. Eng.* **35**, 343–350 (2019).

11. Wang, Y., Grottenmuller, R. & Lorenz, T. Polysilazanes – binders that make a difference. *CoatingsTech* vol. 16 38–45 (2019).

12. Günthner, M., Schütz, A., Glatzel, U., Wang, K., Bordia, R. K., Greißl, O., Krenkel, W. & Motz, G. High performance environmental barrier coatings, Part I: Passive filler loaded SiCN system for steel. *J. Eur. Ceram. Soc.* **31**, 3003–3010 (2011).

13. Barroso, G., Döring, M., Horcher, A., Kienzle, A. & Motz, G. Polysilazane-based coatings with anti-adherent properties for easy release of plastics and composites from metal molds. *Adv. Mater. Interfaces* **7**, 1–14 (2020).

14. *Global polysilazane sales market report 2022.* https://www.xcellentinsights.com/reports/polysilazane-market-3489#description (2022).

15. Yamano, A. & Kozuka, H. Preparation of silica coatings heavily doped with spiropyran using perhydropolysilazane as the silica source and their photochromic properties. *J. Phys. Chem. B* **113**, 5769–5776 (2009).

16. Seyferth, D. & Wiseman, G. H. High-yield synthesis of Si_3N_4/SiC ceramic materials by pyrolysis of a novel poly organosilazane. *J. Am. Ceram. Soc.* **67**, C-132–C-133 (1984).

17. Jones, R. G., Ando, W. & Chojnowski, J. *Silicon-containing polymers: the science and*

technology of their synthesis and applications. (Springer Science & Business Media, 2013).

18. Riedel, R., Mera, G., Hauser, R. & Klonczynski, A. Silicon-based polymer-derived ceramics: Synthesis properties and applications-A review. *J. Ceram. Soc. Japan* **114**, 425–444 (2006).

19. Stock, A. & Somieski, K. Siliciumwasserstoffe, X.: Stickstoffhaltige Verbindungen. *Berichte der Dtsch. Chem. Gesellschaft (A B Ser.* **54**, 740–758 (1921).

20. Krüger, C. R. & Rochow, E. G. Polyorganosilazanes. *J. Polym. Sci. part A* **2**, 3179–3189 (1964).

21. Fink, W. Silicon-nitrogen heterocycles. *Angew. Chemie Int. Ed. English* **5**, 760–776 (1966).

22. Kroke, E., Li, Y. L., Konetschny, C., Lecomte, E., Fasel, C. & Riedel, R. Silazane derived ceramics and related materials. *Mater. Sci. Eng. R Reports* **26**, 97–199 (2000).

23. Hörz, M., Zern, A., Berger, F., Haug, J., Müller, K., Aldinger, F. & Weinmann, M. Novel polysilazanes as precursors for silicon nitride/silicon carbide composites without "free" carbon. *J. Eur. Ceram. Soc.* **25**, 99–110 (2005).

24. Abel, A. E., Kruger, T. A., Mouk, R. W. & Knasiak, G. J. Silazane and/or polysilazane compounds and methods of making. (2001).

25. Wynne, K. J. & Rice, R. W. Ceramics via polymer pyrolysis. *Annu. Rev. Mater. Sci.* **14**, 297–334 (1984).

26. Penn, B. G., Ledbetter, F. E., Clemons, J. M. & Daniels, J. G. Preparation of silicon carbide–silicon nitride fibers by the controlled pyrolysis of polycarbosilazane precursors. *J. Appl. Polym. Sci.* **27**, 3751–3761 (1982).

27. Penn, B. G., Daniels, J. G., Ledbetter, F. E. & Clemons, J. M. Preparation of silicon carbide-silicon nitride fibers by the pyrolysis of polycarbosilazane precursors: A review. *Polym. Eng. Sci.* **26**, 1191–1194 (1986).

28. Bernard, S., Weinmann, M., Gerstel, P., Miele, P. & Aldinger, F. Boron-modified polysilazane as a novel single-source precursor for SiBCN ceramic fibers: synthesis, melt-spinning, curing and ceramic conversion. *J. Mater. Chem.* **15**, 289–299 (2005).

29. Flores, O., Schmalz, T., Krenkel, W., Heymann, L. & Motz, G. Selective cross-linking of oligosilazanes to tailored meltable polysilazanes for the processing of ceramic SiCN fibres. *J. Mater. Chem. A* **1**, 15406–15415 (2013).

30. Motz, G., Hacker, J. & Ziegler, G. Special modified silazanes for coatings, fibers and CMC'S. in *24th Annual Conference on Composites, Advanced Ceramics, Materials, and Structures: B: Ceramic Engineering and Science Proceedings* 307–314 (2008).

31. Kokott, S., Heymann, L. & Motz, G. Rheology and processability of multi-walled carbon nanotubes—ABSE polycarbosilazane composites. *J. Eur. Ceram. Soc.* **28**, 1015–1021 (2008).

32. Jones, R., Szweda, A. & Petrak, D. Polymer derived ceramic matrix composites. *Compos. Part A Appl. Sci. Manuf.* **30**, 569–575 (1999).

33. Schmidt, W. R., Narsavage-Heald, D. M., Jones, D. M., Marchetti, P. S., Raker, D. & Maciel, G. E. Poly(borosilazane) precursors to ceramic nanocomposites. *Chem. Mater.* **11**, 1455–1464 (1999).

34. Rak, Z. S. Novel CMC material based on a Si_3N_4 matrix. *Adv. Eng. Mater.* **2**, 503–507 (2000).

35. Ionescu, E., Kleebe, H. J. & Riedel, R. Silicon-containing polymer-derived ceramic nanocomposites (PDC-NCs): preparative approaches and properties. *Chem. Soc. Rev.* **41**,

5032–5052 (2012).

36. Nghiem, Q. D., Kim, D. & Kim, D.-P. Synthesis of inorganic-organic diblock copolymers as a precursor of ordered mesoporous SiCN ceramic. *Adv. Mater.* **19**, 2351–2354 (2007).

37. Wang, H., Zheng, S. Y., Li, X. D. & Kim, D. P. Preparation of three-dimensional ordered macroporous SiCN ceramic using sacrificing template method. *Microporous Mesoporous Mater.* **80**, 357–362 (2005).

38. Iwamoto, Y., Sato, K., Kato, T., Inada, T. & Kubo, Y. A hydrogen-permselective amorphous silica membrane derived from polysilazane. *J. Eur. Ceram. Soc.* **25**, 257–264 (2005).

39. Graczyk-Zajac, M., Fasel, C. & Riedel, R. Polymer-derived-SiCN ceramic/graphite composite as anode material with enhanced rate capability for lithium ion batteries. *J. Power Sources* **196**, 6412–6418 (2011).

40. Bhandavat, R. & Singh, G. Improved electrochemical capacity of precursor-derived Si(B)CN-carbon nanotube composite as Li-Ion battery anode. *ACS Appl. Mater. Interfaces* **4**, 5092–5097 (2012).

41. Vrankovic, D., Reinold, L. M., Riedel, R. & Graczyk-Zajac, M. Void-shell silicon/carbon/SiCN nanostructures: toward stable silicon-based electrodes. *J. Mater. Sci.* **51**, 6051–6061 (2016).

42. Blum, Y. D., Schwartz, K. B. & Laine, R. M. Preceramic polymer pyrolysis - Part 1 Pyrolytic properties of polysilazanes. *J. Mater. Sci.* **24**, 1707–1718 (1989).

43. Li, Y., Kroke, E., Riedel, R., Fasel, C., Gervais, C. & Babonneau, F. Thermal cross-linking and pyrolytic conversion of poly(ureamethylvinyl)silazanes to silicon-based ceramics. *Appl. Organomet. Chem.* **15**, 820–832 (2001).

44. Mocaer, D., Pailler, R., Naslain, R., Richard, C., Pillot, J. P., Dunogues, J., Gerardin, C. & Taulelle, F. Si-C-N ceramics with a high microstructural stability elaborated from the pyrolysis of new polycarbosilazane precursors. *J. Mater. Sci. 1993 2810* **28**, 2615–2631 (1993).

45. Yive, S. C. K., Corriu, R. J. P., Leclercq, D., Mutin, P. H. & Vioux, A. Silicon carbonitride from polymeric precursors: thermal cross-linking and pyrolysis of oligosilazane model compounds. *Chem. Mater.* **4**, 141–146 (1992).

46. Bahloul, D., Pereira, M., Goursat, P., Yive, N. S. C. K. & Corriu, R. J. P. Preparation of silicon carbonitrides from an organosilicon polymer: I, thermal decomposition of the cross-linked polysilazane. *J. Am. Ceram. Soc.* **76**, 1156–1162 (1993).

47. Müller, S., De Hazan, Y. & Penner, D. Effect of temperature, humidity and aminoalkoxysilane additive on the low temperature curing of polyorganosilazane coatings studied by IR spectroscopy, gravimetric and evolved gas analysis. *Prog. Org. Coat.* **97**, 133–145 (2016).

48. Fedel, M., Rodríguez Gómez, F. J., Rossi, S. & Deflorian, F. Characterization of polyorganosilazane-derived hybrid coatings for the corrosion protection of mild steel in chloride solution. *Coatings* **9**, 680 (2019).

49. Lukacs, A. & Knasiak, G. J. Thermally stable, moisture curable polysilazanes and polysiloxazanes. (2003).

50. Bauer, F., Decker, U., Dierdorf, A., Ernst, H., Heller, R., Liebe, H. & Mehnert, R. Preparation of moisture curable polysilazane coatings Part I. Elucidation of low temperature curing kinetics by FT-IR spectroscopy. *Prog. Org. Coat.* **53**, 183–190 (2005).

51. Chavez, R., Ionescu, E., Balan, C., Fasel, C. & Riedel, R. Effect of ambient atmosphere on crosslinking of polysilazanes. *J. Appl. Polym. Sci.* **119**, 794–802 (2011).

52. Günthner, M., Wang, K., Bordia, R. K. & Motz, G. Conversion behaviour and resulting mechanical properties of polysilazane-based coatings. *J. Eur. Ceram. Soc.* **32**, 1883–1892 (2012).

53. Morlier, A., Cros, S., Garandet, J. P. & Alberola, N. Structural properties of ultraviolet cured polysilazane gas barrier layers on polymer substrates. *Thin Solid Films* **550**, 85–89 (2014).

54. Prager, L., Dierdorf, A., Liebe, H., Naumov, S., Stojanović, S., Heller, R., Wennrich, L. & Buchmeiser, M. R. Conversion of perhydropolysilazane into a SiO_x network triggered by vacuum ultraviolet irradiation: Access to flexible, transparent barrier coatings. *Chem. - A Eur. J.* **13**, 8522–8529 (2007).

55. Kato, C., Tanaka, S., Naganuma, Y. & Shindo, T. Room temperature photochemical fabrication of silica glass coatings using vacuum ultraviolet excimer lamps. *J. Photopolym. Sci. Technol.* **16**, 163–164 (2003).

56. Urabe, Y. & Sameshima, T. Polysilazane precursor used for formation of oxidized insulator. *MRS Online Proc. Libr.* **1066**, 107–111 (2008).

57. Suzurikawa, J., Nakao, M. & Takahashi, H. Surface passivation of the thin-film LAPS with perhydropolysilazane-derived silica treated by O_2 plasma. *IEEJ Trans. Electr. Electron. Eng.* **6**, 392–393 (2011).

58. Mera, G. & Ionescu, E. Silicon-containing preceramic polymers. *Encycl. Polym. Sci. Technol.* (2013).

59. Bill, J. & Aldinger, F. Precursor-derived covalent ceramics. *Adv. Mater.* **7**, 775–787 (1995).

60. Lavedrine, A., Bahloul, D., Goursat, P., Choong Kwet Yive, N., Corriu, R., Leclerq, D., Mutin, H. & Vioux, A. Pyrolysis of polyvinylsilazane precursors to silicon carbonitride. *J. Eur. Ceram. Soc.* **8**, 221–227 (1991).

61. Yive, N. S. C. K., Corriu, R., Leclercq, D., Mutin, P. H. & Vioux, A. Polyvinylsilazane: A novel precursor to silicon carbonitride. *New J. Chem.* **15**, 85–92 (1991).

62. D'Elia, R., Dusserre, G., Del Confetto, S., Eberling-Fux, N., Descamps, C. & Cutard, T. Cure kinetics of a polysilazane system: Experimental characterization and numerical modelling. *Eur. Polym. J.* **76**, 40–52 (2016).

63. Dargère, N., Bounor-Legaré, V., Boisson, F., Cassagnau, P., Martin, G., Sonntag, P. & Garois, N. Hydridosilazanes hydrolysis-condensation reactions studied by ^{1}H and ^{29}Si liquid NMR spectroscopy. *J. Sol-Gel Sci. Technol.* **62**, 389–396 (2012).

64. Kozuka, H., Nakajima, K. & Uchiyama, H. Superior properties of silica thin films prepared from perhydropolysilazane solutions at room temperature in comparison with conventional alkoxide-derived silica gel films. *ACS Appl. Mater. Interfaces* **5**, 8329–8336 (2013).

65. Marceaux, S., Bressy, C., Perrin, F. X. F.-X., Martin, C. & Margaillan, A. Development of polyorganosilazane–silicone marine coatings. *Prog. Org. Coat.* **77**, 1919–1928 (2014).

66. Nakajima, K., Uchiyama, H., Kitano, T. & Kozuka, H. Conversion of solution-derived perhydropolysilazane thin films into silica in basic humid atmosphere at room temperature. *J. Am. Ceram. Soc.* **96**, 2806–2816 (2013).

67. Jung, S. H., Lee, J. S., Oh, J. H., Moon, S. W. & Kim, S. D. Method of low-temperature conversion of pehydropolysilazane into amorphous SiOx in aqueous solutions. *Jpn. J. Appl. Phys.* **49**, 0–7 (2010).

68. Rossi, S., Fedel, M., Petrolli, S. & Deflorian, F. Characterization of the anti-graffiti properties of powder organic coatings applied in train field. *Coatings* **7**, (2017).

69. Lo, T. N. H., Hwang, H. S., Lee, J. & Park, I. Synthesis of new semi-fluorinated polysilazanes and their amphiphobic coating applications. *Prog. Org. Coat.* **148**, 105853 (2020).

70. Wang, K., Gu, M., Motz, N., Flinn, B. D. & Bordia, R. K. Control of surface energy of silicon oxynitride films. *ACS Publ.* **29**, 2889–2896 (2013).

71. Morlier, A., Cros, S., Garandet, J.-P. & Alberola, N. Thin gas-barrier silica layers from perhydropolysilazane obtained through low temperature curings: A comparative study. *Thin Solid Films* **524**, 62–66 (2012).

72. Kubo, T., Tadaoka, E. & Kozuka, H. Formation of silica coating films from spin-on polysilazane at room temperature and their stability in hot water. *J. Mater. Res.* **19**, 635–642 (2004).

73. Kozuka, H., Fujita, M. & Tamoto, S. Polysilazane as the source of silica: The formation of dense silica coatings at room temperature and the new route to organic–inorganic hybrids. *J. sol-gel Sci. Technol.* **48**, 148–155 (2008).

74. Monti, M., Dal Bianco, B., Bertoncello, R. & Voltolina, S. New protective coatings for ancient glass: Silica thin-films from perhydropolysilazane. *J. Cult. Herit.* **9**, e143–e145 (2008).

75. Tanaka, T., Hanaoka, K., Yamaguchi, M., Shindo, T., Kunzelmann, K. H. & Teranaka, T. Silica film coating method for veneering resin composite. *Dent. Mater. J.* **30**, 170–175 (2011).

76. Lee, J. S., Oh, J. H., Moon, S. W., Sul, W. S. & Kim, S. D. A technique for converting perhydropolysilazane to SiO_x at low temperature. *Electrochem. Solid-State Lett.* **13**, 2009–2011 (2009).

77. Furtat, P., Lenz-Leite, M., Ionescu, E., MacHado, R. A. F. & Motz, G. Synthesis of fluorine-modified polysilazanes: Via Si-H bond activation and their application as protective hydrophobic coatings. *J. Mater. Chem. A* **5**, 25509–25521 (2017).

78. Richter, F., Krichel, M., Decker, D., Motz, G. & Shmalz, T. Method for producing thermoplastic pre-ceramic polymers. 1–10 (2015).

79. Corriu, R. J. P., Leclercq, D., Mutin, P. H., Planeix, J. M. & Vioux, A. Silicon-nitrogen bond formation by nucleophilic activation of silicon-hydrogen bonds. *J. Organomet. Chem.* **406**, C1–C4 (1991).

80. Tanabe, Y., Murakami, M., Kitaichi, K. & Yoshida, Y. Mild, effective and selective method for the silylation of alcohols using silazanes promoted by catalytic tetrabutylammonium fluoride. *Tetrahedron Lett.* **35**, 8409–8412 (1994).

81. Tanabe, Y., Okumura, H., Maeda, A. & Murakami, M. Mild and practical method for the silylation of alcohols using hydrosilanes and disilanes promoted by TBAF catalyst. *Tetrahedron Lett.* **35**, 8413–8414 (1994).

82. Zhou, C., Fasel, C., Ishikawa, R., Gallei, M., Ikuhara, Y., Lauterbach, S., Kleebe, H. J., Riedel, R. & Ionescu, E. One-pot synthesis of a C/SiFeN(O)-based ceramic paper with in-situ generated hierarchical micro/nano-morphology. *J. Eur. Ceram. Soc.* **37**, 5193–5203 (2017).

83. Salameh, C., Bernard, S., Gervais, C., Babonneau, F., Bruma, A., Malo, S. & Miele, P. Chemistry of a series of aluminum-modified polysilazanes: Synthesis, pyrolysis behaviour and microstructural evolution. *J. Eur. Ceram. Soc.* **39**, 183–194 (2019).

84. Feng, B., Peter, J., Fasel, C., Wen, Q., Zhang, Y., Kleebe, H. J. & Ionescu, E. High-temperature phase and microstructure evolution of polymer-derived SiZrCN and SiZrBCN ceramic nanocomposites. *J. Am. Ceram. Soc.* **103**, 7001–7013 (2020).

85. Yuan, J., Galetz, M., Luan, X. G., Fasel, C., Riedel, R. & Ionescu, E. High-temperature oxidation behavior of polymer-derived SiHfBCN ceramic nanocomposites. *J. Eur. Ceram. Soc.* **36**, 3021–3028 (2016).

86. Fonblanc, D., Lopez-Ferber, D., Wynn, M., Lale, A., Soleilhavoup, A., Leriche, A., Iwamoto, Y., Rossignol, F., Gervais, C. & Bernard, S. Crosslinking chemistry of poly(vinylmethyl-co-methyl)silazanes toward low-temperature formable preceramic polymers as precursors of functional aluminium-modified Si-C-N ceramics. *Dalt. Trans.* **47**, 14580–14593 (2018).

87. Iwamoto, Y., Kikuta, K. I. & Hirano, S. I. Synthesis of poly-titanosilazanes and conversion into Si_3N_4-TiN ceramics. *J. Ceram. Soc. Japan* **108**, 350–356 (2000).

88. Dressler, W. & Riedel, R. Progress in silicon-based non-oxide structural ceramics. *Int. J. Refract. Met. Hard Mater.* **15**, 13–47 (1997).

89. Yuan, J., Hapis, S., Breitzke, H., Xu, Y., Fasel, C., Kleebe, H. J., Buntkowsky, G., Riedel, R. & Ionescu, E. Single-source-precursor synthesis of hafnium-containing ultrahigh-temperature ceramic nanocomposites (UHTC-NCs). *Inorg. Chem.* **53**, 10443–10455 (2014).

90. Viard, A., Kurz, H., Lale, A., Heymann, L., Weber, B., Bernard, S., Knauer, M. & Motz, G. Superparamagnetic silicon carbonitride ceramic fibers through in situ generation of iron silicide nanoparticles during pyrolysis of an iron-modified polysilazane. *ACS Appl. Mater. Interfaces* **13**, 8745–8753 (2021).

91. Zhou, C., Yang, L., Geng, H., Zheng, Q., Min, H., Yu, Z. & Xia, H. Preparation of Si–C–N–Fe magnetic ceramic derived from iron-modified polysilazane. *Ceram. Int.* **38**, 6815–6822 (2012).

92. Riedel, R., Kienzle, A., Dressler, W., Ruwisch, L., Bill, J. & Aldinger, F. A silicoboron carbonitride ceramic stable to 2,000 °C. *Nature* **382**, 796–798 (1996).

93. Su, K., Remsen, E. E., Zank, G. A. & Sneddon, L. G. Synthesis, characterization, and ceramic conversion reactions of borazine-modified hydridopolysilazanes: New polymeric precursors to SiNCB ceramic composites. *Chem. Mater.* **5**, 547–556 (1993).

94. Riedel, R., Billt, J. & Kienzle, A. Boron-modified inorganic polymers-precursors for the synthesis of multicomponent ceramics. *Appl. Organomet. Chem.* **10**, 241–256 (1996).

95. Weinmann, M., Schuhmacher, J., Kummer, H., Prinz, S., Peng, J., Seifert, H. J., Christ, M., Muller, K., Bill, J. & Aldinger, F. Synthesis and thermal behavior of novel $Si-B-C-N$ ceramic precursors. *Chem. Mater.* **12**, 623–632 (2000).

96. Wang, Z. C., Aldinger, F. & Riedel, R. Novel silicon-boron-carbon-nitrogen materials thermally stable up to 2200°C. *J. Am. Ceram. Soc.* **84**, 2179–2183 (2001).

97. Gottardo, L., Bernard, S., Gervais, C., Weinmann, M. & Miele, P. Study of the intermediate pyrolysis steps and mechanism identification of polymer-derived SiBCN ceramics. *J. Mater. Chem.* **22**, 17923–17933 (2012).

98. Bernard, S., Weinmann, M., Cornu, D., Miele, P. & Aldinger, F. Preparation of high-temperature stable SiBCN fibers from tailored single source polyborosilazanes. *J. Eur. Ceram. Soc.* **25**, 251–256 (2005).

99. Gottardo, L., Bernard, S., Gervais, C., Inzenhofer, K., Motz, G., Weinmann, M., Balan, C. & Miele, P. Chemistry, structure and processability of boron-modified polysilazanes as tailored precursors of ceramic fibers. *J. Mater. Chem.* **22**, 7739–7750 (2012).

100. Wideman, T., Fazen, P. J., Su, K., Remsen, E. E., Zank, G. A. & Sneddon, L. G. Second-generation polymeric precursors for BN and SiNCB ceramic materials. *Appl. Organomet. Chem.* **12**, 681–693 (1998).

101. Nghiem, Q. D. & Kim, D. P. Highly-resistant SiCBN films prepared by a simple spin-coating process with poly(borosilazane). *J. Mater. Chem.* **15**, 2188–2192 (2005).

102. Bhandavat, R. & Singh, G. Synthesis, characterization, and high temperature stability of Si(B)CN-coated carbon nanotubes using a boron-modified poly(ureamethylvinyl)silazane chemistry. *J. Am. Ceram. Soc.* **95**, 1536–1543 (2012).

103. Feng, Z., Guo, Z., Lu, B. & Zhang, Y. Preparation and thermal cycling resistance of SiBCN(O) coating. *Key Eng. Mater.* **602–603**, 393–396 (2014).

104. Hauser, R., Nahar-Borchard, S., Riedel, R., Ikuhara, Y. H. & Iwamoto, Y. Polymer-derived SiBCN ceramic and their potential application for high temperature membranes. *J. Ceram. Soc. Japan* **114**, 524–528 (2006).

105. Lee, S. H. & Weinmann, M. Cfiber/SiCfiller/Si–B–C–Nmatrix composites with extremely high thermal stability. *Acta Mater.* **57**, 4374–4381 (2009).

106. Zhao, H., Chen, L., Luan, X., Zhang, X., Yun, J. & Xu, T. Synthesis, pyrolysis of a novel liquid SiBCN ceramic precursor and its application in ceramic matrix composites. *J. Eur. Ceram. Soc.* **37**, 1321–1329 (2017).

107. Weinmann, M., Kamphowe, T. W., Schuhmacher, J., Müller, K. & Aldinger, F. Design of polymeric Si−B−C−N ceramic precursors for application in fiber-reinforced composite materials. *Chem. Mater.* **12**, 2112–2122 (2000).

108. Yuan, J., Li, D., Johanns, K. E., Fasel, C., Durst, K., Kleebe, H. J., Shen, Z., Riedel, R. & Ionescu, E. Preparation of dense SiHf(B)CN-based ceramic nanocomposites via rapid spark plasma sintering. *J. Eur. Ceram. Soc.* **37**, 5157–5165 (2017).

109. Chen, Y., Yang, X., Cao, Y. & An, L. Effect of pyrolysis temperature on the electric conductivity of polymer-derived silicoboron carbonitride. *J. Eur. Ceram. Soc.* **34**, 2163–2167 (2014).

110. Sujith, R. & Kumar, R. Experimental investigation on the indentation hardness of precursor derived Si–B–C–N ceramics. *J. Eur. Ceram. Soc.* **33**, 2399–2405 (2013).

111. Kumar, R., Cai, Y., Gerstel, P., Rixecker, G. & Aldinger, F. Processing, crystallization and characterization of polymer derived nano-crystalline Si-B-C-N ceramics. *J. Mater. Sci.* **41**, 7088–7095 (2006).

112. Lu, L., Feng, C. X. & Song, Y. C. Curing polysilazane fibres by exposure to boron trichloride. *J. Mater. Sci. Lett.* **17**, 481–484 (1998).

113. Jaschke, B., Klingebiel, U., Riedel, R., Doslik, N. & Gadow, R. Cyclosilazanes and borazines: Polymer precursors to silicon-and boron-containing ceramics. *Appl. Organomet. Chem.* **14**, 671–685 (2000).

114. Ramakrishnan, P. A., Wang, Y. T., Balzar, D., An, L., Haluschka, C., Riedel, R. & Hermann, A. M. Silicoboron–carbonitride ceramics: A class of high-temperature, dopable electronic materials. *Appl. Phys. Lett.* **78**, 3076 (2001).

115. Bhandavat, R., Kuhn, W., Mansfield, E., Lehman, J. & Singh, G. Synthesis of polymer-derived ceramic Si(B)CN-carbon nanotube composite by microwave-induced interfacial polarization. *ACS Appl. Mater. Interfaces* **4**, 11–16 (2012).

116. Zhang, Q., Yang, Z., Jia, D., Chen, Q. & Zhou, Y. Synthesis and structural evolution of dual-boron-source-modified polysilazane derived SiBCN ceramics. *New J. Chem.* **40**, 7034–7042 (2016).

117. Zhao, G., Hu, P., Zhou, S., Chen, G., An, Y., Cheng, Y., An, J., Zhang, X. & Han, W. Ordered silica nanoparticles grown on a three-dimensional carbon fiber architecture substrate with siliconborocarbonitride ceramic as a thermal barrier coating. *ACS Appl. Mater. Interfaces* **8**, 4216–4225 (2016).

118. Wideman, T., Cortez, E., Remsen, E. E., Zank, G. A., Carroll, P. J. & Sneddon, L. G. Reactions of monofunctional boranes with hydridopolysilazane: Synthesis, characterization, and ceramic conversion reactions of new processable precursors to SiNCB ceramic materials. *Chem. Mater.* **9**, 2218–2230 (1997).

119. Bill, J., Kamphowe, T. W., Müller, A., Wichmann, T., Zern, A., Jalowieki, A., Mayer, J., Weinmann, M., Schuhmacher, J., Müller, K., Peng, J., Seifert, H. J. & Aldinger, F. Precursor-derived Si–(B–)C–N ceramics: thermolysis, amorphous state and crystallization. *Appl. Organomet. Chem.* **15**, 777–793 (2001).

120. Viard, A., Fonblanc, D., Lopez-Ferber, D., Schmidt, M., Lale, A., Durif, C., Balestrat, M., Rossignol, F., Weinmann, M., Riedel, R. & Bernard, S. Polymer derived Si–B–C–N ceramics: 30 years of research. *Adv. Eng. Mater.* **20**, 1800360 (2018).

121. Bernard, S. & Miele, P. Polymer-derived ordered mesoporous silicon-boron-carbon-nitrogen (Si/B/C/N) ceramics. *J. Ceram. Sci. Technol.* **4**, 133–122 (2013).

122. Jones, P. R. & Myers, J. K. The hydroboration of methylchlorosilylalkenes. *J. Organomet. Chem.* **34**, C9–C11 (1972).

123. Weinmann, M., Kamphowe, T. W., Fischer, P. & Aldinger, F. Tris(hydridosilylethyl)boranes: highly reactive synthons for polymeric silicon compounds. *J. Organomet. Chem.* **592**, 115–127 (1999).

124. Stock, A. *Hydrides of boron and silicon*. (Cornell University Press, 1933).

125. Schuhmacher, J., Berger, F., Weinmann, M., Bill, J., Aldinger, F. & Müller, K. Solid-state NMR and FT IR studies of the preparation of Si–B–C–N ceramics from boron-modified polysilazanes. *Appl. Organomet. Chem.* **15**, 809–819 (2001).

126. Müller, A., Gerstel, P., Weinmann, M., Bill, J. & Aldinger, F. Correlation of boron content and high temperature stability in Si–B–C–N ceramics. *J. Eur. Ceram. Soc.* **20**, 2655–2659 (2000).

127. Müller, A., Gerstel, P., Weinmann, M., Bill, J. & Aldinger, F. Correlation of boron content and high temperature stability in Si–B–C–N ceramics II. *J. Eur. Ceram. Soc.* **21**, 2171–2177 (2001).

128. Müller, A., Zern, A., Gerstel, P., Bill, J. & Aldinger, F. Boron-modified poly(propenylsilazane)-derived Si–B–C–N ceramics: preparation and high temperature properties. *J. Eur. Ceram. Soc.* **22**, 1631–1643 (2002).

129. Janakiraman, N., Weinmann, M., Schuhmacher, J., Müller, K., Bill, J., Aldinger, F. & Singh, P. Thermal stability, phase evolution, and crystallization in Si-B-C-N ceramics derived from a polyborosilazane precursor. *J. Am. Ceram. Soc.* **85**, 1807–1814 (2002).

130. Tavakoli, A. H., Gerstel, P., Golczewski, J. A. & Bill, J. Effect of boron on the crystallization of amorphous Si–(B–)C–N polymer-derived ceramics. *J. Non. Cryst. Solids* **355**, 2381–2389 (2009).

131. Majoulet, O., Alauzun, J. G., Gottardo, L., Gervais, C., Schuster, M. E., Bernard, S. & Miele, P. Ordered mesoporous silicoboron carbonitride ceramics from boron-modified polysilazanes: Polymer synthesis, processing and properties. *Microporous Mesoporous Mater.* **140**, 40–50 (2011).

132. Sarkar, S., Gan, Z., An, L. & Zhai, L. Structural evolution of polymer-derived amorphous SiBCN ceramics at high temperature. *J. Phys. Chem. C* **115**, 24993–25000 (2011).

133. Viard, A., Fonblanc, D., Schmidt, M., Lale, A., Salameh, C., Soleilhavoup, A., Wynn, M., Champagne, P., Cerneaux, S., Babonneau, F., Chollon, G., Rossignol, F., Gervais, C. & Bernard, S. Molecular chemistry and engineering of boron-modified polyorganosilazanes as new processable and functional SiBCN precursors. *Chem. – A Eur. J.* **23**, 9076–9090

(2017).

134. Wynn, M., Lopez-Ferber, D., Viard, A., Fonblanc, D., Schmidt, M., Rossignol, F., Carles, P., Chollon, G., Gervais, C. & Bernard, S. Tuning of the high temperature behaviour of Si–C–N ceramics via the chemical crosslinking of poly(vinylmethyl-co-methyl)silazanes with controlled borane contents. *Open Ceram.* **5**, (2021).

135. Petríková, I., Parchovianský, M., Švančárek, P., Lenz Leite, M., Motz, G. & Galusek, D. Passive filler loaded polysilazane-derived glass/ceramic coating system applied to AISI 441 stainless steel, part 1: Processing and characterization. *Int. J. Appl. Ceram. Technol.* **17**, 998–1009 (2020).

136. Ohishi, T. Gas barrier characteristics of a polysilazane film formed on an ITO-coated PET substrate. *J. Non. Cryst. Solids* **330**, 248–251 (2003).

137. Hu, L., Li, M., Xu, C., Luo, Y. & Zhou, Y. A polysilazane coating protecting polyimide from atomic oxygen and vacuum ultraviolet radiation erosion. *Surf. Coatings Technol.* **203**, 3338–3343 (2009).

138. Augustinho, T. R., Motz, G., Ihlow, S. & MacHado, R. A. F. Application of hybrid organic/inorganic polymers as coatings on metallic substrates. *Mater. Res. Express* **3**, (2016).

139. Fedel, M., Rossi, S. & Deflorian, F. Polymethyl (hydro)/polydimethylsilazane-derived coatings applied on AA1050: effect of the dilution in butyl acetate on the structural and electrochemical properties. *J. Coatings Technol. Res.* **16**, 1013–1019 (2019).

140. Akutsu, K., Niizeki, T., Nagayama, S., Miyata, N., Sahara, M., Shimomura, A., Yoshii, M. & Hasegawa, Y. Investigation of structure of a thin SiO_2 layer as an antifouling and corrosion-resistant coating. *J. Ceram. Soc. Japan* **124**, 172–176 (2016).

141. Hu, L., Zhang, L., Wang, D., Lin, X. & Chen, Y. Fabrication of biomimetic superhydrophobic surface based on nanosecond laser-treated titanium alloy surface and organic polysilazane composite coating. *Colloids Surfaces A Physicochem. Eng. Asp.* **555**, 515–524 (2018).

142. Coan, T., Barroso, G. S., MacHado, R. A. F., De Souza, F. S., Spinelli, A. & Motz, G. A novel organic-inorganic PMMA/polysilazane hybrid polymer for corrosion protection. *Prog. Org. Coat.* **89**, 220–230 (2015).

143. Ohishi, T., Sone, S. & Yanagida, K. Preparation and gas barrier characteristics of polysilazane-derived silica thin films using ultraviolet irradiation. *Mater. Sci. Appl.* **2014**, 105–111 (2014).

144. Ohishi, T. & Yamazaki, Y. Formation and gas barrier characteristics of polysilazane-derived silica coatings formed by excimer light irradiation on PET films with vacuum evaporated silica coatings. *Mater. Sci. Appl.* **08**, 1–14 (2017).

145. Lenhart, S. J., Blum, Y. D. & Laine, R. M. Corrosion resistance of an aluminum alloy coated with polysilazane-derived ceramics. *Corrosion* **45**, 503–506 (1989).

146. Günthner, M., Kraus, T., Dierdorf, A., Decker, D., Krenkel, W. & Motz, G. Advanced coatings on the basis of Si(C)N precursors for protection of steel against oxidation. *J. Eur. Ceram. Soc.* **29**, 2061–2068 (2009).

147. Chiu, H. T., Sukachonmakul, T., Kuo, M. T., Wang, Y. H. & Wattanakul, K. Surface modification of aluminum nitride by polysilazane and its polymer-derived amorphous silicon oxycarbide ceramic for the enhancement of thermal conductivity in silicone rubber composite. *Appl. Surf. Sci.* **292**, 928–936 (2014).

148. Xiao, F., Zhang, Z., Zeng, F., Luo, Y. & Xu, C. Fabrication of ceramic coatings from polysilazane/aluminum: Effect of aluminum content on chemical composition,

microstructure, and mechanical properties. *Ceram. Int.* **40**, 745–752 (2014).

149. Liu, J., Qiao, Y. L., Zhang, P., Xue, Y. C. & Cai, Z. Synthesis of SiC ceramics from polysilazane by laser pyrolysis. *Surf. Coatings Technol.* **321**, 491–495 (2017).

150. Smokovych, I. & Scheffler, M. Polysilazane-type coatings on Mo–Si–B alloys: A thermodynamic assessment of the phase composition. *Adv. Eng. Mater.* **20**, 1700936 (2018).

151. Parchovianský, M., Petríková, I., Švančárek, P., Lenz Leite, M., Motz, G. & Galusek, D. Passive filler loaded polysilazane-derived glass/ceramic coating system applied to AISI 441 stainless steel, part 2: Oxidation behavior in synthetic air. *Int. J. Appl. Ceram. Technol.* **17**, 1675–1687 (2020).

152. Bill, J. & Heimann, D. Polymer-derived ceramic coatings on C/C-SiC composites. *J. Eur. Ceram. Soc.* **16**, 1115–1120 (1996).

153. Wang, K., Unger, J., Torrey, J. D., Flinn, B. D. & Bordia, R. K. Corrosion resistant polymer derived ceramic composite environmental barrier coatings. *J. Eur. Ceram. Soc.* **34**, 3597–3606 (2014).

154. Neckel, L., Weiss, A. G., Motz, G., Hotza, D. & Fredel, M. C. Particle-filled polysilazane coatings for steel protection. *Adv. Mater. Res.* **975**, 149–153 (2014).

155. Nagahara, T., Matsuo, H., Aoki, T. & Yamada, K. Photosensitive polysilazane composition and method of forming patterned polysilazane film. *U.S. Patent Application* (2004).

156. Kojima, A., Hoshii, S. & Muto, T. Characteristics of polysilazane compound and its application as coating for carbon material. *J. Mater. Sci. Lett.* **21**, 757–760 (2002).

157. Parchovianský, M., Parchovianská, I., Švančárek, P., Medveď, D., Lenz-Leite, M., Motz, G. & Galusek, D. High-temperature oxidation resistance of pdc coatings in synthetic air and water vapor atmospheres. *Molecules* **26**, (2021).

158. Shayed, M. A., Cherif, C., Hund, R. D., Cheng, T. & Osterod, F. Carbon and glass fibers modified by polysilazane based thermal resistant coating. *Text. Res. J.* **80**, 1118–1128 (2010).

159. Shayed, M. A., Hund, R. D. & Cherif, C. Polysilazane-based heat- and oxidation-resistant coatings on carbon fibers. *J. Appl. Polym. Sci.* **124**, 2022–2029 (2012).

160. Sun, C., Wang, D., Xu, C., Chen, W. & Zhang, Z. Comparative study on polysilazane and silicone resins as high-temperature-resistant coatings: *High Perform. Polym.* **34**, 474–486 (2022).

161. Hu, L. H. & Wang, Y. K. Silicon carbonitride ceramic surface-modified nanoporous aluminum alloy by preceramic polysilazane precursor for surface strengthening. *Mater. Sci. Eng. B Solid-State Mater. Adv. Technol.* **267**, 115113 (2021).

162. Emslie, A. G., Bonner, F. T. & Peck, L. G. Flow of a viscous liquid on a rotating Disk. *J. Appl. Phys.* **29**, 858–862 (1958).

163. Lai, J. H. An investigation of spin coating of electron resists. *Polym. Eng. Sci.* **19**, 1117–1121 (1979).

164. Bornside, D. E., Macosko, C. W. & Scriven, L. E. Modeling of spin coating. *J. imaging Technol.* **13**, 122–130 (1987).

165. Lawrence, C. J. The mechanics of spin coating of polymer films. *Phys. Fluids* **31**, 2786 (1998).

166. Ohara, T., Matsumoto, Y. & Ohashi, H. The film formation dynamics in spin coating. *Phys. Fluids A Fluid Dyn.* **1**, 1949 (1998).

167. Hall, D. B., Underhill, P. & Torkelson, J. M. Spin coating of thin and ultrathin polymer films. *Polym. Eng. Sci.* **38**, 2039–2045 (1998).

168. Meyerhofer, D. Characteristics of resist films produced by spinning. *J. Appl. Phys.* **49**, 3993–3997 (1978).

169. Norrman, K., Ghanbari-Siahkali, A. & Larsen, N. B. 6 Studies of spin-coated polymer films. *Annu. Reports Prog. Chem. - Sect. C* **101**, 174–201 (2005).

170. Sahu, N., Parija, B. & Panigrahi, S. Fundamental understanding and modeling of spin coating process: A review. *Indian J. Phys. 2009 834* **83**, 493–502 (2009).

171. Welchel, Z., DeSilva, L. A. & Banadara, T. M. W. J. Properties of tris (8-hydroxyquinoline) aluminum thin films fabricated by spin coating from static and dynamic dispense methods. *Opt. Mater. (Amst).* **108**, 1–7 (2020).

172. Krebs, F. C. Fabrication and processing of polymer solar cells: A review of printing and coating techniques. *Sol. Energy Mater. Sol. Cells* **93**, 394–412 (2009).

173. Daughton, W. J. & Givens, F. L. An investigation of the thickness variation of spun-on thin films commonly associated with the semiconductor industry. *J. Electrochem. Soc.* **129**, 173–179 (1982).

174. Chen, B. T. Investigation of the solvent-evaporation effect on spin coating of thin films. *Polym. Eng. Sci.* **23**, 399–403 (1983).

175. Weill, A. & Dechenaux, E. The spin-coating process mechanism related to polymer solution properties. *Polym. Eng. Sci.* **28**, 945–948 (1988).

176. Givens, F. L. & Daughton, W. J. On the uniformity of thin films: A new technique applied to polyimide. **126**, 269–272 (1979).

177. Spangler, L. L., Torkelson, J. M. & Royal, J. S. Influence of solvent and molecular weight on thickness and surface topography of spin-coated polymer films. *Polym. Eng. Sci.* **30**, 644–653 (1990).

178. Picard, L., Phalip, P., Fleury, E. & Ganachaud, F. Chemical adhesion of silicone elastomers on primed metal surfaces: A comprehensive survey of open and patent literatures. *Prog. Org. Coat.* **80**, 120–141 (2015).

179. de With, G. *Polymer coatings: A guide to chemistry, characterization, and selected applications*. (Wiley-VCH, 2018).

180. Comyn, J. Surface treatment and analysis for adhesive bonding. *Int. J. Adhes. Adhes.* **10**, 161–165 (1990).

181. Ebnesajjad, S. Material surface preparation techniques. in *Handbook of Adhesives and Surface Preparation* 49–81 (William Andrew Publishing, 2011).

182. Kim, M. C., Yang, S. H., Boo, J. H. & Han, J. G. Surface treatment of metals using an atmospheric pressure plasma jet and their surface characteristics. *Surf. Coatings Technol.* **174–175**, 839–844 (2003).

183. Awaja, F., Gilbert, M., Kelly, G., Fox, B. & Pigram, P. J. Adhesion of polymers. *Prog. Polym. Sci.* **34**, 948–968 (2009).

184. Lępicka, M. & Grldzka-Dahlke, M. The initial evaluation of performance of hard anti-wear coatings deposited on metallic substrates: Thickness, mechanical properties and adhesion measurements - A brief review. *Rev. Adv. Mater. Sci.* **58**, 50–65 (2019).

185. DIN EN ISO 2409. at https://www.une.org/encuentra-tu-norma/busca-tu-norma/norma?c=N0052301 (2013).

186. Broitman, E. Indentation hardness measurements at macro-, micro-, and nanoscale: A critical overview. *Tribol. Lett.* **65**, 1–18 (2017).

187. Kariper, I. A. Hardness of thin films and the influential factors. in *Diamond and Carbon Composites and Nanocomposites* 1–20 (IntechOpen, 2016).

188. Pethica, J. B. & Oliver, W. C. Mechanical properties of nanometre volumes of material: Use of the elastic response of small area indentations. *MRS Online Proc. Libr.* **130**, 13–23 (1988).

189. Oliver, W. C. & Pharr, G. M. An improved technique for determining hardness and elastic modulus using load and displacement sensing indentation experiments. *J. Mater. Res.* **7**, 1564–1583 (1992).

190. Li, X. & Bhushan, B. A review of nanoindentation continuous stiffness measurement technique and its applications. *Mater. Charact.* **48**, 11–36 (2002).

191. Oliver, W. C. & Pharr, G. M. Measurement of hardness and elastic modulus by instrumented indentation: Advances in understanding and refinements to methodology. *J. Mater. Res.* **19**, 3–20 (2004).

192. Young, T. III. An essay on the cohesion of fluids. in *Philosophical Transactions of the Royal Society of London* vol. 95 65–87 (1805).

193. Law, K. Y. Definitions for hydrophilicity, hydrophobicity, and superhydrophobicity: Getting the basics right. *J. Phys. Chem. Lett.* **5**, 686–688 (2014).

194. Amrutkar, S., More, A., Mestry, S. & Mhaske, S. T. Recent developments in the anti-graffiti coatings: An attentive review. *J. Coatings Technol. Res. 2022* **19**, 717–739 (2022).

195. Lo, T. N. H., Hong, S. W., Hwang, H. S. & Park, I. Facile synthesis of fluorinated polysilazanes and their durable icephobicity on rough Al surfaces. *Polymers (Basel)*. **14**, 330 (2022).

196. Zhan, Y. Physical properties of spin-on coated polysilazane-derived films. (Technical University of Darmstadt, 2017).

197. Hurst, S. M., Farshchian, B., Choi, J., Kim, J. & Park, S. A universally applicable method for fabricating superhydrophobic polymer surfaces. *Colloids Surfaces A Physicochem. Eng. Asp.* **407**, 85–90 (2012).

198. Hyun, J., Barletta, P., Koh, K., Yoo, S., Oh, J., Aspnes, D. E. & Cuomo, J. J. Effect of Ar^+ ion beam in the process of plasma surface modification of PET films. *J. Appl. Polym. Sci.* **77**, 1679–1683 (2000).

199. Joseph, T. & White, D. Understanding the role of concentrated phosphoric acid solutions as high-temperature silicon nitride etchants. *ECS J. Solid State Sci. Technol.* **10**, 024006 (2021).

200. Lichtenberger, O., Woltersdorf, J. & Riedel, R. Polymere Carbodiimide als Vorstufen für keramische Werkstoffe: Reaktionsmechanismen und Tautomeriebeziehungen. *Zeitschrift fur Anorg. und Allg. Chemie* **628**, 596–607 (2002).

201. Sneh, O., Wise, M. L., Ott, A. W., Okada, L. A. & George, S. M. Atomic layer growth of SiO_2 on Si(100) using $SiCl_4$ and H_2O in a binary reaction sequence. *Surf. Sci.* **334**, 135–152 (1995).

202. Zhao, J., Xu, B., Yu, W. & Wang, X. Silicon tetrahydroborate and silylene dihydroborate with interelement B-H-Si and B=Si bonds. *Organometallics* **35**, 3272–3280 (2016).

203. Légaré, M. A., Courtemanche, M. A. & Fontaine, F. G. Lewis base activation of borane-dimethylsulfide into strongly reducing ion pairs for the transformation of carbon dioxide to methoxyboranes. *Chem. Commun.* **50**, 11362–11365 (2014).

204. Cao, F., Liu, K., Fang, Z. & Wang, S. Hydrolysis mechanism of borazine-derived boron nitride pyrolysized below 1200 °C. *J. Mater. Sci. Technol.* **28**, 956–960 (2012).

205. Banu, T., Debnath, T., Ash, T. & Das, A. K. Hydrolysis of ammonia borane and metal amidoboranes: A comparative study. *J. Chem. Phys.* **143**, 194305 (2015).

206. Sorarù, G. D., Dallabona, N., Gervais, C. & Babonneau, F. Organically modified SiO_2-B_2O_3 gels displaying a high content of borosiloxane (=B-O-Si≡) bonds. *Chem. Mater.* **11**, 910–919 (1999).

207. Long, X., Shao, C. & Wang, Y. Effects of boron content on the microwave-transparent property and high-temperature stability of continuous SiBN fibers. *J. Am. Ceram. Soc.* **103**, 4436–4444 (2020).

208. Fengling, M., Huimin, Q., Yaping, Z., Xiaowen, R. & Fan, W. Thermal cure and ceramization kinetics of perhydropolysilazane. *Key Eng. Mater.* **575–576**, 81–86 (2013).

209. Condon, J. B., Holcombe, C., Johnson, D. & Steckel, L. The kinetics of the boron plus nitrogen reaction. *Inorg. Chem.* **15**, 2173–2179 (1976).

210. Baik, S., Suh, B. L., Byeon, A., Kim, J. & Lee, J. W. In-situ boron and nitrogen doping in flue gas derived carbon materials for enhanced oxygen reduction reaction. *J. CO_2 Util.* **20**, 73–80 (2017).

211. Liu, Y., Peng, S., Cui, Y., Chang, X., Zhang, C., Huang, X., Han, K. & Yu, M. Fabrication and properties of precursor-derived SiBN ternary ceramic fibers. *Mater. Des.* **128**, 150–156 (2017).

212. Zhao, X., Han, K., Peng, Y., Yuan, J., Li, S. & Yu, M. A novel precursor route for the production of Si-B-N ceramic fibers. *Mater. Lett.* **65**, 2717–2720 (2011).

213. Soraru, G. D., Ravagni, A., Maschio, R. D., Carturan, G. & Babonneau, F. Polymer-derived $Si_3N_4-ZrO_2$ nanocomposite powders. *J. Mater. Res.* **7**, 1266–1270 (1992).

214. Zhou, C., Gao, X., Xu, Y., Buntkowsky, G., Ikuhara, Y., Riedel, R. & Ionescu, E. Synthesis and high-temperature evolution of single-phase amorphous Si–Hf–N ceramics. *J. Eur. Ceram. Soc.* **35**, 2007–2015 (2015).

215. Toury, B., Cornu, D., Chassagneux, F. & Miele, P. Complete characterisation of BN fibres obtained from a new polyborylborazine. *J. Eur. Ceram. Soc.* **25**, 137–141 (2005).

216. Tersoff, J. New empirical approach for the structure and energy of covalent systems. *Phys. Rev. B* **37**, 6991 (1988).

217. Aiyama, T., Fukunaga, T., Niihara, K., Hirai, T. & Suzuki, K. An X-ray diffraction study of the amorphous structure of chemically vapor-deposited silicon nitride. *J. Non. Cryst. Solids* **33**, 131–139 (1979).

218. Ténégal, F., Flank, A. M., Cauchetier, M. & Herlin, N. Nanometric Si/C/N powders: Description of the short range atomic structure by X-ray absorption spectroscopy. *Nucl. Instruments Methods Phys. Res. Sect. B Beam Interact. with Mater. Atoms* **133**, 77–83 (1997).

219. Hagenmayer, R. M., Müller, U., Benmore, C. J., Neuefeind, J. & Jansen, M. Structural studies on amorphous silicon boron nitride $Si_3B_3N_7$: neutron contrast technique on nitrogen and high energy X-ray diffraction. *J. Mater. Chem.* **9**, 2865–2869 (1999).

220. Jin, C., Lin, F., Suenaga, K. & Iijima, S. Fabrication of a freestanding boron nitride single layer and Its defect assignments. *Phys. Rev. Lett.* **102**, 195505 (2009).

221. Andriotis, A. N., Richter, E. & Menon, M. Prediction of a new graphenelike Si_2BN solid. *Phys. Rev. B* **93**, 081413 (2016).

I. Curriculum Vitae

PERSONAL DATA

Name	Ying Zhan
Date of Birth	18.07.1991
Nationality	China

EDUCATION

04/2018–10/2022	Ph.D. Candidate in Materials Science **Technical University of Darmstadt**, Darmstadt, Germany
09/2014–09/2017	M.Sc. in Materials Science **Technical University of Darmstadt**, Darmstadt, Germany
09/2010–06/2014	B. Eng. in Materials Science and Engineering **Hunan University**, Changsha, China

RESEARCH EXPERIENCE

Since 01/2021	EU Project: *Sodium-ion and sodium metal batteries for efficient and sustainable next-generation energy storage*
Since 01/2017	Industrial Project (*Merck KGaA*): *Preparation, characterizations, and applications of polysilazane-derived films*
08/2016–12/2016	Industrial Project (*SGL epo GmbH*): *Influence of additives on the thermal properties of FT114 resin system for prepreg preparation*
10/2015–04/2016	Research Project: *Influence of film thickness and synthetic approach on the optical properties of Ta_3N_5 and $BaTaO_2N$ thin film photoanodes for solar water splitting*
09/2013–06/2014	Research Project: *Thermal and electromagnetic shielding performance of multi-functional carbon coating*
04/2012–04/2013	Research Project: *Automotive lightweight material – carbon fiber reinforced PC/ABS composite material*

II. Publications

Statement of Personal Contribution

The personal contribution of the author herself to the following research articles is listed.

[1] **Y. Zhan**, R. Grottenmüller, W. Li, F. Javaid, R. Riedel, Evaluation of mechanical properties and hydrophobicity of room-temperature, moisture-curable polysilazane coatings, *Journal of Applied Polymer Science*, 138 (2021) 50469.

The idea behind this publication originated in the discussion of Ying Zhan, Dr. Ralf Grottenmüller, and Prof. Ralf Riedel. The methodology was designed by Ying Zhan under the supervision of Dr. Ralf Grottenmüller and Prof. Ralf Riedel. The preparation and most of the characterization of the investigated samples were done by Ying Zhan. SEM was performed by Wei Li. Nanoindentation was performed by Prof. Farhan Javaid. All data were analyzed and visualized as Figures or Tables by Ying Zhan. The manuscript was written by Ying Zhan. The rest of the authors revised and approved the manuscript before publication.

[2] **Y. Zhan**, W. Li, R. Grottenmüller, C. Minnert, T. Krasemann, Q. Wen, R. Riedel, Rapid curing of polysilazane coatings at room temperature via chloride-catalyzed hydrolysis/condensation reactions, *Progress in Organic Coatings*, 167 (2022) 106872.

The idea behind this publication originated in the discussion of Ying Zhan, Dr. Ralf Grottenmüller, and Prof. Ralf Riedel. The methodology was designed by Ying Zhan with the assistance of Prof. Qingbo Wen. The preparation and most of the characterization of the investigated samples were done by Ying Zhan. SEM and EDX were performed by Wei Li. Nanoindentation was performed by Christian Minnert. GPC was performed by Thomas Krasemann. All data were analyzed and visualized as Figures or Tables by Ying Zhan. The manuscript was written by Ying Zhan. Wei Li, Dr. Ralf Grottenmüller, Christian Minnert, Prof. Qingbo Wen, and Prof. Ralf Riedel revised and approved the manuscript before publication.

[3] **Y. Zhan**, W. Li, T. Jiang, C. Fasel, E. Ricohermoso, J. Bernauer, Z. Yu, Z. Wu, F. Müller-Plathe, L. Molina-Luna, R. Grottenmüller, R. Riedel, Boron-modified perhydropolysilazane towards facile synthesis of amorphous SiBN ceramic with excellent thermal stability, *Journal of Advanced Ceramics*, 11 (2022) 1104–1116.

The idea behind this publication originated in the discussion of Ying Zhan and Wei Li, under the supervision of Prof. Zhaoju Yu, Dr. Ralf Grottenmüller, and Prof. Ralf Riedel. The methodology was designed by Ying Zhan and Wei Li. The synthesis of the precursors and FTIR were done by Ying Zhan. The pyrolysis, XRD, SEM, and EDX of the investigated samples were performed by Wei Li. TEM was performed by Tianshu Jiang under the supervision of Prof. Leopoldo Molina-Luna. TGA was performed by Claudia Fasel. The graphical abstract was plotted by Emmanuel III Ricohermoso. Jan Bernauer assisted in the pyrolysis of the samples. Molecular dynamic simulation was carried out by Dr. Zhenghao Wu, under the supervision of Prof. Florian Müller-Plathe. All data were analyzed by Ying Zhan and Wei Li, and visualized as Figures or Tables by Ying Zhan. The manuscript was written by Ying Zhan, Wei Li, and Dr. Zhenghao Wu. The rest of the authors revised and approved the manuscript before publication.

Signatures of Co-Authors

Ralf Riedel		Ralf Grottenmüller	
Wei Li		Farhan Javaid	
Christian Minnert		Thomas Krasemann	
Qingbo Wen		Zhaoju Yu	
Claudia Fasel		Tianshu Jiang	
Zhenghao Wu		Leopoldo Molina-Luna	
Florian Müller-Plathe		Jan Bernauer	
Emmanuel Ricohermoso			

ARTICLE

Evaluation of mechanical properties and hydrophobicity of room-temperature, moisture-curable polysilazane coatings

Ying Zhan[1] | **Ralf Grottenmüller[2]** | **Wei Li[1]** | **Farhan Javaid[1,3]** | **Ralf Riedel[1]**

[1]Institute of Materials and Earth Sciences, Technical University of Darmstadt, Darmstadt, Germany

[2]Performance Materials, Merck KGaA, D-64293, Darmstadt, Germany

[3]School of Chemical and Materials Engineering, National University of Sciences & Technology, Islamabad, Pakistan

Correspondence
Ying Zhan and Ralf Riedel, Institute of Materials and Earth Sciences, Technical University of Darmstadt, D-64287 Darmstadt, Germany.
Email: ying.zhan@tu-darmstadt.de (Y. Z.) and ralf.riedel@tu-darmstadt.de (R. R.)

Funding information
Merck KGaA

Abstract

Polysilazane coatings have a broad need in real-life applications, which require low processing or working temperature. In this work, five commercially available polysilazanes have been spin-coated on polycarbonate substrates and cured in ambient environment and temperature to obtain transparent, crack-free, and dense films. The degree of crosslinking is found to have a significant impact on the hardness and Young's modulus of the polysilazane films but has a minor influence on the film thickness and hydrophobicity. Among all five polysilazane coatings, the inorganic perhydropolysilazane-based coating exhibits the largest hardness (2.05 ± 0.01 GPa) and Young's modulus (10.76 ± 0.03 GPa) after 7 days of curing, while the polyorganosilazane-derived films exhibit higher hydrophobicity. The molecular structure of polysilazanes plays a key role in mechanical properties and hydrophobicity of the associated films, as well as the adhesion of coatings to substrates, providing an intuitive and reliable way for selecting a suitable polysilazane coating material for a specific application.

KEYWORDS

coatings, crosslinking, mechanical properties, structure-property relationships, surfaces and interfaces

1 | INTRODUCTION

Polysilazanes are polymers with a Si—N—Si backbone consisting of various substituted reactive or inert side groups at the Si and N atom sites. A wide product portfolio of polysilazanes is commercially available on the market and has been reported to be ideal precursors to ternary SiCN ceramics,[1] ceramic matrix composites,[2] ceramic fibers,[3,4] and ceramic or SiO_x rich polymeric coatings.[5,6]

Due to its liquid nature, most of the economic and simple coating methods are applicable to polysilazane systems, such as, spray coating, dip coating, and spin coating. Additionally, the well-known good adhesion of polysilazane to a variety of substrate materials, such as,

metals, glasses, ceramics, and plastics makes it a favorable material for the coating industry.[6]

Polysilazane coatings can be transformed into SiCO, SiCN, or Si_3N_4 ceramic coatings by pyrolyzing at high temperatures in air, N_2, or Ar atmosphere.[7–9] They are promising candidates for inter-layer dielectrics,[10] oxidation, or wear protection coatings[11,12] for high-temperature applications because of their good thermal shock resistance and thermal stability. However, the high-temperature applications require processing temperatures beyond 800°C, which is impracticable for certain applications owing to the limitation of the substrate or manufacturing process.

In recent years, low temperature curing of polysilazane-based coatings has been studied for

applications, such as, gas barrier,[13] marine anti-fouling coating,[14] anti-graffiti coating for public transportation,[15] and anti-adherent coating for demolding.[16] Polysilazane coatings can be cured and converted into thermoset polymeric coatings by several types of treatment, such as, thermal crosslinking,[17] UV radiation,[18] O₂ plasma treatment,[19] and moisture curing by hydrolysis and condensation reactions.[20] Studies have been undertaken to explore in detail the low-temperature curing behavior and mechanism of polysilazane coatings.[21–25] When exposing polysilazanes to moist air, it was reported by Müller et al.[22] that the hydrolysis and condensation reactions are predominant even at elevated temperature during the curing process. In this context, the room temperature (RT) moisture curable polysilazane coatings prepared by simple methods draw attention to some researchers.[14,21,26,27] Nevertheless, from the best of our knowledge, the curing behavior and the corresponding properties of polysilazane coatings under long-term ambient conditions have not been reported yet.

In this work, comprehensive characterizations of the curing behavior, film thickness, surface morphology, as well as the mechanical properties and hydrophobicity of five commercially available polysilazane-derived films cured under ambient atmosphere and temperature for 30 days were performed. The curing rate and the degree of crosslinking of the coatings were investigated by monitoring the changes of hardness, Young's modulus, and contact angle with increasing curing time for 30 days, by means of nanoindentation and contact angle measurement. Moreover, the moisture-curing behavior of a bulk polysilazane was investigated by elemental analysis and Fourier-transform infrared spectroscopy (FTIR). In addition, the adhesion of polysilazane coatings to the polycarbonate substrates was assessed by standard cross-cut tests (DIN EN ISO 2409) in a 7-day curing period. Finally, based on the results of this study, a benchmark evaluation of the mechanical properties and hydrophobicity of different polysilazane-derived coatings is proposed.

2 | MATERIALS AND METHODS

Five commercially available polysilazanes were provided by Merck KGaA, Darmstadt, Germany, and used as received without further purification. Figure 1 depicts the simplified linear molecular structure of different polysilazanes employed in this work. To specify, Durazane 1500 rapid cure (D1500-rc), Durazane 1500 slow cure (D1500-sc), and Durazane 1800 (D1800) are denoted as polyorganosilazanes. The perhydropolysilazane (PHPS)-
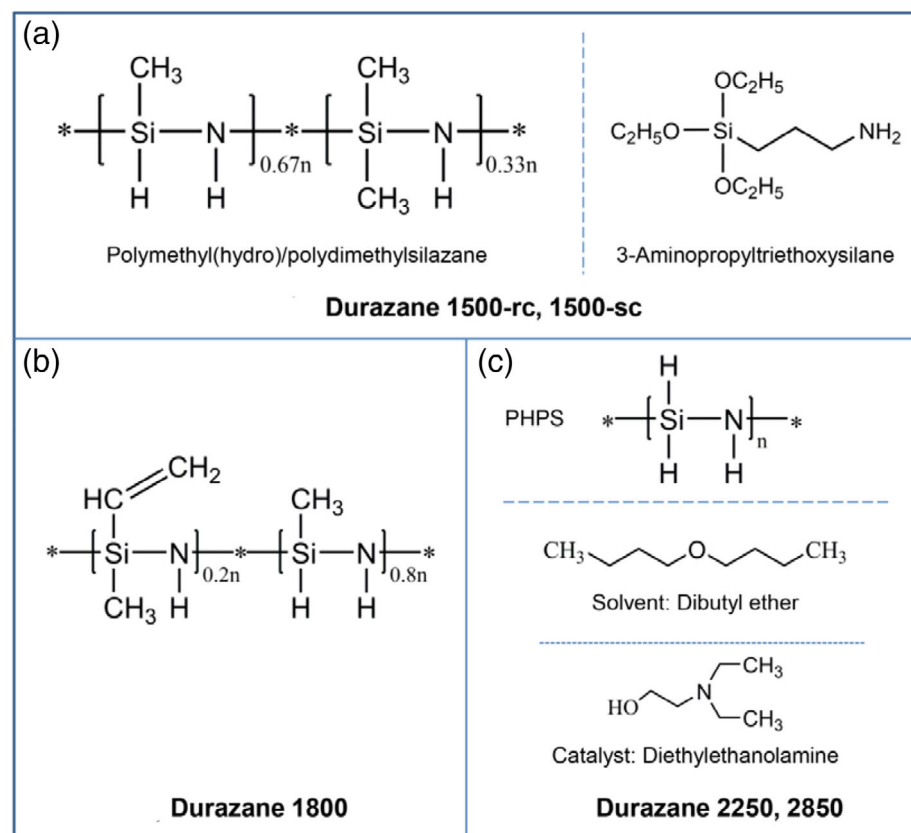
FIGURE 1 Molecular structures of Durazane polysilazanes. (a) Durazane 1500 (incl. rapid cure and slow cure). Durazane 1500 rapid cure has a higher fraction of 3-aminopropyltriethoxysilane than Durazane 1500 slow cure. (b) Durazane 1800. (c) Durazane 2250 (20 wt% solution of PHPS in dibutyl ether). Durazane 2850 is produced by further adding 0.5 wt% of diethylethanolamine as a catalyst [Color figure can be viewed at wileyonlinelibrary.com]

based polysilazanes Durazane 2250 (D2250) and Durazane 2850 (D2850) are denoted as inorganic polysilazanes.

To investigate the curing behavior of the polysilazane at RT (23°C), two flasks with 50 ml of D1500-rc liquid were bubbled with ambient air (with 40% to 55% relative humidity) and synthetic air (water content less than 2 ppmv) for 7 days, respectively. The chemical compositions of the cured samples were determined using elemental analysis (performed by Mikroanalytisches Labor Pascher, Germany) under an inert atmosphere for the nitrogen and oxygen contents. The changes of the organic groups in the cured samples were recorded by FTIR ranging from 550 to 4000 cm^{-1} on a Varian IR-670 spectrometer (Agilent) in the attenuated total reflection (ATR) mode.

All five polysilazanes were spin-coated on polycarbonate (PC) plates (Makrolon®, Bayer AG, Germany) and cured at RT in ambient atmosphere for 30 days to prepare the polysilazane films. The spin speed was tuned between 500 and 1500 rpm to achieve the industrially favorable thickness of ca. 6 μm. The thickness of the polysilazane films was measured using a stylus profilometer (DektakXT®, Bruker Corporation, Germany). The corresponding surface morphology was observed under a Philips XL30 FEG high-resolution scanning electron microscope (SEM, FEI Company).

In addition to profilometry and SEM, nanoindentation, and contact angle measurement were performed to access the variation of mechanical properties and hydrophobicity of the resultant polysilazane films during curing. The adhesion of the polysilazane coatings to the PC substrates was investigated by standard cross-cut test (DIN EN ISO 2409), using a Cross Hatch Cutter test kit (Model 295, ERICHSEN GmbH & Co. KG, Germany). The tested areas were observed and evaluated by optical microscopy (VHX-6000, KEYENCE DEUTSCHLAND GmbH, Germany). It is worth noting that the aforementioned characterization methods were only applied after the polysilazane films were dry to touch. All dried films were transparent, colorless, and adherent to the PC substrates.

The hardness and Young's modulus of the films and PC substrate were measured using a G200 nanoindenter (Keysight Technologies), equipped with a Berkovich diamond indenter tip. A continuous stiffness measurement method and a strain rate of 0.05 s^{-1} were applied in all nanoindentation experiments. On each sample, nine indentations were performed with an indentation depth up to 2000 nm (depending on the corresponding film thickness). The displayed data were chosen from an indentation depth of approximately 10% of the film thickness to avoid possible substrate effects. The hardness and Young's modulus were subsequently calculated via Oliver-Pharr method.[28]

The hydrophobicity of the polysilazane films was characterized by static contact angle measurement using an OCA-20 goniometer (DataPhysics Instruments GmbH, Germany). At least three areas of each film and PC substrate were tested using the sessile drop method. The equilibrium shape of the water drop was described by the Young-Laplace equation and the water contact angle was estimated by fitting the contour of the drop as a function of interfacial and gravity forces.

3 | RESULTS AND DISCUSSION

3.1 | Curing behavior of bulk Durazane 1500 rapid cure

In this work, Durazane 1500-rc was applied as a reference for the investigation of the curing behavior of polysilazanes in ambient and dry air at RT. Figure 2 depicts the theoretical crosslinking reaction paths based on the following simplifying assumptions: (a) The polymethyl(hydro)/polydimethylsilazane and 3-aminopropyltriethoxysilane (AMEO) are physically mixed in D1500-rc polysilazane solution. (b) With the presence of water, all of the Si—H, Si—NH, and Si—OC$_2$H$_5$ groups are consumed and transformed to Si—O groups via hydrolysis and condensation reactions. The oxygen and nitrogen contents in D1500-rc before and after complete curing were calculated. Before curing, D1500-rc contains 16.8 wt% nitrogen and 7.2 wt% oxygen (from AMEO). After complete crosslinking, the nitrogen content decreases to 2.3 wt%, while the oxygen content increases to 29.1 wt%.

Elemental analysis of oxygen and nitrogen contents in bulk D1500-rc cross-linked for 1, 24, 72, and 168 h were carried out, respectively. As shown in Figure 3(a), without moisture, D1500-rc remains unchanged after 168 h of exposure to dry air. While in the case of curing under ambient atmosphere (with 40% to 55% relative humidity), the nitrogen content of cured D1500-rc decreases and the oxygen content increases with curing time. Within the first 24 h, the N— and O—contents were almost halved. After 72 h of curing, the oxygen content tends to be saturated, while the nitrogen content keeps declining at a relatively low rate. After 168 h, the nitrogen content decreases from 15.0 ± 0.1 wt% to 4.7 ± 0.1 wt%, and the oxygen content increases from 7.4 to 28.2 wt% ± 0.3 wt% as compared with the pristine D1500-rc polysilazane. The experimentally obtained oxygen content is in good agreement with the theoretical calculation. In this context, the crosslinking degree of D1500-rc is calculated and depicted in Figure 3b. It is obvious that 90.2% ± 0.7% of the crosslinking reactions have been completed after
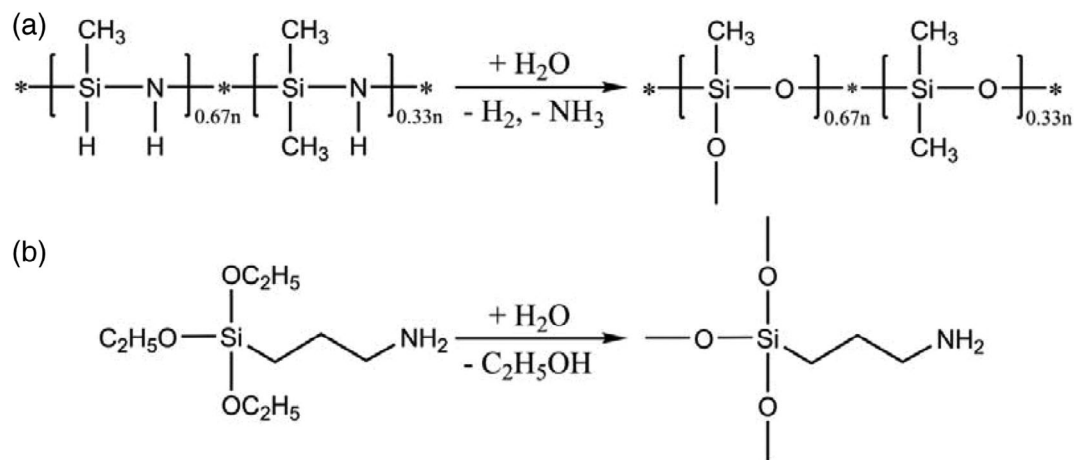
FIGURE 2 Theoretical crosslinking reaction paths of Durazane 1500-rc containing additions of 3-aminopropyltriethoxysilane
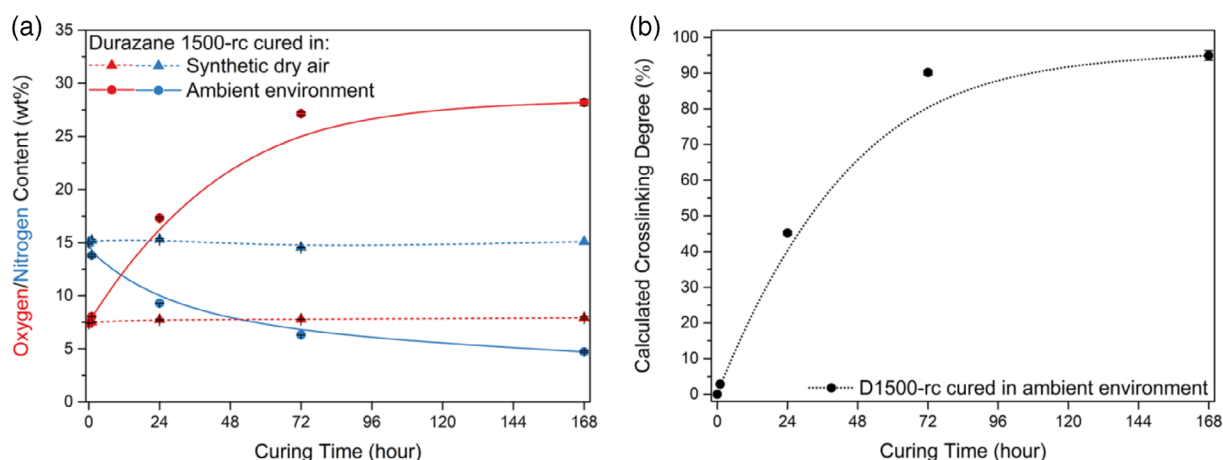
FIGURE 3 (a) Variation of elemental oxygen and nitrogen contents in the Durazane 1500-rc cured in synthetic air and ambient environment at RT for 168 h, respectively. (b) Crosslinking degree of D1500-rc as a function of curing time (based on the calculation of theoretical oxygen content) [Color figure can be viewed at wileyonlinelibrary.com]

72 h of curing in ambient environment and temperature. Further hydrolysis and condensation reactions occur slowly and 95.0% ± 1.4% of the reactions have been completed after 168 h of curing.

The ATR-FTIR spectra shown in Figure 4 correlate well with the elemental analysis result. During curing in ambient environment at RT, hydrolysis, and condensation reactions[2] occur. The hydrolysis reaction leads to the loss of nitrogen by releasing NH_3 with the consumption of the N—H groups (at 1168 cm^{-1}). In the meanwhile, the Si—H groups (at ca. 2125 cm^{-1}) are consumed, and H_2 is released. The Si—O—R units (at 1077 and 1105 cm^{-1}) from the 3-aminopropyltriethoxysilane are gradually transformed into Si—O—Si (at ca. 1022 cm^{-1}) with the releasing of C_2H_5OH.[21,29] In addition, Si—O—Si units are formed via condensation reaction increasing the oxygen content. In the first 24 h of curing, there are residual Si—H and N—H groups in considerable quantities. After

72 h of curing, most of the hydrolyzable groups in D1500-rc are consumed and the hydrolysis and condensation reactions slow down. After 168 h of curing, almost all of the Si—H and N—H groups in D1500-rc disappear and the curing of D1500-rc reaches a plateau state. Thus, it can be concluded that the existence of water in the atmosphere is the crucial factor for the curing process of polysilazane, while the polysilazane is stable against oxidation in air at room temperature.

## 3.2 | Thickness of spin-coated polysilazane films

The polysilazanes were spin-coated on PC substrates and dry to touch in ambient environment at RT. The inorganic polysilazane D2250 and D2850 coatings exhibit the shortest dry to touch time, which is around 30 s (for

D2850) to 5 min (for D2250) under the same conditions. The D1500-rc film is dry to touch in about 30 min, while the D1500-sc film requires 1 to 2 h. The D1800 film requires about 32 h to reach the dry to touch condition.

The thickness of the dry polymer films can be controlled by the spin speed (angular velocity) and the concentration of the polymer solution. The generalized correlation is empirically derived according to the following Equation[30,31]:

$$h_f = k\omega^{-\alpha} \tag{1}$$

where h_f is the film thickness (μm), ω is the spin speed (rpm), while k and α are empirical constants. A set of
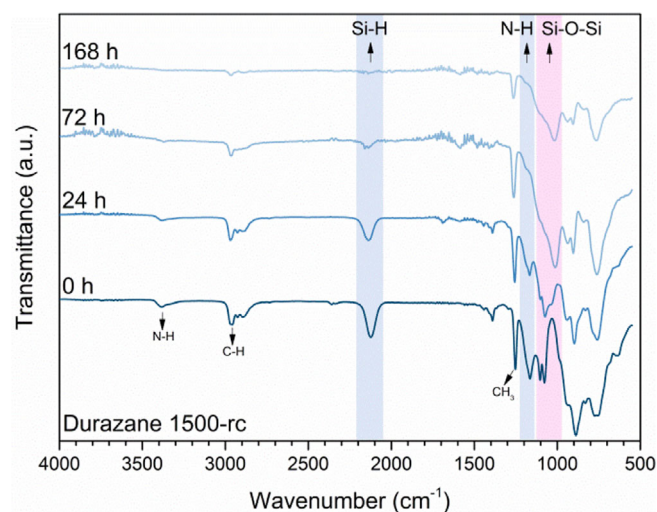
factors influence the value of constants k and α, including the intrinsic properties of the polymer, type of solvent, concentration and viscosity of the polymer solution, and interaction between the solution and the substrate.

Among these five investigated polysilazanes, Durazane 1800 possesses the highest viscosity in the range of 20 to 50 mPa·s, followed by Durazane 1500-sc (20 to 30 mPa·s) and Durazane 1500-rc (12 to 20 mPa·s). Durazane 2250 and Durazane 2850 exhibit the lowest viscosity of less than 5 mPa·s at 20°C because of the presence of 80% of solvent. The influence of solution viscosity on the resulting film thickness is indicated in Figure 5(a). At the same spin speed, the higher the solution viscosity, the thicker the resulting spin-coated film.

On the other hand, the film thickness of all five polysilazane coatings decreases with the increase of the spin speed. The experimental data points are statistically fitted with Equation (1) to obtain the constants k and α. Regarding the pure polyorganosilazanes D1500-rc, D1500-sc, and D1800, the values of k are 710, 2107, 697, while α amounts 0.76, 0.88, and 0.7, respectively. As the polysilazanes D2250 and D2850 have relatively low viscosities, they have lower α values of 0.59 and 0.41, and the k value amounts 41 and 18, respectively. This phenomenon may be explained by the effect of fluid inertia.[32]

In order to further characterize the polysilazane coatings without considering the effect of film thickness on the curing process, specific spin speed was selected for each polysilazane to achieve an industrially favorable film with a thickness of 5 to 7 μm. Regarding the spin parameter, that means 500 rpm for D1500-rc with a 6.12 ± 0.21 μm film, 700 rpm for D1500-sc with a 6.11 ± 0.07 μm film, and 1500 rpm for D1800 with a
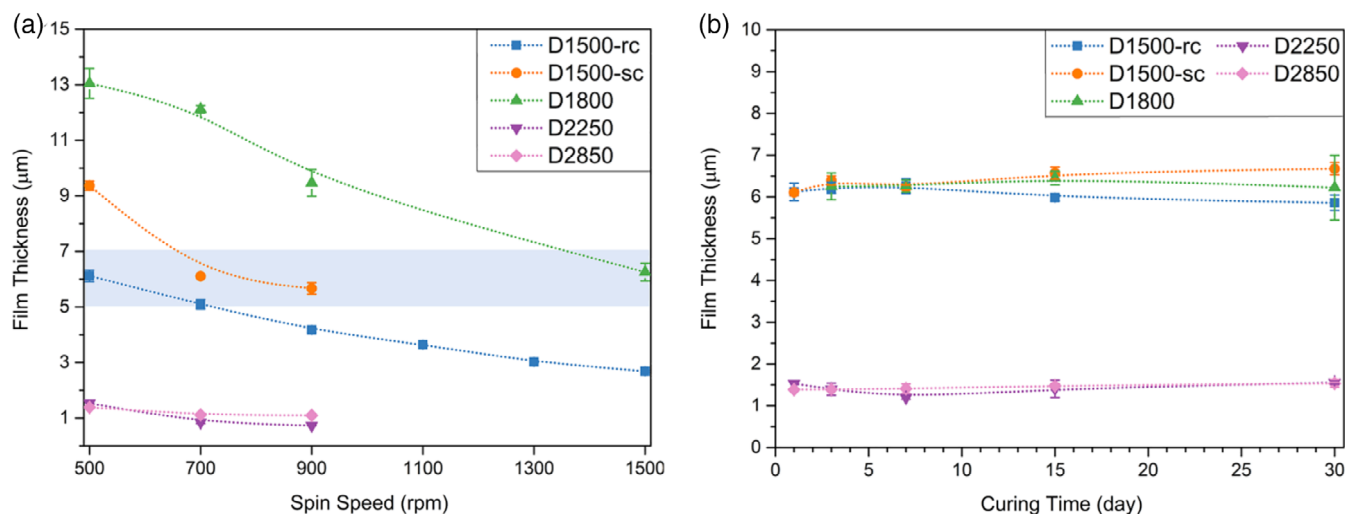

FIGURE 4 ATR-FTIR spectra of Durazane 1500-rc after 0, 24, 72, and 168 h of curing in ambient environment [Color figure can be viewed at wileyonlinelibrary.com]

FIGURE 5 Film thickness of polysilazane coatings as a function of (a) spin speed and (b) curing time [Color figure can be viewed at wileyonlinelibrary.com]

6.25 ± 0.32 μm film. However, due to the low viscosity, the thickest D2250 and D2850 films that can be obtained without sacrificing the homogeneity have thicknesses of 1.53 ± 0.01 μm and 1.39 ± 0.01 μm. The applied spin speed is limited to 500 rpm in both cases.

The as-obtained polysilazane coatings were cured in ambient environment at RT for 30 days. The development of the film thickness is recorded and shown in Figure 5(b). Although there are marginal variations during the 30 days of curing, the eventual film thickness of all five coatings is within the same range as the initial state, which indicates a minor impact of the crosslinking degree on the coating thickness. Therefore, the influence of the film thickness on subsequent characterizations can be eliminated.

3.3 | Surface morphology of polysilazane coatings

The surface morphology and cross-section of the as-obtained polysilazane coatings were further studied by scanning electron microscopy. Figure 6 shows SEM micrographs of the surface and cross-section of a Durazane 1500-rc coating after 30 days of crosslinking in ambient environment and temperature. The SEM images of D1500-sc, D1800, D2250, and D2850 coatings are shown in Figure S1 (supporting information) accordingly. The resultant films are dense, crack-free, and with a smooth surface.

3.4 | Mechanical properties of polysilazane coatings

Nanoindentation was employed to characterize the mechanical properties of the polyorganosilazane coatings with thicknesses of about 6 μm and inorganic polysilazane coatings with thicknesses of about 1.5 μm. The progression of the hardness and Young's modulus of the mentioned polysilazane coatings during the 30 days of

curing in ambient environment at RT were investigated and are shown in Figure 7.

As illustrated, the inorganic polysilazane (D2250 and D2850) films exhibit higher hardness and Young's modulus values as compared to the group of polyorganosilazane films (D1500-rc, D1500-sc, and D1800). After curing for 7 days, the D2850 coating reaches the highest value of hardness $(2.05 \pm 0.01$ GPa) and Young's modulus $(10.76 \pm 0.03$ GPa) among all investigated films. The subsequent slight decrease in hardness and Young's modulus is discussed in terms of microcracks formed in the coating during the indentation.[33]

In the case of the D2250-derived coating, the hardness and Young's modulus reach values of 0.64 and 3.59 ± 0.01 GPa, respectively, after 15 days of curing. Compared with polyorganosilazanes, the inorganic polysilazanes have a considerably higher amount of hydrolyzable Si—H groups, that react with water to form Si—OH groups, which in turn condensate to form a highly cross-linked Si—O—Si network.

Among the three polyorganosilazane coatings cured for 30 days, the D1500-rc coating shows the highest hardness and Young's modulus of 0.29 and 2.9 GPa, respectively. Durazane 1500-sc coating, which contains less hydrolyzable 3-aminopropyltriethoxysilane substituted groups if compared with D1500-rc and thus exhibits lower hardness and Young's modulus of 0.11 and 1.4 GPa, respectively. Durazane 1800 coating possesses the lowest hardness and modulus of 0.05 and 0.4 GPa, respectively, since it has the least number of hydrolyzable groups, which leads to the lowest degree of crosslinking among all the investigated polysilazanes. Moreover, the additional vinyl groups in D1800 may sterically hinder the crosslinking reactions.

For all coatings, the hardness and Young's modulus increase rapidly during the first three days of curing. Then, the corresponding growth rate slows down because of the reduced number of hydrolysis and condensation reactions owing to the insufficient hydrolyzable groups after a certain period. Besides, the hardened surface of the coating prevents the diffusion of atmospheric H_2O into the polysilazane and further slows down the
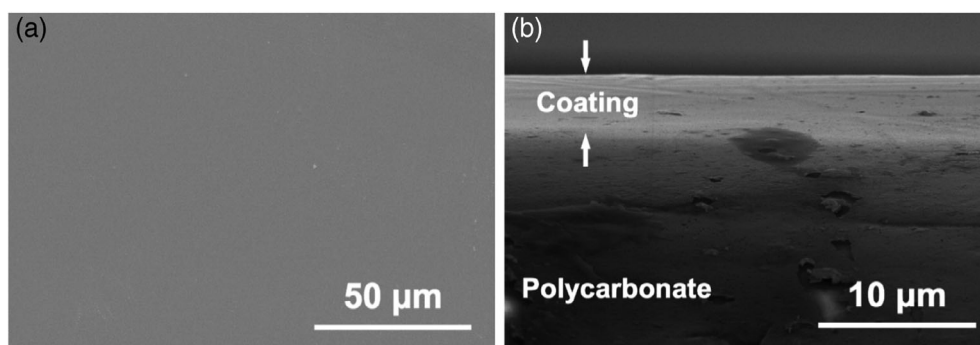
FIGURE 6 SEM images of (a) the surface and (b) cross-section of Durazane 1500-rc coating cured in ambient environment and RT for 30 days
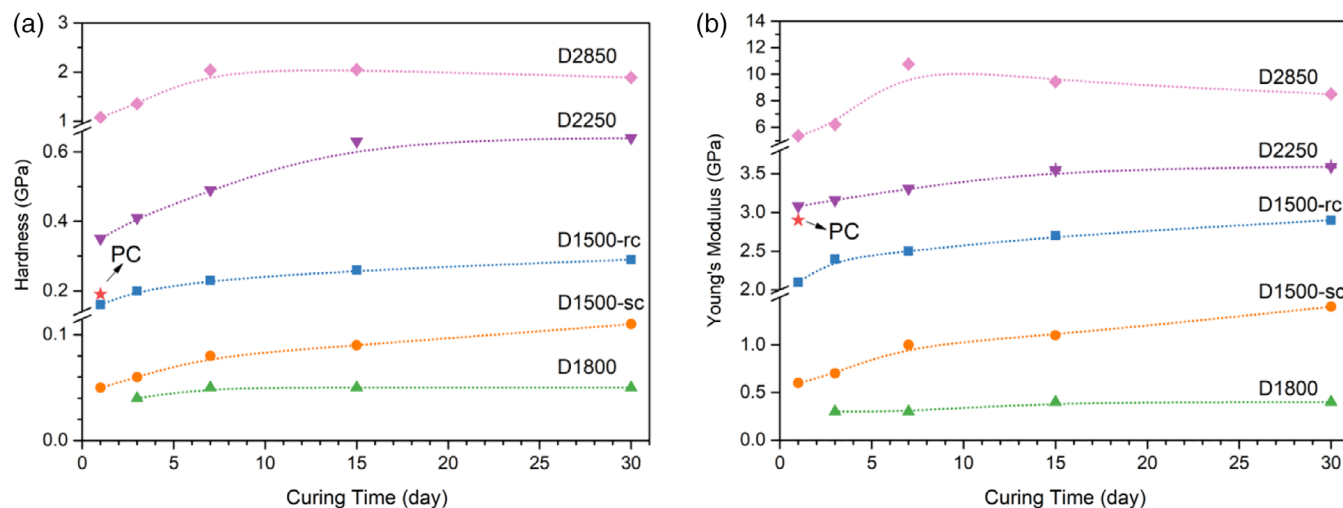
FIGURE 7 (a) Hardness and (b) Young's modulus of polysilazane coatings on PC as a function of the curing time [Color figure can be viewed at wileyonlinelibrary.com]

hardness/Young's modulus growth. After 7 or 15 days of curing, the above values of D2250, D2850, and D1800 coatings reach plateaus gradually, which to a certain extent indicates the limits of the crosslinking degree for the specific polysilazane coatings cured in ambient environment at RT. However, the hardness and Young's modulus of D1500-rc and D1500-sc coatings grow further slowly but continuously after 30 days of curing. Taking into account the results shown in Figure 3 and 4, it is interesting to see that even though the hydrolysis and condensation reactions seem to reach plateaus after 3 days of curing, the 3D-network of D1500-rc obviously further crosslinks, indicating possible physical crosslinking processes through hydrophobic interaction and chain entanglement[34] in addition to chemical crosslinking reactions.

The hardness and Young's modulus of the used polycarbonate substrate are measured as 0.19 and 2.9 GPa, respectively. The relatively higher values of D1500-rc, D2250, and D2850 films imply potential applications of the polysilazanes as protective coatings on PC-based materials.

3.5 | Hydrophobicity of polysilazane coatings

Hydrophobicity is considered to be a crucial factor for anti-fouling and anti-graffiti coatings. Figure 8(a) shows the water contact angle of polysilazane coatings during curing under ambient conditions at RT for 30 days. A similar tendency describing the change in contact angle with curing time for all coatings can be observed. Consider the D1500-rc coating as an example, the hydrophobic groups, such as, Si—H[16] and Si—CH$_3$[23] result in a hydrophobic surface with a contact angle of 94.6° ± 0.5°.

During the crosslinking reactions, the formation of hydrophilic Si—OH and Si—NH$_2$ groups as well as the consumption of hydrophobic Si—H groups lead to the reduction of the water contact angle to 90.4° ± 0.8°.[35] Subsequently, a hydrophobic recovery[36,37] appears, which could be explained by the combined effect of condensation reaction, diffusion, and reorientation of polar groups. On the one hand, the number of hydrophilic Si—OH and Si—NH$_2$ groups is reduced due to condensation reactions. On the other hand, the molecular mobility is hindered by the highly cross-linked Si-O-Si network and thus the reorientation of polar Si—O bonds[38] toward the polar water droplet becomes difficult. In the end, a contact angle of 95.4° ± 0.7° is obtained for the D1500-rc coating after curing under ambient conditions for 30 days.

From Figure 8b, the D1800 coating exhibits the highest contact angle of 103.3° ± 0.5° because of the existence of a large number of hydrophobic groups, such as, Si—CH$_3$ and Si—CH═CH$_2$ groups which cannot be involved in the crosslinking reactions at RT. Comparatively, D1500-rc and D1500-sc coatings are less hydrophobic with contact angles of 95.4° ± 0.7° and 98.4° ± 2.4°, respectively. Furthermore, the PHPS-based D2250 and D2850 coatings present less hydrophobicity with contact angles of 83.9° ± 0.8° and 85.9° ± 0.8°, respectively. Moreover, the contact angle of the uncoated PC substrate is measured as 97.3° ± 1.3°.

3.6 | Adhesion of polysilazane coatings to polycarbonate substrate

The adhesion of polysilazane to most surfaces is known to be good due to the chemical reactions of Si—H, Si—NH
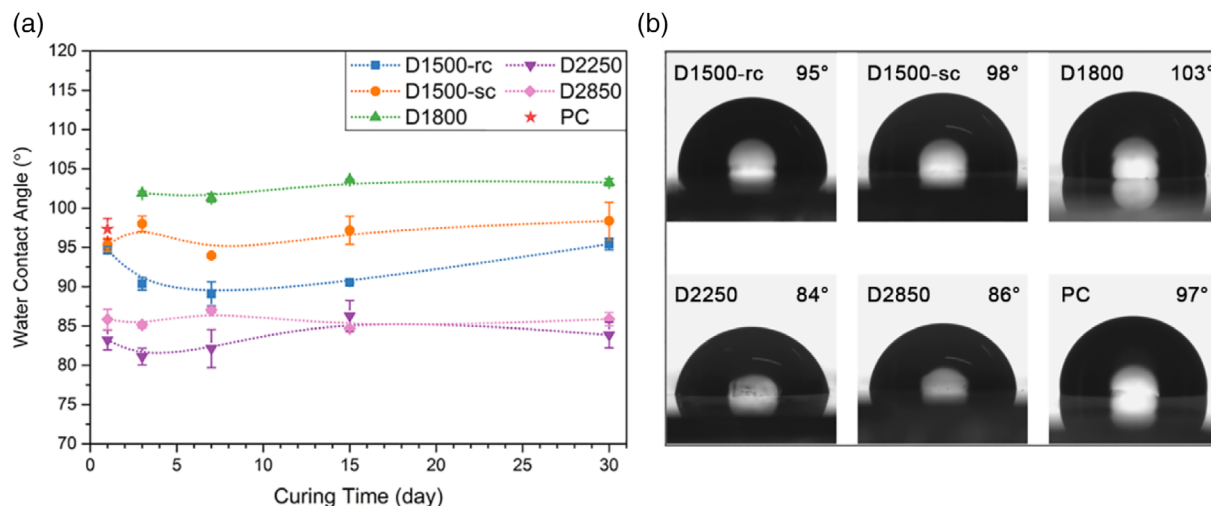
FIGURE 8 (a) Water contact angle of polysilazane coatings on PC as a function of curing time. (b) Sessile water droplets on polysilazane coatings after 30 days of curing and PC [Color figure can be viewed at wileyonlinelibrary.com]
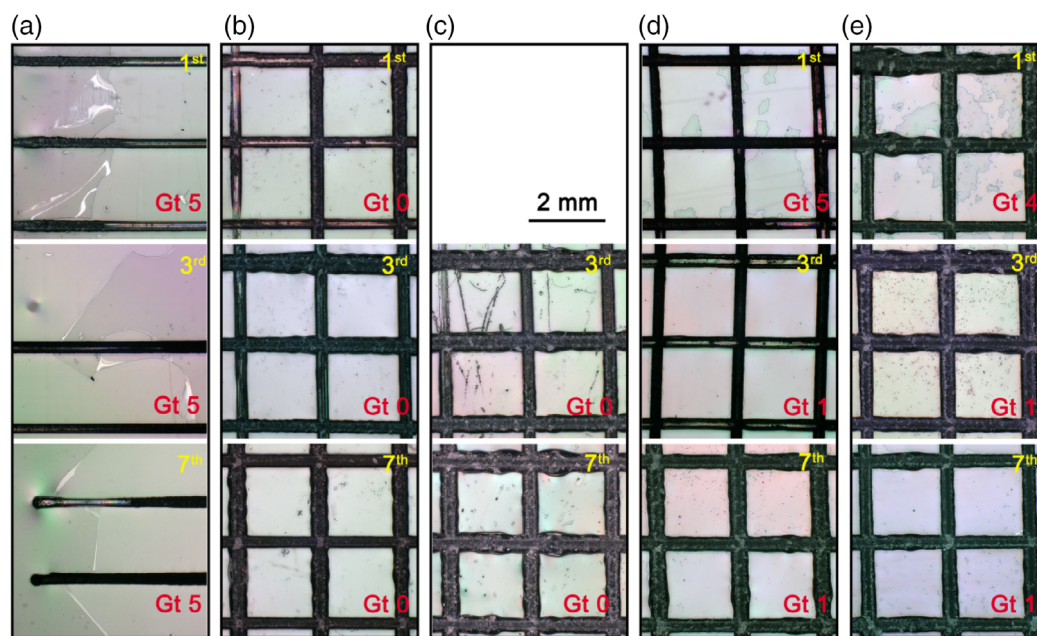
FIGURE 9 Optical microscopy images of polysilazane coatings on polycarbonate substrates after standard DIN EN ISO 2409 cross-cut tape test: (a) D1500-rc, (b) D1500-sc, (c) D1800, (d) D2250, (e) D2850 coatings after 1, 3, and 7 days of curing in ambient environment, respectively [Color figure can be viewed at wileyonlinelibrary.com]

groups with the —OH groups and the adsorbed water molecules on surface, which form subsequently oxygen bridges between the polysilazane coating and the substrate.[16,39,40] Figure 9 shows the optical microscopy images of five polysilazane coatings cured after 1, 3, and 7 days and with the standard cross-cut tape test being performed. According to the DIN EN ISO 2409, coatings are classified from Gt 0 (best adhesion, without any detachment of the coating after the test) to Gt 5 (worst adhesion, detachment of the coating >65% of the tested area). Among all five polysilazane coatings, D1500-sc

(Figure 9(b)) and D1800 (Figure 9(c)) coatings exhibit excellent adhesion to polycarbonate substrates, showing no coating spalling once they are dry to touch. Due to the higher fraction of 3-aminopropyltriethoxysilane in D1500-rc, the adhesion of the coating to the PC substrate is not enough to withstand the pull-off strength of the tape and the entire coating has been peeled off (Figure 9(a)).

Unlike the aforementioned polyorganosilazane coatings, the adhesion of the inorganic polysilazane coatings to the PC substrates improved along with the curing time.

After one day of crosslinking, D2250 (Figure 9(d)) and D2850 (Figure 9(e)) coatings display poor adhesion to the substrates, which is attributed to the lower amount of oxygen bridge between the diluted polysilazane (contains dibutyl ether as solvent) and substrate surface. As curing time increased, due to the much thinner thickness (ca. 1.5 μm), water molecules from the atmosphere reach the interface of the coating and substrate to further form oxygen bridges. Hence, the adhesion of D2250 and D2850 coatings to the PC substrates is improved from Gt 5 and Gt 4 to Gt 1, respectively.

4 | CONCLUSIONS

This work reports on a comprehensive investigation of the mechanical properties and hydrophobicity of five commercially available Durazane polysilazane films that are moisture-curable at room temperature and provides a guideline on the coating material selection. It can be confirmed that water is indispensable for the crosslinking of the polysilazane. In wet air, hydrolysis and condensation reactions result in the crosslinking of the polysilazanes and formation of a 3-dimensional polymeric network, while, the polysilazanes are stable against oxidation in dry air at RT.

Spin coating was proved to be an effective technique for the preparation of dense and crack-free polysilazane coatings. The relation between the film thickness and spin speed was empirically derived and can be applied for future research to adjust the coating thickness by selecting appropriate spin parameters. Moreover, it is found that the coating thickness is independent of the curing time.

The hardness and Young's modulus of the polysilazane coatings were determined by nanoindentation. PHPS-based polysilazane coatings have higher values than that of the polyorganosilazane coatings and the used PC substrate. This feature makes PHPS a candidate material as protective coatings for PC-based materials. Unlike the other polysilazane coatings with hardness and Young's modulus reaching plateaus after 7 or 15 days of curing, D1500-rc and D1500-sc coatings continue to harden even after 30 days of curing, indicating that in addition to chemical crosslinking reactions, physical crosslinking occurs as well during the curing process.

The water contact angle measurements show that the polyorganosilazane coatings are more hydrophobic than that of the PHPS-derived coatings. Different from the continuous increase of hardness and Young's modulus, the water contact angles of the polysilazane films firstly decrease at the early stage of curing, then, go through a recovery process and finally reach similar values as measured at the early stage.

Finally, the analyzed properties of the different polysilazane coatings cured in ambient atmosphere at room temperature can be roughly ranked as follows:

1. Curing rate: D2850 > D2250 > D1500-rc > D1500-sc > D1800
2. Hardness and Young's modulus: D2850 > D2250 > D1500-rc > D1500-sc > D1800
3. Hydrophobicity: D1800 > D1500-sc > D1500-rc > D2250 > D2850.
4. Adhesion to polycarbonate: D1500-sc = D1800 > D2250 = D2850 > D1500-rc

CONFLICT OF INTEREST

The authors declare no potential conflict of interest.

AUTHOR CONTRIBUTION

Ying Zhan, Conceptualization, Methodology, Validation, Investigation, Data Curation, Writing-Original Draft, Visualization. Ralf Grottenmüller, Conceptualization, Methodology, Resources, Writing-Review & Editing, Supervision, Funding acquisition. Wei Li, Validation, Investigation, Writing-Review & Editing. Farhan Javaid, Validation, Investigation, Writing-Review & Editing. Ralf Riedel, Conceptualization, Resources, Writing-Review & Editing, Supervision, Project administration, Funding acquisition.

ORCID

Ying Zhan 🔟 https://orcid.org/0000-0003-0331-4147

REFERENCES

[1] P. Colombo, G. Mera, R. Riedel, G. D. Soraru, _J. Am. Ceramic Soc._ **2010**, _93_, 1805.
[2] P. Colombo, R. Riedel, G. D. Sorarù, H.-J. Kleebe, _Polymer derived Ceramics: from Nano-structure to Applications_, DEStech Publications, Inc, Lancaster, Pennsylvania **2010**.
[3] W. Verbeek, Production of shaped articles of homogeneous mixtures of silicon carbide and nitride, **1974**.
[4] S. Yajima, J. Hayashi, M. Omori, _Chem. Lett._ **1975**, _4_, 931.
[5] J. Bill, D. Heimann, _J. European Ceramic Soc._ **1996**, _16_, 1115.
[6] G. Barroso, Q. Li, R. K. Bordia, G. Motz, _J Mater. Chem. A_ **2019**, _7_, 1936.
[7] K. Wang, J. Unger, J. D. Torrey, B. D. Flinn, R. K. Bordia, _J European Ceramic Soc_ **2014**, _34_, 3597.

[8] T. Kraus, M. Günthner, W. Krenkel, G. Motz, *Adv Appl Ceramics* **2009**, *108*, 476.

[9] G. Motz, J. Hacker, G. Ziegler, *24th Annual Conference on Composites, Advanced Ceramics, Materials, and Structures: B*, Ceramic Engineering and Science Proceedings, Vol. 21, John Wiley & Sons, Inc., Hoboken, NJ, USA **2000**, 307.

[10] S.-D. Kim, P.-S. Ko, K.-S. Park, *Semiconductor Sci. Technol.* **2013**, *28*, 035008.

[11] S. Brand, A. Dierdorf, H. Liebe, F. Osterod, G. Motz, M. Guenthner, Coatings comprising polysilazanes for preventing scaling and corrosion, Google Patents, **2012**.

[12] R. Riedel, G. Mera, R. Hauser, A. Klonczynski, *J. Ceramic Soc. Japan* **2006**, *114*, 425.

[13] A. Morlier, S. Cros, J.-P. Garandet, N. Alberola, *Thin Solid Films* **2012**, *524*, 62.

[14] S. Marceaux, C. Bressy, F.-X. Perrin, C. Martin, A. Margaillan, *Prog. Org. Coat.* **2014**, *77*, 1919.

[15] S. Rossi, M. Fedel, S. Petrolli, F. Deflorian, *Coatings* **2017**, *7*, 67.

[16] G. Barroso, M. Döring, A. Horcher, A. Kienzle, G. Motz, *Adv. Mater. Interfaces* **2020**, *7*, 1901952.

[17] E. Kroke, Y.-L. Li, C. Konetschny, E. Lecomte, C. Fasel, R. Riedel, *Mater. Sci. Eng.: R: Reports* **2000**, *26*, 97.

[18] C. Kato, S. Tanaka, Y. Naganuma, T. Shindo, *J. Photopolym. Sci. Technol.* **2004**, *16*, 163.

[19] J. Suzurikawa, M. Nakao, H. Takahashi, *IEEJ Trans. Electrical Electronic Eng.* **2011**, *6*, 392.

[20] A. Lukacs III, G.J. Knasiak, Thermally stable, moisture curable polysilazanes and polysiloxazanes, **2003**.

[21] F. Bauer, U. Decker, A. Dierdorf, H. Ernst, R. Heller, H. Liebe, R. Mehnert, *Prog. Org. Coat.* **2005**, *53*, 183.

[22] S. Müller, Y. de Hazan, D. Penner, *Prog. Org. Coat.* **2016**, *97*, 133.

[23] H. Kozuka, M. Fujita, S. Tamoto, *J. Sol–Gel Sci. Technol.* **2008**, *48*, 148.

[24] K. Nakajima, H. Uchiyama, T. Kitano, H. Kozuka, *J. Am. Ceramic Soc.* **2013**, *96*, 2806.

[25] R. Chavez, E. Ionescu, C. Balan, C. Fasel, R. Riedel, *J. Appl. Polym. Sci.* **2011**, *119*, 794.

[26] M. Fedel, S. Rossi, F. Deflorian, *J. Coat. Technol. Res.* **2019**, *16*, 1013.

[27] T. Kubo, E. Tadaoka, H. Kozuka, *J. Mater. Res.* **2004**, *19*, 635.

[28] W. C. Oliver, G. M. Pharr, *J. Mater. Res.* **1992**, *7*, 1564.

[29] M. Günthner, K. Wang, R. K. Bordia, G. Motz, *J. European Ceramic Soc.* **2012**, *32*, 1883.

[30] K. Norrman, A. Ghanbari-Siahkali, N. B. Larsen, *Annu. Rep. Section C (Phys. Chem.)* **2005**, *101*, 174.

[31] J. H. Lai, *Polym. Eng. Sci.* **1979**, *19*, 1117.

[32] C. J. Lawrence, *Phys Fluids* **1988**, *31*, 2786.

[33] F. Javaid, E. Bruder, K. Durst, *Acta Mater.* **2017**, *139*, 1.

[34] J. George, C. C. Hsu, L. T. B. Nguyen, H. Ye, Z. Cui, *Biotechnol. Adv.* **2019**, *42*, 107370.

[35] S. R. Kunst, H. R. P. Cardoso, C. T. Oliveira, C. I. Silva Filho, V. H. V. Sarmento, T. L. Menezes, *Int. J. Electrochem. Sci.* **2013**, *8*, 11984.

[36] S. M. Hurst, B. Farshchian, J. Choi, J. Kim, S. Park, *Colloids Surf., A: Physicochem. Eng. Aspects* **2012**, *407*, 85.

[37] J. Hyun, P. Barletta, K. Koh, S. Yoo, J. Oh, D. E. Aspnes, J. J. Cuomo, *J. Appl. Polym. Sci.* **2000**, *77*, 1679.

[38] K. Wang, M. Gunthner, G. Motz, B. D. Flinn, R. K. Bordia, *Langmuir* **2013**, *29*, 2889.

[39] D. Amouzou, L. Fourdrinier, F. Maseri, R. Sporken, *Appl. Surface Sci.* **2014**, *320*, 519.

[40] L. Picard, P. Phalip, E. Fleury, F. Ganachaud, *Prog. Org. Coat.* **2015**, *80*, 120.

SUPPORTING INFORMATION

Additional supporting information may be found online in the Supporting Information section at the end of this article.

Supporting Information

Evaluation of Mechanical Properties and Hydrophobicity of Room-Temperature, Moisture-Curable Polysilazane Coatings

Ying Zhan [a, *], Ralf Grottenmüller [b], Wei Li [a], Farhan Javaid [a, c], Ralf Riedel [a, *]

[a.] Institute of Materials and Earth Sciences, Technical University of Darmstadt, D-64287 Darmstadt, Germany

[b.] Merck KGaA, D-64293 Darmstadt, Germany

[c.] School of Chemical and Materials Engineering, National University of Sciences & Technology, 44000 Islamabad, Pakistan

[*.] Corresponding authors: ying.zhan@tu-darmstadt.de (Y. Zhan), ralf.riedel@tu-darmstadt.de (R. Riedel)
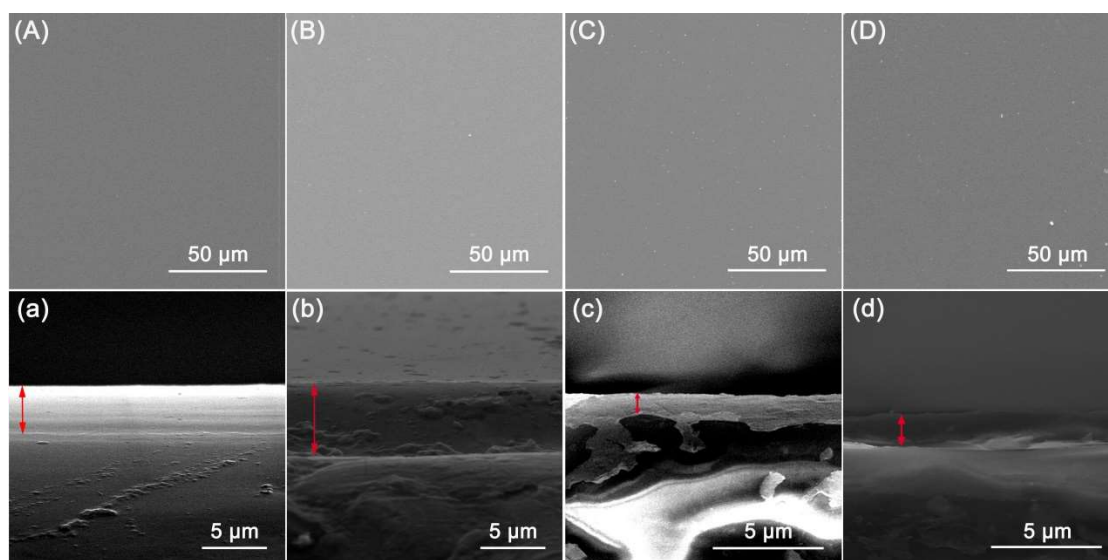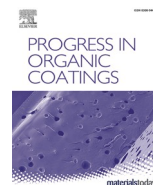
Figure S1. SEM images of the (A-D) surface and (a-d) cross-section of D1500-sc, D1800, D2250, D2850 coatings, respectively, cured in ambient environment and temperature for 30 days.

Rapid curing of polysilazane coatings at room temperature via chloride-catalyzed hydrolysis/condensation reactions

Ying Zhan [a,*], Wei Li [a], Ralf Grottenmüller [b], Christian Minnert [a], Thomas Krasemann [b], Qingbo Wen [c], Ralf Riedel [a,*]

[a] *Institute of Materials and Earth Sciences, Technical University of Darmstadt, D-64287 Darmstadt, Germany*
[b] *Merck KGaA, Performance Materials, D-64293 Darmstadt, Germany*
[c] *State Key Laboratory of Powder Metallurgy, Central South University, Changsha 410083, China*

ARTICLE INFO

ABSTRACT

Moisture curing of polysilazane coatings at room temperature is of advantage to industrial applications, though it often takes a longer time than the other curing methods. To tackle this problem, tetrabutylammonium chloride (TBAC) is applied in this work as an efficient catalyst for the hydrolysis and condensation reactions of polymethyl (hydro)/polydimethylsilazane coatings under ambient conditions. In the suggested catalytic mechanism, the Si–H group is nucleophilically attacked by chloride ions to form a transient Si–Cl group, which is then nucleophilically substituted by a hydroxyl group from the moisture environment. It is found that by adding TBAC in the polysilazane coating, 1.6 times more of the reactive groups (Si–H, Si–NH) are consumed during the curing process in a shorter time (the dry-to-touch time for the uncatalyzed and the TBAC-catalyzed polysilazane coatings are ca. 19 h and 1 h, respectively), while 2 times more of the Si–O–Si groups are formed. Owing to the significantly enhanced crosslinking rate and degree, the coating quality and the mechanical properties are greatly improved. The hardness and the elastic modulus of the coating are increased by a factor of two and four, respectively.

1. Introduction

Coatings are often applied to modify the surface properties of materials that are required to meet the growing demand for multi-purpose applications in the competitive market. Over the last two decades, silicon-based polymers that can be simply coated by most of the deposition methods [1,2], have received much attention as suitable coating materials with good thermal stability and chemical resistance. Polysilazanes (PSZ), which have a Si–N–Si basic backbone with various reactive and/or inert side groups, have been widely studied because of their strong adhesion to nearly all kinds of substrate materials by chemical bonding [3,4], and potential to be modified and tailored to meet different requirements for applications such as dielectric [5], environmental barrier [6], thermal barrier [7], anti-fouling [8], anti-graffiti [9], protective hydrophobic [10], and anti-adherent [11] coatings.

Polysilazane-based coatings can be converted to thermoset polymer or ceramic coatings via crosslinking and pyrolysis processes [12–15].

The most common crosslinking processes of polysilazanes are induced by thermal treatment [16–21], vacuum ultraviolet (VUV) radiation [22–24], and by exposure to moisture [25–27]. Moisture curing is advantageous for a cost-effective and easy-to-handle preparation of polysilazane coatings at low temperature or even at room temperature. Polysilazanes with moisture sensitive groups, e.g., Si–H and Si–NH groups, can be crosslinked under humid atmosphere via hydrolysis and condensation reactions [28,29]. However, polyorganosilazanes that have abundant inert or less reactive side groups (such as Si–CH$_3$ and Si–CH=CH$_2$ groups) crosslink slowly in this way and often require external assistance.

A large number of studies have employed temperature (up to 400 °C) to increase the curing rate because of its simplicity and the possibility for batchwise processing [3,9,11,16,26,30]. However, substrate materials with a low melting point, e.g., polymer and aluminum, may be degraded or deformed after thermal treatment. Müller et al. [25] have investigated the effect of humidity on the curing of PSZ coatings at room temperature (22–26 °C) and found that the hydrolysis rate could be

enhanced by increasing the humidity, but only to an insignificant extent in the ambient environment. The influence of humidity on the PSZ curing is only evident in very dry atmosphere, which has a relative humidity lower than 7%. In some papers, it has been studied that the crosslinking of PSZ coatings was greatly promoted with the help of suitable catalysts or initiators. Ammonia, as one of the common catalysts, has been widely proved to be able to accelerate the moisture curing of polysilazane both in solution and gaseous phase [22,31–33]. Dicumyl peroxide has been used by several researchers as a radical initiator to lower the curing temperature [10,34,35]. In recent years, tetrabutylammonium fluoride (TBAF) stood out as a nucleophilic catalyst for controllable and selective crosslinking of polyorganosilazanes [10,11,36]. However, the reaction between TBAF and PSZ is excessively fierce and often requires the addition of calcium borohydride as the inhibitor. In the mentioned studies, the crosslinking rate and degree of polyorganosilazanes have been improved to a certain extent. Nevertheless, extra equipment (e.g., ovens, climate chambers) or inhibitors are required to either control the reaction environment or the reaction rate, which is complicated or less cost-effective for industrial applications.

In the present work, tetrabutylammonium chloride (TBAC) is selected as a catalyst for the crosslinking of polymethyl(hydro)/polydimethylsilazane in ambient atmosphere and temperature without applying any inhibitors. The crosslinking rate and degree of the polysilazane with and without the addition of TBAC have been investigated by Fourier-transform infrared spectroscopy and gel permeation chromatography. With the most favorable catalyst content, the polysilazanes have been spin-coated and characterized with profilometer, scanning electron microscopy coupled with energy dispersive X-ray spectroscopy, nanoindentation, cross-cut test, and contact angle measurement.

2. Materials and methods

A commercially available polymethyl(hydro)/polydimethylsilazane, Durazane 1033 (D1033, supplied by Merck KGaA, Darmstadt, Germany), was investigated as received without further purification. Different amounts (0.5 wt%–4 wt% of the solution) of tetrabutylammonium chloride (TBAC, ≥97.0%, Sigma-Aldrich Chemie GmbH, Germany) were mixed with D1033 (2 g) and stirred for 2 h under Ar. The well-mixed solution was transferred to a fume hood and crosslinked in the ambient environment at room temperature (~23 °C) with 45% to 60% relative humidity (RH). The crosslinking progress of the bulk materials after different curing time was monitored and evaluated by Fourier-transform infrared (FTIR) attenuated total reflection (ATR) spectroscopy within the range of 550–4000 cm^{-1} on a Varian IR-670 spectrometer (Agilent Technologies, USA). The shown relative absorbance was calculated from the integrated peak area of each functional group employing Si–CH$_3$ as the reference peak. To compare the crosslinking degree of the cured samples, gel permeation chromatography (GPC) was employed to evaluate their average molecular weight (M$_w$) using the Agilent 1260 Infinity II Quaternary System (Agilent Technologies, Inc., USA). A combination of three Shodex columns (KF-801, KF-802, KF-806, Showa Denko K.K., Japan) was equipped and polystyrene (analytical standard, for GPC, PSS GmbH, Germany) was used for calibration. 50 mg of the crosslinked polysilazane was diluted in 1 mL tetrahydrofuran (THF) with the addition of toluene (~3 μL) as an internal standard. The sample solution was stirred for 3 h under Ar and filtered with a syringe filter (0.2 μm). The filtered analyte was eluted with THF and 1.5 wt% bis(trimethylsilyl)amine at 1 mL/min and 40 °C. In this circumstance, particles and insoluble material were filtered out and would not be analyzed by GPC.

Polysilazanes with and without TBAC were spin-coated on Si(100) wafers (3 in., thickness = 381 ± 25 μm, p-type (Boron), Micro-Chemicals, Germany) with a spin speed of 700 rpm for 2 min. The obtained coatings were crosslinked in the fume hood (45%–60% RH, ~23 °C) and characterized as well with ATR-FTIR spectroscopy. The

thickness and roughness of the polysilazane films were measured after 7 days of curing using a stylus profilometer (DektakXT®, Bruker Corporation, Germany). The surface and cross-section morphology were observed under a Philips XL30 FEG high-resolution scanning electron microscope (SEM, FEI Company, USA). In the meanwhile, the chemical composition of the coatings was analyzed with the affiliated energy dispersive X-ray spectroscopy (EDX). The results shown were the average of at least 5 measurements in different areas of each coating.

Hardness and elastic modulus of the polysilazane coatings were determined using an iNano® Nanoindenter (Nanomechanics Inc., a KLA-Tencor Company, USA), equipped with a Berkovich diamond indenter tip (Synton-MDP, Switzerland). The system was calibrated according to Oliver and Pharr using fused silica as reference material [37,38]. All tests were conducted using a continuous stiffness measurement (CSM) method with a constant indentation strain rate of 0.05 s^{-1} and a maximum indentation depth of 1000 nm. For the CSM oscillation a dynamic displacement of 2 nm and a dynamic frequency of 110 Hz were applied. For each sample, 16 measurements in different areas were tested. The Poisson's ratio was assumed to be 0.3.

Adhesion of the polysilazane coatings to the Si substrate was evaluated after 7 d of curing by cross-cut tests, employing a Cross Hatch Cutter (Model 295, ERICHSEN GmbH & Co. KG, Germany) and following DIN EN ISO 2409 standard [39]. The examined areas were observed with an optical microscope (VHX-6000, KEYENCE DEUTSCHLAND GmbH, Germany).

Hydrophobicity of the cured polysilazane coatings was assessed by static contact angle measurement using the sessile drop method on an OCA-20 goniometer (DataPhysics Instruments GmbH, Germany). The water contact angle was estimated by placing a 3 μL water droplet on the surface and fitting the equilibrium shape of the drop as a function of interfacial force and gravity following the Young-Laplace equation. For each coating and Si substrate, 9 different areas were tested.

3. Results and discussion

3.1. Catalytic effect of tetrabutylammonium chloride on the moisture curing of bulk polysilazane

With the aim of improving the crosslinking rate and degree of polymethyl(hydro)/polydimethylsilazane (Durazane 1033) in ambient temperature and atmosphere, ten potential catalysts were added respectively and the corresponding crosslinking reactions have been investigated by the employment of ATR-FTIR (shown in Fig. S1). Among the investigated catalysts, tetrabutylammonium chloride (TBAC) stood out as a suitable catalyst for the moisture curing of polysilazane because of its good catalytic ability, relatively low price, and colorless feature.

As shown in Fig. 1a, the ATR-FTIR spectrum of pristine D1033 (black line) shows typical transmittance peaks of N–H (1160, 3382 cm^{-1}), C–H (2953 cm^{-1}), Si–H (2120 cm^{-1}), and Si–CH$_3$ (1252 cm^{-1}) groups [18,22]. After curing under ambient conditions for 24 h (grey line), the signals of Si–H and N–H groups decrease slightly and Si–O–Si vibration is observed at the wavenumber of 1051 cm^{-1}. It is well-documented that polysilazane crosslinks in the presence of water via hydrolysis and condensation reactions, namely, Si–H and N–H groups react with H$_2$O to form Si–OH groups, which are subsequently condensed to Si–O–Si [1].

With the addition of TBAC, crosslinking of D1033 in ambient environment (45–60% RH) and temperature (~23 °C) has been greatly improved. Fig. 1b presents the relative absorbance of reacted functional groups calculated by integrating the corresponding peak area using Si–CH$_3$ (which is considered to be inert) as the reference peak. The spectrum of pristine D1033 is set as the start point (1 for Si–H and Si–NH groups, 0 for Si–O–Si group). If compared with the pure D1033, it is apparent that by adding TBAC more Si–H and N–H groups are consumed, while more Si–O–Si groups are formed, indicating an increase in the crosslinking reactions. The proposed catalytic mechanism of TBAC on the hydrolysis and condensation reactions of polysilazane is
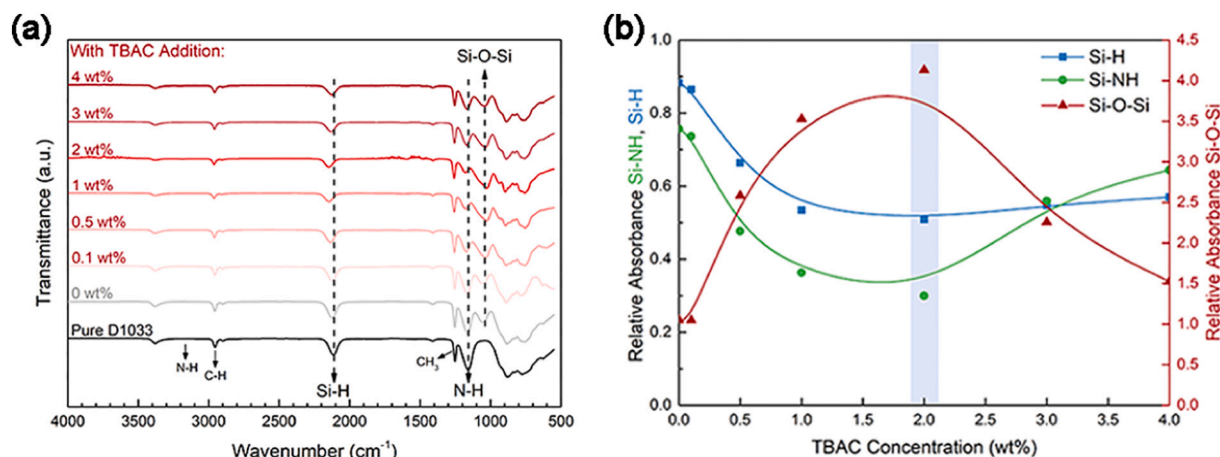
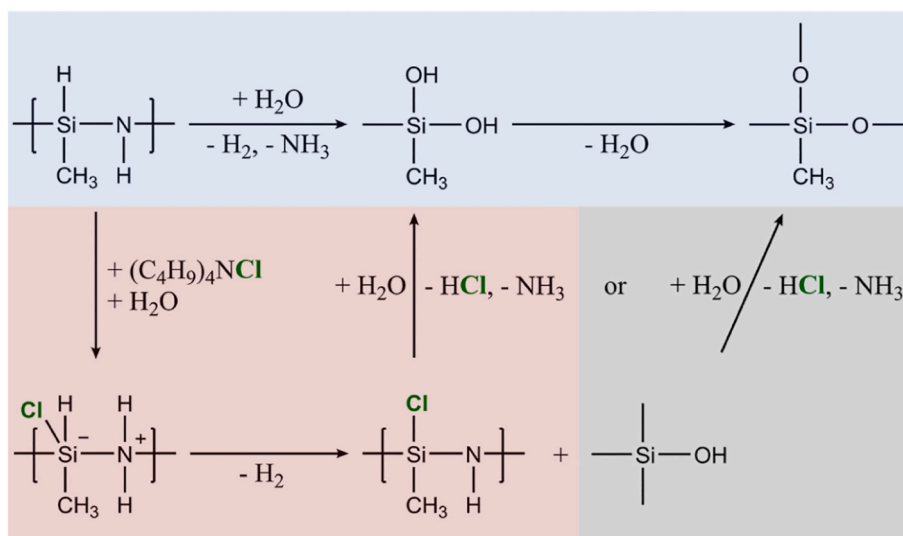**Fig. 1.** (a) ATR-FTIR spectra of pristine Durazane 1033 and with the addition of different amounts of tetrabutylammonium chloride (TBAC) after 24 h of curing in ambient environment and temperature. (b) Calculated relative absorbance (relative to Si–CH₃) of Si–H, Si–NH, and Si–O–Si groups as a function of TBAC concentration.

demonstrated in Scheme 1. The reaction paths with blue background present the typical hydrolysis and condensation processes of polysilazane. With the addition of nucleophilic catalyst tetrabutylammonium chloride ((C₄H₉)₄NCl), the electrophilic silicon from the polarized Si–N bond is under attack and the nitrogen is protonated at the same time [40–42]. A Si–Cl bond is then generated with the release of H₂. In the second step, the transient Si–Cl bond is nucleophilically substituted by a hydroxyl group from the water molecule (red box). The byproduct HCl provides an acidic environment wherein the hydrolysis of polysilazane is further catalyzed [40]. Consequently, the hydrolysis reaction of PSZ is accelerated with more Si–OH groups being generated. In the grey box, a possible reaction between Si–Cl and Si–OH is hypothesized based on the reports of Sneh et al. [43] and Lu et al. [44] (however, different experimental conditions were applied). With further consumption of Si–OH groups via condensation, increasing number of Si–O–Si groups are formed, which is in good accordance with the FTIR results shown in Fig. 1. Furthermore, there is clearly an upper limit to the catalytic effect of TBAC on the moisture crosslinking of PSZ (Fig. 1b). As the TBAC content increases from 0.1 wt% to 2 wt%, around 49% and 70% of the Si–H groups (blue) and Si–NH groups (green) are consumed, respectively, and the Si–O–Si group rises to a relative absorbance of

4.13. When more TBAC (3 wt% and 4 wt%) is added to the polysilazane, the catalytic activity is diminished. This decrease in the catalytic effect is discussed to be attributed to the steric hindrance of the tetrabutylammonium cation ((C₄H₉)₄N⁺) during the nucleophilic attack of the polysilazane [45]. On this account, 2 wt% of TBAC has been selected as the most efficient catalyst content for further research.

It is common knowledge that the molecular weight of polysilazane increases with the increase of the crosslinking degree [12,46]. Hence, gel permeation chromatography was employed to investigate the effect of TBAC on the crosslinking degree of the cured polysilazanes. As a well-known thermosetting polymer, highly crosslinked polysilazane with three-dimensional network is difficult to dissolve in tetrahydrofuran. During the measurements, the sample solution was filtered with a syringe filter (0.2 μm) before injecting into the GPC device. The filtration process removes all particles and insoluble material and only the clear soluble portion of the sample was measured. Fig. 2a compares the average molecular weight of polysilazanes with and without TBAC after curing for 3 h to 10 d under ambient conditions. The M_w is calculated from the corresponding molar mass distribution as shown in Fig. 2b and Fig. S2. It is straightforward that the average molecular weight of the catalyzed polysilazane reaches the highest measurable point after 6 h of

Scheme 1. Suggested catalytic mechanism of tetrabutylammonium chloride on the hydrolysis and condensation reactions (blue box) of polysilazane Durazane 1033. Red box: nucleophilic substitution reaction paths. Grey box: possible reaction between Si–Cl and Si–OH groups.
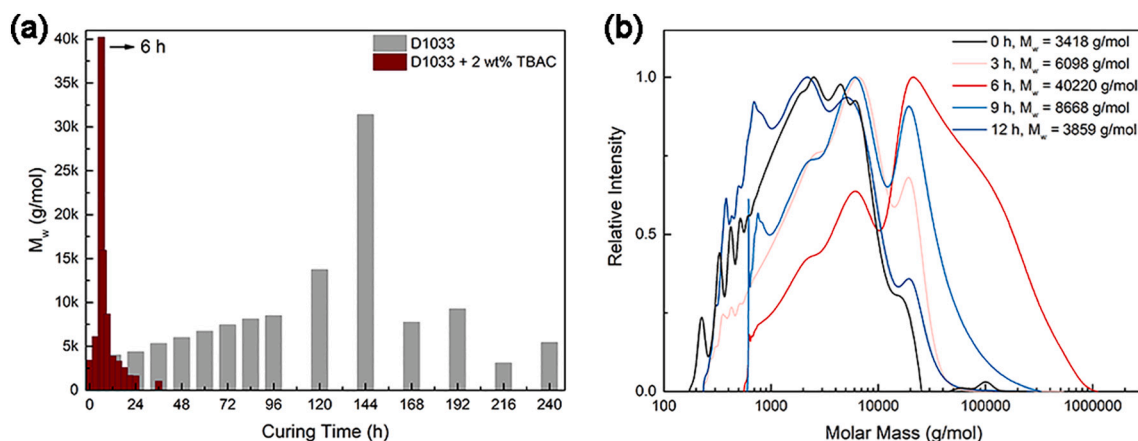
Fig. 2. (a) Average molecular weight (M_w) of Durazane 1033 and with the addition of 2 wt% of TBAC as a function of curing time. (b) Molar mass distribution of soluble TBAC-catalyzed D1033 after curing for 0, 3, 6, 9, and 12 h in ambient environment and temperature. Note that insoluble material and particles with sizes larger than 0.2 μm were filtered out.

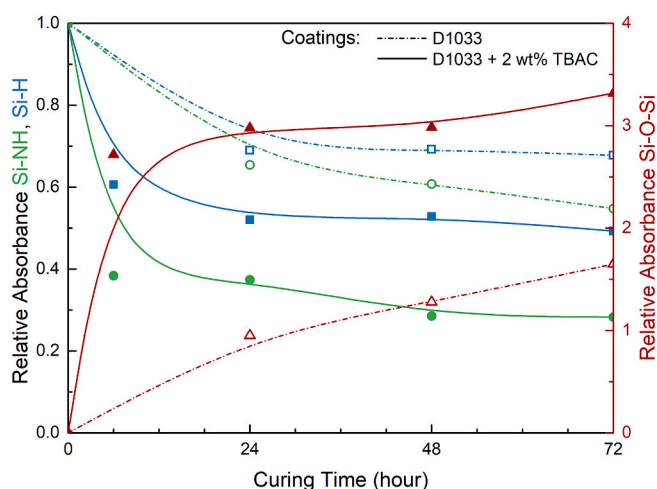curing, which is about 24 times faster than that of the pure PSZ sample (that needs 144 h). After 6 h, the crosslinked samples contain a large amount of the three-dimensional network that cannot be dissolved in THF, indicating much higher crosslinking degrees. The GPC data comparison supports the previous finding of FTIR and confirms the catalytic effect of TBAC on the moisture curing of polysilazane.
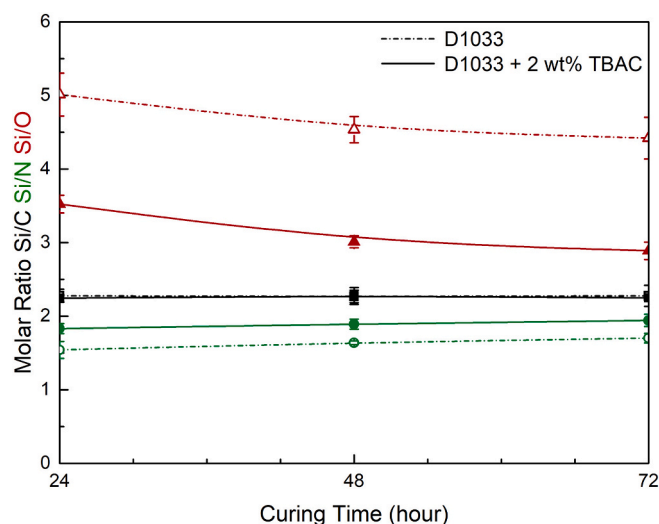
3.2. Catalytic effect of tetrabutylammonium chloride on the moisture curing of polysilazane coating

The pure Durazane 1033 and that with 2 wt% of TBAC were spin-coated on Si wafers with a spin speed of 700 rpm and crosslinked in ambient environment and temperature. The Durazane 1033 coating is dry to touch in around 19 h, while the TBAC-catalyzed polysilazane coating is considerably faster to reach the dry-to-touch state, which only takes ca. 1 h. The crosslinking process of both coatings has been monitored by FTIR after dry-to-touch. The integrated peak intensities of the involved Si–H, Si–NH, and Si–O–Si groups are shown in Fig. 3 as a function of curing time. As noted in the GPC results, the average molecular weight of the TBAC-catalyzed polysilazane increased dramatically within the first 6 h of curing. A similar trend is found in the FTIR result. After 6 h of curing, around 39% of the Si–H and 62% of the Si–NH

groups of the TBAC-catalyzed polysilazane coating are consumed. After 24 h, the Si–H and Si–NH vibrations are reduced by 48% and 63%, respectively, compared to 31% and 35% for the uncatalyzed polysilazane coating. After that, the uncatalyzed PSZ coating slowly crosslinks and has 68% and 55% of the Si–H and Si–NH groups left after 72 h of curing, respectively. During the same time, the crosslinking process of the TBAC-catalyzed PSZ coating slows down and ends up having 49% and 28% of the remaining Si–H and Si–NH groups, respectively. It is confirmed by Dargère et al. [28] that this half amount of the Si–H groups remain unreacted because of their low sensitivity to hydrolysis compared to the Si–NH groups. Besides, some of the residual Si–H groups are trapped in the highly crosslinked polymer network and therefore stay away from further hydrolysis. Still, it is clear that 1.6 times more reactive groups are consumed when the TBAC is added. After 72 h of curing, the Si–O–Si vibration of the catalyzed PSZ coating reaches the highest relative absorbance point of 3.32, which is about 2 times more compared to 1.64 for the uncatalyzed PSZ coating. Based on the stated results, TBAC is evidently an efficient catalyst for moisture curing of polysilazane coatings.

Fig. 4. Calculated Si/C (black), Si/N (green), and Si/O (red) molar ratios of Durazane 1033-derived coatings with (solid line) and without (dash-dot line) the addition of 2 wt% of TBAC after 24, 48, and 72 h of curing under ambient conditions. Detailed elemental compositions are listed in Table S1. (For interpretation of the references to colour in this figure legend, the reader is referred to the web version of this article.)

Fig. 3. Calculated relative absorbance (relative to Si–CH₃) of Si–H, Si–NH, and Si–O–Si groups as a function of curing time obtained from the ATR-FTIR spectra of Durazane 1033-derived coating (dash-dot line) and with the addition of 2 wt % of TBAC (solid line).

Fig. 4 compares the Si/C, Si/N, and Si/O molar ratios of the uncatalyzed and TBAC-catalyzed polysilazane coatings after 24, 48, and 72 h of curing in ambient environment and temperature. The molar ratios are calculated from the corresponding elemental compositions (Table S1) obtained from EDX. As expected, the coatings consist of Si, O, N, and C. Note that hydrogen is not detectable by the EDX. During the crosslinking process the Si/C molar ratio stays constant (~2.27), which supports that the Si–CH$_3$ is excluded from the hydrolysis and condensation reactions. As the curing time increases, the Si/N molar ratio of both coatings increases and the Si/O molar ratio decreases, indicating the loss of N and the gain of O. In addition, the TBAC-catalyzed PSZ coating has a larger amount of O incorporated (with less N left) in the network compared to the uncatalyzed PSZ coating, indicating a higher crosslinking degree, which further verifies the catalytic performance of TBAC on the moisture curing of polysilazane coating.

3.3. Coating characterizations

In order to achieve an industrially favorable thickness (5–7 μm), the pure Durazane 1033 and that with 2 wt% of TBAC were spin-coated on Si(100) wafers with a spin speed of 700 rpm based on the former experience [27]. The thickness of the uncatalyzed and TBAC-catalyzed PSZ coatings was measured by a profilometer after 7 d of curing under ambient conditions, which are 5.3 ± 2.7 μm and 4.9 ± 0.2 μm, respectively. The surface profiles were analyzed and the average roughnesses (Ra) of the uncatalyzed and TBAC-catalyzed PSZ coatings are 2.6 ± 1.1 μm and 0.3 ± 0.1 μm, respectively.

The morphological images of the coatings shown in Fig. 5 confirm the profilometry results. As can be seen in Fig. 5a and b, the uncatalyzed polysilazane coating has a moon-like surface full of bowl-shaped cavities and uneven bumps and ridges. On the contrary, the TBAC-catalyzed PSZ coating (Fig. 5d, e) evidences an even and smooth surface free from large irregularities. The remarkable difference in the surface morphology is explained by the different curing rates of the coatings. During the crosslinking process, gases like H$_2$ and NH$_3$ are generated and escape from the coating, which may leave a hole on the film surface. When the hydrolysis and condensation reactions are accelerated by TBAC, the polysilazane coating crosslinks to a solid film rapidly before the liquid phase starts to deform and shrink to form the cavities. Fig. 5c presents cross-sections of an uncatalyzed polysilazane coating at different spots. There are clear differences in the film thickness ranging from 1 to 10 μm. Compared to that, the cross-section of TBAC-catalyzed PSZ coating (Fig. 5f) shows a uniform film thickness of ca. 5 μm throughout the entire surface. On combining the graphical observations with the profilometry results, it is concluded that the addition of TBAC significantly improves the quality of the polysilazane coating.

As it is well known, polysilazane has good adhesion to most of the substrate materials owing to oxygen bridges formed between the coating and the substrate induced by chemical reactions of the Si–H, Si–NH groups (in the PSZ) and the –OH groups (on the substrate). The adhesion of the pure polysilazane coating and that with 2 wt% of TBAC to the Si wafer is evaluated by a cross-cut tape test following the DIN EN ISO 2409 standard. The test was made after the coatings were crosslinked in ambient environment and temperature for 7 d. As can be seen in the optical images (Fig. 6) of the films, the uncatalyzed PSZ coating has several defect areas showing colorful interference patterns, indicating thinner film thickness in these areas. Oppositely, the TBAC-catalyzed PSZ coating exhibits a smooth and even surface morphology. After the cross-cut tape tests, the adhesion of both coatings are classified as Gt 2, namely, 5% to 15% of the film is detached from the tested area after the tape peeling. However, the detachments show different appearances on the films. Owing to the thickness inequality, the uncatalyzed PSZ coating has more detachments in the area with thicker film thickness, and almost no detachments in the very thin areas. In contrast to that, even and constant detachments appear along the cutting line of the TBAC-catalyzed PSZ coating.

The mechanical properties of the coatings are determined by nano-indentation. The results were averaged over a penetration depth range of 500 to 800 nm to exclude any influence of the substrate. As shown in Fig. 7, the uncatalyzed polysilazane coating has a hardness of 0.09 ± 0.002 GPa and an elastic modulus of 0.4 ± 0.01 GPa after 30 d of curing under ambient conditions. With the curing process being catalyzed by TBAC, the polysilazane coating reaches a hardness of 0.16 ± 0.005 GPa and an elastic modulus of 1.63 ± 0.05 GPa, which is almost double and quadruple to that of the uncatalyzed coating, respectively. The significant improvement in the mechanical properties is explained by an increased crosslinking degree of the coating network.

Hydrophobicity is an important characteristic for applications such as protective, anti-graffiti, and anti-adherent coatings. Water contact angle (CA) is employed here to access the wettability of the coatings. It can be seen in Fig. S3 that the Durazane 1033 coating oscillates between being hydrophilic or hydrophobic and has an average CA of 88.7° ± 3.4°, which is considered to be slightly hydrophilic (CA < 90°). This relatively large error bar is attributed to the highly uneven film thickness. The TBAC-catalyzed PSZ coating has a water contact angle of 90.6° ± 1.3°, which is considered to be hydrophobic (CA ≥ 90°). It can be concluded that the addition of TBAC does not change the wetting property of the polysilazane coating evidently. Nevertheless, a more homogeneous wetting state is obtained throughout the entire surface because of the improved coating quality.
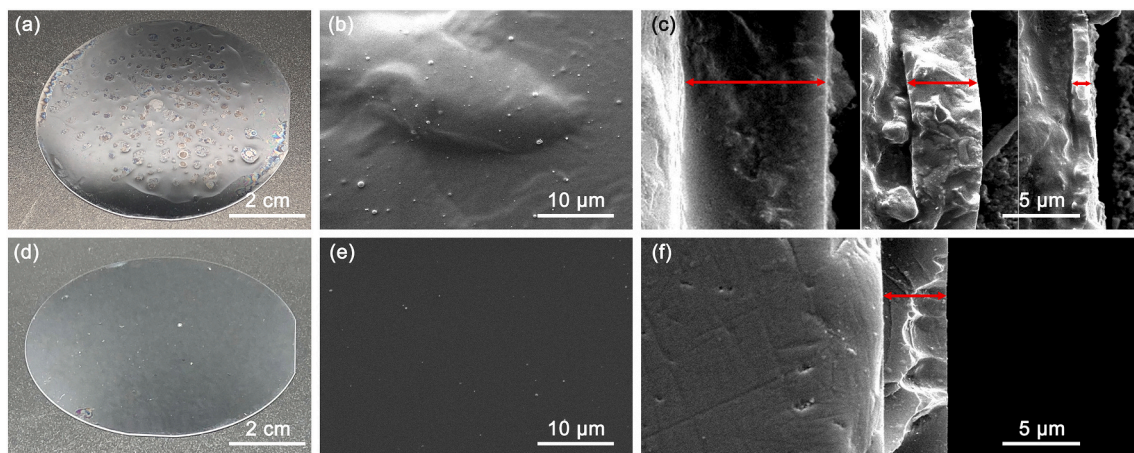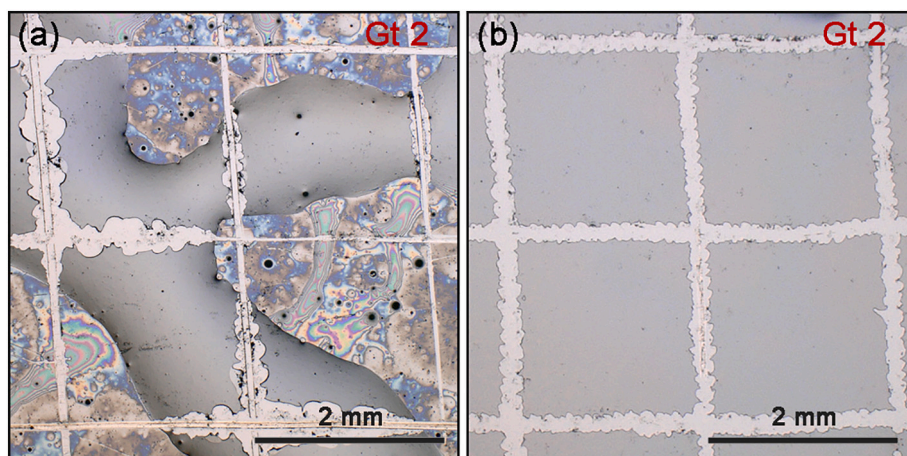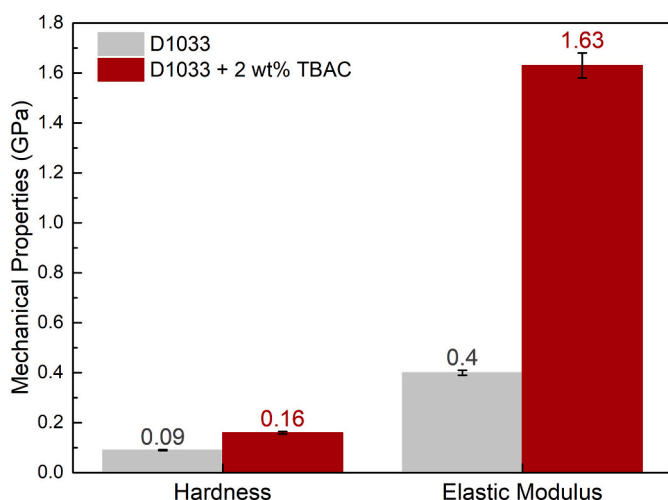

Fig. 5. Photos and SEM images of the spin-coated Durazane 1033 (a, b, c) and with the addition of 2 wt% of TBAC (d, e, f) on Si wafers after 7 d of curing in ambient environment and temperature. (c) and (f) are the corresponding cross-sections.

Fig. 6. Optical microscopy images of polysilazane coatings on Si wafers after standard DIN EN ISO 2409 cross-cut tape test: (a) Durazane 1033 and (b) with the addition of 2 wt% of TBAC after 7 d of curing in ambient environment and temperature.

Fig. 7. Hardness and elastic modulus of spin-coated Durazane 1033 and with the addition of 2 wt% of TBAC on Si wafers after 30 d of curing in ambient environment and temperature.

4. Conclusions

In this work, tetrabutylammonium chloride (TBAC) is proved to be an efficient catalyst for moisture curing of polysilazane (PSZ) at room temperature. The catalytic effect of TBAC has been confirmed by Fourier-transform infrared spectroscopy (FTIR) and gel permeation chromatography. With the addition of TBAC, the Si–H group is activated by chloride ions (while the nitrogen of the Si–N group is protonated) to form a transient Si–Cl group. The subsequent substitution of the Si–Cl group by an OH group and the reaction between Si–Cl and Si–OH groups as well as condensation of two Si–OH groups promote the formation of Si–O–Si group. It is found by FTIR that there is an upper limit of the catalytic effect of the TBAC due to the steric hindrance of the tetrabutylammonium molecule. Therefore, 2 wt% of the TBAC has been selected as the most efficient catalyst content for moisture curing of the PSZ coating.

The polysilazanes have been spin-coated on Si(100) wafers and crosslinked under ambient conditions to obtain transparent and solid films with a thickness of ca. 5 μm. The uncatalyzed polysilazane coating is dry to touch in 19 h, which is far longer than the 1 h to dry to touch for the TBAC-catalyzed PSZ coating. The FTIR results show that 1.6 times more of the reactive groups (Si–H, Si–NH) are consumed in the TBAC-catalyzed PSZ coating, while 2 times more of the Si–O–Si groups are formed compared to the uncatalyzed coating. In addition, energy dispersive X-ray spectroscopy supports the finding, showing that a considerably larger amount of O is incorporated in the TBAC-catalyzed PSZ coating than the uncatalyzed one.

Notably, the surface of the TBAC-catalyzed PSZ coating is flat and smooth, which is a significant improvement compared to the moon-like surface (full of cavities, bumps and ridges) of the uncatalyzed polysilazane coating. Owing to the highly improved coating quality and the much higher crosslinking degree, the TBAC-catalyzed polysilazane coating exhibits improved mechanical properties if compared with the uncatalyzed PSZ coating, and amounts double value of the hardness and quadruple value of the elastic modulus. The adhesion of the coating to the Si wafer and the wetting property of the two coatings are considered to be comparable.

In summary, tetrabutylammonium chloride has been shown to be an efficient catalyst for moisture curing of polysilazanes. It not only accelerates the hydrolysis and condensation reactions but also increases the degree of crosslinking, which results in a polysilazane film with significantly improved coating quality and enhanced mechanical properties.

CRediT authorship contribution statement

Ying Zhan: Conceptualization, Methodology, Validation, Formal analysis, Investigation, Data curation, Writing – original draft, Visualization. **Wei Li:** Validation, Formal analysis, Investigation, Writing – review & editing. **Ralf Grottenmüller:** Conceptualization, Methodology, Resources, Writing – review & editing, Supervision, Funding acquisition. **Christian Minnert:** Validation, Investigation, Writing – review & editing. **Thomas Krasemann:** Validation, Investigation. **Qingbo Wen:** Methodology, Formal analysis, Writing – review & editing. **Ralf Riedel:** Conceptualization, Resources, Writing – review & editing, Supervision, Project administration, Funding acquisition.

Declaration of competing interest

The authors declare that they have no known competing financial interests or personal relationships that could have appeared to influence the work reported in this paper.

Acknowledgments

Physical Metallurgy Division of TU Darmstadt, Germany (Prof. K. Durst) for the provision of the nanoindentation experimental facilities.

Appendix A. Supplementary data

Supplementary data to this article can be found online at https://doi.org/10.1016/j.porgcoat.2022.106872.

References

[1] P. Colombo, R. Riedel, G.D. Sorarù, H.-J. Kleebe, Polymer Derived Ceramics: From Nano-structure to Applications, DEStech Publications, Inc, 2010.

[2] G. Barroso, Q. Li, R.K. Bordia, G. Motz, Polymeric and ceramic silicon-based coatings–a review, J. Mater. Chem. A 7 (2019) 1936–1963, https://doi.org/10.1039/c8ta09054h.

[3] D. Amouzou, L. Fourdrinier, F. Maseri, R. Sporken, Formation of Me-O-Si covalent bonds at the interface between polysilazane and stainless steel, Appl. Surf. Sci. 320 (2014) 519–523, https://doi.org/10.1016/j.apsusc.2014.09.109.

[4] L. Picard, P. Phalip, E. Fleury, F. Ganachaud, Chemical adhesion of silicone elastomers on primed metal surfaces: a comprehensive survey of open and patent literatures, Prog. Org. Coat. 80 (2015) 120–141, https://doi.org/10.1016/j.porgcoat.2014.11.022.

[5] S.D. Kim, P.S. Ko, K.S. Park, Perhydropolysilazane spin-on dielectrics for inter-layer-dielectric applications of sub-30 nm silicon technology, Semicond. Sci. Technol. 28 (2013) 35008, https://doi.org/10.1088/0268-1242/28/3/035008.

[6] M. Günthner, A. Schütz, U. Glatzel, K. Wang, R.K. Bordia, O. Greißl, W. Krenkel, G. Motz, High performance environmental barrier coatings, part I: passive filler loaded SiCN system for steel, J. Eur. Ceram. Soc. 31 (2011) 3003–3010, https://doi.org/10.1016/J.JEURCERAMSOC.2011.05.027.

[7] Y. Wang, R. Grottenmuller, T. Lorenz, in: Polysilazanes – Binders That Make a Difference 16, CoatingsTech, 2019, pp. 38–45.

[8] X. Zhang, D. Brodus, V. Hollimon, H. Hu, A brief review of recent developments in the designs that prevent bio-fouling on silicon and silicon-based materials, Chem. Cent. J. 11 (2017), https://doi.org/10.1186/S13065-017-0246-8.

[9] S. Rossi, F. Deflorian, M. Fedel, Polysilazane-based coatings: corrosion protection and anti-graffiti properties, Surf. Eng. 35 (2019) 343–350, https://doi.org/10.1080/02670844.2018.1465748.

[10] P. Furtat, M. Lenz-Leite, E. Ionescu, R.A.F. MacHado, G. Motz, Synthesis of fluorine-modified polysilazanes: via Si-H bond activation and their application as protective hydrophobic coatings, J. Mater. Chem. A 5 (2017) 25509–25521, https://doi.org/10.1039/c7ta07687h.

[11] G. Barroso, M. Döring, A. Horcher, A. Kienzle, G. Motz, Polysilazane-based coatings with anti-adherent properties for easy release of plastics and composites from metal molds, Adv. Mater. Interfaces 7 (2020) 1–14, https://doi.org/10.1002/admi.201901952.

[12] P. Colombo, G. Mera, R. Riedel, G.D. Soraru, Polymer-derived ceramics: 40 years of research and innovation in advanced ceramics, J. Am. Ceram. Soc. 93 (2010) 1805–1837, https://doi.org/10.1111/j.1551-2916.2010.03876.x.

[13] R. Riedel, G. Mera, R. Hauser, A. Klonczynski, Silicon-based polymer-derived ceramics: synthesis properties and applications-a review dedicated to prof. Dr. Fritz Aldinger on the occasion of his 65th birthday, J. Ceram. Soc. Jpn. 114 (2006) 425–444, https://doi.org/10.2109/jcersj.114.425.

[14] K.J. Wynne, R.W. Rice, Ceramics via polymer pyrolysis, Annu. Rev. Mater. Sci. 14 (1984) 297–334, https://doi.org/10.1146/annurev.ms.14.080184.001501.

[15] D. Seyferth, G.H. Wiseman, High-yield synthesis of Si3N4/SiC ceramic materials by pyrolysis of a novel poly organosilazane, J. Am. Ceram. Soc. 67 (1984) C-132–C-133.

[16] R. Chavez, E. Ionescu, C. Balan, C. Fasel, R. Riedel, Effect of ambient atmosphere on crosslinking of polysilazanes, J. Appl. Polym. Sci. 119 (2011) 794–802, https://doi.org/10.1002/app.32777.

[17] H. Kozuka, M. Fujita, S. Tamoto, Polysilazane as the source of silica: the formation of dense silica coatings at room temperature and the new route to organic–inorganic hybrids, J. Sol-Gel Sci. Technol. 48 (2008) 148–155, https://doi.org/10.1007/s10971-008-1793-1.

[18] M. Günthner, K. Wang, R.K. Bordia, G. Motz, Conversion behaviour and resulting mechanical properties of polysilazane-based coatings, J. Eur. Ceram. Soc. 32 (2012) 1883–1892, https://doi.org/10.1016/j.jeurceramsoc.2011.09.005.

[19] T.R. Augustinho, G. Motz, S. Ihlow, R.A.F. MacHado, Application of hybrid organic/inorganic polymers as coatings on metallic substrates, Mater. Res. Express 3 (2016), https://doi.org/10.1088/2053-1591/3/9/095301.

[20] R.M. Laine, Y. Blum, D. Tse, R. Glaser, Synthetic routes to oligosilazanes and polysilazanes, Inorg. Organomet. Polym. (1988), https://doi.org/10.1021/bk-1988-0360.ch010.

[21] L.V. Interrante, K. Moraes, Q. Liu, N. Lu, A. Puerta, L.G. Sneddon, Silicon-based ceramics from polymer precursors, Pure Appl. Chem. 74 (2003) 2111–2117, https://doi.org/10.1351/pac200274112111.

[22] F. Bauer, U. Decker, A. Dierdorf, H. Ernst, R. Heller, H. Liebe, R. Mehnert, Preparation of moisture curable polysilazane coatings part I. Elucidation of low temperature curing kinetics by FT-IR spectroscopy, Prog. Org. Coat. 53 (2005) 183–190, https://doi.org/10.1016/j.porgcoat.2005.02.006.

[23] A. Morlier, S. Cros, J.P. Garandet, N. Alberola, Structural properties of ultraviolet cured polysilazane gas barrier layers on polymer substrates, Thin Solid Films 550 (2014) 85–89, https://doi.org/10.1016/J.TSF.2013.10.140.

[24] L. Prager, A. Dierdorf, H. Liebe, S. Naumov, S. Stojanović, R. Heller, L. Wennrich, M.R. Buchmeiser, Conversion of perhydropolysilazane into a SiOx network triggered by vacuum ultraviolet irradiation: access to flexible, transparent barrier coatings, Chem.Eur. J. 13 (2007) 8522–8529, https://doi.org/10.1002/chem.200700351.

[25] S. Müller, Y. De Hazan, D. Penner, Effect of temperature, humidity and aminoalkoxysilane additive on the low temperature curing of polyorganosilazane coatings studied by IR spectroscopy, gravimetric and evolved gas analysis, Prog. Org. Coat. 97 (2016) 133–145, https://doi.org/10.1016/j.porgcoat.2016.03.021.

[26] M. Fedel, F.J.R. Gómez, S. Rossi, F. Deflorian, F.J. Rodríguez Gómez, S. Rossi, F. Deflorian, Characterization of polyorganosilazane-derived hybrid coatings for the corrosion protection of mild steel in chloride solution, Coatings 9 (2019) 680, https://doi.org/10.3390/coatings9100680.

[27] Y. Zhan, R. Grottenmüller, W. Li, F. Javaid, R. Riedel, Evaluation of mechanical properties and hydrophobicity of room-temperature, moisture-curable polysilazane coatings, J. Appl. Polym. Sci. 138 (2021) 50469, https://doi.org/10.1002/APP.50469.

[28] N. Dargère, V. Bounor-Legaré, F. Boisson, P. Cassagnau, G. Martin, P. Sonntag, N. Garois, Hydridosilazanes hydrolysis-condensation reactions studied by 1H and 29Si liquid NMR spectroscopy, J. Sol-Gel Sci. Technol. 62 (2012) 389–396, https://doi.org/10.1007/s10971-012-2738-2.

[29] A. Lukacs G.J. Knasiak , Thermally stable, moisture curable polysilazanes and polysiloxazanes, U.S. Patent No. 6,652,978., 2003.

[30] T.N.H. Lo, H.S. Hwang, J. Lee, I. Park, Synthesis of new semi-fluorinated polysilazanes and their amphiphobic coating applications, Prog. Org. Coat. 148 (2020), 105853, https://doi.org/10.1016/j.porgcoat.2020.105853.

[31] K. Nakajima, H. Uchiyama, T. Kitano, H. Kozuka, Conversion of solution-derived perhydropolysilazane thin films into silica in basic humid atmosphere at room temperature, J. Am. Ceram. Soc. 96 (2013) 2806–2816, https://doi.org/10.1111/jace.12513.

[32] A. Morlier, S. Cros, J.-P. Garandet, N. Alberola, Thin gas-barrier silica layers from perhydropolysilazane obtained through low temperature curings: a comparative study, Thin Solid Films 524 (2012) 62–66, https://doi.org/10.1016/j.tsf.2012.09.065.

[33] H. Kozuka, K. Nakajima, H. Uchiyama, Superior properties of silica thin films prepared from perhydropolysilazane solutions at room temperature in comparison with conventional alkoxide-derived silica gel films, ACS Appl. Mater. Interfaces 5 (2013) 8329–8336, https://doi.org/10.1021/AM400845Y.

[34] A. Kojima, S. Hoshii, T. Muto, Characteristics of polysilazane compound and its application as coating for carbon material, J. Mater. Sci. Lett. 21 (2002) 757–760, https://doi.org/10.1023/A:1015709818240.

[35] C. Vakifahmetoglu, I. Menapace, A. Hirsch, L. Biasetto, R. Hauser, R. Riedel, P. Colombo, Highly porous macro- and micro-cellular ceramics from a polysilazane precursor, Ceram. Int. 35 (2009) 3281–3290, https://doi.org/10.1016/J.CERAMINT.2009.05.022.

[36] O. Flores, T. Schmalz, W. Krenkel, L. Heymann, G. Motz, Selective cross-linking of oligosilazanes to tailored meltable polysilazanes for the processing of ceramic SiCN fibres, J. Mater. Chem. A 1 (2013) 15406–15415, https://doi.org/10.1039/C3TA13254D.

[37] W.C. Oliver, G.M. Pharr, An improved technique for determining hardness and elastic modulus using load and displacement sensing indentation experiments, J. Mater. Res. 7 (1992) 1564–1583, https://doi.org/10.1557/jmr.1992.1564.

[38] W.C. Oliver, G.M. Pharr, Measurement of hardness and elastic modulus by instrumented indentation: advances in understanding and refinements to methodology, J. Mater. Res. 19 (2004) 3–20, www.mrs.org/publications/jmr/policy.html (accessed January 16, 2022).

[39] DIN EN ISO 2409. https://www.une.org/encuentra-tu-norma/busca-tu-norma/norma?c=N0052301, 2013.

[40] A.E. Abel T.A. Kruger R.W. Mouk G.J. Knasiak , Silazane and/or polysilazane compounds and methods of making, U.S. Patent No. 6,329,487, 2001.

[41] T. Joseph, D. White, Understanding the role of concentrated phosphoric acid solutions as high-temperature silicon nitride etchants, ECS J. Solid State Sci. Technol. 10 (2021), 024006, https://doi.org/10.1149/2162-8777/abe422.

[42] O. Lichtenberger, J. Woltersdorf, R. Riedel, Polymere carbodiimide als vorstufen für keramische werkstoffe: reaktionsmechanismen und tautomeriebeziehungen, zeitschrift fur anorg, Und Allg.Chem. 628 (2002) 596–607, https://doi.org/10.1002/1521-3749(200203)628:3<596::AID-ZAAC596>3.0.CO;2-9.

[43] O. Sneh, M.L. Wise, A.W. Ott, L.A. Okada, S.M. George, Atomic layer growth of SiO2 on Si(100) using SiCl4 and H2O in a binary reaction sequence, Surf. Sci. 334 (1995) 135–152, https://doi.org/10.1016/0039-6028(95)00471-8.

[44] L. Lu, C.X. Feng, Y.C. Song, Curing polysilazane fibres by exposure to boron trichloride, J. Mater. Sci. Lett. 17 (1998) 481–484, https://doi.org/10.1023/A:1006580427640.

[45] J. Hapke, G. Ziegler, Synthesis and pyrolysis of liquid organometallic precursors for advanced Si-Ti-C-N composites, Adv. Mater. 7 (1995) 380–384, https://doi.org/10.1002/ADMA.19950070407.

[46] A. Viard, D. Fonblanc, D. Lopez-Ferber, M. Schmidt, A. Lale, C. Durif, M. Balestrat, F. Rossignol, M. Weinmann, R. Riedel, S. Bernard, Polymer derived Si–B–C–N ceramics: 30 years of research, Adv. Eng. Mater. 20 (2018) 1800360, https://doi.org/10.1002/adem.201800360.

Supporting Information

Rapid Crosslinking of Polysilazane-Derived Coatings at Room Temperature via Chloride-Catalyzed Hydrolysis/Condensation Reactions

Ying Zhan [a, *], Wei Li [a], Ralf Grottenmüller [b], Christian Minnert [a], Thomas Krasemann [b], Qingbo Wen [c], Ralf Riedel [a, *]

[a.] Institute of Materials and Earth Sciences, Technical University of Darmstadt, D-64287 Darmstadt, Germany

[b.] Merck KGaA, Performance Materials, D-64293 Darmstadt, Germany

[c.] State Key Laboratory of Powder Metallurgy, Central South University, Changsha 410083, China

[*.] Corresponding authors: ying.zhan@tu-darmstadt.de (Y. Zhan), ralf.riedel@tu-darmstadt.de (R. Riedel)
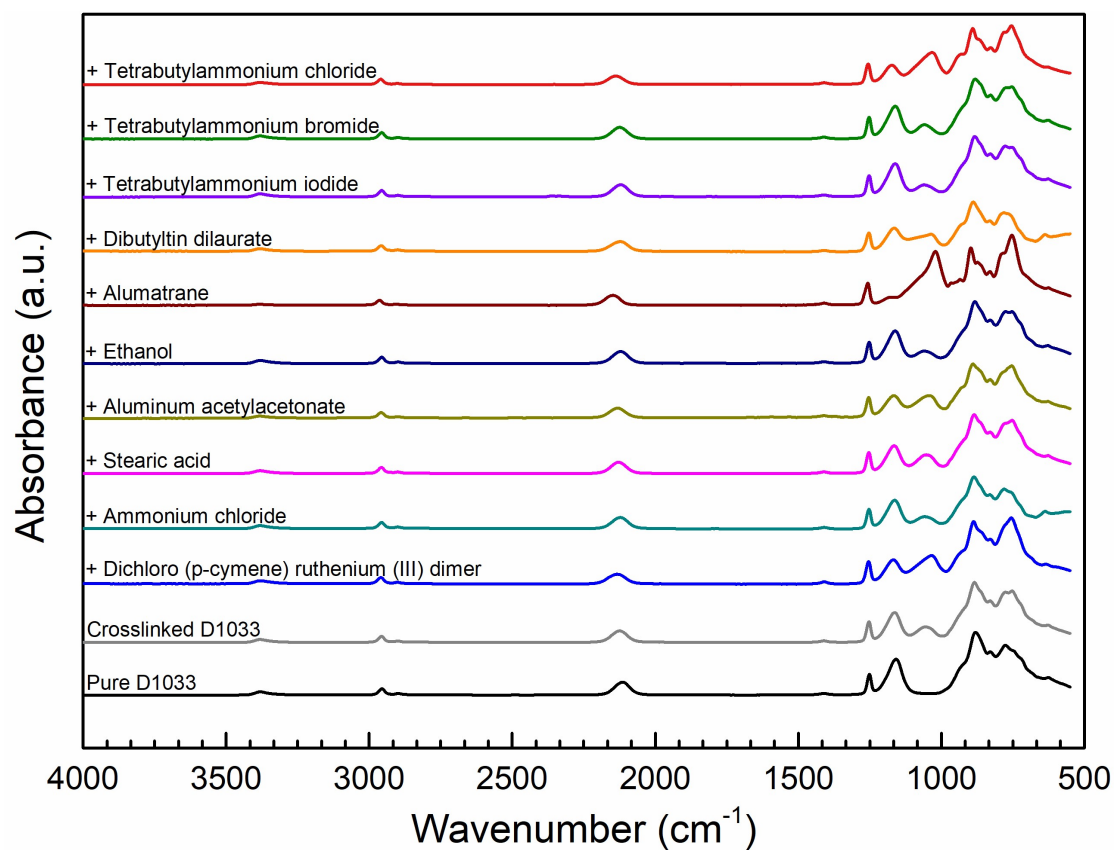
Figure S1 ATR-FTIR spectra of Durazane 1033 with the addition of different catalysts (1 wt%) after 24 h of curing in ambient environment and temperature. Tetrabutylammonium chloride is selected as a suitable catalyst for the moisture curing of polysilazane because of its good catalytic ability, relatively low price, and colorless feature. (The catalytic effect of alumatrane is under further investigation and will not be illustrated in this paper.)
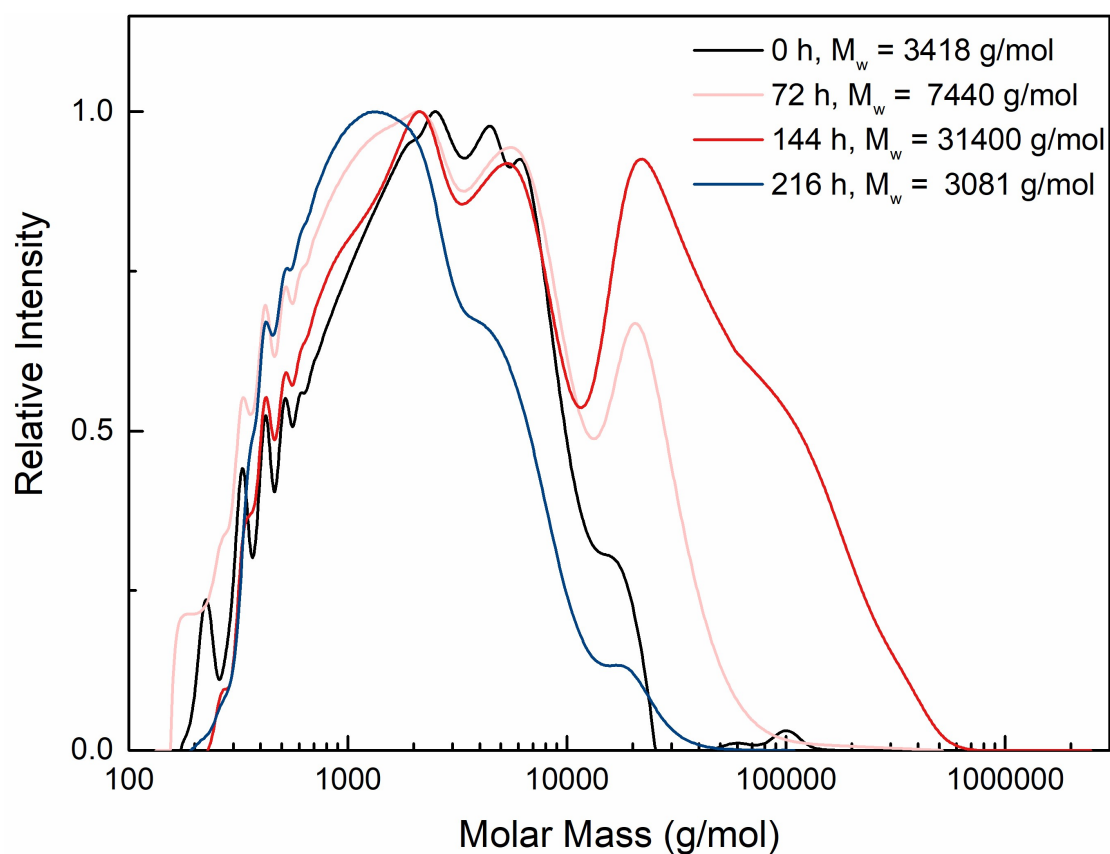
Figure S2 Molar mass distribution of soluble D1033 after curing for 0, 72, 144, and 216 h

Table S1 Elemental compositions of Durazane 1033-derived coatings with and without the addition of 2 wt% of TBAC after 24, 48, and 72 h of curing under ambient conditions

| Samples	Curing Time (h)	Elements (wt%)				Calculated Molar Ratio		
		Si	O	N	C	Si/C	Si/N	Si/O
D1033	24	61.18 ± 1.22	7.05 ± 0.32	20.20 ± 1.19	11.57 ± 0.37	2.28 ± 0.09	1.54 ± 0.11	5.01 ± 0.29
	48	61.64 ± 0.19	7.82 ± 0.31	18.83 ± 0.31	11.71 ± 0.38	2.27 ± 0.09	1.64 ± 0.03	4.53 ± 0.18
	72	61.43 ± 0.78	8.07 ± 0.41	18.16 ± 0.56	11.75 ± 0.59	2.28 ± 0.14	1.70 ± 0.07	4.42 ± 0.28
TBAC-catalyzed D1033	24	61.43 ± 0.58	10.00 ± 0.31	16.84 ± 0.46	11.74 ± 0.16	2.24 ± 0.05	1.83 ± 0.07	3.52 ± 0.12
	48	60.73 ± 0.55	11.57 ± 0.36	16.14 ± 0.47	11.56 ± 0.47	2.27 ± 0.11	1.89 ± 0.07	3.01 ± 0.08
	72	60.60 ± 0.72	12.07 ± 0.34	15.75 ± 0.55	11.58 ± 0.23	2.25 ± 0.04	1.94 ± 0.08	2.89 ± 0.12

3
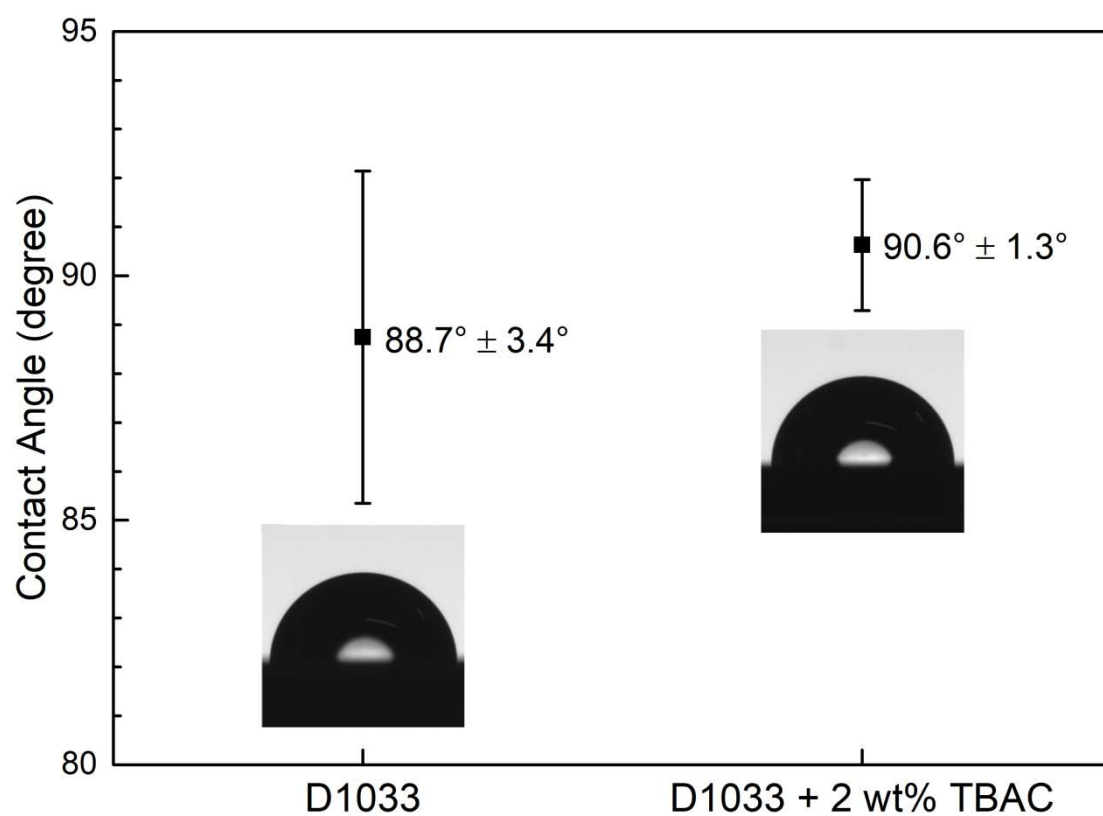
Figure S3 Water contact angle of spin-coated Durazane 1033 and with the addition of 2 wt% of TBAC on Si wafers after 30 d of curing in ambient environment and temperature. Insets are the corresponding photos of the sessile water droplet.

Research Article

Boron-modified perhydropolysilazane towards facile synthesis of amorphous SiBN ceramic with excellent thermal stability

Ying ZHAN[a,†], Wei LI[a,†], Tianshu JIANG[a], Claudia FASEL[a],
Emmanuel III RICOHERMOSO[a], Jan BERNAUER[a], Zhaoju YU[b,*],
Zhenghao WU[c,*], Florian MÜLLER-PLATHE[c], Leopoldo MOLINA-LUNA[a],
Ralf GROTTENMÜLLER[d], Ralf RIEDEL[a]

[a]*Department of Materials and Earth Sciences, Technical University of Darmstadt, D-64287 Darmstadt, Germany*
[b]*College of Materials, Key Laboratory of High Performance Ceramic Fibers* (*Xiamen University*),
Ministry of Education, Xiamen 361005, China
[c]*Eduard-Zintl-Institut für Anorganische und Physikalische Chemie, Technical University of Darmstadt,
D-64287 Darmstadt, Germany*
[d]*Merck KGaA, Performance Materials, D-64293, Darmstadt, Germany*

Abstract: SiBN ceramics are widely considered to be the most promising material for microwave-transparent applications in harsh environments owing to its excellent thermal stability and low dielectric constant. This work focuses on the synthesis and ceramization of single-source precursors for the preparation of SiBN ceramics as well as the investigation of the corresponding microstructural evolution at high temperatures including molecular dynamic simulations. Carbon- and chlorine-free perhydropolysilazanes were reacted with borane dimethyl sulfide complex at different molar ratios to synthesize single-source precursors, which were subsequently pyrolyzed and annealed under N_2 atmosphere (without ammonolysis) to prepare SiBN ceramics at 1100, 1200, and 1300 ℃ with high ceramic yield in contrast to previously widely-used ammonolysis synthesis process. The obtained amorphous SiBN ceramics were shown to have remarkably improved thermal stability and oxidation resistance compared to amorphous silicon nitride. Particularly, the experimental results have been combined with molecular dynamics simulation to further study the amorphous structure of SiBN and the atomic-scale diffusion behavior of Si, B, and N at 1300 ℃. Incorporation of boron into the Si–N network is found to suppress the crystallization of the formed amorphous silicon nitride and hence improves its thermal stability in N_2 atmosphere.

Keywords: polymer-derived ceramics (PDCs); SiBN; crystallization; molecular dynamics; oxidation resistance

---

1 Introduction

Nitride ceramics, such as Si_3N_4 and BN, have been ever-increasingly applied in several key areas owing to their chemical stability, relatively high thermal conductivity, and outstanding oxidation resistance even under extremely harsh environments [1–7]. However, the intrinsic weakness of creep and thermal shock resistance limits their scope of application. To tackle these shortcomings, adjustments can be performed at the microscale by lowering the atomic diffusivity and reducing stress concentrations [8–13], which are achievable in materials with amorphous networks. It has been reported that in materials having three or more elements with different and specific coordination numbers, the formation of a crystalline phase can be sufficiently suppressed [1,14–17]. However, the adaptability of this concept to nitride materials is challenging. Due to their low self-diffusion coefficients, ternary nitrides are difficult to be prepared via solid-state synthesis routes. In this context, the polymer-derived ceramic (PDC) route proves itself to be a promising method for preparing multielement ceramic nanocomposites. As polymer precursors can be tailored at the molecular level, end products with tunable chemical composition and homogeneous element distribution can be consequently achieved [18–23].

In recent years, ternary ceramics composed of Si, B, and N have attracted widespread attention due to their advanced properties as compared to single-component ceramics of Si_3N_4 and BN. Particularly, SiBN ceramics and Si_3N_4/BN composites with low dielectric constant are considered to be the most promising microwave-transparent materials for use in microwave windows and radomes under harsh environments. Various studies have been reported regarding the synthesis of ternary SiBN ceramics via molecular and PDC routes [14,24–31]. However, most of the reported polymer precursors used to prepare SiBN ceramics inevitably contain a certain amount of carbon. In order to eliminate the influence of carbon, complex and expensive pyrolysis (e.g., pyrolysis under NH_3 atmosphere) and annealing (under N_2 atmosphere) processes have to be applied to synthesize carbon-free SiBN ceramics [14,24,26,27,32]. Not only that, chlorine-containing precursors were employed, in which the chlorine is difficult to be removed during pyrolysis. Moreover, most studies have focused on the modification of precursors and the polymer-to-ceramic transformation, exclusively, and there is limited research on amorphous SiBN ceramic and its thermal stability.

In this work, carbon- and chlorine-free single-source precursor (boron-modified perhydropolysilazane) derived amorphous SiBN ceramics with varying chemical compositions were successfully prepared under N_2 (without expensive ammonolysis process). Molecular structure and the possible reaction mechanisms of the polymer precursors, as well as the relationship between microstructural evolution and the early stage crystallization of SiBN ceramics were investigated. Besides, the influence of Si/B ratio in the SiBN ceramics on both high temperature stability and resistance to crystallization was assessed. In addition to the experimental techniques, molecular dynamics (MD) simulation is employed to shed light onto the molecular structure and the atomic-level diffusion behavior of amorphous silicon nitride and SiBN, which provides a rational explanation for the polymer-to-ceramic transformation of SiBN ceramics.

2 Materials and methods

2.1 Synthesis and pyrolysis of single-source precursors

All the chemical syntheses were carried out under an argon atmosphere using standard Schlenk technique except where otherwise stated. Commercially available perhydropolysilazane solution (20 wt% of PHPS in dibutyl ether, Merck, KGaA, Germany) and borane dimethyl sulfide complex (BMS, Sigma-Aldrich, Germany) were used to synthesize the single-source precursors for the preparation of SiBN ceramics. To investigate the effect of boron content on phase composition, microstructural evolution, and oxidation resistance of the obtained SiBN ceramics, the Si/B molar ratios of the precursors were set to be 1, 2, and 5, according to the amount of BMS added to the PHPS solution. The synthesized boron-modified perhydropolysilazanes are denoted as BPSZ*X* (*X* is the set Si/B molar ratio) accordingly. Here, a representative synthesis process of the BPSZ2 is stated as follows: a solution of BMS (2.4 mL, 25 mmol) in anhydrous toluene (5 mL) was added dropwise to a solution of PHPS (11.25 g, 50 mmol, based on one monomer unit) with stirring at ~ −78 ℃ (dry ice/acetone bath) for 2 h and naturally warmed up to room temperature. After stirring for 24 h continuously, the mixture was heated up to 80 ℃ for

3 h followed by vacuum drying at 50 ℃ to yield a milky white gel-like solid precursor. The dried solid single-source precursor was subsequently transferred into Schlenk tube furnace under the protection of argon and heated to 1100 ℃ for 2 h at a heating rate of 50 ℃/h under a constant flow of N_2. The as-pyrolyzed specimen was annealed at 1200 and 1300 ℃ for 2 h in N_2 atmosphere to investigate their high-temperature crystallization behavior and stability against thermal decomposition.

2. 2 Characterizations

The synthesis and the crosslinking process of the single-source precursors were analyzed *ex situ* by Fourier transform infrared (FTIR) spectroscopy on a Varian IR-670 spectrometer (Agilent Technologies, USA), using attenuated total reflection (ATR) mode in the range of 550–4000 cm^{-1}. Background corrections and baseline corrections of the spectra have been done automatically by the device. The quantitative elemental analyses of the synthesized precursor (BPSZ2) and BPSZ2-derived ceramic (pyrolyzed at 1100 ℃) were performed at Mikroanalytisches Labor Pascher (Remagen, Germany). Silicon and boron contents were measured using inductively coupled plasma-atomic emission spectrometry (ICP-AES). Hydrogen content was determined by combustion in pure oxygen and the detection of water using infrared spectroscopic. Nitrogen and oxygen contents in ceramic samples were detected by thermal conductivity and IR-analysis, respectively. Nitrogen and oxygen contents in polymeric sample were detected volumetrically and by thermal conductivity detection, respectively. Carbon analysis of samples annealed at 1300 ℃ was carried out by an LECO C-200 analyzer (LECO Corporation, St. Joseph, Michigan, USA). The phase compositions of the ceramic samples were investigated by X-ray diffraction (XRD) with a STADI P powder diffractometer (STOE & Cie GmbH, Germany, Mo Kα1 radiation source). To investigate the microstructure of the as-obtained ceramics, transmission electron microscopy (TEM) experiments were performed on an atomic resolution microscope (ARM) Jeol JEM-200F (JEOL Ltd, Tokyo, Japan) under electron beam energy of 200 keV. The high-resolution TEM images were filtered using an average background subtraction filter or a Wiener filter [33]. In parallel, scanning electron microscopy (SEM) was employed with a Philips XL30 FEG high-resolution scanning electron microscope (FEI Company, Hillsboro, Oregon,

USA), coupled with an energy-dispersive X-ray (EDX) spectroscope (Mahwah, New Jersey, USA). The polymer-to-ceramic transformation of the different precursors was characterized by means of thermogravimetric analysis/differential thermal analysis (TGA/DTA) in flowing nitrogen atmosphere with an STA 449C Jupiter (Netzsch Gerätebau GmbH, Germany) *in situ* coupled with a mass spectrometer (MS, QMS 403C Aëolos, Netzsch Gerätebau GmbH, Germany). The heating rate was set at 5 ℃/min. TGA was employed as well to investigate the oxidation behavior of SiBN ceramic powders by observing their weight change from room temperature to 1350 ℃ with a heating rate of 5 ℃/min in synthetic air.

2. 3 Molecular dynamics simulation

Molecular dynamics simulations of amorphous silicon nitride and SiBN ceramics have been conducted using the large-scale atomic/molecular massively parallel simulator (LAMMPS) [34]. Many-body Tersoff potentials [35] were employed to describe the interactions among Si, B, and N. Structural properties, e.g., coordination number and pair distribution functions, of amorphous silicon nitride and SiBN materials simulated using this Tersoff potential have been demonstrated to be reasonably reproduced compared with experimental measurements [36]. Four amorphous ceramics systems, namely Si_3N_4, $Si_3B_{0.6}N_{4.6}$, $Si_3B_{1.5}N_{5.5}$, and $Si_3B_3N_7$, have been simulated to study the influence of the boron content on the thermal stability of the amorphous ceramics at temperature $T = 1300$ ℃, similar to the experiments. Initially, around 10,000 atoms were randomly placed in the simulation box at a density of ~2.5 g/cm^3 (consistent with the experimental measurement for the bulk material at ~1500 K [37]) for all systems, giving a cubic dimension of ~5 nm. Details of the simulated systems can be found in the Electronic Supplementary Material (ESM). Subsequently, the system was pre-equilibrated for 20 ps at $T = 8000$ K to eliminate the impact of the initial atomic arrangement and to avoid its trapping in local energy minima. A fast quench under constant volume to $T = 1300$ ℃ followed. The quenched system was then subjected to an additional equilibration of 100 ps. The equilibration of the simulation was monitored via tracking its total potential energy. After about 20 ps, the potential energy reaches a plateau as seen in an example of $Si_3B_3N_7$ given in the ESM. After equilibration, the simulation was continued as production run (~5000 ps) for the

extraction of data. All simulations were performed with a time step 0.2 fs under constant temperature and volume conditions using a Nose–Hoover thermostat with a coupling parameter of 0.02 ps [38,39].

The structural properties of amorphous Si_3N_4, $Si_3B_{0.6}N_{4.6}$, $Si_3B_{1.5}N_{5.5}$, and $Si_3B_3N_7$ have been characterized via pair distribution functions, defined as

$$g_{ij}(r) = \frac{V}{N_i N_j} \frac{dN_j(r)}{4\pi r^2 dr} \quad (1)$$

where V is the volume of the simulation box. N_i and N_j denote the number of atoms of elements i and j, respectively. $\delta N_j(r)$ represents the number of atoms of element j within a shell of thickness dr at the distance of r. The coordination number of element j around element i can then be calculated by

$$Z_{ij} = \rho_j \int_0^{r_c} 4\pi r^2 g_{ij}(r) dr \quad (2)$$

where r_c is the position of the first minimum in the pair distribution function between elements i and j. ρ_j is the average number density of element j.

The atomic dynamics have been measured via the mean-square-displacement (MSD), given by

$$MSD(t) = \langle (r(t) - r(0))^2 \rangle \quad (3)$$

where $\langle \cdot \rangle$ denotes the ensemble average and $r(t)$ is the atomic position vector at time t. The diffusion coefficient has been derived by the Einstein relation:

$$D = \frac{1}{6} \frac{dMSD(t)}{dt} \quad (4)$$

# 3   Results and discussion

3. 1   Synthesis of the single-source precursors

A set of boron-modified perhydropolysilazanes with different Si/B molar ratios were synthesized under Ar atmosphere and investigated with FTIR spectroscopy. The FTIR spectra of BMS, dried PHPS, and the obtained BPSZ*X* precursors are shown and compared in Fig. 1. Typical absorption bands of N–H (1120 and 3302 cm^{-1}), Si–H (2159 cm^{-1}), and Si–N–Si (830–1050 cm^{-1}) groups are expectedly shown in the FTIR spectrum of PHPS. With the addition of BMS into PHPS, the N–H and Si–H groups of PHPS and the B–H (2391 cm^{-1}, stretching vibration) groups of BMS are consumed, while B–N groups (1315 cm^{-1}) are formed simultaneously,

as shown in the spectra of BPSZ*X* precursors. Hence, dehydrocoupling reactions between the N–H (Si–H) and B–H groups are proposed as reaction mechanisms and are shown schematically in Fig. 2 [40,41]. Unlike the N–H groups, which are reacted in a high amount, only a small number of the Si–H groups are involved in the modification process. It was reported by Hapke and Ziegler [42] that the reaction of Si–H groups is affected by steric hindrance during the chemical modification of the PHPS. Additionally, the existence of B–H (1091 cm^{-1}) groups in BPSZ1 and BPSZ2 reveals that the silazane-bonded B–H groups have not been completely reacted. The C–H vibrations (2786–2995 cm^{-1}) detected in the spectra of the BPSZ*X* samples stem from the residual solvent dibutyl ether.

The elemental analyses of precursor BPSZ2 (Table 1) confirm the presence of boron atoms, indicating the successful incorporation of boron into the PHPS network. The empirical Si/B molar ratio (5.49) is larger than the set value (2), indicating boron loss during the
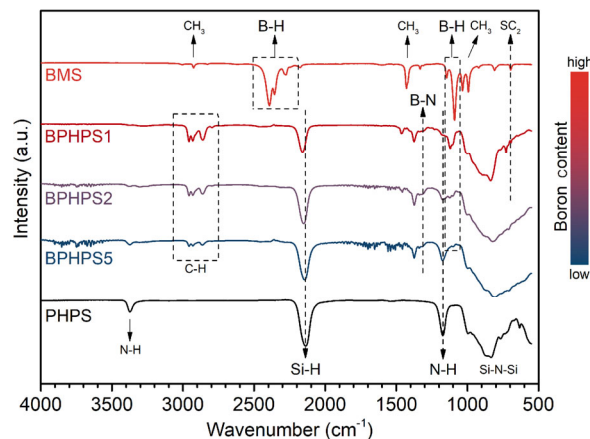
Fig. 1 FTIR spectra of dried PHPS, BPSZ5, BPSZ2, BPSZ1, and BMS (the intensity of all the spectra was normalized to [0, 1] in order to compare the FTIR results in a uniform interval).
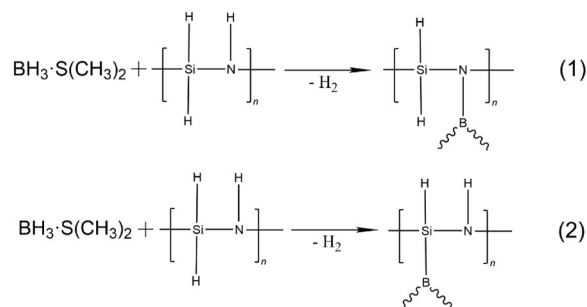
Fig. 2 Two possible reaction pathways of PHPS and BMS. The spectroscopic evidence reveals that reaction (1) is favored.

Table 1 Elemental composition of BPSZ2 precursor and BPSZ2-derived ceramic (pyrolyzed at 1100 ℃)

| Sample	Composition (wt%)						Calculated Si/B ratio	Empirical formula
	Si	B	N	H	C	O		
BPSZ2	55.80	3.99	24.00	5.07	3.90	6.49	5.49	$Si_{1.00}B_{0.18}N_{0.86}(C_{0.16}O_{0.21}H_{0.55})$
BPSZ2-derived ceramic	68.50	2.56	23.00	0.84	3.36	1.36	10.51	$Si_{1.00}B_{0.10}N_{0.67}(C_{0.11}O_{0.04}H_{0.34})$

synthesis process. The loss of boron is discussed in terms of (i) the evaporation of BMS during the synthesis and drying process and (ii) borane did not react with PHPS stoichiometrically due to steric hindrance imposed by the polymer structure, which is in good agreement with the observation of Viard *et al.* [40]. The found amounts of carbon and oxygen are attributed to the residual solvent dibutyl ether and the water contamination during the elemental analysis. The elemental content of the ceramics will be discussed in Section 3.2.

3.2 Polymer-to-ceramic conversion

The polymer-to-ceramic transformation and ceramic yield of the single-source precursors BPSZ*X* were investigated via a combination of *ex situ* FTIR and *in situ* TGA/DTA measurements coupled with evolved gas analysis (EGA). As demonstrated in the TG curves (Fig. 3(a)), starting from room temperature to approximately 170 ℃, the dried PHPS shows a minor weight loss of 1 wt%, while the BPSZ5, BPSZ2, and BPSZ1 samples present obvious mass loss of 4, 3, and 8 wt%, respectively. Volatiles (*m/z* = 27–72) identified in the MS results (partly shown in Fig. 3(c) and Figs. S1(b) and S1(c) in the ESM) indicate that the mass loss of boron-modified BPSZ*X* samples is due to the volatilization and decomposition of low-molecular-weight oligomers, especially silane and solvent (dibutyl ether). In addition, the exothermic peak of BPSZ2 shown in

Fig. 3(b) indicates proceeding dehydrocoupling reactions between Si–H (N–H) and B–H groups, with the release of H_2 that has been detected with MS shown in Fig. 3(c). This assumption is further supported by the FTIR spectra of BPSZ2 shown in Fig. 4. The characteristic absorption bands of Si–H, N–H, and B–H groups decrease considerably, and the bands of C–H vibrations caused by the solvent disappear completely.

In the temperature range of 170–800 ℃, the dried PHPS shows a major weight loss of 22 wt%, where typical crosslinking reactions via dehydrocoupling and transamination take place, along with bond redistribution and thermal decomposition [43]. The weight loss is completed at ~800 ℃ with a ceramic yield of 77 wt%, which is in accordance with former reported data [44]. With the addition of boron, the weight loss of the precursor is significantly reduced from 23 wt% to at least 12 wt%. The second weight loss of BPSZ*X* samples occurs between 170 and ~600 ℃. Similar to the dried PHPS, crosslinking of residual Si–H, N–H, and B–H groups takes place through dehydrocoupling reactions, which is confirmed by the continuous release of H_2 detected by MS and supported by the corresponding *ex situ* FTIR spectra. However, due to the large consumption of N–H groups during the synthesis of the precursors, there is no obvious detection of NH_3 in the TGA/EGA experiment, indicating that only few transamination reactions occur. Thanks to the
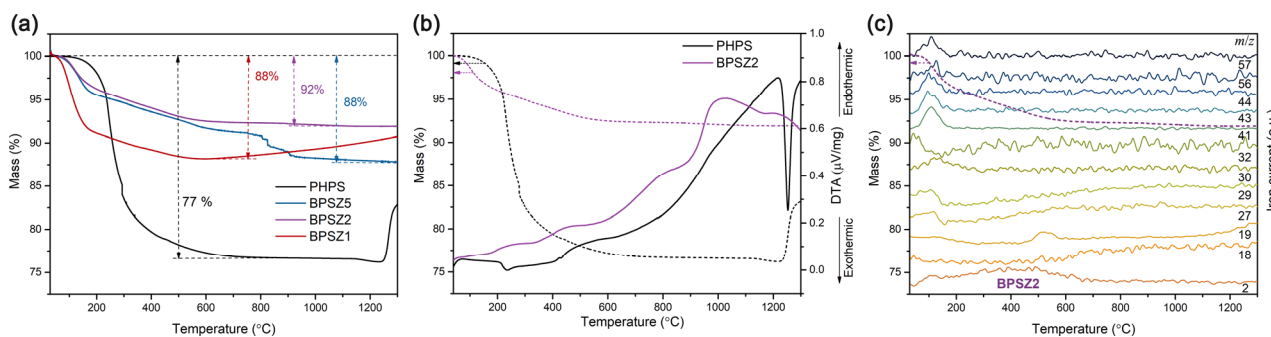
Fig. 3 (a) TG curves recorded for dried PHPS and BPSZ*X* (*X* = Si/B molar ratio) under N_2. (b) TG (dashed lines) and DTA (bold lines) curves of dried PHPS and BPSZ2 under N_2. (c) Ion current profiles (bold lines) of typical mass fragments during pyrolysis of BPSZ2 up to 1300 ℃ under N_2:hydrogen (*m/z* = 2), water (*m/z* = 18, 19), C_2H_3 (*m/z* = 27), SiH_4 (*m/z* = 29, 30, 32), amines (*m/z* = 41, 43, derivatives of Me_2NH), CO_2 (*m/z* = 44), C_4H_9 (*m/z* = 56, 57). Dashed line represents the corresponding TG curve.
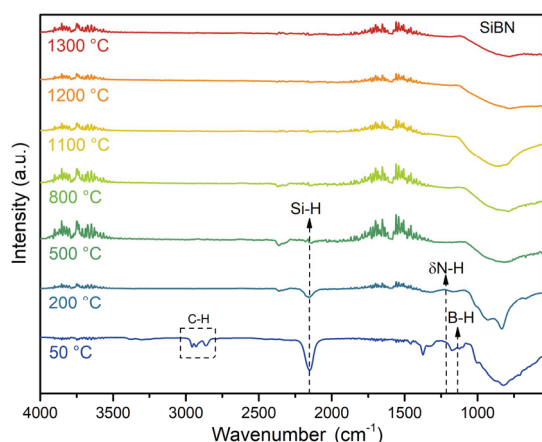
Fig. 4 FTIR spectra of BPSZ2 recorded at different temperatures.

high crosslinking degree of BPSZ*X* samples due to the incorporation of boron into PHPS, depolymerization and thermolysis at higher temperature are diminished. Therefore, a significantly increased ceramic yield is obtained with the boron-modified precursors.

Beyond 600 ℃, the thermal behavior of the BPSZ*X* samples with different Si/B molar ratio differs in the TGA measurements. The BPSZ2 sample exhibits the best thermal stability with a negligible mass loss and has a final ceramic yield of 92 wt% at 1300 ℃, indicating that the polymer-to-ceramic transformation has been already accomplished at ~600 ℃. The ceramization process is supported by the *ex situ* FTIR spectra (Fig. 4), where the absorption bands of Si–H and N–H almost completely vanish beyond 500 ℃. On this account, further investigations focus more on the BPSZ2 sample. With less boron content, the BPSZ5 sample goes through a sudden mass loss (3 wt%) between 800 and 930 ℃, which is attributed to the thermal decomposition of the preceramic polymer, as confirmed by the endothermic peak shown in the DTA curve (Fig. S1(a) in the ESM). Nevertheless, the ceramic yield of BPSZ5 is still higher than that of dried and pristine PHPS, and ends up as 88 wt% at 1300 ℃. With more boron incorporation, the BPSZ1 sample gains 3 wt% of mass between 600 and 1300 ℃, and has a final ceramic yield of ~91 wt%. The analyzed mass gain is ascribed to the reaction between residual boron and N₂ [45,46]. Additionally, the dried PHPS shows a mass gain of 6 wt% at ~1250 ℃ due to the crystallization process in N₂, which will be discussed in Section 3.3.

The chemical composition of the obtained BPSZ2-derived ceramic pyrolyzed at 1100 ℃ shown in Table 1

confirms the formation of SiBN ceramic. During the polymer-to-ceramic conversion, another fraction of boron is lost due to the further volatilization of borane species, resulting in a final Si/B molar ratio of 10.51. In addition, the elemental analysis of BPSZ-derived ceramics (Table 2) confirms the removal of carbon after annealing at 1300 ℃. In summary, compared with the former reported ceramic yield (~55 wt% [27], 72 wt% [32]) of SiBN ceramics obtained via other synthesis methods, higher ceramic yield was achieved with the current method (88–92 wt%).

3.3 Crystallization and microstructural evolution of the as-prepared ceramics

The structural evolution and crystallization behavior of annealed PHPS and BPSZ*X* samples have been investigated after heat treatment at various temperatures (1100, 1200, and 1300 ℃) by XRD, TEM, and EDX spectroscopy. The XRD patterns of the PHPS- and BPSZ*X*-derived ceramics obtained upon annealing at different temperatures are shown in Fig. 5. At 1100 ℃, all the as-prepared ceramics are predominantly X-ray amorphous. At 1200 ℃, the boron-free PHPS-derived specimen exhibits a low-intensity reflection of α-Si₃N₄, while all the BPSZ*X*-derived ceramics remain X-ray amorphous. As the annealing temperature further increases to 1300 ℃, crystallization of α-Si₃N₄ is induced in the annealed PHPS sample. According to the weight gain (6 wt%) presented in the TG curve and the exothermal peak shown in the DTA curve (Fig. 3(b)), the crystallization temperature of PHPS-derived ceramic is suggested to be in the range of 1200–1300 ℃ [47]. In the meantime, as the boron content increases in the BPSZ*X* samples, the emergence of α-Si₃N₄ is hindered. The crystallization of BPSZ5- and BPSZ2-derived ceramics gradually takes place at temperature up to 1300 ℃, while the XRD pattern of the BPSZ1-derived ceramic is still X-ray amorphous. These results clearly demonstrate that the incorporation of boron into Si–N network suppresses the crystallization of Si₃N₄, which is attributed to the higher crystallization temperature of the formed ternary Si–B–N system, and which thereby restricts the crystallization of both Si₃N₄ and BN [15,48].

**Table 2　Carbon content of BPSZ1-, BPSZ2-, and BPSZ5-derived ceramics (annealed at 1300 ℃)**

Sample	BPSZ1-derived ceramic	BPSZ2-derived ceramic	BPSZ5-derived ceramic
Carbon content (wt%)	0.35	0.49	0.24
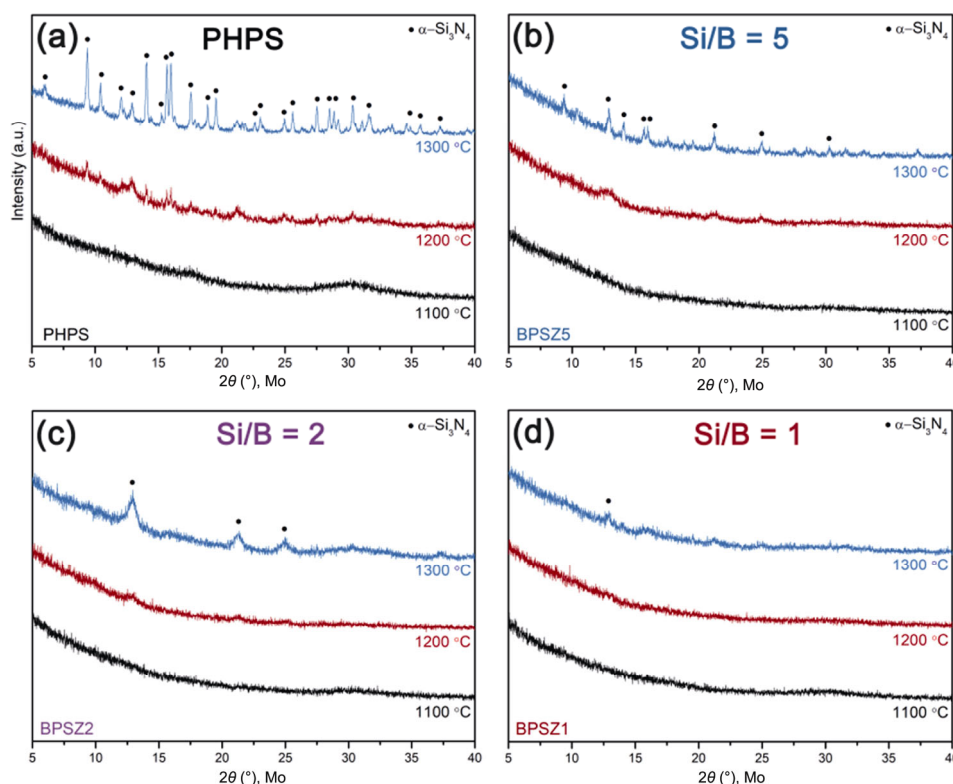
Fig. 5 XRD patterns of the as-pyrolyzed (a) PHPS and (b–d) BPSZ*X* (*X* = Si/B molar ratio) samples annealed at different temperatures. All samples annealed at 1100 ℃ are X-ray amorphous. The PHPS-derived ceramic starts to crystallize upon 1200 ℃, while the boron-modified BPSZ*X* samples remain X-ray amorphous. Along with the increase of the boron content (from b to d), the crystallization of BPSZ*X* samples is suppressed.

The microstructure of the as-prepared PHPS and BPSZ2-derived ceramics annealed at 1300 ℃ were further investigated by TEM along with the selected area electron diffraction (SAED) pattern, SEM, and EDX spectroscopy. As shown in Fig. 6(a), the high-resolution TEM (HRTEM) image of the annealed PHPS-derived ceramic exhibits a typical nanocrystalline structure with a lattice spacing of 0.21 nm, which corresponds to the *d*-spacing of the (202) α-Si$_3$N$_4$ lattice plane (JPCDS

Card No. 09-0250). Furthermore, the SAED pattern (inset in Fig. 6(a)) presents diffraction spots of α-Si$_3$N$_4$ crystals, which agrees with the XRD results (Fig. 5). As revealed by Fig. 6(b), both the TEM image and the SAED pattern affirm that the as-prepared BPSZ2-derived ceramic remains amorphous, which is consistent with the results obtained from the XRD as well. The SEM micrograph (Fig. 7(a)) of BPSZ2-derived ceramic annealed at 1300 ℃ shows a dense structure. As can be
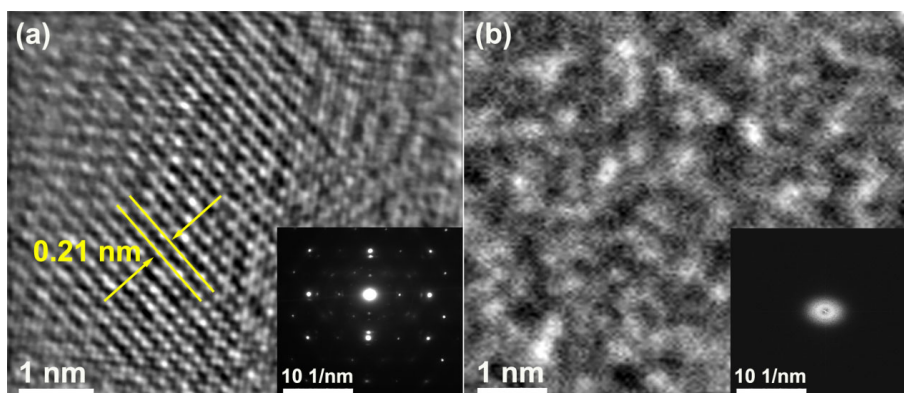
Fig. 6 Filtered HRTEM images of (a) PHPS- and (b) BPSZ2-derived ceramics annealed at 1300 ℃. Insets are the corresponding SAED patterns.
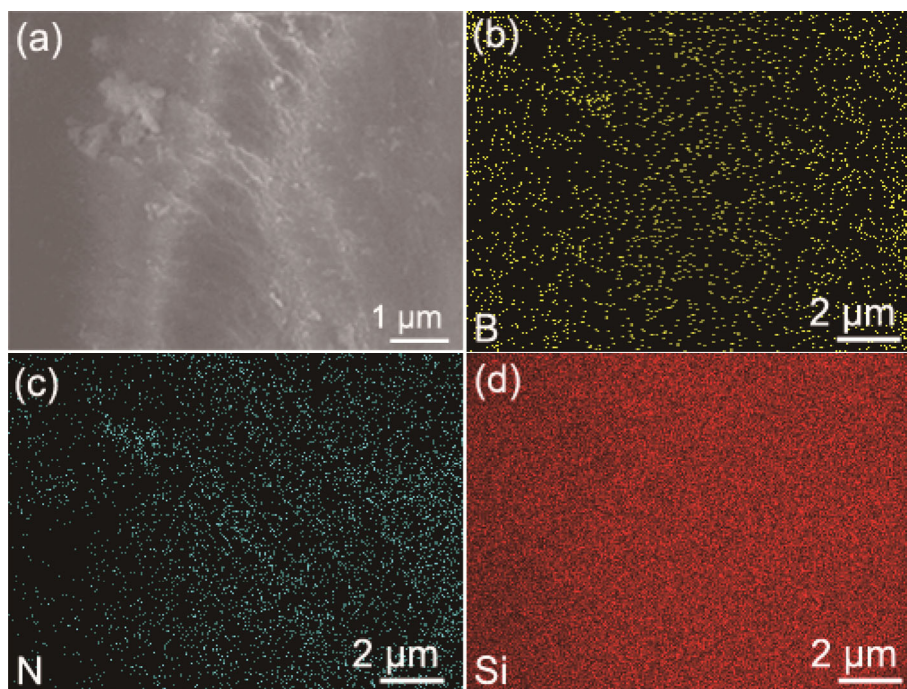
**Fig. 7**   SEM graph and elemental mappings of the BPSZ2-derived ceramic prepared with a Si/B ratio of 2:1 and annealed at 1300 ℃, indicating a dense SiBN ceramic structure with homogeneous Si, B, and N elemental distributions.

seen from the corresponding elemental mapping (obtained from EDX) displayed in Figs. 7(b)–7(d), Si, B, and N elements are distributed homogenously in the amorphous structure with no obvious agglomeration being observed.

3. 4   Molecular dynamics simulations

According to previous theoretical calculation studies [16,36,49], boron incorporation has a significant influence on the crosslinking and pyrolysis processes of Si–N networks. Short-range atomic arrangements are characterized by total and partial pair distribution functions (PDF) of amorphous Si_3N_4 and SiBN ceramics with different boron content. As shown in Figs. 8(a) and 8(b), all PDFs converge to a constant value of 1 for radii larger than 0.5 nm, indicating long-range amorphous disorder in the ceramics. As shown in Fig. 8(b), the first peak of SiBN ceramics at a distance of 0.149 nm is not only closer than that of any other pair, but also much higher. It corresponds to B–N distances and indicates the strong bonding between these elements. This characteristic distance is in good agreement with the range of B–N bond lengths obtained from experiments and density functional theory calculations
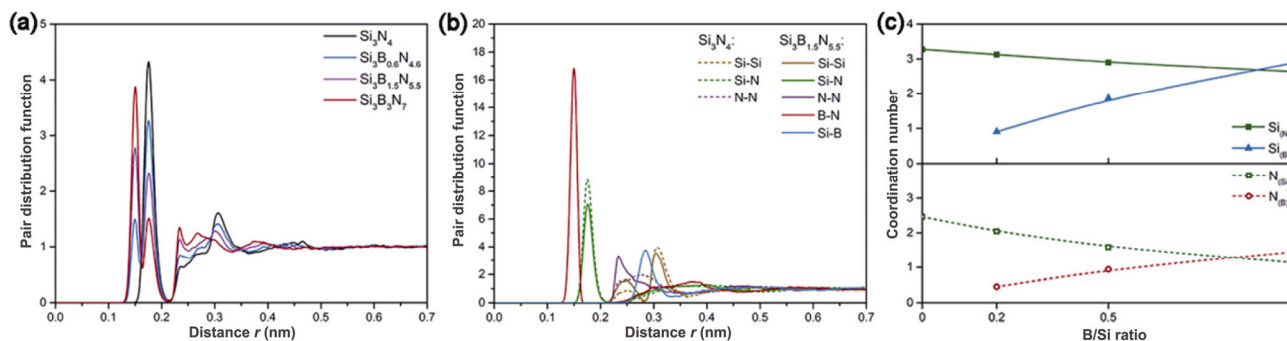
Fig. 8   (a) Total pair distribution functions for amorphous ceramics Si_3N_4 (black), $Si_3B_{0.6}N_{4.6}$ (blue), $Si_3B_{1.5}N_{5.5}$ (purple), and $Si_3B_3N_7$ (red); (b) partial pair distribution functions calculated from Si_3N_4 (dashed lines) and $Si_3B_{1.5}N_{5.5}$ (solid lines) for Si–Si, Si–N, N–N, B–N, and Si–B pairs; (c) coordination numbers as a function of B/Si ratio for center atoms of Si (top) surrounded by N atoms and B atoms, and N (bottom) surrounded by Si atoms and B atoms.

(0.144–0.156 nm) [50,51]. Moreover, the height of this peak increases with boron content, suggesting that more boron atoms surrounding any given nitrogen atom. Sharp peaks at a distance of ~0.17 nm are seen in the total PDFs for all investigated ceramics, which are due to Si–N pairs in the partial PDFs. The Si–N bond length is found here to be roughly 0.17 nm, which is similar to the value estimated from experiments (0.173–0.175 nm) [52–54]. In addition, peak for Si–B pairs (~0.28 nm) has a much lower height than that for Si–N or B–N observed in the partial PDFs of SiBN ceramics, suggesting that the formation of Si–B bonds is disfavored.

From the PDFs, the coordination numbers have been calculated. In Fig. 8(c), the coordination numbers of central Si and N atoms are shown as a function of the B/Si atomic ratio. The coordination number of Si surrounded by B (Si–B) increases as the B/Si atomic ratio increases, which implies that the Si–B bonds are more likely to form when more boron atoms are added. In the meantime, the coordination number of $Si_{(N)}$ (Si–N) slightly decreases. On the other hand, the coordination number of $N_{(Si)}$ (N–Si) decreases rapidly as B/Si atomic ratio increases, while the coordination number of $N_{(B)}$ (N–B)

increases, indicating that the boron incorporation influences more on the N atoms than Si atoms.

The atomic mobility was also investigated in amorphous silicon nitride and various SiBN ceramics. The obtained mean-square displacements (MSDs) of Si, N, and B atoms are shown in Figs. 9(a)–9(c), respectively. The MSDs of Si are similar in all investigated ceramics, indicating a minor influence of boron incorporation on the Si diffusivity. In contrast, the MSDs of N in all SiBN ceramics are lower than that in Si_3N_4, and they decrease further with increasing boron content. This suggests that the incorporation of boron into the Si–N network restricts the atomic motion of both boron and nitrogen in the Si–B–N systems because of the formation of B–N bonds. These B–N bonds are not only copious (cf. Fig. 8), but also strong, and the system stability is hence improved.

From the limiting slopes of MSD curves, the atomic self-diffusion coefficients have been evaluated using the Einstein relation (Eq. (4)) [55]. For each element, its slope has been obtained from a linear part of the respective MSD within the time period of 900–1100 ps. As shown in Fig. 9(d), the self-diffusion coefficient of silicon is basically unaffected by the boron concentration
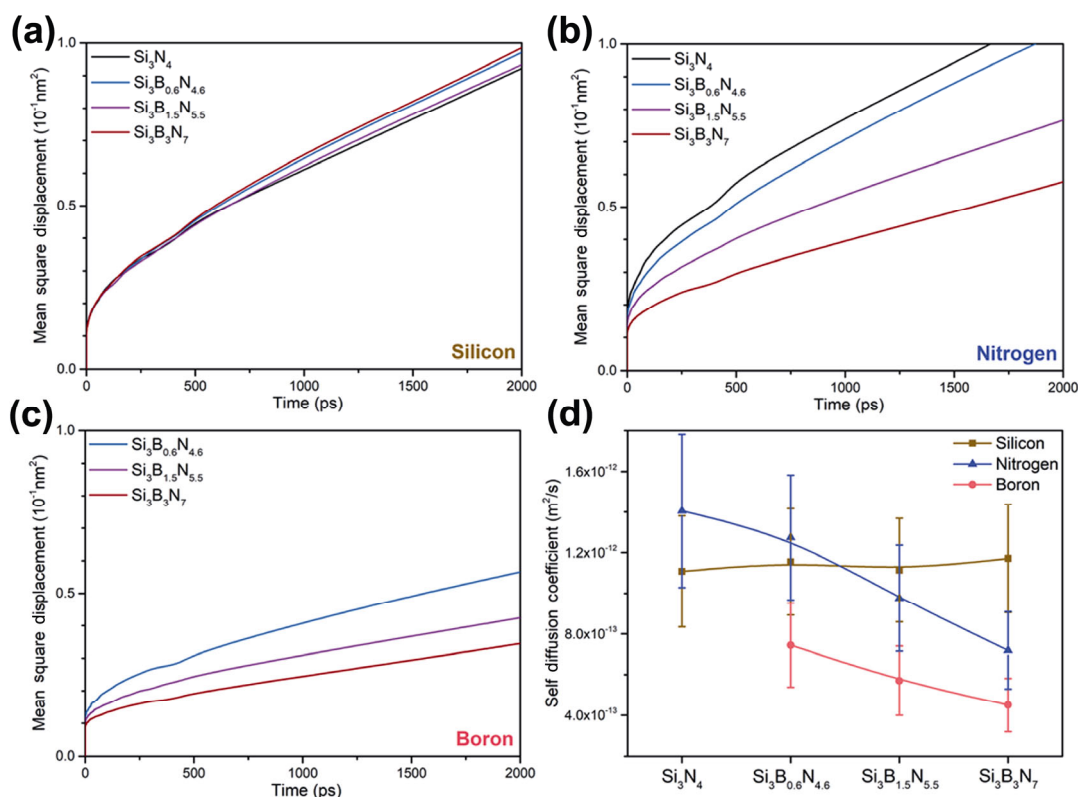

Fig. 9 Mean-square displacement curves of (a) silicon, (b) nitrogen, and (c) boron atoms, and (d) corresponding atomic self-diffusion coefficients in SiBN ceramics with different elemental compositions at 1300 ℃.

within the margin of error. In contrast, the atomic diffusion coefficients of nitrogen and boron decrease significantly with increasing boron content, consistent with the formation of B–N bonds as seen in the peaks of B–N pairs in the pair distribution functions (Fig. 8). This is due to the strong mutual attraction of B and N, which in the Tersoff potential is much stronger than Si–B and B–B interactions. Furthermore, the presence of B–N bonds prevents N atoms from diffusing in the Si–B–N network and plays the part of rigid linkages. This impedes the formation of crystallites even at high temperatures. Similar behaviors are also found in the relaxation properties such as Van-Hove correlation functions and intermediate scattering functions in the ceramics with different boron contents. Detailed discussion can be found in the ESM. In conclusion, the addition of boron enables the formation of rigid B–N bonds and consequently reduces the atomic diffusivity of nitrogen atom in the network, and therefore, the thermal stability of amorphous Si–B–N is considerably enhanced relative to amorphous Si–N.
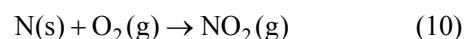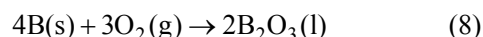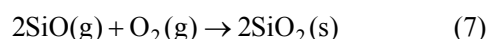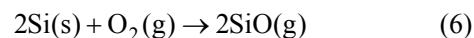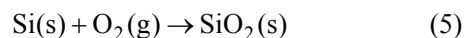
3. 5   Oxidation behavior

The BPSZ*X*-derived ceramics were annealed at 1300 ℃ and oxidized in air at a temperature up to 1350 ℃. The oxidation resistance of the corresponding ceramics was studied by the TG curves shown in Fig. 10, in which the triangle markers represent the amorphous silicon nitride data extracted from the work of Ma *et al.* [56]. Starting from 30 to 1000 ℃, the amorphous silicon nitride exhibits a significant weight gain of 25.7 wt%.
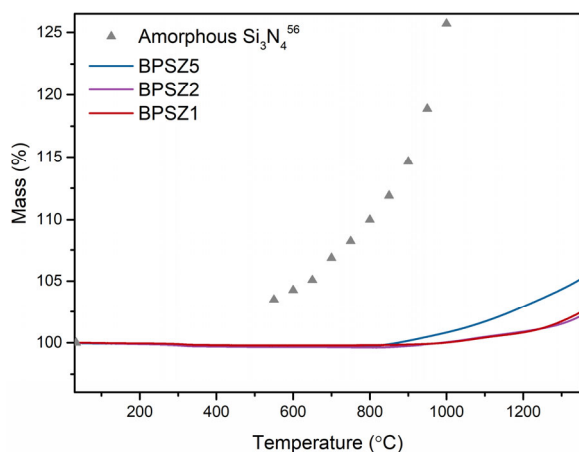
Fig. 10   TG curves of the as-prepared BPSZ*X*-derived ceramics (annealed at 1300 ℃) performed within a temperature range from ambient temperature to 1350 ℃ in air. TG data points of amorphous silicon nitride are extracted from the work of Ma *et al.* [56].

It is well documented in the literature that large numbers of unsaturated Si–N and Si dangling bonds in amorphous silicon nitride, such as Si dangling bonds and N vacancies, lead to severe vacancy oxidation (nitrogen vacancies occupied by oxygen atoms) and replacement oxidation (nitrogen atoms being replaced by oxygen atoms) [56,57]. In contrast, amorphous BPSZ5-derived ceramic displays negligible weight gain of 0.8 wt%, and the BPSZ2-, and BPSZ1-derived ceramics present no weight change at the temperature of 1000 ℃. Moreover, by oxidation at 1350 ℃, the BPSZ5-, BPSZ2-, and BPSZ1-derived amorphous ceramics yield mass gains of 5.1, 2.1, and 2.4 wt%, respectively, indicating improved oxidation resistance if compared with amorphous silicon nitride. As afore-mentioned, the presence of B atoms in amorphous Si–N networks not only occupies part of the unsaturated spaces, but also promotes the formation of B–N rigid linkages, resulting in superior oxidation resistance compared to amorphous silicon nitride. The proposed oxidation mechanisms of SiBN ceramics are illustrated in Eqs. (5)–(10) [58,59], which are suggested to be responsible for the weight gains between 1000 and 1350 ℃. Due to the formation of B_2O_3 in the silica, boron silicate glass is formed, which limits the O_2 inward diffusion and further B_2O_3 volatilization. Furthermore, as reported by former research studies [60,61], with the addition of boron, a dual surface layer of B–N–O/SiO_2 is formed during oxidation to protect the ceramic from further oxidation, and hence increases the oxidation resistance.

$$Si(s) + O_2(g) \rightarrow SiO_2(s) \qquad (5)$$

$$2Si(s) + O_2(g) \rightarrow 2SiO(g) \qquad (6)$$

$$2SiO(g) + O_2(g) \rightarrow 2SiO_2(s) \qquad (7)$$

$$4B(s) + 3O_2(g) \rightarrow 2B_2O_3(l) \qquad (8)$$

$$2N(s) + O_2(g) \rightarrow 2NO(g) \qquad (9)$$

$$N(s) + O_2(g) \rightarrow NO_2(g) \qquad (10)$$

4   Conclusions

In the present work, ternary SiBN ceramics with different Si/B molar ratios have been successfully prepared via the PDC route starting from carbon- and chlorine-free single-source precursors, synthesized by modifying perhydropolysilazane (PHPS) with borane dimethyl sulfide complex (BMS). It has been proved

that both Si–H and N–H bonds of the PHPS react with B–H bonds of BMS through dehydrocoupling reaction during the synthesis of the BPSZ*X* precursors. The precursor-to-ceramic transformation was investigated systematically with respect to crosslinking and crystallization. The TGA and FTIR results reveal that incorporation of boron considerably improves the crosslinking degree of the preceramic polymer, and consequently, the ceramic yield increases from 77 wt% (PHPS) to 88–92 wt% (BPSZ*X*) upon pyrolysis under N_2 atmosphere. Besides, without employing the costly ammonia, our reported method proves itself to be a facile and economic method for the synthesis of SiBN ceramic with high ceramic yield as opposed to former reported ammonolysis synthesis process. Furthermore, the resultant BPSZ*X*-derived ceramics are shown to possess remarkable resistance against crystallization in comparison to PHPS-derived boron-free Si_3N_4 ceramics. This characteristic is ascribed to the decreased self-diffusion coefficient of nitrogen in the ternary ceramic, due to the formation of rigid B–N bonds in the Si–B–N network. In conclusion, the boron modification of Si–N via the PDC route presents a significant effect on its high-temperature resistance behavior with respect to crystallization and oxidation, which is of great significance for the design and manufacture of ternary Si-based and/or boron-containing ceramics.

The influence of boron on the phase evolution, mechanical and functional properties of SiBN ceramics, such as Young's modulus, hardness, high-temperature self-healing capability, thermal and electrical conductivities, as well as the related applications have not been clarified unambiguously so far, and will be investigated in future studies.

Acknowledgements

Declaration of competing interest

The authors have no competing interests to declare that are relevant to the content of this article.

Electronic Supplementary Material

Supplementary material is available in the online version of this article at https://doi.org/10.1007/s40145-022-0597-z.

References

[1] Riedel R, Kienzle A, Dressler W, *et al*. A silicoboron carbonitride ceramic stable to 2,000 ℃. *Nature* 1996, **382**: 796–798.

[2] Riley FL. Silicon nitride and related materials. *J Am Ceram Soc* 2000, **83**: 245–265.

[3] Bocanegra-Bernal MH, Matovic B. Mechanical properties of silicon nitride-based ceramics and its use in structural applications at high temperatures. *Mater Sci Eng A* 2010, **527**: 1314–1338.

[4] Ionescu E, Kleebe H-J, Riedel R. Silicon-containing polymer-derived ceramic nanocomposites (PDC-NCs): Preparative approaches and properties. *Chem Soc Rev* 2012, **41**: 5032−5052.

[5] Eichler J, Lesniak C. Boron nitride (BN) and BN composites for high-temperature applications. *J Eur Ceram Soc* 2008, **28**: 1105–1109.

[6] Zhou Y, Hyuga H, Kusano D, *et al*. Development of high-thermal-conductivity silicon nitride ceramics. *J Asian Ceram Soc* 2015, **3**: 221–229.

[7] Colombo P, Mera G, Riedel R, *et al*. Polymer-derived ceramics: 40 years of research and innovation in advanced ceramics. *J Am Ceram Soc* 2010, **93**: 1805–1837.

[8] Mukhopadhyay A, Basu B. Consolidation-microstructure-property relationships in bulk nanoceramics and ceramic nanocomposites: A review. *Int Mater Rev* 2007, **52**: 257–288.

[9] Sommers A, Wang Q, Han X, *et al*. Ceramics and ceramic matrix composites for heat exchangers in advanced thermal systems—A review. *Appl Therm Eng* 2010, **30**: 1277–1291.

[10] Wang H, Singh RN. Thermal shock behaviour of ceramics and ceramic composites. *Int Mater Rev* 1994, **39**: 228–244.

[11] Riedel R, Ruswisch LM, An LN, *et al*. Amorphous silicoboron carbonitride ceramic with very high viscosity at temperatures above 1500 ℃. *J Am Ceram Soc* 1998, **81**: 3341–3344.

[12] Wang ZC, Aldinger F, Riedel R. Novel silicon-boron-carbon-nitrogen materials thermally stable up to 2200 ℃. *J Am Ceram Soc* 2001, **84**: 2179–2183.

[13] Wan JL, Duan RG, Gasch MJ, *et al*. Highly creep-resistant silicon nitride/silicon carbide nano-nano composites. *J Am Ceram Soc* 2006, **89**: 274–280.

[14] Ge KK, Ye L, Han WJ, *et al*. Pyrolysis of polyborosilazane and its conversion into SiBN ceramic. *Adv Appl Ceram* 2014, **113**: 367–371.

[15] Zhou C, Gao X, Xu Y, *et al*. Synthesis and high-temperature

evolution of single-phase amorphous Si–Hf–N ceramics. *J Eur Ceram Soc* 2015, **35**: 2007–2015.

[16] Liao NB, Xue W, Zhang M. Molecular dynamics investigation of Si–B–N ceramics: Effects of boron content. *Model Simul Mat Sci Eng* 2012, **20**: 035009.

[17] Yu ZJ, Yang YJ, Mao KW, *et al.* Single-source-precursor synthesis and phase evolution of SiC–TaC–C ceramic nanocomposites containing core–shell structured TaC@C nanoparticles. *J Adv Ceram* 2020, **9**: 320–328.

[18] Wen QB, Xu YP, Xu BB, *et al.* Single-source-precursor synthesis of dense SiC/HfC$_x$N$_{1-x}$-based ultrahigh-temperature ceramic nanocomposites. *Nanoscale* 2014, **6**: 13678–13689.

[19] Ionescu E, Bernard S, Lucas R, *et al.* Polymer-derived ultra-high temperature ceramics (UHTCs) and related materials. *Adv Eng Mater* 2019, **21**: 1900269.

[20] Liu XM, Yu ZJ, Ishikawa R, *et al.* Single-source-precursor derived RGO/CNTs–SiCN ceramic nanocomposite with ultra-high electromagnetic shielding effectiveness. *Acta Mater* 2017, **130**: 83–93.

[21] Wen QB, Yu ZJ, Riedel R. The fate and role of *in situ* formed carbon in polymer-derived ceramics. *Prog Mater Sci* 2020, **109**: 100623.

[22] Yu ZJ, Lv X, Lai SY, *et al.* ZrC–ZrB$_2$–SiC ceramic nanocomposites derived from a novel single-source precursor with high ceramic yield. *J Adv Ceram* 2019, **8**: 112–120.

[23] Yu ZJ, Lv X, Mao KW, *et al.* Role of *in situ* formed free carbon on electromagnetic absorption properties of polymer-derived SiC ceramics. *J Adv Ceram* 2020, **9**: 617–628.

[24] Jin SY, Guo KK, Qi HM, *et al.* High yield polyborosilazane precursor for SiBN ceramics. *Adv Mater Res* 2014, **1004–1005**: 409–414.

[25] Li WH, Wang J, Xie ZF, *et al.* Preparation of hollow Si–B–N ceramic fibers by partial curing and pyrolysis of polyborosilazane fibers. *Mater Lett* 2012, **78**: 1–3.

[26] Liu Y, Chen KZ, Dong FB, *et al.* Effects of hydrolysis of precursor on the structures and properties of polymer-derived SiBN ceramic fibers. *Ceram Int* 2018, **44**: 10199–10203.

[27] Liu Y, Peng S, Cui YJ, *et al.* Fabrication and properties of precursor-derived SiBN ternary ceramic fibers. *Mater Des* 2017, **128**: 150–156.

[28] Long X, Shao CW, Wang YD. Effects of boron content on the microwave-transparent property and high-temperature stability of continuous SiBN fibers. *J Am Ceram Soc* 2020, **103**: 4436–4444.

[29] Baldus P, Jansen M, Sporn D. Ceramic fibers for matrix composites in high-temperature engine applications. *Science* 1999, **285**: 699–703.

[30] Baldus H-P, Jansen M. Novel high-performance ceramics—Amorphous inorganic networks from molecular precursors. *Angew Chem Int Ed Engl* 1997, **36**: 328–343.

[31] Baldus H-P, Wagner O, Jansen M. Synthesis of advanced ceramics in the systems Si–B–N and Si–B–N–C employing novel precursor compounds. *MRS Proceedings* 1992, **271**: 821.

[32] Zhao X, Han KQ, Peng YQ, *et al.* A novel precursor route for the production of Si–B–N ceramic fibers. *Mater Lett* 2011, **65**: 2717–2720.

[33] Kilaas R. Optimal and near-optimal filters in high-resolution electron microscopy. *J Microsc* 1998, **190**: 45–51.

[34] LAMMPS molecular dynamics simulator. Available at https://www.lammps.org/.

[35] Tersoff J. New empirical approach for the structure and energy of covalent systems. *Phys Rev B* 1988, **37**: 6991.

[36] Matsunaga K, Iwamoto Y. Molecular dynamics study of atomic structure and diffusion behavior in amorphous silicon nitride containing boron. *J Am Ceram Soc* 2001, **84**: 2213–2219.

[37] Guraya MM, Ascolani H, Zampieri G, *et al.* Bond densities and electronic structure of amorphous SiN$_x$:H. *Phys Rev B* 1990, **42**: 5677.

[38] Nosé S. A unified formulation of the constant temperature molecular dynamics methods. *J Chem Phys* 1984, **81**: 511–519.

[39] Hoover WG. Canonical dynamics: Equilibrium phase-space distributions. *Phys Rev A* 1985, **31**: 1695.

[40] Viard A, Fonblanc D, Schmidt M, *et al.* Molecular chemistry and engineering of boron-modified polyorganosilazanes as new processable and functional SiBCN precursors. *Chem Eur J* 2017, **23**: 9076.

[41] Masuda T, Nakayama M, Saito K, *et al.* A cyclopentasilane-borane compound as a liquid precursor for p-type semiconducting Si. *J Mater Chem C* 2021, **9**: 5387–5395.

[42] Hapke J, Ziegler G. Synthesis and pyrolysis of liquid organometallic precursors for advanced Si–Ti–C–N composites. *Adv Mater* 1995, **7**: 380–384.

[43] Colombo P, Riedel R, Sorarù GD, *et al. Polymer Derived Ceramics: From Nano-Structure to Applications*. Lancaster, USA: DEStech Publications, Inc, 2010.

[44] Ma FL, Qi HM, Zhu YP, *et al.* Thermal cure and ceramization kinetics of perhydropolysilazane. *Key Eng Mater* 2013, **575–576**: 81–86.

[45] Condon JB, Holcombe CE, Johnson DH, *et al.* The kinetics of the boron plus nitrogen reaction. *Inorg Chem* 1976, **15**: 2173–2179.

[46] Baik S, Suh BL, Byeon A, *et al. In-situ* boron and nitrogen doping in flue gas derived carbon materials for enhanced oxygen reduction reaction. *J CO$_2$ Util* 2017, **20**: 73–80.

[47] Sorarù GD, Ravagni A, dal Maschio R, *et al.* Polymer-derived Si$_3$N$_4$–ZrO$_2$ nanocomposite powders. *J Mater Res* 1992, **7**: 1266–1270.

[48] Toury B, Cornu D, Chassagneux F, *et al.* Complete characterisation of BN fibres obtained from a new polyborylborazine. *J Eur Ceram Soc* 2005, **25**: 137–141.

[49] Zhang M, Liao NB, Xue W, *et al.* Large-scale molecular dynamics modeling of boron-doped amorphous SiCO ceramics. *J Mol Model* 2017, **23**: 178.

[50] Jin CH, Lin F, Suenaga K, *et al.* Fabrication of a freestanding boron nitride single layer and its defect assignments. *Phys Rev Lett* 2009, **102**: 195505.

[51] Andriotis AN, Richter E, Menon M. Prediction of a new graphenelike Si_2BN solid. *Phys Rev B* 2016, **93**: 081413.

[52] Aiyama T, Fukunaga T, Niihara K, *et al*. An X-ray diffraction study of the amorphous structure of chemically vapor-deposited silicon nitride. *J Non Cryst Solids* 1979, **33**: 131–139.

[53] Ténégal F, Flank AM, Cauchetier M, *et al*. Nanometric Si/C/N powders: Description of the short range atomic structure by X-ray absorption spectroscopy. *Nucl Instrum Methods Phys Res B* 1997, **133**: 77–83.

[54] M Hagenmayer R, Müller U, J Benmore C, *et al*. Structural studies on amorphous silicon boron nitride $Si_3B_3N_7$: Neutron contrast technique on nitrogen and high energy X-ray diffraction. *J Mater Chem* 1999, **9**: 2865–2869.

[55] Einstein A. On the movement of small particles suspended in stationary liquids required by the molecular kinetic theory of heat. *Ann Phys* 1905, **17**: 549–560.

[56] Ma DH, Wang HJ, Niu M, *et al*. Oxidation behavior of amorphous silicon nitride nanoparticles. *Ceram Int* 2018, **44**: 1443–1447.

[57] Zhang LD, Mo CM, Wang T, *et al*. Structure and bond properties of compacted and heat-treated silicon nitride particles. *phys stat sol* (*a*) 1993, **136**: 291–300.

[58] Li DX, Yang ZH, Jia DC, *et al*. High-temperature oxidation resistance of dense amorphous boron-rich SiBCN monoliths. *Corros Sci* 2019, **157**: 312–323.

[59] Dai J, Zhang Y, Gao D, *et al*. Oxidation behavior of amorphous Si–(B)–C–N ceramic in ambient air. *Rare Metal* 2011, **30**: 557–562.

[60] Braue W, Paul G, Baldus HP. Microstructural response of $SiBN_3C$-fibers upon annealing in oxidizing and reducing atmospheres. In: *High Temperature Ceramic Matrix Composites*. Krenkel W, Naslain R, Schneider H, Eds. Germany: Wiley-VCH, 2001: 96–98.

[61] Cinibulk MK, Parthasarathy TA. Characterization of oxidized polymer-derived SiBCN fibers. *J Am Ceram Soc* 2001, **84**: 2197–2202.

Boron-Modified Perhydropolysilazane Towards Facile Synthesis of Amorphous SiBN Ceramic with Excellent Thermal Stability

Ying Zhan [a, §], Wei Li [a, §], Tianshu Jiang [a], Claudia Fasel [a], Emmanuel III Ricohermoso [a], Jan Bernauer [a], Zhaoju Yu [b, *], Zhenghao Wu [c, *], Florian Müller-Plathe [c], Leopoldo Molina-Luna [a], Ralf Grottenmüller [d], Ralf Riedel [a]

a. Department of Materials and Earth Sciences, Technical University of Darmstadt, D-64287 Darmstadt, Germany

b. College of Materials, Key Laboratory of High Performance Ceramic Fibers (Xiamen University), Ministry of Education, Xiamen 361005, China

c. Eduard-Zintl-Institut für Anorganische und Physikalische Chemie, Technical University of Darmstadt, D-64287 Darmstadt, Germany

d. Merck KGaA, Performance Materials, D-64293, Darmstadt, Germany

§. These authors contributed equally to this work.

*. Corresponding authors: zhaojuyu@xmu.edu.cn (Z. Yu), z.wu@theo.chemie.tu-darmstadt.de (Z. Wu)
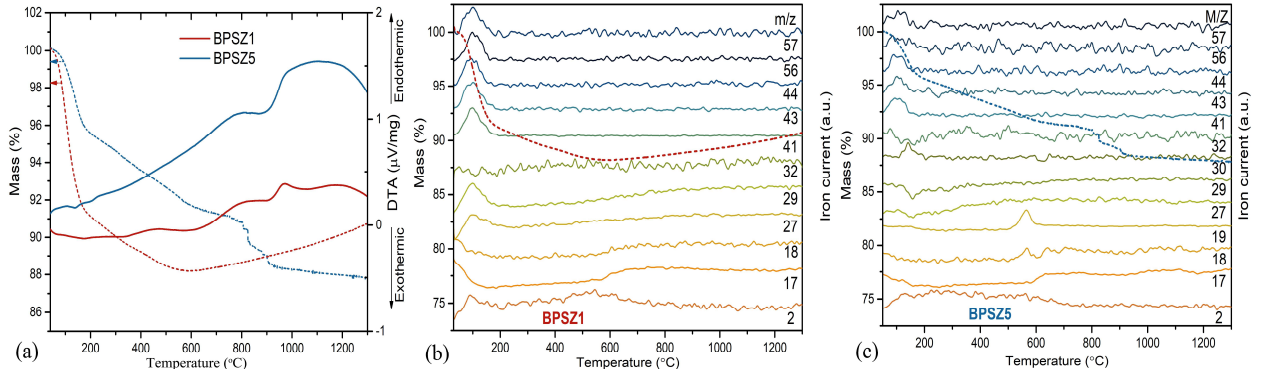
1. Polymer-to-ceramic Conversion

Fig. S1 (a) TG (dashed lines) and DTA (bold lines) curves recorded for BPSZ1 and BPSZ5 under N_2, and typical mass fragment profiles of evolved gases during pyrolysis of BPSZ1 (b) and BPSZ5 (c) up to 1570 K under N_2: hydrogen (m/z = 2), NH_3 (m/z = 17), water (m/z = 18, 19), C_2H_3 (m/z = 27), SiH_4 (m/z = 29, 30, 32), amines (m/z = 41, 43), CO_2 (m/z = 44), C_4H_9 (m/z = 56, 57).

2. Molecular Dynamics Simulations

2.1 System Information

Table S1 Simulation Details [1]

System	N_{Si}	N_N	N_B	Box Size
Si_3N_4	3000	4000	0	45.25
$Si_3B_{0.6}N_{4.6}$	3000	4600	600	46.80
$Si_3B_{1.5}N_{5.5}$	3000	5500	1500	48.94
$Si_3B_3N_7$	3000	7000	3000	52.15

N_{Si}: number of Si atoms; N_N: number of N atoms; N_B: number of B atoms.
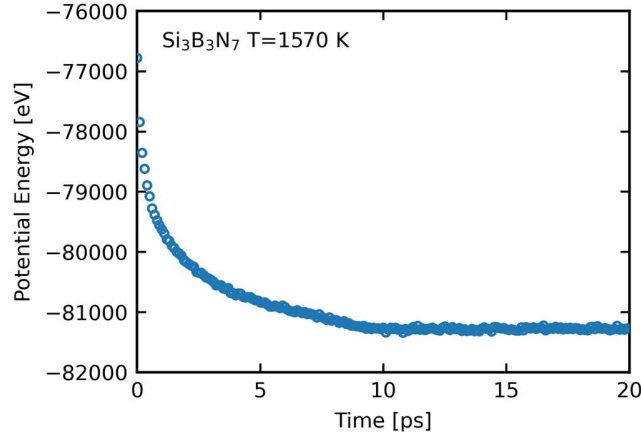
2.2 Equilibration of the System

Fig. S2 Total potential energy of an example system $Si_3B_3N_7$ as a function of time during the equilibration step at temperature $T = 1570$ K

2.3 Self-part van-Hove Correlation Functions

The self-part of the van-Hove Correlation functions $G_{self}(r, \Delta t)$ are computed to measure the probability density that a particle moves a distance r within a time interval Δt [2]:

$$G_{self}(r, \Delta t) = \frac{1}{N} \sum_{i=1}^{N} \delta[r + r_i(t_0) - r_i(t_0 + \Delta t)]$$

where $r_i(t_0)$ is the position of the particle i at time t_0 and r is the position in the space. The space integral of $G_{self}(r, \Delta t)$ is a conserved quantity. Thus, we plot $4\pi r^2 G_{self}(r, \Delta t)$ as a function of distance at several distinct time interval for Si, N and B atoms of ceramics with different boron contents in Fig. S3. Generally, the behavior of $4\pi r^2 G_{self}(r, \Delta t)$ for all studied species of systems is consistent with that of the liquid state [1, 3-4]. Specifically, all curves show a Gaussian-like shape, especially for

those at short times. However, a pronounced tail can be found in those at long times, e.g., $t = 2073.83$ ps, the behavior of which is also seen in super-cooled liquids [4]. As seen in Fig. S3 (a), with increasing the boron concentration, the curves of $4\pi r^2 G_{self}(r, \Delta t)$ are almost unaffected at all time intervals studied in this work. By contrast, the boron concentration does impose obvious influences on the van-Hove correlation functions for N and B at both short and long-time intervals. The probability to find both N and B at the same distance r becomes higher as increasing the boron concentration at all times. This behavior probably suggests that the addition of boron atoms enhances the stability of N and B atoms in SiBN ceramics.

2.4 Self-part Intermediate Scattering Functions

Translational dynamics is characterized via the self-part intermediate scattering functions, where q is the wave vector, $r_j(t_0)$ is the position of the particle j at time t, and N is the number of particles for analysis; The wavenumber q ≈ 2.39 is employed for calculating the wave vectors, which is comparable to the first local peak in the structure factor (An example plots from $Si_3B_3N_7$ shown in Fig. S4). The self-part intermediate scattering function F_{self} is corresponding to time-resolved incoherent neutron scattering results. We employ a double stretched exponential equation to fit the $F_{self,q}(t)$ data:

$$F_{self,q}(t) = Aexp\left[-(\frac{t}{\tau_f})^{\beta_f} + Bexp(-(\frac{t}{\tau_s})^{\beta_s})\right]$$

where the first and second terms are associated with the fast beta and slow alpha relaxation processes for the super-cooled liquids. In this equation, A and B represent the contributions from respective processes; Relaxation times τ_f and τ_s are the characteristic relaxation times for the short and long relaxation times, respectively, and β_f and β_s are

the stretched exponents. Here, we define the relaxation time for a specific type of atoms using the long characteristic time τ_s. The $F_{self,q}(t)$ and relaxation times of atoms Si, B and N from ceramics with different boron contents are depicted in Figure S5. Firstly, all $F_{self,q}(t)$ have well-developed two regimes corresponding to aforementioned fast beta ($0 \sim 10^{-1}$ ps) and slow alpha ($10^{-1} \sim 10^5$ ps) relaxation processes for the amorphous. Specifically, it is observed that the $F_{self,q}(t)$ for Si atoms (Figure S5a) is barely affected by the content of the boron atoms, consistent with the behavior of relaxation times in Figure S5d. In contrast, the $F_{self,q}(t)$ of N and B (Fig. S5 b and c) is obviously influenced by the content of boron atoms. The relaxation times of N and B atoms increase as increasing the boron content. The relative increase of the relaxation times of N and B atoms with increasing the same amount of boron atoms is similar, probably implying the strong bonding between N and B atoms.
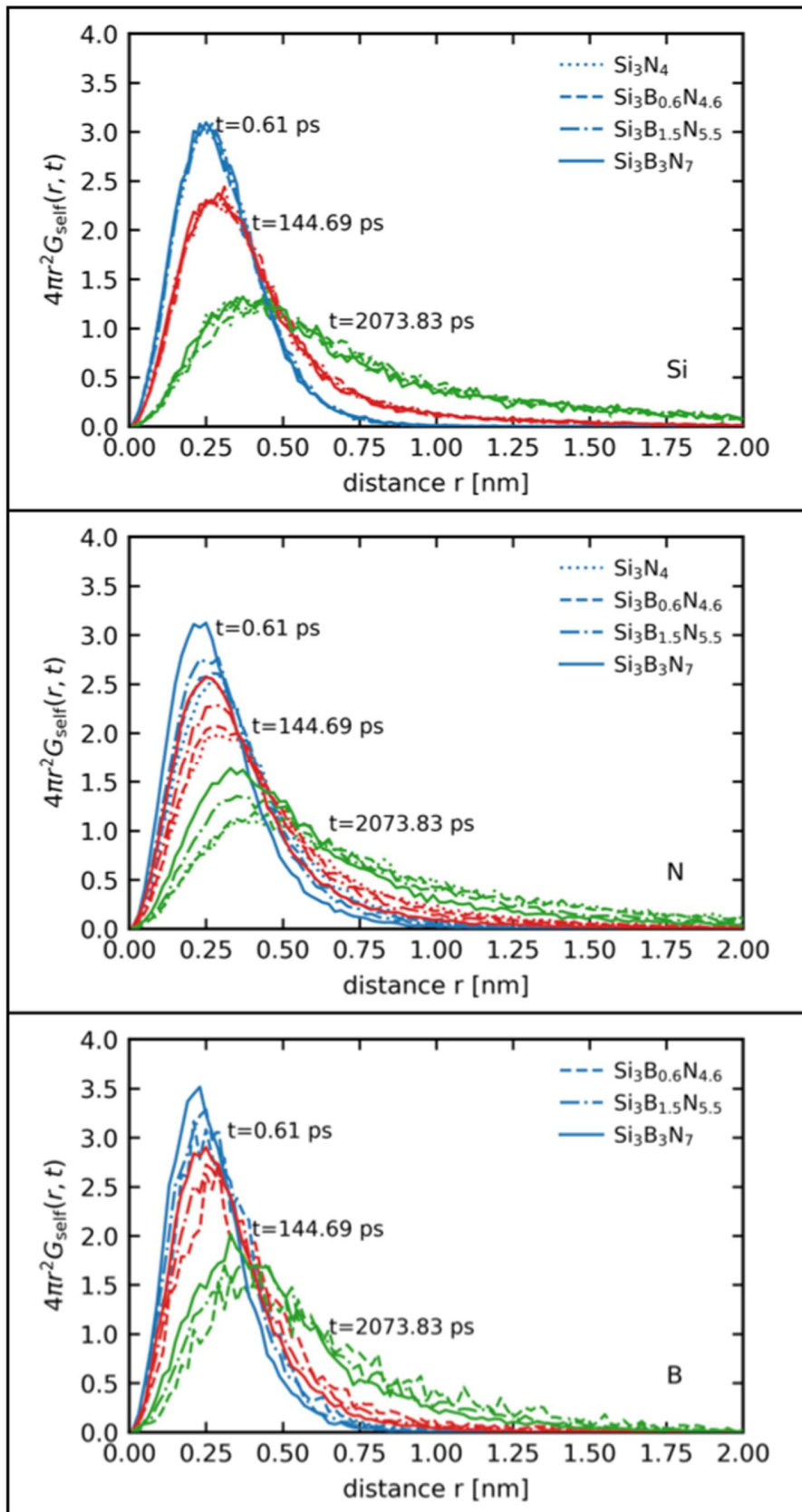
Fig. S3 Self-part van-Hove correlation functions, $4\pi r^2 G_{self}(r, \Delta t)$, for Si (a), N (b) and B (c) atoms from systems of Si_3N_4 (dotted lines), $Si_3B_{0.6}N_{4.6}$ (dashed lines), $Si_3B_{1.5}N_{5.5}$ (dot dashed lines) and $Si_3B_3N_7$ (solid lines) versus distance r at various time intervals $t = 0.61$ ps (blue), $t = 144.69$ ps (red) and $t = 2073.83$ ps (green).
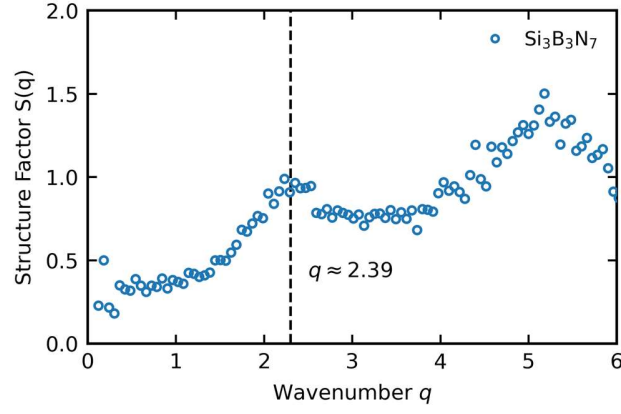

Fig. S4 Structure factor $S(q)$ versus wavenumber (q) for an example system $Si_3B_3N_7$ at temperature $T = 1573$ K. The dashed line is the placed at the position ($q \approx 2.39$) of first local peak in $S(q)$.
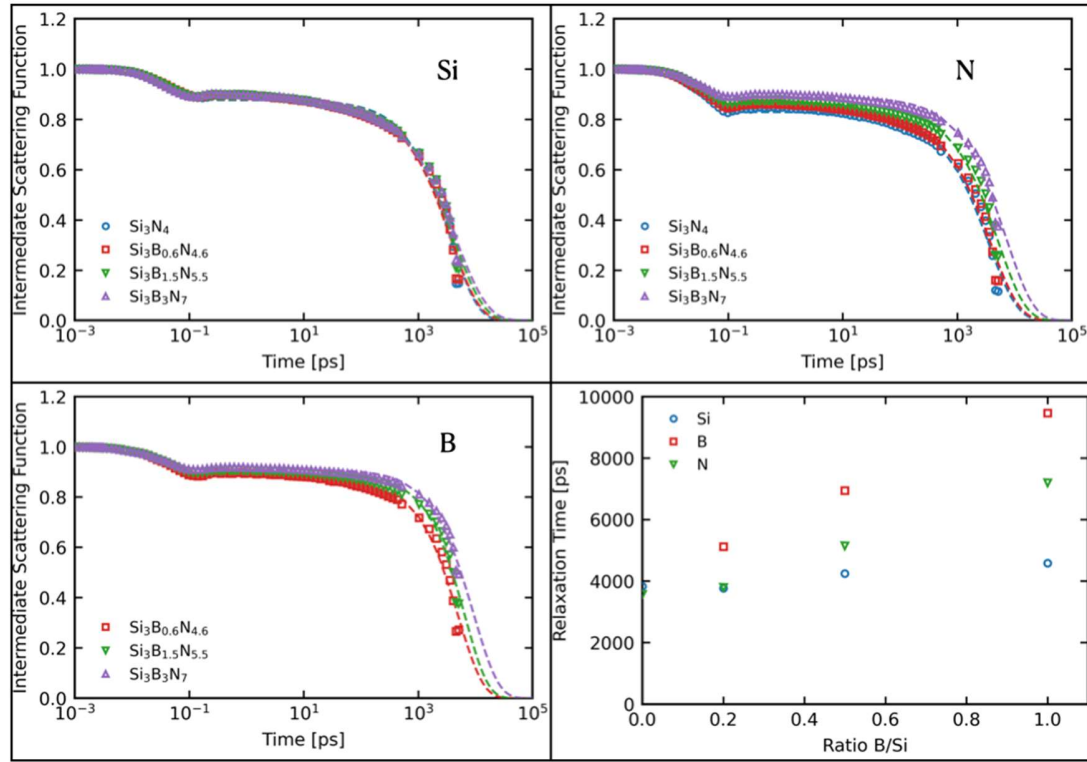
Fig. S5 Self-part intermediate scattering functions as a function of time for Si (a), N (b) and B (c) atoms from systems of Si_3N_4 (blue), $Si_3B_{0.6}N_{4.6}$ (red), $Si_3B_{1.5}N_{5.5}$ (green) and $Si_3B_3N_7$ (purple). Dashed lines: double stretched exponential fittings. (d) is the relaxation times calculated from (a), (b) and (c) for Si (blue), B (red) and N (green) versus B/Si ratio.

References

[1] Donati C; Glotzer S C; Poole P H, et al. Spatial correlations of mobility and immobility in a glass-forming Lennard-Jones liquid. *Physical Review E* 1999, **60:** 3107-3119.

[2] Hansen J-P; McDonald I R. Theory of Simple Liquids: with Applications to Soft Matter. *Elesvier* 2013.

[3] Gebremichael Y; Schrøder T B; Starr F W, et al. Spatially correlated dynamics in a simulated glass-forming polymer melt: Analysis of clustering phenomena. *Physical Review E* 2001, **64:** 051503.

[4] Vogel M; Glotzer S C. Temperature dependence of spatially heterogeneous dynamics in a model of viscous silica. *Physical Review E* 2004, **70:** 061504.